UNIVERSITY OF ADELAIDE LIBRARY
11.11.71

STUDIES OF X-RAYS AND COSMIC RAYS OF GALACTIC ORIGIN

by

Leighton Reginald Barnden, B.Sc. (Hons)

Department of Physics

A thesis

presented for the degree of

Doctor of Philosophy

in the

University of Adelaide

March 1971

CONTENTS

		Page
SUMMARY		*i*
ACKNOWLEDGEMENTS		*iv*
	PART A	
CHAPTER 1	COSMIC RAY ORBITS IN THE INTERPLANETARY MAGNETIC FIELD	1
1.1	Introduction	1
1.2	The Interplanetary Magnetic Field	2
1.3	The Calculation of the Basic Orbital Parameters	5
1.4	Application 1 for Cosmic Ray Orbits	10
1.5	Application 2 for Cosmic Ray Orbits	14
1.6	The Accuracy of the Numerical Calculations	18
CHAPTER 2	THE HELIO-ASYMPTOTIC DIRECTIONS	22
2.1	Introduction	22
2.2	The Conditions for which Asymptotic Directions are Calculated	23
2.3	The Helio-asymptotic Directions	26
2.4	Variations as the Sector Structure Rotates past the Earth	31
CHAPTER 3	TERRESTRIAL EFFECTS OF A GALACTIC ANISOTROPY	38
3.1	Introduction	38
3.2	Solar Effects on a Galactic Anisotropy	40
3.3	Sidereal Variations, Case 1	48
3.4	Sidereal Variations, Case 2	53
3.5	Modulation by the Rotating Sector Structure	56
3.6	The Yearly Average Sidereal Variations	60
CHAPTER 4	THE ORIGIN-OF-SCATTER COEFFICIENTS - THEORY	66
4.1	Introduction	66
4.2	The General Analytical Approach	68
4.3	The Fundamental Flux Increment, $f_{ij}(r,T)$ The Source Function, S	71

Page

4.4 Properties of a cone of Directions in Space 75
The Variation with r of the Separation between Two Guiding Centers.
The Separation of Two Trajectories with Equal Pitch Angles.
The Separation of Two Trajectories with Unequal Pitch Angles.
Summary.

4.5 The Equation for the Origin-of-Scatter Coefficient 84

CHAPTER 5 THE ORIGIN-OF-SCATTER COEFFICIENTS - THE CALCULATIONS 88

5.1 Introduction 88

5.2 The Standard Set of Orbits 89

5.3 Non Orbital Parameters 95
The Spectral Weights of the 10 Rigidity Intervals.
The Scattering Mean Free Paths.

5.4 The Origin-of-Scatter Coefficients 99

CHAPTER 6 COSMIC RAY VARIATIONS ASSOCIATED WITH RADIAL NUMBER DENSITY GRADIENTS 107

6.1 Introduction 107

6.2 The Long Term Average Diurnal Variation 109
The Second Harmonic in the Theoretical Daily Variation.

6.3 Short Term Effects in the Diurnal Variation 121
The Effect of Changing the Amplitude of the Gradient.
The Effect of Changing the Rigidity Dependence of the Gradient.
The Effect of a non-linear gradient.
Changes in the Daily Average with Different Mean Free Paths.

Page

6.4 The Step Gradient - The Forbush Decrease 128
The Effect of Different Approach Velocities V_R.
The Profiles at Different Geographic Longitudes.
The Profiles at Different Geographic Latitudes.
Simulation of an Observed Event.
Increases Prior to Forbush Decreases.
6.5 The Rigidity Dependence of the Forbush Decrease 141
6.6 The Effects of Departures from the Ideal Magnetic Field 142
North-South Anisotropies Associated with Forbush Decreases.
6.7 Conclusions 146

PART B

CHAPTER 7 INSTRUMENTATION FOR TWO EXPERIMENTS TO OBSERVE CELESTIAL X-RAYS 149
7.1 Introduction 149
7.2 The Skylark Vehicle 151
7.3 Experiment Design Considerations 152
7.4 The Flight III Experiment 160
7.5 The Flight IV General Design 165
7.6 Flight IV Electronics 170
7.7 Flight IV Preparation 174

CHAPTER 8 THE RESULTS OF THE ROCKET X-RAY EXPERIMENTS 176
8.1 Introduction 176
8.2 The Flight III Attitude Solution 177
8.3 Countrate Analysis 184
8.4 The Source in Cetus 186
8.5 Observations of Other Sources 191

APPENDICES 193
BIBLIOGRAPHY 212
PUBLICATIONS 216

SUMMARY

This thesis discusses the results of research in two independent fields. Part A presents an analysis of cosmic ray variations using techniques evolved from the calculation of cosmic ray trajectories in a spiral interplanetary magnetic field model, while Part B discusses the design, preparation and results of two rocket-borne X-ray astronomy experiments.

The cosmic ray section divides into a consideration of galactic cosmic rays which (a) reach the Earth without being appreciably scattered, and (b) experience significant scattering en-route to Earth.

In category (a), for selected energies ($\gtrsim$ 50GeV) and for 24 times of day, asymptotic directions at the edge of the solar cavity are calculated in a 4-sector spiral interplanetary magnetic field model, for cosmic rays which arrive in the equatorial plane. These asymptotic directions are strongly dependent on the position of the Earth within the sector structure, and when used to derive the sidereal variations associated with a 1-way and 2-way anisotropy in the galaxy, this dependence causes a 27 cycle/year (13·5 day period) modulation in both the diurnal and semidiurnal variations. For a 1-way galactic anisotropy the diurnal and semidiurnal variations have approximately the same amplitude and the diurnal variation is further modulated at 1 and 2 cycles/year, and the semidiurnal at 1 cycle/year.

In category (b) a new technique is developed which allows the daily variation associated with any arbitrary dependence of cosmic ray number density on heliocentric radius r, to be calculated. For 24 times

of day T, "origin-of-scatter" coefficients $\zeta(r,T)$ are computed, which relate the cosmic ray number density between r and r + Δr to the flux of cosmic rays observed on Earth, which were *last*-scattered in that region. The number density gradients associated with the average, enhanced and asymmetric diurnal variations and with different Forbush decrease profiles are calculated. In addition, an estimate of the average scattering mean free paths in interplanetary space is given. A small semidiurnal variation is predicted when linear radial gradients are considered. Forbush decrease profiles are shown to vary strongly with the effective radial approach velocity of the shock; with preliminary decreases becoming prominant at very low velocities ($\lesssim$ 400km/sec). It is shown that the general features of the world-wide variation in the Forbush decrease profiles for a given event can be explained in terms of the approach of a simple step decrease in cosmic ray number density. A mechanism to account for the N-S anisotropy which accompanies some Forbush decreases is suggested, and a brief discussion of further applications is given.

The X-ray astronomy section discusses flights III and IV prepared by the Universities of Adelaide and Tasmania (UAT). Flight III was partially successful, with two detectors, each of 11·7 cm^2 area, out of a total sensitive area of 150 cm^2, working satisfactorily. Superposition of several scans yielded evidence for a new X-ray source Cet XR-1 at high galactic lattitude, and an upper limit to the flux from the variable Cen XR-2. Flight IV carried 9 independent detector systems of total area > 2000 cm^2, but a vehicle malfunction caused the

experiment to be destroyed and there were no results. Apart from the recovered flight III package, the flight IV instrumentation was all newly developed. The factors influencing its general design are discussed and a brief account is given of the on-board pulse-height-analysis and associated logic systems, and of the calibration and environmental-testing procedures used.

This thesis contains no material which has been accepted for the award of any other degree or diploma in any University.

To the best of my knowledge and belief, the thesis contains no material previously published or written by another person except where due reference is made in the text.

Leighton Barnden

ACKNOWLEDGEMENTS

The first part of my degree was spent on experimental work. However the greater part of my thesis (Part A) deals with the cosmic ray analysis performed during the period following this. The author acknowledges the guidance given, and the suggestions made by Prof. K.G. McCracken in this work. In addition the author is indebted to Dr. L.J. Gleeson, Mr. I.D. Palmer and Mr. I. Urch for many helpful comments and valuable discussions. The computer subroutines for the calculation of cosmic ray orbits in interplanetary space were developed by Mr. D. O'Brien.

The experimental work (Part B) was carried out by the author as a member of the joint Universities of Adelaide and Tasmania (UAT) rocket x-ray astronomy group. The author worked in close association with Mr. R.J. Francey of the University of Tasmania on UAT flights III and IV, and Mr. I.R. Tuohy of the University of Adelaide (flight IV). The author would like to thank Mr. Francey and Mr. Tuohy for the enthusiastic way in which they approached their work, and for the many memorable hours of close cooperation spent working with them. Where one of us was responsible for a particular aspect of experiment development, acknowledgement is made in the text. I am indebted to Mr. L.E. Doherty, who was able to transform the specifications given to him for the flight IV on-board data analysis system into a reliable hardware unit.

The author was wholly responsible for the flight III attitude solution and data analysis. There were no results from flight IV.

The author gratefully acknowledges the willing advice and encouragement given by his supervisor Dr. A.G. Gregory throughout this degree.

I am indebted to Rosemary Kampschroer for the excellent job she made of the indian ink drawings used in this thesis. Finally I would like to thank my wife for her perseverance and for the invaluable assistance given with the plotting of the diagrams.

UNIVERSITY OF ADELAIDE LIBRARY

PART A

CHAPTER 1

COSMIC RAY ORBITS IN THE INTERPLANETARY MAGNETIC FIELD

1.1 Introduction

In order to gain a better understanding of the variations in cosmic ray intensity observed at the Earth's surface the detailed histories of selected cosmic rays are examined. To do this a model of the solar system is constructed in which those parameters which influence the motion of cosmic rays are given the average observed values. Using this model cosmic ray orbits are traced backwards from the Earth to establish the details of their past behaviour.

The factors which influence the cosmic ray motion include the magnetic and electric fields present within the solar system. Initially it is the Earth's magnetic field which is experienced and then, beyond this, the interplanetary magnetic field. Electric fields are taken to be zero everywhere; this is a simplification which is valid for the high particle energies considered herein. The effects of the Earth's magnetic field have been investigated by Malmfors (1945); Brunberg and Dattner (1953); Jory (1956); McCracken et al (1962), and numerous other authors. In each of these investigations, the "asymptotic directions" were calculated for a comprehensive range of cosmic ray energies and directions of arrival. In these studies the asymptotic direction of a cosmic ray was the

direction in which it was travelling just outside the Earth's magnetosphere. Because the details of a cosmic ray orbit are strongly dependent upon the locality of the detector under consideration, these asymptotic directions were necessarily calculated for particular points on the Earth's surface.

In this chapter this earlier work is extended and a method to investigate the cosmic ray orbits in the interplanetary magnetic field is developed. In section 1.2 observations of the interplanetary magnetic field are discussed and the model chosen to represent it is described. Section 1.3 gives a brief account of the basic orbital calculation method, while sections 1.4 and 1.5 discuss the calculation of further orbital parameters which are required for two different applications in later chapters.

1.2 The Interplanetary Magnetic Field

Direct observations of the interplanetary magnetic field (Wilcox and Ness, 1965) have shown that near 1 AU the average field strength is about 5 gamma ($1\gamma = 10^{-5}$ oersted), and the average field direction lies about 45° west of the Earth-Sun line. These and later observations (Fairfield and Ness, 1967; Coleman et al, 1967) confirm the predictions of Parker, 1963 for a magnetic field in which the lines of force are in the shape of Archimedes spirals.

In addition these observations revealed two other important features of the interplanetary magnetic field; namely

(a) The polarity of the large-scale magnetic field defines "sectors" in interplanetary space, such that within each sector one polarity is predominant, and at the sector boundary there is a sharp transition to the opposite polarity. In the early observations (until mid 1965), four well defined sectors were observed during each rotation of the Sun. Three of these sectors were of the same extent in solar longitude, while the fourth was approximately half this size. With the approach of solar maximum the sector structure slowly became more random, until by 1966 it was changing markedly over the solar rotation period. Schatten et al (1968) have observed the evolution of new sectors to be associated with areas of enhanced activity on the Sun's surface.

(b) On a small scale the interplanetary magnetic field is highly variable in magnitude and direction. Often the idealised spiral structure of Parker can only be seen by averaging over several hours of data. Over a time scale of minutes the magnetic field strength may vary from 3-20 gamma and the longitude and latitude of the magnetic field vector may change by 90° or more. These so called irregularities in the interplanetary magnetic field will scatter cosmic rays from the guiding center spiral motions determined by the large scale magnetic field.

The Mathematical Model of the Spiral Field

In this analysis the strength and direction of the interplanetary magnetic field at 1 AU are given by B_E and G_E respectively. G_E is commonly called the garden hose angle. The radial component B_{rE}, of the field at 1 AU is then

$$B_{rE} = B_E \cos G_E$$

Spherical polar co-ordinates (r, θ, ϕ) with the origin at the Sun are used. The OXY plane is defined by the Earth's equatorial plane and for simplicity this is considered to be coplanar with the ecliptic. The OX axis is defined by the Earth-Sun line as shown in Figure 1.1. In spherical co-ordinates the components of the magnetic field (B_r, B_θ, B_ϕ), at any point (r, θ, ϕ) are given by

$$B_r(r, \theta, \phi) = B_{rE} \left(\frac{r_E}{r}\right)^2$$

$$B_\theta(r, \theta, \phi) = 0$$

$$B_\phi(r, \theta, \phi) = B_r(r, \theta, \phi) \frac{r\Omega}{v} \sin\theta$$

Where r_E is the heliocentric radius at the orbit of Earth, Ω is the angular velocity of rotation of the Sun and v is the solar wind velocity. In the expression for B_ϕ, the factor $r\Omega/v$ is tan G, where G is the garden-hose angle at the point in question.

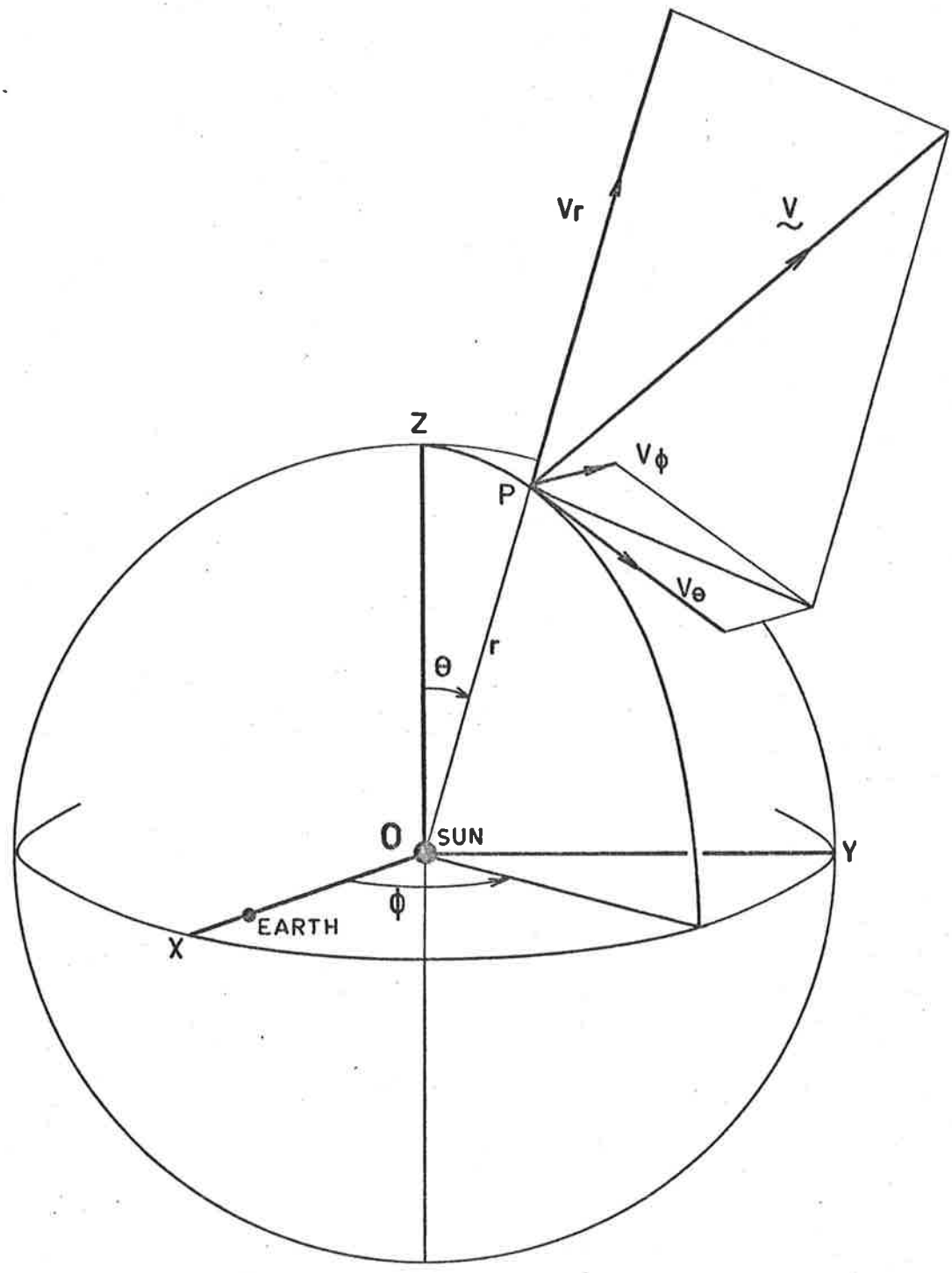

Figure 1.1 The spherical polar coordinate system showing (r,θ,ϕ) and (V_r, V_θ, V_ϕ)

1.3 The Calculation of the Basic Orbital Parameters

The basic parameters at any point along the orbit are the position and direction of the cosmic ray given by (r, θ, ϕ) and (V_r, V_θ, V_ϕ) respectively (see Figure 1.1) in spherical polar co-ordinates. These are obtained point by point along the orbit by numerical integration of the equations of motion of the cosmic ray. In common with earlier work of this nature, the trajectory is traced backwards by solving the equations of motion for a negatively charged cosmic ray ejected from the Earth in the direction of arrival and with the same magnitude of velocity of arrival as the real cosmic ray. In this way, for a particular model of the interplanetary magnetic field we can investigate the trajectory of a real cosmic ray (of positive charge) using a knowledge of its arrival parameters alone.

For the purpose of these calculations the cosmic rays are ejected from the point corresponding to the center of the Earth, and it is assumed that they immediately experience the interplanetary magnetic field. In terms of the actual physical situation, the effects of the Earth's magnetic field are accounted for by ejecting the cosmic ray in the asymptotic direction corresponding to the required direction of arrival at the detector of interest.

The Equations of Motion

A cosmic ray of inertial mass m and charge q, moving in a magnetic field $\underset{\sim}{B}$ with a velocity $\underset{\sim}{V}$ or $\frac{d\underset{\sim}{r}}{dt}$, where $\underset{\sim}{r}$ is its position vector, obeys the equation

$$m \frac{d^2\underset{\sim}{r}}{dt^2} = q \frac{d\underset{\sim}{r}}{dt} \times \underset{\sim}{B} \qquad (1.2)$$

or $$\underset{\sim}{F} = q (\underset{\sim}{V} \times \underset{\sim}{B})$$

in the M.K.S. system of units, where $\underset{\sim}{F}$ is the force vector experienced by the particle. It can be seen that by replacing q and $\underset{\sim}{V}$ by -q and $-\underset{\sim}{V}$ the same equation is obtained, so that the technique of calculating orbits by ejecting an oppositely charged cosmic ray back in the direction of arrival (i.e. with $-\underset{\sim}{V}$) is valid. This results in an enormous simplification of the problem.

In spherical polar co-ordinates equation (1.2) can be written as the six following first order differential equations

$$\frac{dV_r}{dt} = \frac{e}{m} (V_\theta B_\phi - V_\phi B_\theta) + \frac{V_\theta^2}{r} + \frac{V_\phi^2}{r}$$

$$\frac{dV_\theta}{dt} = \frac{e}{m} (V_\phi B_r - V_r B_\phi) - \frac{V_r V_\theta}{r} + \frac{V_\phi}{r \tan\theta}$$

$$\frac{dV_\phi}{dt} = \frac{e}{m}(V_r B_\theta - V_\theta B_r) - \frac{V_r V_\phi}{r} - \frac{V_\theta V_\phi}{r \tan\theta}$$

$$\frac{dr}{dt} = V_r$$

$$\frac{d\theta}{dt} = \frac{V_\theta}{r} \qquad (1.3)$$

$$\frac{d\phi}{dt} = \frac{V_\phi}{r \sin\theta}$$

B_r, B_θ and B_ϕ are defined at any point (r, θ, ϕ) according to equations (1.1), so the above set of differential equations can be integrated numerically.

The numerical solution of the above equations is achieved using Hamming's modified predictor-corrector method as described in the IBM System/360 Scientific Subroutine Package. At the end of each step (i.e. a small interval of time) this method yields a new set of r, θ, ϕ, V_r, V_θ, V_ϕ, thereby defining a new section of the orbit. Each new $(\underset{\sim}{r}, \underset{\sim}{V})$ is calculated from the previous four $(\underset{\sim}{r}, \underset{\sim}{V})$ on the orbit, so that this method is not self-starting (there is only one $(\underset{\sim}{r}, \underset{\sim}{V})$ to begin with). To obtain the four starting points a special Runge-Kutta procedure (also described in the above reference) is added to the predictor-corrector method. If the interplanetary magnetic field is given a sector structure, then each time a sector boundary

is crossed, the Runge-Kutta procedure is used to restart the iteration from the point where the orbit crosses the sector boundary, but with the polarity of the magnetic field reversed.

The step length which determines the separation of adjacent points along the orbit is included as a variable within the program. Typically this takes the value $\Delta t = 0{\cdot}5$ seconds near $r = 1$ AU, so that the points are separated by $1{\cdot}5 \times 10^{8}$m or 10^{-3}AU. The choice of the step length is influenced by two requirements:

(i) To maintain satisfactory accuracy. The errors in the iteration programme increase strongly with increasing step length.

(ii) To minimize the time required to compute the orbit out to the required distance.

Increasing the step length saves time, but the accuracy suffers, and vice-versa. A good compromise is reached by varying the step length as a function of the heliocentric radius of the point along the orbit. The step length is halved when the heliocentric radius is reduced by a factor of $\sqrt{2}$, and doubled when the radius is increased by a factor of $\sqrt{2}$.

The accuracy of the numerical solution is monitored along the

orbit by calculating the fractional change in velocity ε of the cosmic ray, where

$$\varepsilon = \frac{(V_r^2 + V_\theta^2 + V_\phi^2)^{\frac{1}{2}}}{V_i} - 1.0 \qquad (1.4)$$

where V_i is the initial or ejection velocity. ε is typically 10^{-9} at the end of an orbit. The seriousness of this error is evaluated by calculating the change in rigidity dP ($\simeq$ energy) corresponding to ε. The step lengths are chosen to keep dP/P < 1%, from the beginning to the end of the orbit (see section 1.6).

The subroutines to carry out these numerical integration procedures were developed by Mr. D. O'Brien. The author corrected these and added all of the facilities which are described beyond this point.

The basic method of orbit tracing described above is used in two different applications:

(i) The calculation of asymptotic directions outside the solar cavity for use in the study of the sidereal variation.

(ii) The calculation of the detailed behaviour of the orbits in the interplanetary magnetic field for use in the study of the solar daily variations.

The special parameters required in each of these applications, and the methods used to derive them, are discussed in sections 1.4 and 1.5 respectively.

1.4 Application 1 for Cosmic Ray Orbits

The first application of the orbital calculations is to find the directions from which the observed cosmic rays arrive at the boundary of the solar cavity or heliosphere, by tracing orbits from Earth out to this distance. The solar cavity is that region of space influenced by the solar wind and which therefore contains the spiral solar magnetic field. Such "asymptotic" directions are only meaningful of course for those high energy cosmic rays which are not scattered in traversing the solar cavity to the Earth. The population of cosmic rays which meets this requirement is described in more detail in Chapter 3. The cosmic ray directions at the edge of the solar cavity are analogous to the asymptotic directions (at the edge of the magnetosphere) of McCracken et al, 1962. To avoid confusion where both types of directions are being referred to, the directions just outside the Earth's magnetic field are called geo-asymptotic directions and directions just outside the Sun's magnetic field are called helio-asymptotic directions.

The helio-asymptotic directions are calculated in a 4-sector

interplanetary magnetic field, where all sectors are of the same extent (90°) in heliocentric longitude and the sector boundaries are taken to extend 'upwards' normal to the ecliptic. The sector structure is incorporated into the basic numerical method as follows.

After each iteration a test is made to find whether the new point, P, is across a sector boundary relative to the last point. To do this the angle δ, between the sector boundary and P, defined by $\angle S'OP$ in Figure 1.2 is calculated. From Figure 1.2

$$\delta = \phi + \angle S'OE$$

$$= \phi + \Delta - \angle S'OS$$

where Δ is the angular separation of the Earth from the reference sector OS'S. Now $\angle S'OS$ is the angular separation between two points on the same line of force but at different heliocentric radii. Any one line of force is simply the locus of volume elements of plasma emitted from a single region on the Sun. For field line OS'S the angle between the radius vector OT through the emitting region on the Sun and the radius vector through the point $S'(r, \theta, \phi)$, is the angle through which the emitting ragion has rotated in the time t taken by the plasma to reach S'. The plasma has a radial velocity v_p, therefore

$$t = \frac{r}{v_p}$$

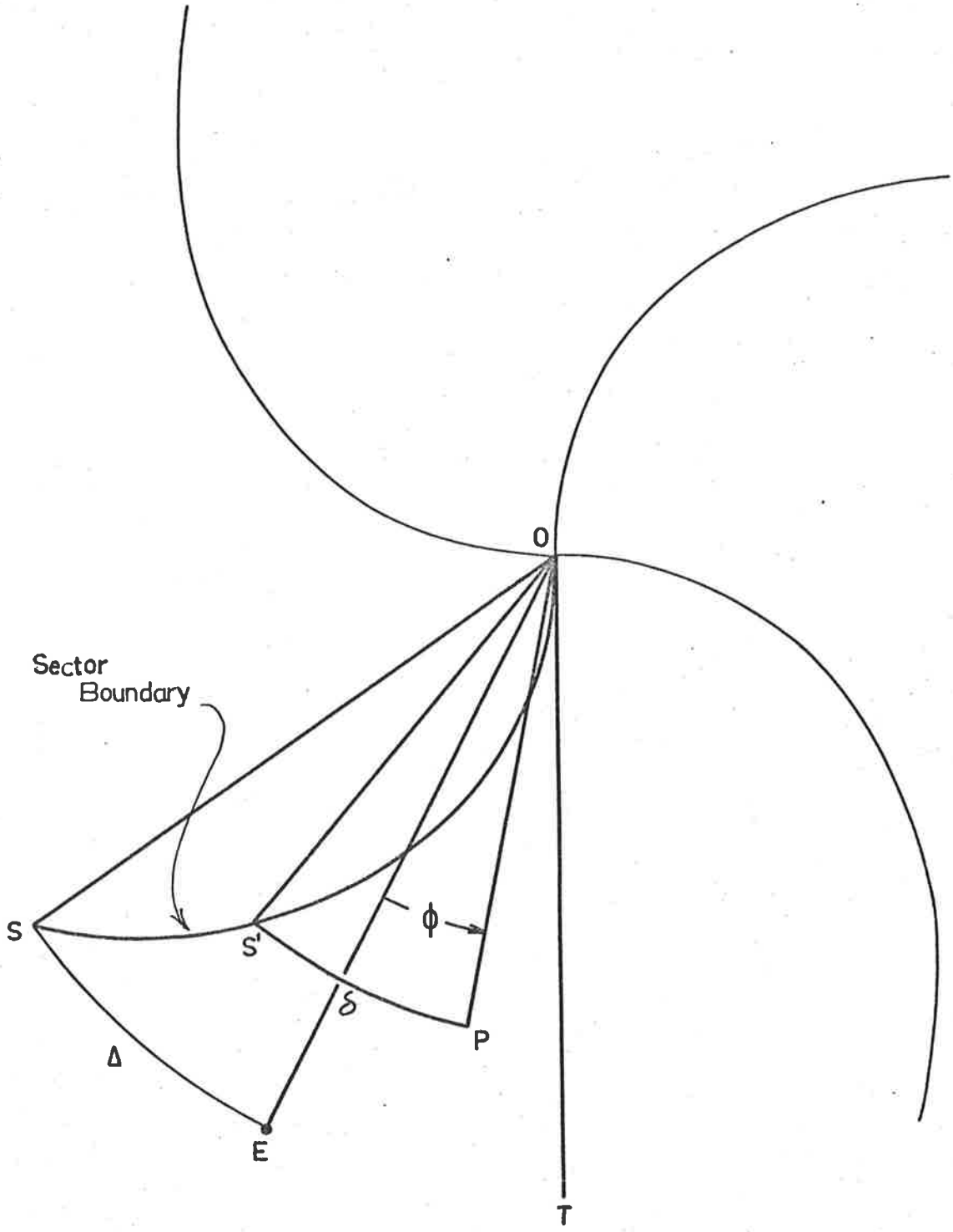

Figure 1.2 The geometry used in the calculation of the angular separation of point P from the approaching sector boundary.

$$\text{and} \quad \angle TOS' = \Omega t = \frac{\Omega r}{v_p}$$

where Ω is angular velocity of Sun.

$$\text{similarly} \quad \angle TOS = \frac{\Omega r_E}{v_p}$$

$$\text{Therefore} \quad \angle S'OS = \angle TOS - \angle TOS' = \frac{\Omega}{v_p} \cdot (r_E - r)$$

$$\text{and} \quad \delta = \phi + \Delta - \frac{\Omega}{v_p} \cdot (r_E - r) \qquad (1.5)$$

In this way δ_2 is calculated for each new point and compared with the value δ_1 for the previous point.

$$\text{If } \delta_2 \leq \frac{n\pi}{2} < \delta_1 \quad \text{or} \quad \delta_1 \leq \frac{n\pi}{2} < \delta_2$$

where n is an integer, the two points are considered to be on different sides of a sector boundary. In this event the last point on the orbit before the boundary crossing (i.e. $\delta = \delta_1$) is returned to the Runge-Kutta subroutine and the numerical process is restarted from that point but with the opposite polarity field.

The helioasymptotic direction of arrival is taken to be the direction of the (negatively charged) cosmic ray velocity vector at r = 10 AU. The choice of 10 AU for the extent of the solar cavity is discussed in Chapter 2.1. The helioasymptotic direction is expressed

in terms of longitude and latitude (Λ, Ψ) relative to the axes shown in Figure 1.1.

To estimate this longitude and latitude, consider the axes PX', PY', PZ' at P such that PX'//OX, PY'//OY and PZ'//OZ where OX, OY and OZ are the axes shown in Figure 1.1. In Figure 1.3 the velocity components at P relative to the new axes are shown. PR is the component of $\underset{\sim}{V}$ parallel to the ecliptic, and RQ is the component of $\underset{\sim}{V}$ normal to the ecliptic. PS is the component of PR parallel to the plane containing V_r and V_θ, and SR is the component of PR normal to this plane.

From Figure 1.3

$$RQ = V_r \cos\theta - V_\theta \sin\theta$$

$$PS = V_r \sin\theta + V_\theta \cos\theta$$

$$SR = V_\phi$$

Now $$\Lambda = \angle RPQ = \arctan\left(\frac{QR}{PR}\right)$$

$$= \arctan\left(\frac{PU}{PR}\right)$$

$$= \arctan\left(\frac{V_r\cos\theta - V_\theta\sin\theta}{((V_r\sin\theta + V_\theta\cos\theta)^2 + V_\phi^2)^{0.5}}\right) \qquad (1.6)$$

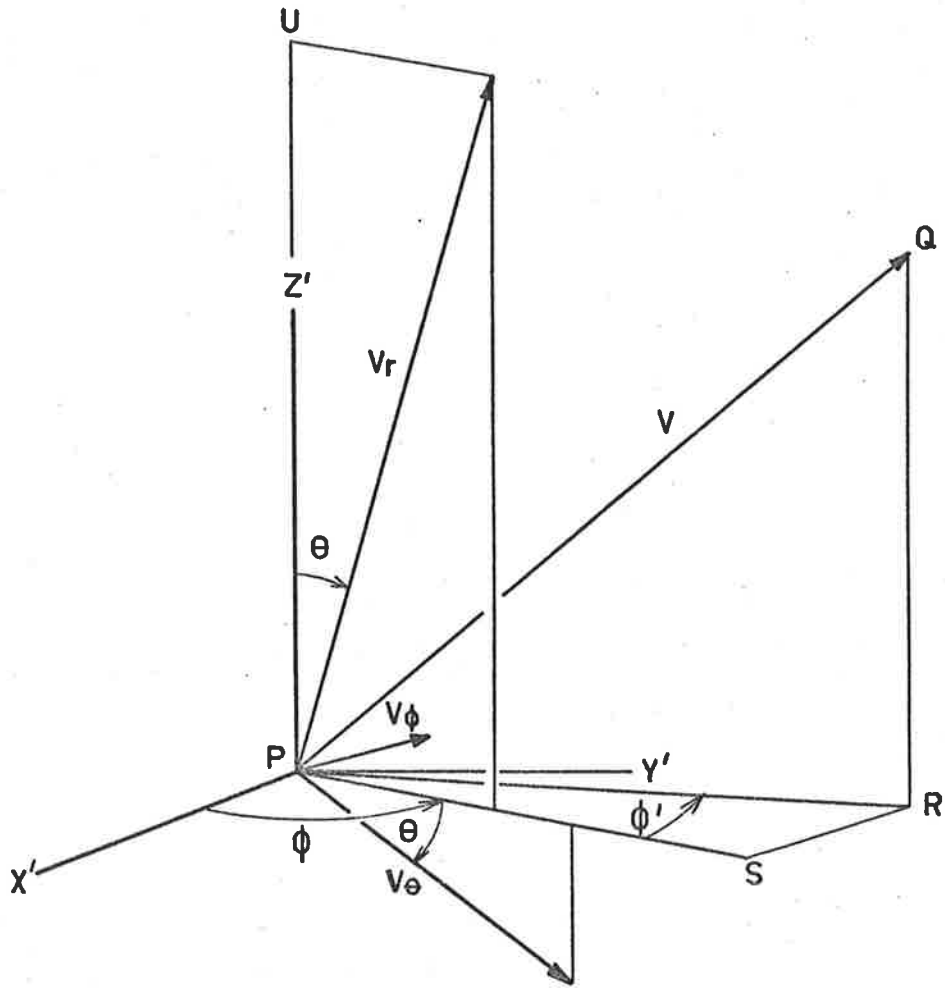

Figure 1.3 The geometry used in the calculation of the cosmic ray helio-asymptotic direction (Λ,Ψ).

and $$\Psi = \angle X'PR = \phi + \phi'$$

$$= \phi + \arctan\left(\frac{SR}{PS}\right)$$

$$= \phi + \arctan\left(\frac{V_\phi}{V_r \sin\theta + V_\theta \cos\theta}\right) \qquad (1.7)$$

These expressions yield the helio-asymptotic direction from the $(r, \theta, \phi, V_r, V_\theta, V_\phi)$ at 10 AU.

1.5 Application 2 for Cosmic Ray Orbits

The orbits computed in this category are used to investigate solar controlled variation phenomena in the cosmic ray intensity. The cosmic rays which exhibit these intensity variations lie between 0 and $\sim$ 60GV, and as such experience significant scattering in the interplanetary medium. It is convenient here to work in terms of rigidity P rather than energy E. $P \simeq E$ except when $P \lesssim 1$GV; the exact relationship between P and E is given in appendix 1.

The cosmic rays in this rigidity range follow well behaved guiding center motions and their guiding centers approximate closely to a spiral magnetic field line. It is therefore considered unnecessary to include a sector structure in the model of the interplanetary magnetic field adopted for these orbital calculations.

The special requirement for this application is the calculation of several orbital parameters whenever the guiding center of the orbit crosses a sphere defined by $r = \frac{N}{25}$ AU, where r is heliocentric radius and N is an integer. The parameters which are necessary for this application - the calculation of the "origin of scatter" coefficients in Chapters 4 and 5 - are

(i) The distance x around the orbit between the point P and the Earth.

(ii) The distance x folded with $\frac{1}{r}$, i.e. $y = \sum_i \frac{\ell_i}{r_i}$ where ℓ_i is the distance advanced along the orbit in iteration step i, and r_i is the heliocentric radius in AU of that section of orbit.

(iii) The pitch angle of the orbit at P.

In all 180 orbits are calculated with typically 75 read-out points per orbit.

In addition to the three parameters listed above, there are further parameters which are necessarily computed as stepping stones to these three, and which are also stored on magnetic tape. These are

(iv) The co-ordinates (r, θ, ϕ) of the point P on the orbit.

(v) The magnetic field strength $|B|$ at P.

(vi) The guiding center co-ordinates (r_c, θ_c, ϕ_c) corresponding to point P on the orbit.

(vii) The radius of gyration ρ of the orbit at point P.

Calculation of the guiding center co-ordinates

The equation of motion of a charged particle in a magnetic field can be written

$$\frac{d\underset{\sim}{p}}{dt} = q\,\underset{\sim}{V} \times \underset{\sim}{B} \qquad (1.8)$$

where $\underset{\sim}{p}$ is momentum, $\underset{\sim}{V}$ is velocity, $\underset{\sim}{B}$ is magnetic field strength and q is charge.

Since the term on the right hand side of this equation is perpendicular to $\underset{\sim}{V}$, the absolute value of the momentum and therefore the velocity remains constant. The motion is therefore a superposition of a motion parallel to $\underset{\sim}{B}$ ($V_\parallel$ in the diagram) and a circular motion in the plane normal to $\underset{\sim}{B}$ ($V_\perp$ in the diagram). The instantaneous center of the circular motion is called the center of gyration.

Consider the circular motion in the plane normal to $\underset{\sim}{B}$. We can equate the inward force expressed in equation 1.8 above, to the outward or centrifugal force.

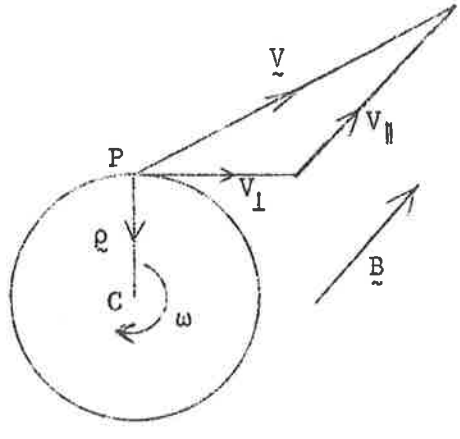

$$\text{i.e.} \quad m\omega^2 \underset{\sim}{\rho} = q \underset{\sim}{V} \times \underset{\sim}{B} \tag{1.9}$$

where m is inertial mass, ω is angular frequency of circular motion and $\underset{\sim}{\rho}$ is vector from P on the orbit, to the center of gyration C. If we now replace $\underset{\sim}{V}$ by $\underset{\sim}{V}_{\parallel} + \underset{\sim}{V}_{\perp}$ equation (1.9) becomes

$$m\omega^2\rho = q\, V_{\perp}\, B$$

$$\text{or since} \quad V_{\perp} = \omega\rho$$

$$\omega = \frac{qB}{m}$$

substituting this in equation (1.9) yields

$$\underset{\sim}{\rho} = \frac{m}{qB^2} \underset{\sim}{V} \times \underset{\sim}{B} \tag{1.10}$$

Having found $\underset{\sim}{\rho}$ the position vector $\underset{\sim}{r}_c$ of the guiding center C, corresponding to the point P($\underset{\sim}{r}$, $\underset{\sim}{V}$) on the orbit, is given by

$$\underset{\sim}{r}_c = \underset{\sim}{r} + \underset{\sim}{\rho} \tag{1.11}$$

In this way the guiding center heliocentric radius r_c is calculated for each new P($\underset{\sim}{r}$, $\underset{\sim}{V}$) to test whether an $r = \frac{N}{25}$ AU surface has been crossed. If the test is negative the next iteration is carried out, a new r_c is derived and the test repeated. If the test is positive some further calculations are carried out to produce the remaining orbital parameters. The magnetic field strength at P is given by

$|B| = (B_r^2 + B_\phi^2)^{\frac{1}{2}}$. The other guiding center co-ordinates θ_c and ϕ_c are given by

$$\theta_c = \arccos\left(\frac{z_c}{r_c}\right) \tag{1.12}$$

$$\phi_c = \arccos\left(\frac{x_c}{(x_c^2 + y_c^2)^{\frac{1}{2}}}\right) \tag{1.13}$$

The pitch angle α at P is derived using

$$\underset{\sim}{V} \cdot \underset{\sim}{B} = |V|.|B| \cos\alpha = V_x B_x + V_y B_y + V_z B_z$$

$$\text{i.e.} \quad \alpha = \arccos \frac{V_x B_x + V_y B_y + V_z B_z}{VB} \tag{1.14}$$

The proximity of the read-out points to $r = \frac{N}{25}$ AU is $\leq \ell$, the iteration step length along the orbit. For steps of 0·5 seconds, $\ell = 10^{-3}$ AU (assuming V = c), so the maximum error is $\sim$ 2·5% of $^1/_{25}$ AU, (the fundamental distance increment used here). Over the many orbits used in each calculation (see Chapter 5) this error will tend to average itself out.

1.6 The Accuracy of the Numerical Calculations

At each read-out point the program gives an estimate of the error in the form $\frac{dV}{V}$ (see equation 1.4). Such an error can be regarded as the result of the particle changing its rigidity P as it

progresses along its orbit. The following calculation relates the actual velocity change to the effective rigidity change.

Particle momentum $p = m_o V (1 - V^2/c^2)^{-\frac{1}{2}}$

Thus rigidity $P = \frac{pc}{Zq} = \frac{m_o c}{Zq} \cdot V(1 - V^2/c^2)^{-\frac{1}{2}}$

where m_o = rest mass of cosmic ray, V is its velocity, Zq is its charge, and c = velocity of light.

Differentiating with respect to V we obtain

$$\frac{dP}{dV} = \frac{m_o c}{Z} (1 - V^2/c^2)^{-3/2}$$

Now $E = m_o c^2 (1 - V^2/c^2)^{-\frac{1}{2}}$

so $E^3 = m_o{}^3 c^6 (1 - V^2/c^2)^{-3/2}$

Hence $\frac{dP}{dV} = \frac{E^3}{M_o^2 c^5 Zq}$

or $dP = (\frac{E}{q})^3 \cdot (\frac{q}{m_o})^2 \cdot \frac{1}{c^4 Z} \cdot \frac{dV}{c}$ volts

$= E^3 (GeV) \cdot 10^{27} \cdot 10^{16} \cdot \frac{10^{-32}}{81} \cdot 10^{-9} \cdot \frac{dV}{c}$ GV

for a hydrogen atom.

Thus $dP = 1{\cdot}2\ E^3 (GeV) \cdot \frac{dV}{c}$ GV

$\simeq 1{\cdot}2\ E^3 (GeV) \cdot \frac{dV}{V}$ GV

$\frac{dV}{V}$ is calculated in the program and E is known.

Table 1.1 shows the maximum error ε (= $\frac{dV}{V}$) encountered over all orbits calculated for each cosmic ray energy considered. The corresponding fractional change in particle rigidity is also given.

TABLE 1.1

Errors in the Orbital Calculations

Energy E GeV	Rigidity P GV	Step Length at 1 AU	Maximum Error dV/V	Equivalent dP/P
0·83	1·5	0·3 sec	9×10^{-5}	5×10^{-5}
2·69	3·5	0·3	1×10^{-6}	1×10^{-5}
4·64	5·5	0·3	3×10^{-7}	7×10^{-6}
6·62	7·5	0·3	1×10^{-7}	5×10^{-6}
8·61	9·5	0·4	2×10^{-7}	2×10^{-5}
12·10	13·0	0·5	2×10^{-7}	3×10^{-5}
16·09	17·0	1·0	8×10^{-7}	2×10^{-4}
24·08	25·0	1·0	3×10^{-7}	1×10^{-4}
34·07	35·0	0·5	9×10^{-8}	1×10^{-4}
44·07	45·0	0·5	1×10^{-8}	2×10^{-5}
75·0	75·93	0·5	5×10^{-7}	2×10^{-3}
100·0	100·93	0·5	6×10^{-7}	7×10^{-3}
200·0	200·93	0·5	2×10^{-7}	8×10^{-3}
400·0	400·93	0·5	7×10^{-8}	1×10^{-2}

Most orbits had errors 2 orders of magnitudes smaller than these worst cases. Furthermore, in these worst cases the large error was frequently present immediately after the initial Runge-Kutta

starting iteration, and beyond this only a relatively small error was introduced.

The maximum errors in the cosmic ray orbits are such as to have no significant effect on the conclusions drawn in their respective applications.

CHAPTER 2

THE HELIO-ASYMPTOTIC DIRECTIONS

2.1 Introduction

The helio-asymptotic direction of a cosmic ray is defined to be the direction from which the cosmic ray arrives at the boundary of the solar cavity. I will now discuss the helio-asymptotic directions computed using the numerical methods described in sections 1.3 and 1.4. The solar cavity referred to above is an idealised model consisting of a volume of space, inside which there is ordered flow of the solar wind and which therefore contains the solar magnetic field. Outside the solar cavity lies the interstellar medium with its own large scale magnetic field and possibly an anisotropic cosmic ray flow. Schatten and Wilcox (1969) designate the solar cavity as the heliosphere and its boundary the heliopause, suggesting the analogy which exists with the magnetosphere and the magnetopause. Contemporary estimates of the extent of the solar cavity at solar minimum range from 5 - 50 AU (Quenby, 1967; Wang, 1970). For the present purpose the directions of travel of the cosmic rays at 10 AU are taken to be the helio-asymptotic directions. Much of the discussion given in this chapter and in chapter 3 is accurate only for times of solar minimum, for it is only then that the interplanetary magnetic field has a well defined sector structure, as has been incorporated in the model used here.

2.1

A helio-asymptotic direction is defined by (Λ,Ψ), where Λ is asymptotic latitude and Ψ is asymptotic longitude. Λ is measured from the equatorial plane (assumed here to be the same as the ecliptic), and Ψ is measured eastwards from the Sun-Earth direction (see Figure 2.1a). In the remainder of this chapter and in chapter 3, the term helio-asymptotic is abbreviated to asymptotic.

In section 2.2 the properties of the individual cosmic rays for which asymptotic directions are calculated, and the values used for the parameters of the interplanetary magnetic field model, are specified. Section 2.3 presents the asymptotic directions and discusses the features which emerge with reference to plots of selected orbits. All directions given in this section were calculated for the Earth in a fixed position relative to the interplanetary sector structure. In section 2.4 asymptotic directions for another two positions of the Earth relative to the sector structure are presented, and the features of the asymptotic directions which vary over the three positions are discussed, again with reference to plots of representative orbits.

2.2 The Conditions for which Asymptotic Directions are Calculated

The asymptotic directions calculated here are ultimately used to study sidereal cosmic ray intensity variations in chapter 3. With this in mind an average interplanetary magnetic field is chosen,

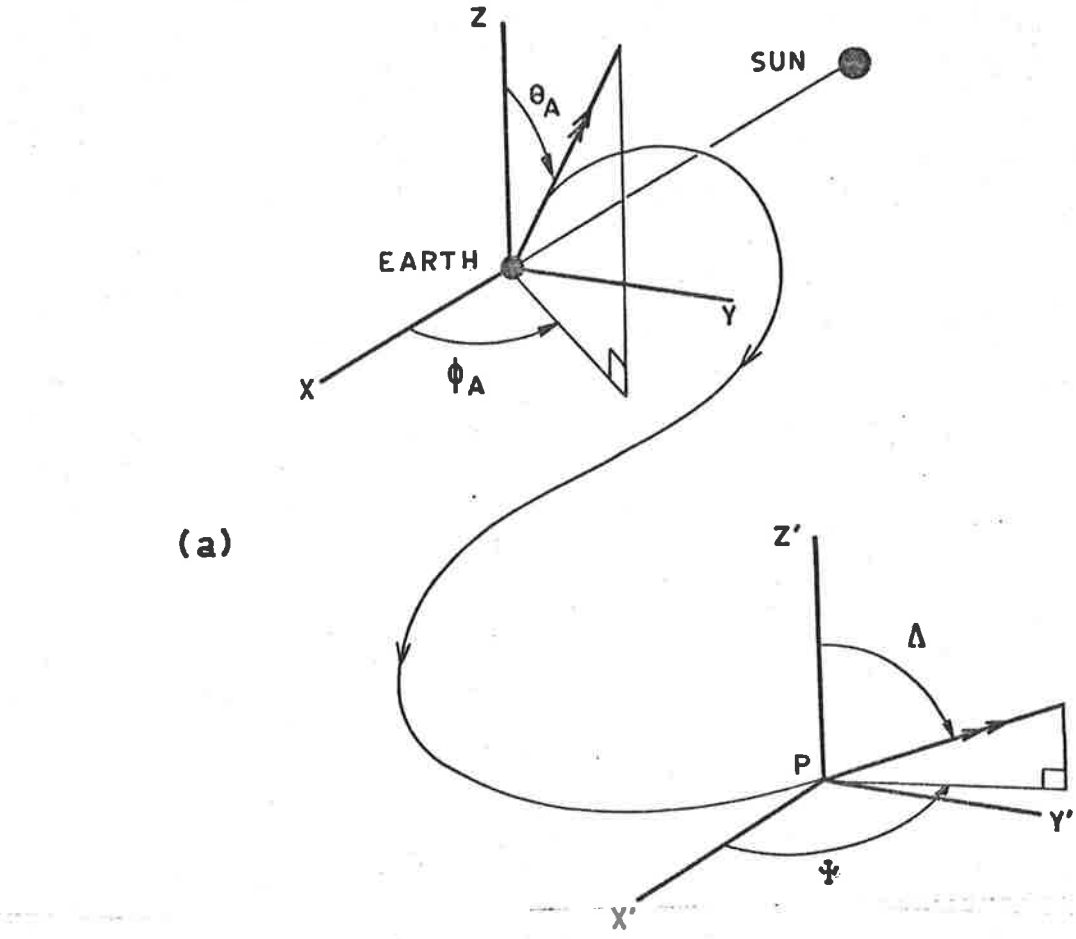

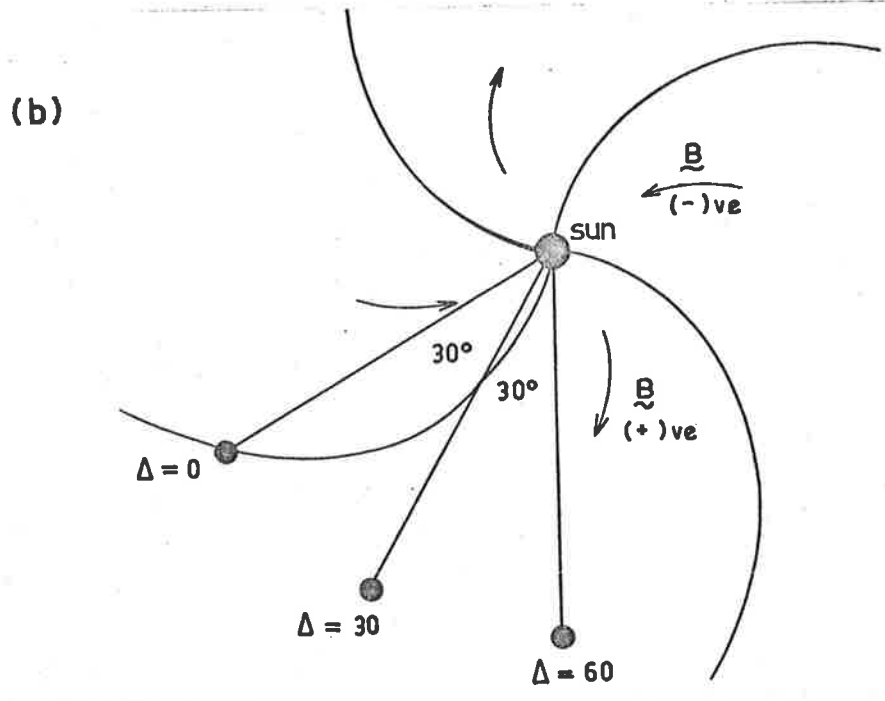

Figure 2.1(a) Cosmic ray arrival direction (θ_A,ϕ_A) and helio-asymptotic direction (Λ,Ψ); (b) The three positions of the Earth with the sector structure.

and a representative set of asymptotic directions is calculated. The spiral magnetic field model which is used has a field strength and garden hose angle of + 5·445 gamma and 50^{o} respectively at 1 AU. The radial component of the field B_{rE} at 1 AU is therefore + 3·5 gamma. The positive field strength indicates that the field is directed away from the Sun.

To obtain a representative set of asymptotic directions, the orbital calculations of sections 1.3 and 1.4 are carried out for

(i) different values of cosmic ray energy

(ii) different directions of cosmic ray arrival.

(iii) different positions of the Earth relative to the interplanetary sector structure.

The values which these parameters take are now described.

(a) The cosmic ray energies considered are 75, 100, 200 and 400 GeV.

(b) The directions of arrival of a cosmic ray near Earth is given by (θ_A , ϕ_A) , where θ_A is the geo-asymptotic co-latitude of arrival, and ϕ_A is the geo-asymptotic longitude of arrival relative to the midnight meridian. This is shown in Figure 2.1(a) in which the XY plane defines

the Earth's equatorial plane (and the ecliptic). All arrival directions used have $\theta_A = 90^\circ$, so that only geo-asymptotic directions parallel to the equatorial plane are considered. This is not an unrealistic approach because many detectors view equatorially, and it was not practical in terms of the available computing time to consider other value of θ_A. Values of θ_A are chosen for 24 equispaced directions of arrival in the equatorial plane, so that the asymptotic directions are in effect calculated at hourly intervals. The 24 values of ϕ_A are ϕ_A = 0, 15, 30, 45, ..., 330, 345°.

(c) The position of the Earth relative to the sector structure is described by Δ, the angular separation between the Earth and the sector boundary which is approaching the Earth (the sector structure corotates with the Sun). Three values of Δ are used, namely $\Delta = 60^\circ$, $\Delta = 30^\circ$ and $\Delta = 0^\circ$ as shown in Figure 2.1(b).

It should be noted that because both ϕ_A and Ψ are measured from the Sun-Earth line, both the direction of arrival (θ_A, ϕ_A) for a given time of day, and its corresponding asymptotic direction (Λ,Ψ) remain constant as the Earth revolves in its orbit about the Sun.

2.3 The Helio-asymptotic Directions

This section discusses the results obtained for the Earth in a fixed position relative to the interplanetary sector structure.

Figure 2.2 shows the asymptotic directions for $\Delta = 60^{\circ}$ plotted on a mercator type projection of latitude versus longitude. Tables of all these asymptotic directions are given in Appendix 2. For each of the four energies considered, 24 asymptotic directions are plotted corresponding to the 24 equispaced directions of arrival described in the previous section.

The most striking feature of these direction distributions is the absence of asymptotic directions with longitudes near 180° (the Earth-Sun direction), this effect being most marked at lower energies. To investigate the mechanisms which produce this effect, it is instructive to examine how the asymptotic directions evolve as ϕ_A, the longitude of arrival is incremented. To this end, Figure 2.3 shows a plot of (a) asymptotic latitude Λ vs ϕ_A, and (b) asymptotic longitude Ψ vs ϕ_A, for 100 GeV and 200 GeV cosmic rays. In figure 2.3(a) and (b), the dashed lines indicate the values which would result if the orbits were straight lines (namely $\Lambda = \theta_A = 0^{\circ}$, $\Psi = \phi_A$). Because at these energies cosmic rays are not seriously deflected by the Earth's magnetic field (i.e. geo-asymptotic direction $\simeq$ direction of arrival). Figure 2.3 can also be regarded as showing

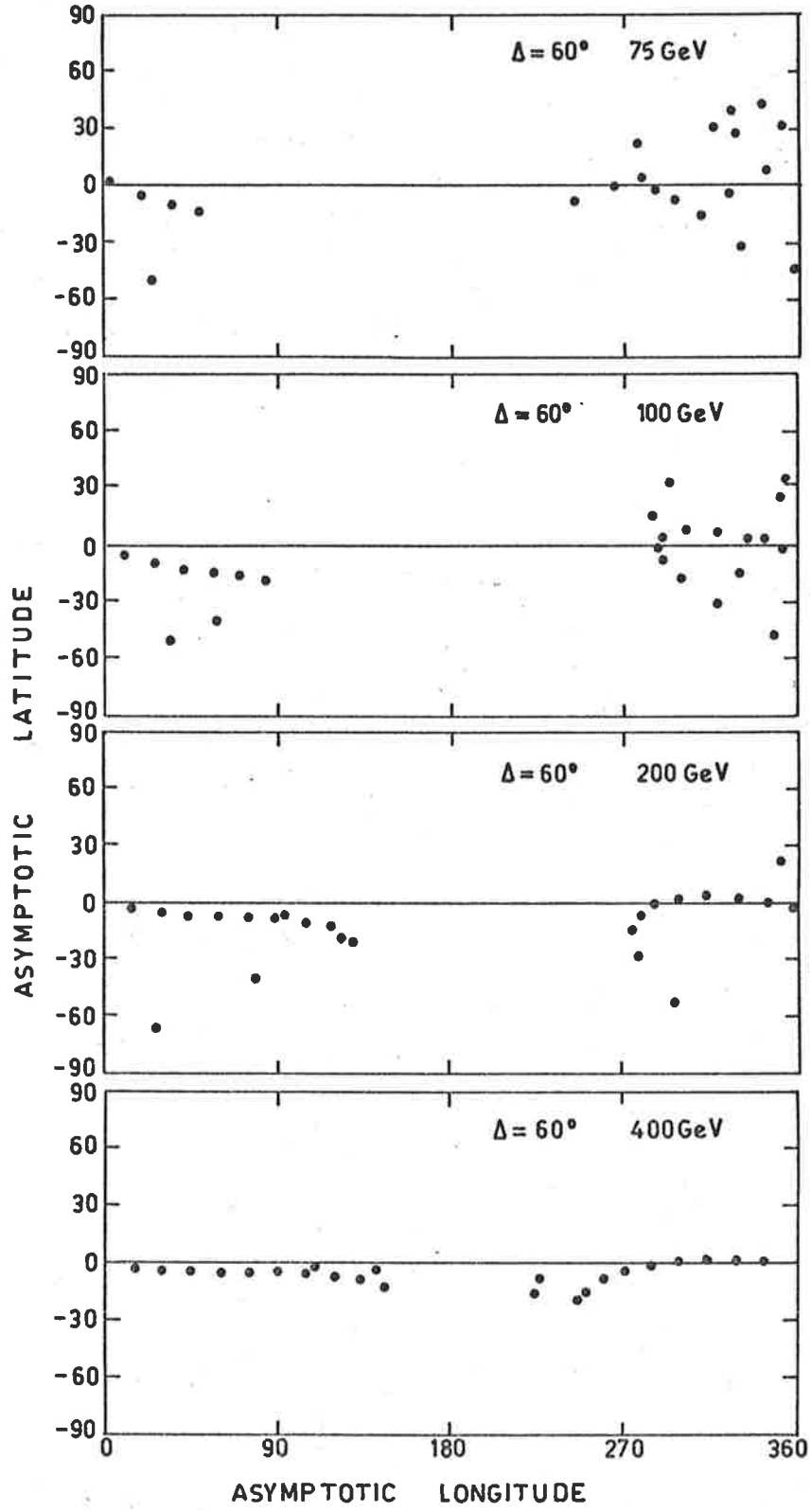

Figure 2.2 The helioasymptotic directions (Λ,Ψ) at 24 times of day for $\Delta = 60^{\circ}$.

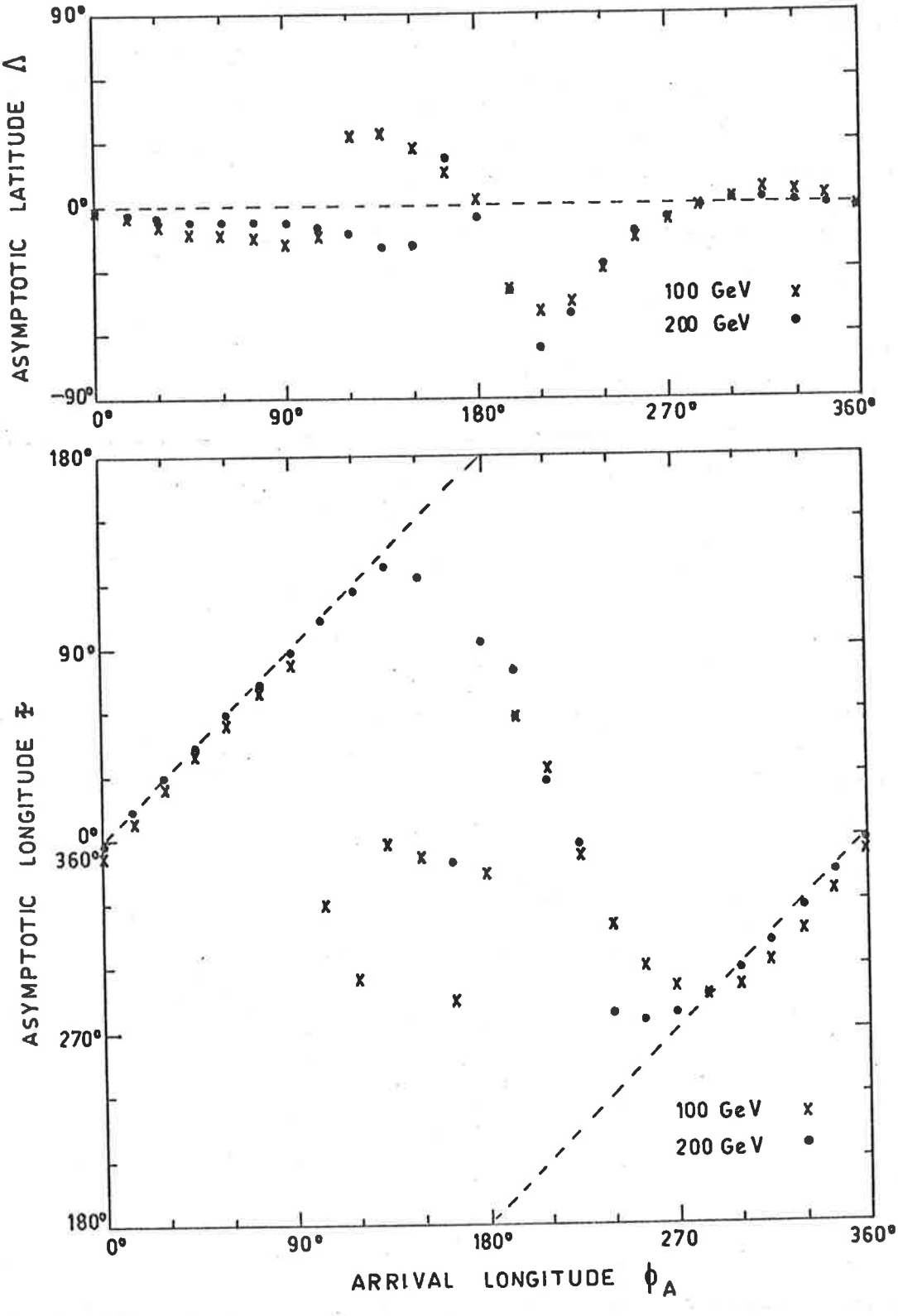

Figure 2.3 Helio-asymptotic latitude Λ and longitude Ψ vs arrival longitude ϕ_A (in ecliptic) for 100 and 200GeV. The dashed lines represent values for straight line orbits.

the variation in Λ and Ψ with time of day. $\phi_A = 0^\circ$ can thus be taken as the direction of vertical viewing at 0000 hours LT; $\phi_A = 15^\circ$ at 0100 LT; .....; $\phi_A = 345^\circ$ at 2300 LT.

Figure 2.3 shows that cosmic rays arriving with $\phi_A = 0^\circ$ (the anti-sun direction) have Λ and Ψ close to the values for straight line trajectories. As ϕ_A is increased from 0°, Λ and to a lesser extent Ψ, become further displaced from these straight line values, the differences being larger at the lower energy (100 GeV). Initially the differences increase gradually, but at $\phi_A = 105^\circ$ (100 GeV) and $\phi_A = 150^\circ$ (200 GeV) there are abrupt changes in both Λ and Ψ indicating that the cosmic rays have experienced severe deflection. As ϕ_A is increased beyond these values through 180° (when a cosmic ray arrives at the Earth from the Sun direction), the values of Λ and Ψ continue to indicate strong deflection, until near $\phi_A = 225^\circ$ they begin to approach straight line values in a systemmatic way.

It is at once obvious that the strong deflection experienced by a cosmic ray arriving from near the Sun direction ($\phi_A = 180^\circ$) is caused by the intense magnetic fields inside the orbit of Earth. The other features of Figures 2 and 3, in particular the abrupt changes in Λ and Ψ, cannot be explained in such general terms. An understanding of these features can be gained however, by plotting the 100 GeV orbits for $\phi_A = 75^\circ$, 90°, 105° and 120° (for $\Delta = 60^\circ$). Figure 2.3 suggests that the first two of these orbits approximate to

straight lines, whereas the last two undergo strong deflection.

Figure 2.4(a) is a polar plot of radius r vs longitude ϕ for these four orbits, which approximates to a projection of the orbits onto the ecliptic for small values of orbit latitude λ (= 90-θ). The orbits are plotted out to 4 AU, beyond which the deflection is minor, so that the orbit direction near 4 AU gives a good indication of the asymptotic longitude (at 10 AU). Figure 2.4(a) shows the orbits in 2 dimensions only. To obtain a more complete picture this must be supplemented with Figure 2.4(b), a plot of ϕ vs λ for the orbits with $\phi_A = 90^\circ$ and 105°. The open circles denote the points where a sector boundary is crossed, and the points corresponding to r = 1·0, 2·0, and 4·0 AU are marked. Figures 2.4(a) and (b) show the 3-dimensional nature of the orbits. Hence the sharp bend in the $\phi_A = 105^\circ$ plot near 2 AU in Figure 2.4(a) is simply a projection of the circular section of orbit shown more clearly in Figure 2.4(b). In the same way, the apparently straight section of the $\phi_A = 90^\circ$ orbit between 1·0 and 1·8 AU in Figure 2.4(a), is in fact curving upwards away from the ecliptic as shown in Figure 2.4(b).

The orbits depicted in this Figure suggest the explanation for the sudden and unexpected change in Λ and Ψ between $\phi_A = 90^\circ$ and $\phi_A = 105^\circ$ shown in Figure 2.3. It is seen (1) that at the sector boundaries the reversal of orbit curvature causes perturbations in the

Figure 2.4(a) A plot of heliocentric r vs ϕ for 100 GeV cosmic rays with arrival direction (θ_A, ϕ_A) = (90,75), (90,90), (90,105), (90,120) for $\Delta=60^o$.

Figure 2.4(b) A plot of heliocentric θ vs ϕ for 100 GeV cosmic rays with (θ_A, ϕ_A) = (90,90) and (90,105). The open circles denote sector boundary crossings, and the points where r = 1, 2, and 4AU are marked.

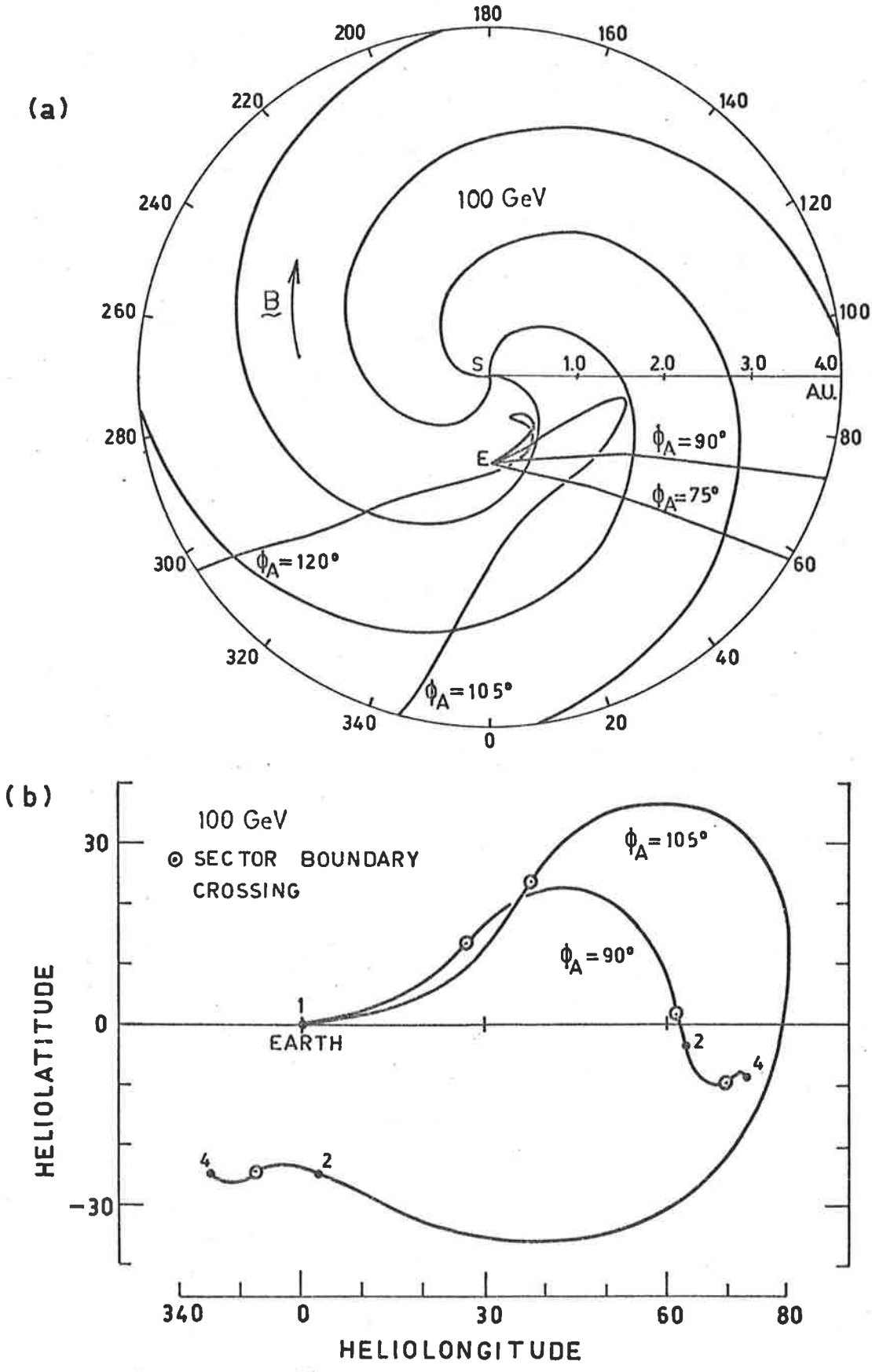
(a)
100 GeV
B
S
1.0
2.0
3.0
4.0
A.U.
E
$\phi_A = 90°$
$\phi_A = 75°$
$\phi_A = 120°$
$\phi_A = 105°$
180
200
160
220
140
240
120
260
100
280
80
300
60
320
40
340
20
0
(b)
100 GeV
⊙ SECTOR BOUNDARY CROSSING
$\phi_A = 105°$
$\phi_A = 90°$
EARTH
1
2
4
4
2
30
0
−30
HELIOLATITUDE
340
0
30
60
80
HELIOLONGITUDE

orbit which strongly influence the asymptotic direction, and (2) that "mirroring" is occurring for orbits which approach the Sun (e.g. the $\phi_A = 120^\circ$ orbit). The most important sector boundary crossings are those nearest the Sun where the curvature changes are largest; it can be seen in Figure 2.4 that crossings beyond $\sim$ 2 AU have relatively little effect.

It is proposed therefore that the abnormally large changes in Λ and Ψ for the adjacent arrival longitudes 90° and 105° in Figure 2.3, are a result of the difference in the sequence of sector boundary crossings for the two orbits close to the Earth. Both orbits cross a sector boundary about 0·5 AU from Earth with similar results. The 90° orbit crosses a second boundary near $r = 1{\cdot}8$ AU after curving through about half a gyration (Figure 2.4(b)), which reverses the curvature but does not cause any appreciable deflection in longitude. Subsequent boundary crossings have little effect. The 105° orbit, however, traverses more intense magnetic fields nearer the Sun, with the result that its curvature is tight enough to reverse its direction (Figures 2.4(a) and (b)) before it reaches the second sector boundary. This orbit therefore mirrors and finishes travelling in almost the opposite direction to its arrival direction. The second sector boundary it crosses is near $r = 3$ AU where there is only a small deflection. The importance of sector boundaries in determining asymptotic directions is discussed in greater depth in the next section.

Another feature of Figures 2.2 and 2.3 is the variation with energy of the asymptotic direction distributions. It was pointed out that the scarcity of directions with Ψ near 180° is most marked at lower energies. This can be explained in terms of the relative effect of a given magnetic field on cosmic rays of different energies. The instantaneous radius of gyration of a cosmic ray is given by $\rho = \frac{P\sin\alpha}{Bc}$, where P is rigidity, α is pitch angle, B is magnetic field strength, and c is the velocity of light. For the energies considered here $P \simeq E$, $\rho \propto E$ so that ρ is smaller for the lower energies; i.e. the curvature and therefore the deflection is greater, so that for the lower energies the trajectories tend towards guiding center motions about the field lines for the field strengths inside the orbit of Earth. Figure 2.5, a plot of four orbits each with $\phi_A = 135^{\circ}$, illustrates this energy dependence. The 200 and 400 GeV cosmic rays are not seriously deflected and so have Ψ near 135°, whereas (negative) 75 and 100 GeV particles ejected from the Earth follow the spiral field line to the inner solar system where they are mirrored; or equivalently, positive cosmic rays entering the solar cavity from 135° longitude cannot penetrate to the Earth through the intense fields near the Sun, so that the only way such a cosmic ray can arrive at the Earth with $\phi_A = 135^{\circ}$ is to approach from the Earthward side of the Sun, pass to the region inside the Earth's orbit and then be reflected back to arrive with $\phi_A = 135^{\circ}$.

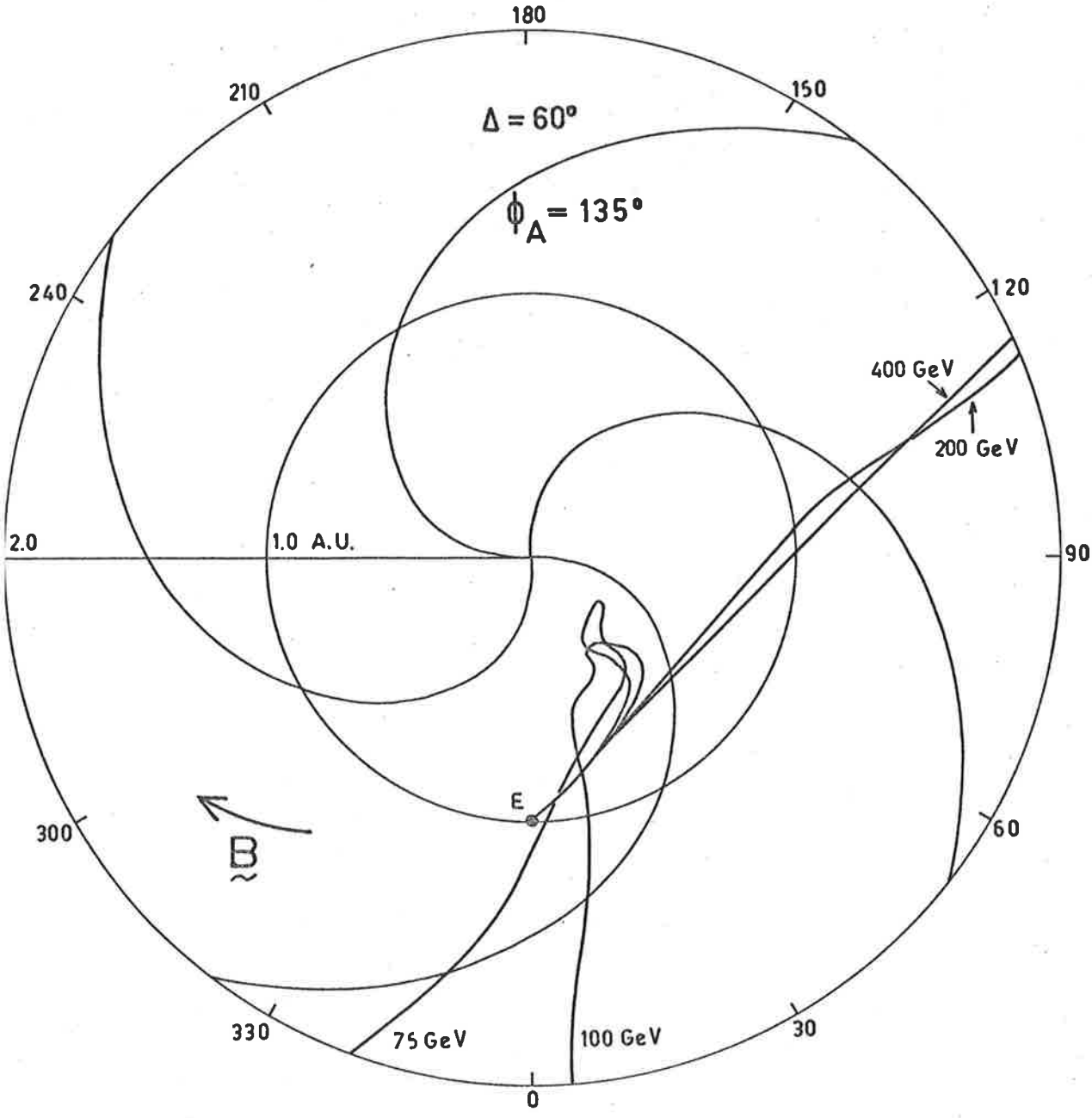

Figure 2.5 Orbits for 75, 100, 200 and 400 GeV cosmic rays which arrive with $(\theta_A, \phi_A) = (90, 135)$ when $\Delta = 60^\circ$.

2.4 Variations as the Sector Structure Rotates past the Earth

We now consider the asymptotic directions when the Earth is situated in two other positions relative to the interplanetary magnetic field sector structure, namely for $\Delta = 30^{\circ}$ and $\Delta = 0^{\circ}$ (see Figure 2.1b). Figures 2.6 and 2.7 show the distributions of asymptotic directions for $\Delta = 30^{\circ}$ and $\Delta = 0^{\circ}$ respectively, (a), (b), (c) and (d) being the distributions for 75, 100, 200 and 400 GeV in both Figures. When these direction distributions are examined together, four features emerge which are outlined and discussed below.

(i) There are 'forbidden' ranges of longitude where there is a very low density of asymptotic directions, and which become progressively smaller with increasing energy. An explanation for these forbidden regions of longitude was given in section 2.2 and the same reasoning holds for this more general case.

(ii) For 400 GeV and to a lesser degree, 200 and 100 GeV, the forbidden ranges of longitude are all centered near $\Psi = 200^{\circ}$, and for one particular energy are of about the same extent for the three values of Δ. At 75 GeV however, most of the asymptotic directions are clustered within $\sim 90^{\circ}$ of longitude for each value of Δ, and the central or average longitude changes from 323° ($\Delta = 60^{\circ}$) to 231° ($\Delta = 30^{\circ}$) to

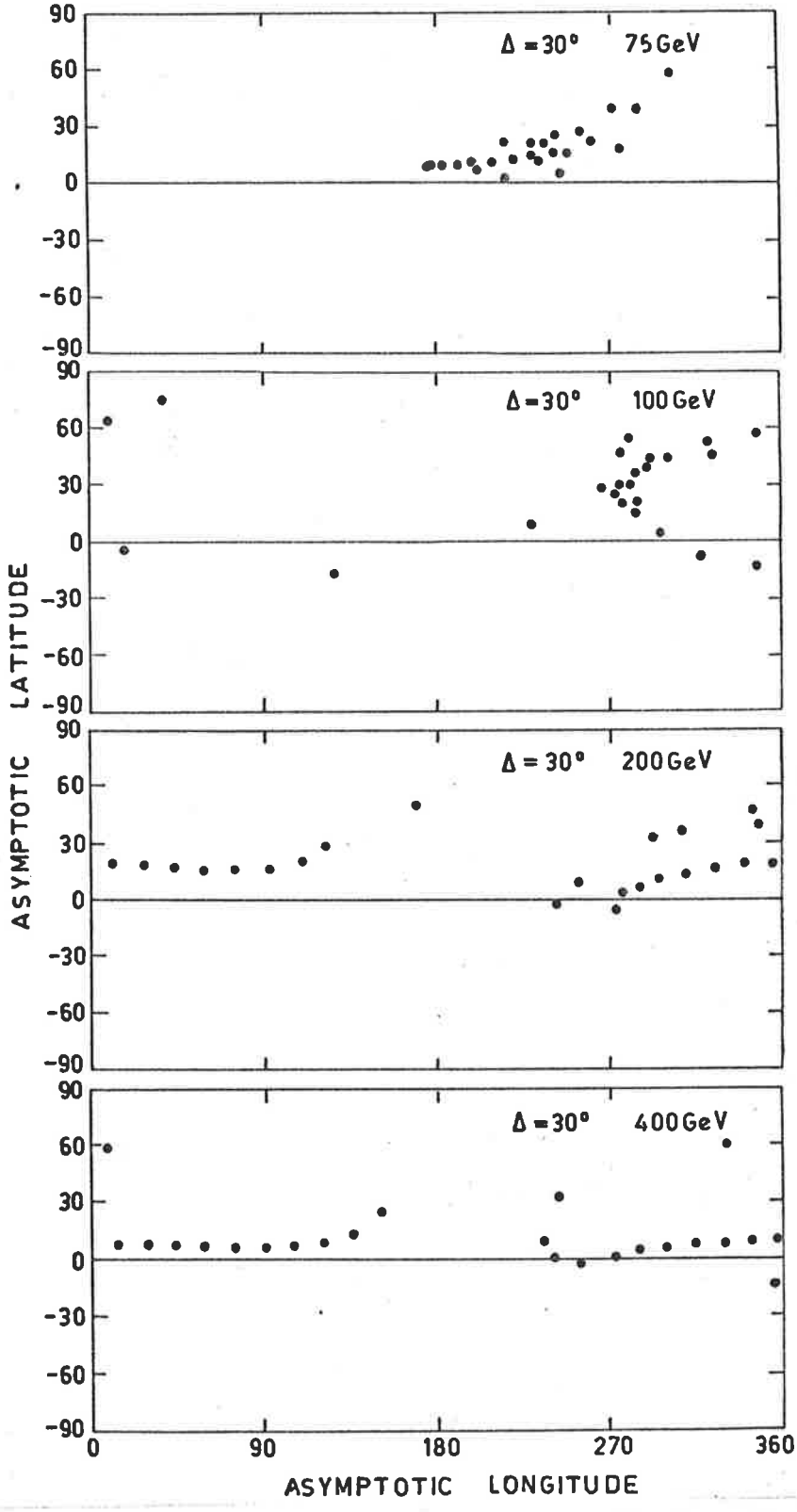

Figure 2.6 The helioasymptotic directions (Λ, Ψ) at 24 times of day for $\Delta = 30^{\circ}$.

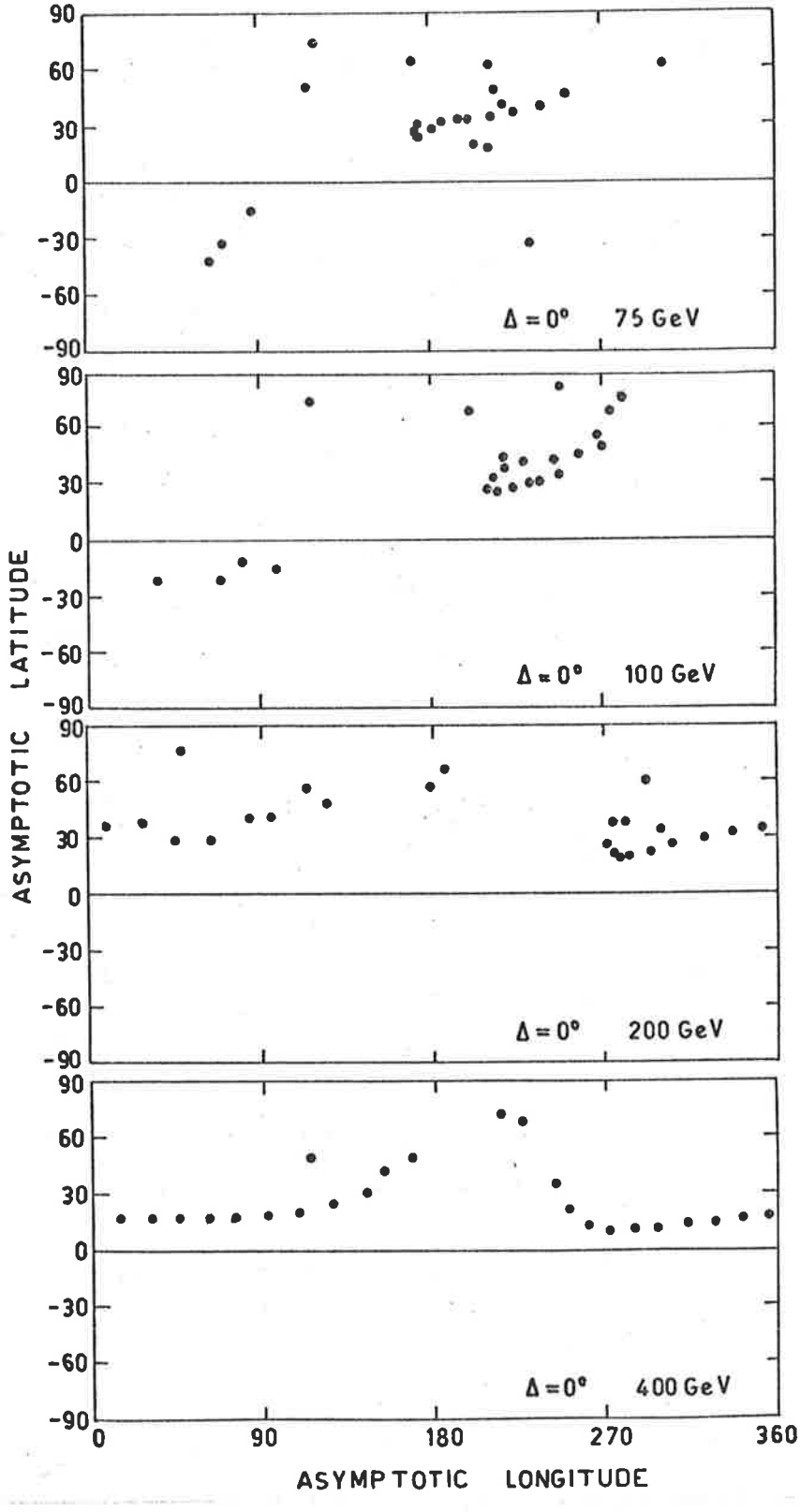

Figure 2.7 The helioasymptotic directions (Λ,Ψ) at 24 times of day for $\Delta = 0^{\circ}$.

185° ($\Delta = 0^{\circ}$). For a clear comparison of the 75 GeV directions for the three values of Δ, refer to Figure 2.8; the vertical dashed lines show the average longitude for each distribution. Figure 2.8 also shows that the degree of clustering is a function of Δ.

(iii) Several of the distributions have exclusively positive latitudes. It should be noted that when the Earth is in the corresponding position in an adjacent sector (where the field has opposite polarity), the asymptotic directions have latitudes with opposite sign to those shown in Figures 2.2, 2.6 and 2.7. Hence we have asymptotic directions for six positions of the Earth within the sector structure. The direction distributions for corresponding positions in adjacent sectors are mirror images.

(iv) For 400 and 200 GeV, sequences of asymptotic directions corresponding to sequences of arrival directions can be distinguished. The latitudes of the directions in these sequences are almost constant for directions well removed from the forbidden region of longitudes, but as the direction longitudes approach this region, the latitudes move systematically away from this constant value. For 100 and 75 GeV, the sequences of asymptotic directions are

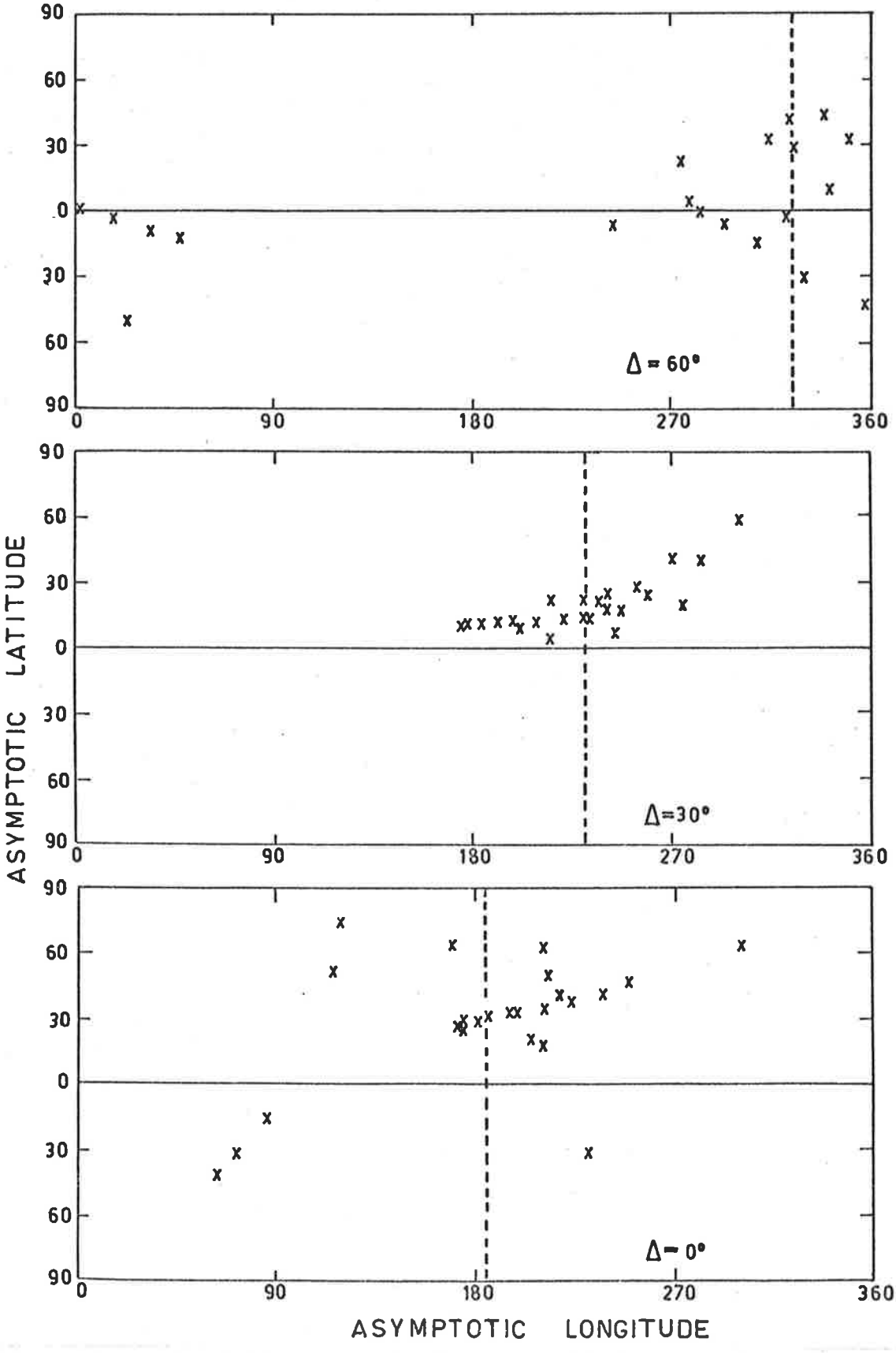

Figure 2.8 The helioasymptotic directions (Λ,Ψ) at 24 times of day for 75 GeV cosmic rays.

obscured. These effects have been illustrated more clearly in Figure 2.3 for $\Delta = 60^{\circ}$.

The clustering of the 75 GeV asymptotic directions mentioned in (ii) will now be investigated. The dependence of this clustering on Δ can be understood using Figures 2.9 and 2.10. Both of these diagrams show eight 75 GeV cosmic ray orbits with arrival directions in the ecliptic with $\phi_A = 0, 45, 90, 135, 180, 225, 270$ and 315°. Figure 2.9 has an Earth-sector boundary separation of $\Delta = 60^{\circ}$, while Figure 2.10 has the separation $\Delta = 30^{\circ}$. In terms of a negative cosmic ray ejected from Earth in the arrival direction, these orbits exhibit the following general behaviour.

In the immediate vicinity of Earth the cosmic ray tends to spiral about the local field line with radius of gyration given by $0{\cdot}3 \sin\alpha$ at 1 AU, where α is the pitch angle of the cosmic ray motion. A cosmic ray which initially spirals in towards the Sun mirrors and passes the Earth moving outwards with roughly the same pitch angle and radius of gyration it had on ejection (at these energies $\sin^2\alpha/B$ is not rigorously conserved, hence equality does not pertain). This means then, that all 75 GeV trajectories ultimately spiral outwards from the Earth about field lines which pass close to the Earth. As the cosmic ray moves further away from the Sun and the field strength decreases, both its gyroradius and gyroperiod increase so that it

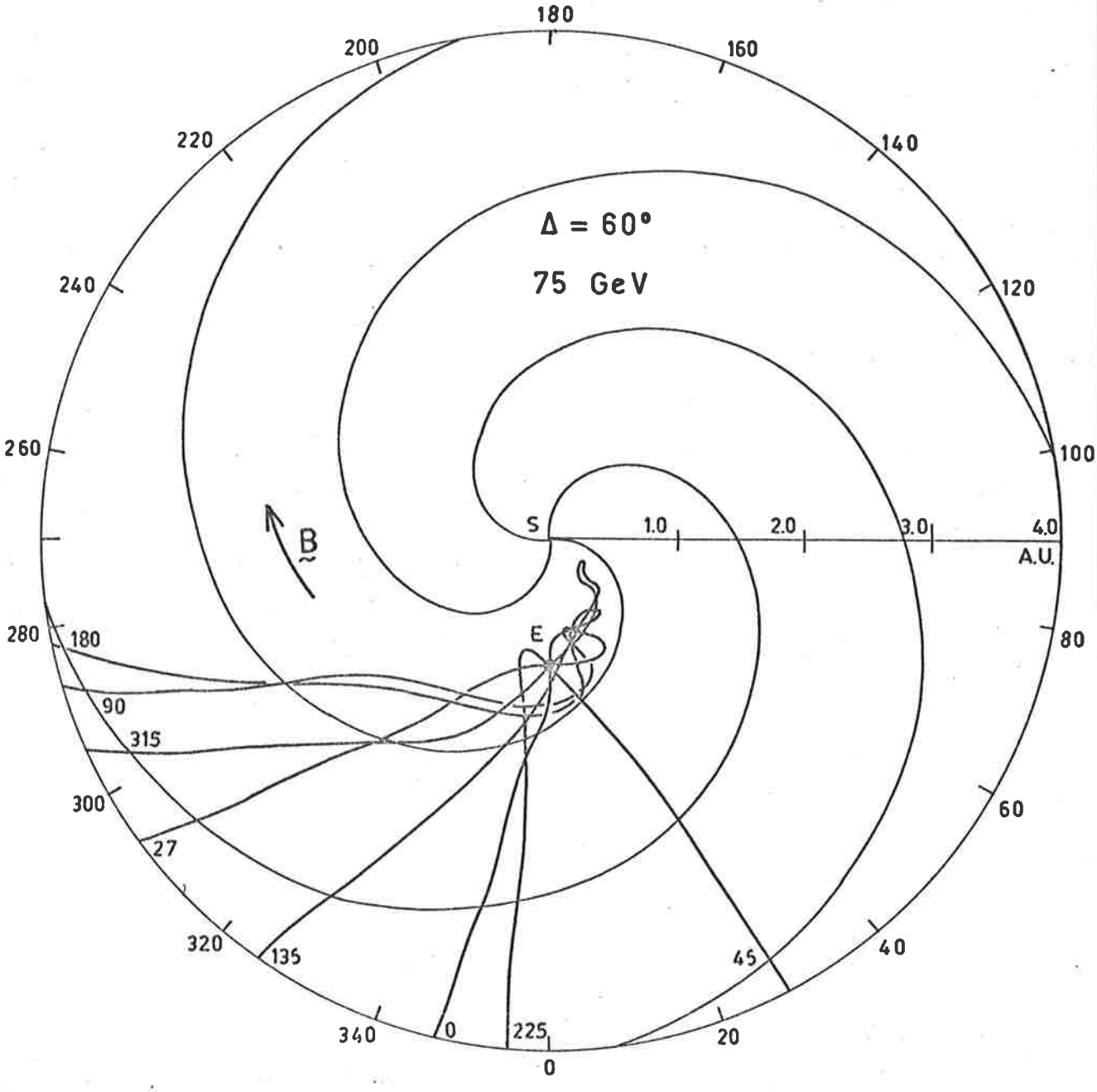

Figure 2.9 Orbits for eight 75 GeV cosmic rays which arrive in Earth's equatorial plane ($\theta_A = 90^\circ$) with equispaced arrival longitudes ($\phi_A = 0$, 45, 90, 135, 180, 225, 270, and 315°) when $\Delta = 60^\circ$.

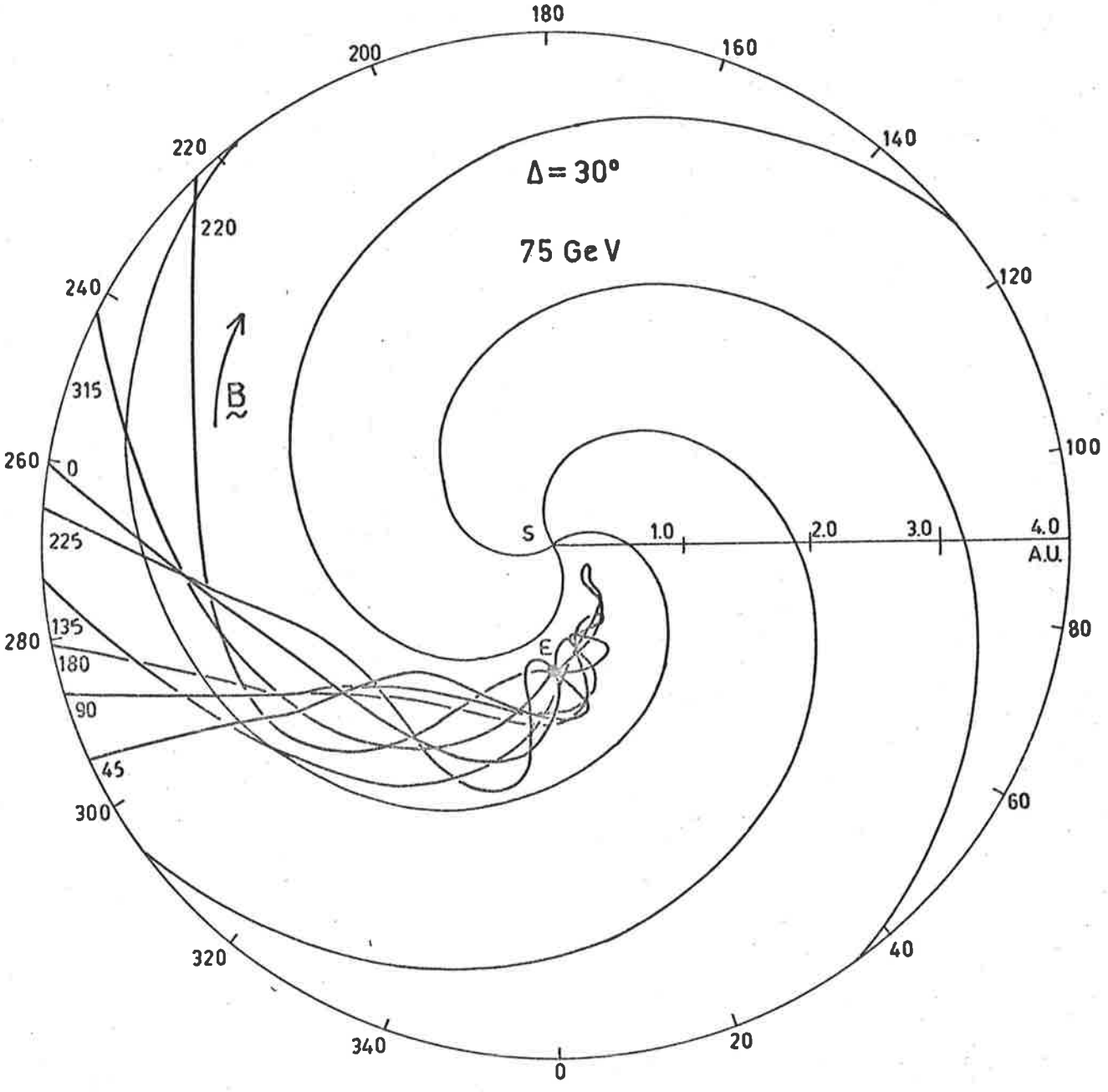

Figure 2.10 Orbits for eight 75 GeV cosmic rays which arrive in Earth's equatorial plane ($\theta_A = 90^o$) with equispaced arrival longitudes (ϕ_A = 0, 45, 90, 135, 180, 225, 270 and 315^o) for $\Delta = 30^o$.

travels more and more closely in a straight line.

This simple picture in which all orbits are effectively moving outwards about the same field line, but with different pitch angles, can be expected to yield a clustered set of asymptotic directions. When a sector structure is imposed on the interplanetary magnetic field the orbits will suffer the type of perturbation shown in the below diagram.

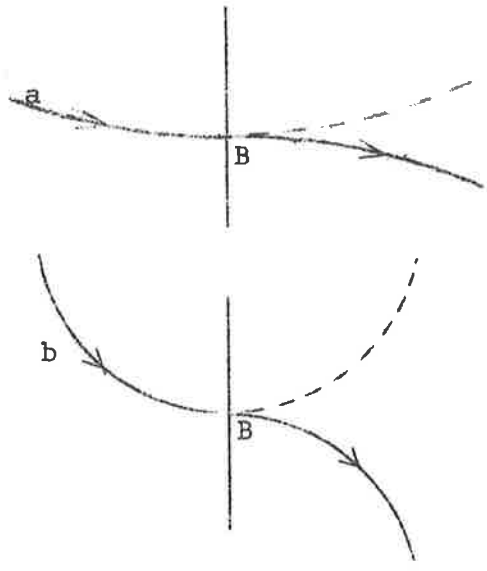

This diagram shows the projection of two orbits (a) and (b) onto the plane normal to the local interplanetary magnetic field direction, so that only the circular component of the motion is seen. Orbit (a) represents the case of a particle with a large gyroradius at $r \geq 1{\cdot}5$ AU, while orbit (b) shows the case of a particle close to the Sun. Both orbits cross a sector boundary at B; the broken lines indicate the orbit for no sector boundary crossing at B. It can be seen that the asymptotic direction of a cosmic ray which crosses a sector boundary close to the Sun as in case (b), will be very different if the same cosmic ray does not cross a sector boundary

until it reaches the heliocentric radius which yields case (a). Consequently the distribution of asymptotic directions will be strongly dependent on the position of the Earth relative to the sector boundaries.

This is the factor which makes such a difference between the asymptotic directions in Figures 2.9 and 2.10. The orbits in Figure 2.10 do not cross a sector boundary until they are $\sim 2{\cdot}5$ AU from the Sun, whereas in Figure 2.9 the crossings occur near 1.5 AU. At subsequent boundary crossings the field is weak and most cosmic rays are moving radially and so perpendicular to the field lines which approximate to concentric circles in projection. A motion perpendicular to the field lines tends to deflect the orbits upwards or downwards, and so to change their asymptotic latitudes. However, because the field is so weak and the sector boundaries are approximately equi-spaced, the deflection is slight and is compensated in large part by an opposite deflection in the next sector.

Figure 2.10 shows that $\Delta = 30^{\circ}$ is nearly the optimum value of Δ for minimum perturbation of 75 GeV cosmic ray orbits due to sector boundary crossings. It is seen that the Earth could be 10° closer to the approaching sector boundary ($\Delta = 20^{\circ}$) before any orbits crossed this boundary. This then would be the position ($\Delta = 20^{\circ}$) where we could expect the strongest clustering of the asymptotic

directions (for 75 GeV cosmic rays).

These results indicate the manner in which a detector at Earth will respond to a sidereal cosmic ray anisotropy (i.e. one existing outside the solar cavity). At times of well defined sector structure, a detector sensitive to cosmic rays between say 60 and 100 GeV, would effectively have an angular response of only $\sim 90^{\circ}$ in longitude and considerably less than 90° in latitude outside the solar cavity. Thus even though the detector scans through 360° in longitude in 24 hours of sidereal time in the co-ordinate system at Earth, there is virtually no scanning in helio-asymptotic longitude throughout the sidereal day. Hence the response to a sidereal anisotropy would be minimal. As the sector structure rotated past the detector, the angular response in helio-asymptotic longitude would on occasions extend to over 180°. Furthermore as the Earth progressed around its orbit throughout the year, the detector would sense cosmic rays coming from progressively different helio-asymptotic longitudes (as measured in the frame of reference of the fixed stars). Hence the sidereal anisotropy would result in an annual variation in daily mean cosmic ray intensity. Consequently the data obtained by such a detector would exhibit variations due to the sidereal anisotropy; however they will be more complex than those suggested by the naive assumption of rectilinear cosmic ray propagation.

In the next chapter the details of the temporal variations due to a sidereal anisotropy will be calculated for one specific model of the interplanetary magnetic field, to yield a qualitative understanding of the variations that might be observed in practice.

CHAPTER 3

TERRESTRIAL EFFECTS OF A GALACTIC ANISOTROPY

3.1 Introduction

Analysis of high energy cosmic ray data in recent years has established, at a relatively high level of confidence, the existence of a small sidereal variation for cosmic rays of energy $E \sim 100$ GeV. Jacklyn and Vrana (1969) find this to be predominantly a semidiurnal variation and have proposed a bidirectional (or 2-way) galactic anisotropy aligned with the local spiral arm of our galaxy to explain their observations. Swinson (1969a) has suggested that it may be possible to account for a large component of the observed sidereal diurnal variation in terms of a net flow of cosmic rays ($E \lesssim 75$ GeV) perpendicular to the plane of the ecliptic. A detector which looks in a direction d° from the Earth's axis would view such a flow from angles which vary (with a period of 1 sidereal day) between $(23{\cdot}5 - d)^{\circ}$ and $(23{\cdot}5 + d)^{\circ}$, where $23{\cdot}5^{\circ}$ is the angle the Earth's spin axis makes with the flow direction. The N-S flow arises as a consequence of a radial gradient in cosmic ray number density, which is a solar produced phenomenon. Both models predict that the phase of the yearly average diurnal variation will be near 0600 S.T. for northern hemisphere detectors, and near 1800 S.T. for southern hemisphere detectors, in agreement with the observations (S.T. = Sidereal Time).

There is therefore some uncertainty regarding the origin of the sidereal variations. In this chapter a galactic anisotropy is assumed to exist and the resulting sidereal variations on Earth are derived using the helio-asymptotic directions discussed in chapter 2. There are two factors which will tend to obscure a true galactic anisotropy from an observer on Earth, and both of these increase with decreasing cosmic ray energy. These factors are

(i) Cosmic ray trajectories in the interplanetary magnetic field become less linear and tend to describe guiding center motions about the field lines at lower energies (e.g. Figure 2.10). At these low energies a detector does not effectively scan and so no sidereal daily variation is observed.

(ii) Scattering by irregularities in the interplanetary magnetic field becomes increasingly important at lower energies. A cosmic ray which has been scattered, no longer carries information about its direction of arrival at the boundary of the solar cavity.

In section 2 the methods used to calculate the sidereal variation at Earth, given an arbitary galactic anisotropy, are outlined. In addition the ability of a detector on Earth to observe a galactic anisotropy at different energies, taking into account the effects ((i) and (ii) above) of the interplanetary magnetic field, is investigated.

Sections 3 and 4 present the sidereal effects calculated for two particular (1-way and 2-way) galactic anisotropies and section 5 investigates the effects of the corotating sector structure on these variations. In section 6 the results discussed in earlier sections are presented in a format which permits direct comparison with observational results.

3.2 Solar Effects on a Galactic Anisotropy

In Chapter 2 the asymptotic directions corresponding to 24 equi-spaced directions of arrival in the equatorial plane were presented. These asymptotic directions were defined relative to a heliocentric system of co-ordinates (Λ,Ψ) which rotates with the Earth about the Sun (see Figure 2.1). We now require to use these asymptotic directions to deduce the flux at Earth due to an anisotropic flow of cosmic rays outside the solar cavity in a direction fixed relative to the stars. To do this the asymptotic directions must be expressed relative to axes fixed in space; in this case celestial co-ordinates (α,δ) are used (α = R.A., δ = Dec.). Since $\delta = 0$ is the equatorial plane, the R.A. and Dec. of an asymptotic direction are calculated by the following co-ordinate transformation

$$\text{R.A.} = \alpha = \alpha_o(T) + \Psi$$

$$\text{Dec.} = \delta = \Lambda \qquad (3.1)$$

where $\alpha_o(T)$ is the right ascension of the Sun-Earth line at time of year T in question.

Consider a galactic anisotropy which results in a net flow of amplitude $G(\varepsilon)$ from the directions which are separated from the anisotropy axis (direction of maximum flow) by the angle ε. The flux observed on Earth due to the anisotropic component of the galactic radiation can therefore be determined if ε, the angular separation between the asymptotic direction of viewing of the detector and the anisotropy axis, is known. If $G(\varepsilon)$ is expressed as a fraction of the isotropic flux outside the solar cavity, then the anisotropic flux at Earth relative to the background or average flux will also be $G(\varepsilon)$.

For a galactic anisotropy with direction of maximum (α_M, δ_M), the angular separation ε for an asymptotic direction of viewing (α_v, δ_v) is given by the spherical trigonometry relation

$$\cos \varepsilon = \sin\delta_M \sin\delta_v + \cos\delta_M \cos\delta_v \cos (\alpha_v - \alpha_M)$$

Here $\alpha_v = \alpha_o(T) + \Psi$ where $\alpha_o(T)$ is the R.A. of the Sun-Earth line at time of year T, and Ψ is asymptotic longitude. In this analysis, the anisotropic cosmic ray flux at Earth is calculated at 24 equispaced times of day, for one day in each month of the year. The days considered are taken at monthly intervals from the day in

September (month 9) when the Sun-Earth line is directed towards 0° R.A. For month M, $\alpha_{o} = (M-9) \times 30^{\circ}$ so that

$$\alpha_{v} = (M-9) \times 30^{\circ} + \Psi$$

$$\delta_{v} = \Lambda$$

For each of the 12 days corresponding to the 12 values of M, the flux is calculated at 0000, 0100, 0200, ..., 2300 hours S.T. (sidereal time). Sidereal Time is used here to facilitate comparison of the results with observational data which is also recorded in sidereal time.

At this point it is possible to investigate how the sensitivity of an Earth based detector to a galactic anisotropy changes, due to its scanning capability being impaired (see (i) on P39), as we change the cosmic ray energy. To do this an anisotropy of the form $G(\varepsilon) = \cos\varepsilon$ with its axis in the equatorial plane is used. The 24 hourly values for the flux at Earth due to the anisotropic component outside the solar cavity are calculated using the corresponding 24 asymptotic directions for each of four cosmic ray energies (75, 100, 200 and 400 GeV). The relative amplitude of the sidereal diurnal variation at each of these energies was obtained by harmonic analysis of these 24 values, and is shown in Figure 3.1. Each point on Figure 3.1 represents the average amplitude for the three positions of the Earth in the sector structure for which asymptotic directions were

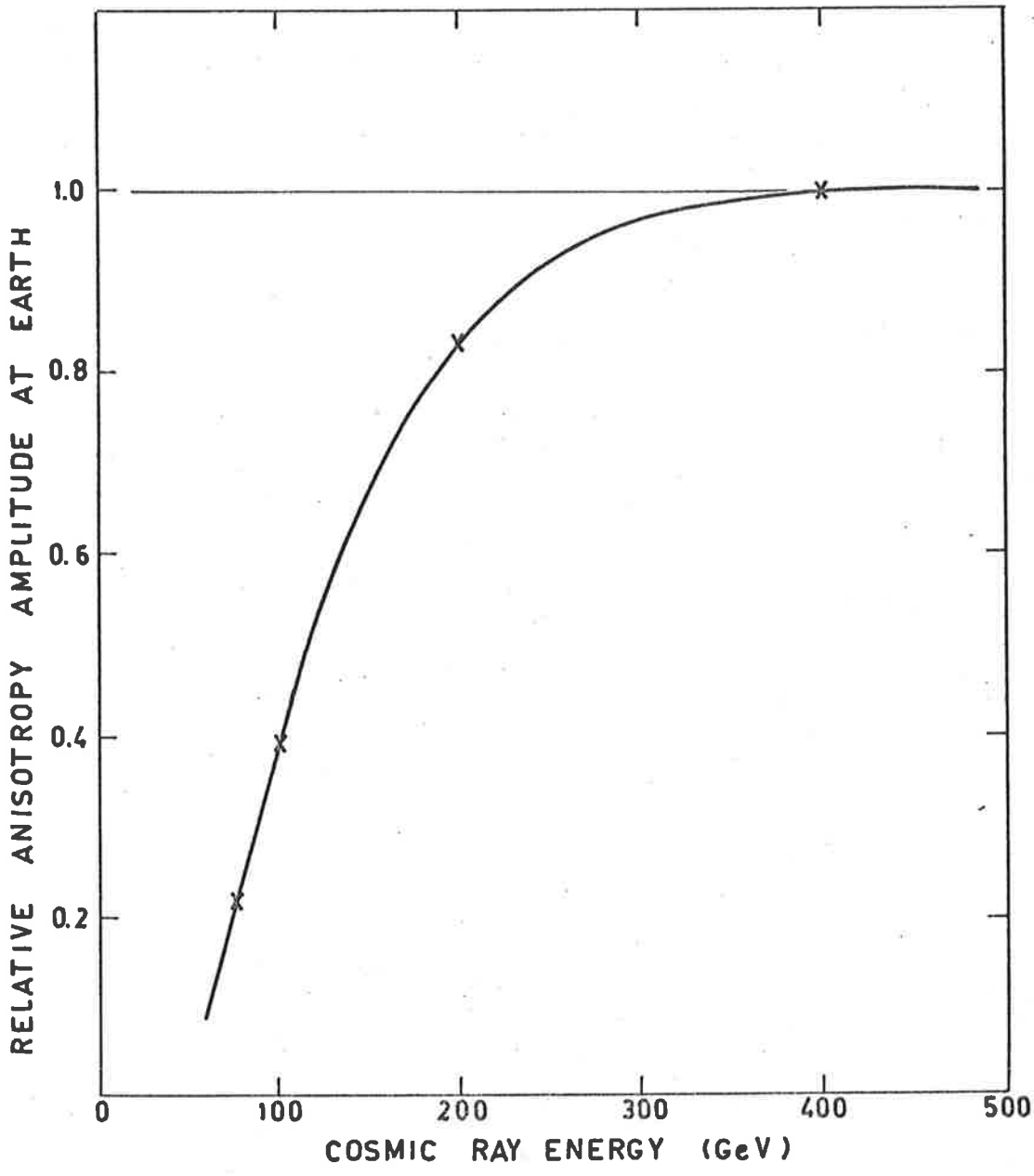

Figure 3.1 The amplitude of a sidereal anisotropy at Earth relative to the amplitude of the anisotropy outside the solar cavity for different energy cosmic rays. Solar cavity radius = 10AU.

calculated. These results were obtained for the time of year when the Earth-Sun line was perpendicular to the anisotropy axis direction.

Figure 3.1 shows that above about 400 GeV the observed sidereal anisotropy has the amplitude of the galactic anisotropy (1 unit), but that for lower energies the galactic anisotropy is gradually obscured, until below about 70 GeV the sidereal variation amplitude is reduced to less than 5% of the galactic anisotropy amplitude. Hence the presence of the large-scale interplanetary magnetic field imposes a lower limit of about 75 GeV for the observation of galactic anisotropies from Earth.

In the analysis which follows the four energies for which asymptotic directions were calculated are taken as representative of energy intervals which span the energy range of interest. For each hour of the day, the flux at Earth due to the anisotropic component $G(\varepsilon_i)$, of the galactic flux (outside the solar cavity), is calculated for energy interval i and weighted by W_i.

The anisotropic countrate N_i for hour i is then given by

$$N_i = \sum_{i=1}^{4} W_i \, G(\varepsilon_i) \qquad (3.3)$$

The weight W_i of energy interval i is a function of

a. The energy spectrum of the galactic anisotropy. This determines the relative number of cosmic rays within each energy interval.

b. The energy response of the detector. This determines the fraction of the cosmic rays incident on the detector, which is recorded.

c. The scattering properties of the interplanetary magnetic field. Since it is assumed that after a scattering event, any direction of travel is equally probable, only that fraction which reaches the detector without being scattered can contribute to the sidereal variation caused by the galactic anisotropy.

Factors (a) and (b) are found combined in the differential response function of the detector (if we assume that the anisotropic component of the flux outside the solar system has the same spectrum as the isotropic component). The differential response function is given by

$$\frac{dN(E)}{dE} = S(E) \cdot \frac{dJ(E)}{dE} \qquad (3.4)$$

where dN/dE is the contribution to the counting rate of the detector from particles with energies E to E + dE, S(E) is the specific

yield function (factor (b)) and dJ(E)/dE is the primary cosmic ray spectrum (factor (a)). The differential response function is normally expressed in terms of rigidity P (e.g. Mathews, 1963; Lockwood and Webber, 1967), but for the energies involved here, E and P are interchangeable.

Factor (c) is accounted for by multiplying the differential response function by the fraction of the cosmic ray flux at Earth which has not been scattered in the interplanetary medium.

Figure 3.1 indicates that the detectors best suited for the observation of sidereal effects are those sensitive to cosmic rays of energy $E \gtrsim 75$ GeV, because such a detector minimises the background modulation caused by solar effects at lower energies, while observing all of the available sidereal effects. For the purpose of this study a meson monitor at 40 m.w.e. (meters water equivalent) is considered. The differential response function for such a detector (Mathews, 1963) is shown in curve A of Figure 3.2. This shows that a considerable fraction of the countrate of such a detector is caused by primaries with $E < 75$ GeV. The choice of a 40 m.w.e. detector was also influenced by the availability of data from these detectors.

The fraction of galactic cosmic rays which reach the Earth unscattered can be expressed in terms of the scattering mean free

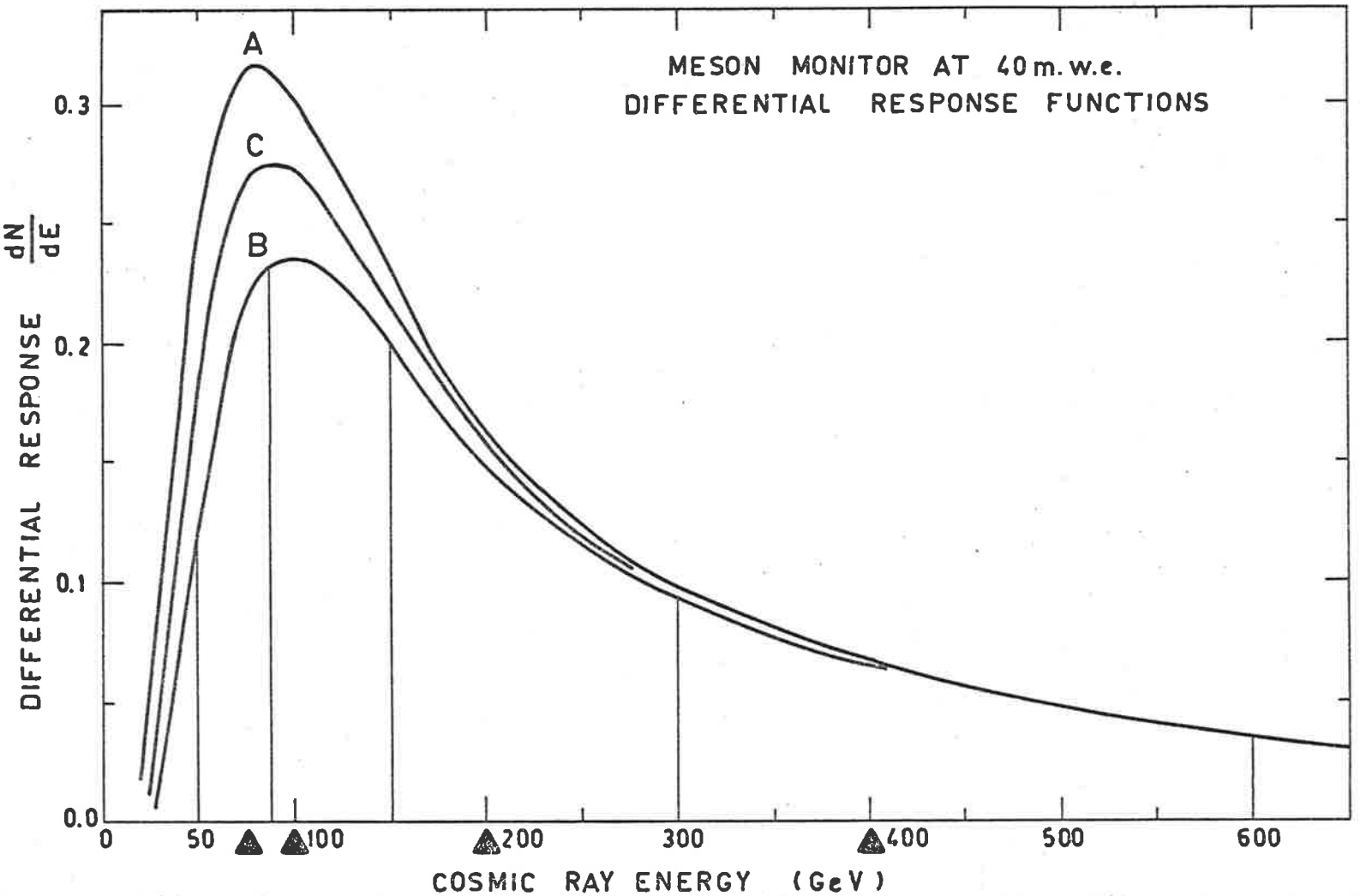

Figure 3.2 Curve A: The differential response function (Mathews, 1959) for a meson monitor at at 40 m.w.e.

Curve B: The differential response function multiplied by the fraction of cosmic rays which reach Earth unscattered for r_s = 10AU, $\lambda \alpha r$.

Curve C: same as curve B but for r_s = 50AU, $\lambda \alpha r^2$.

path $\lambda(E)$, and the radius of the solar cavity r_s. Estimates of these mean free paths have been made from spacecraft observations of the frequency spectrum of the interplanetary magnetic field, but only for regions of space near 1 AU and for energies up to $\sim$ 10 GeV. An indication of the mean free paths for energies > 75 GeV is obtained by extrapolation of this data. Figure 3.3 shows mean free paths derived from Mariner II (1962) and Mariner IV (1964-1965) data by Wibberenz et al (1969), and Jokipii and Coleman (1968), respectively. The dotted line shows the extrapolation which gives the mean free paths used here. The r-dependence of the mean free paths has been investigated by Quenby(1968) who concludes that the 11 year variation in cosmic ray intensity is consistent with

$$\text{(i)} \quad \lambda \propto r \ , \ r_s = 10 \text{ AU}$$

$$\text{(ii)} \quad \lambda \propto r^2 \ , \ r_s = 50 \text{ AU}$$

where r_s is the radius of the solar cavity at solar minimum. The parameters in case (i) above are now used to estimate the effect of scattering on the differential response function.

As a first approximation we take all orbits to be radial, and assume that they can be represented by the straight-line orbit EG in the diagram. Let I be the unscattered intensity at r (see

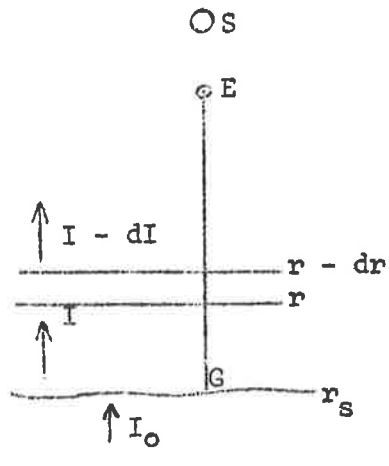

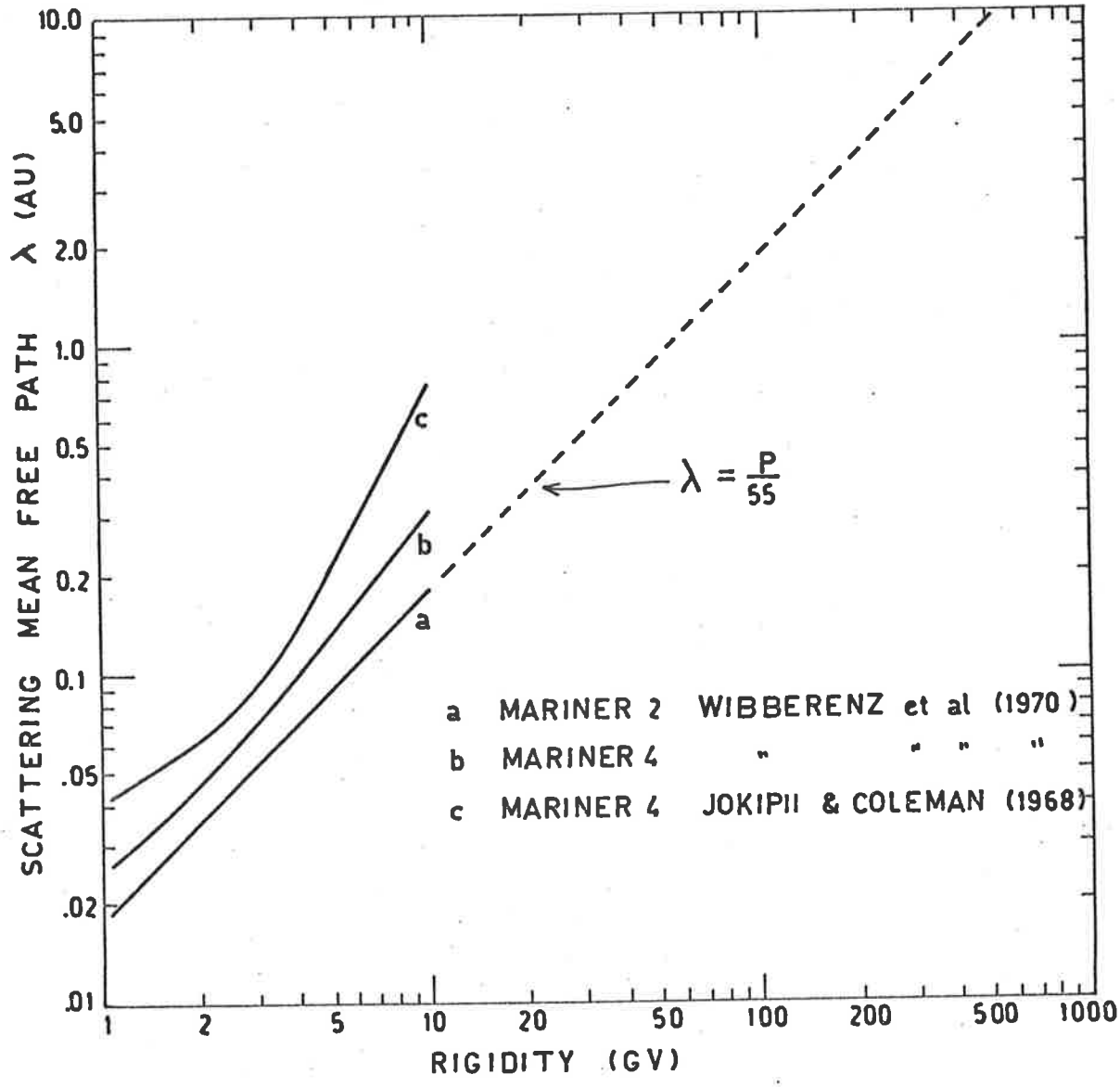

Figure 3.3 The scattering mean free paths at 1AU. The values used are given by $\lambda(P) = P/55$.

the diagram) then the change in unscattered intensity dI, between r and r - dr is

$$dI = -\left(I \cdot \frac{-dr}{\lambda}\right)$$

now $\lambda = \lambda_E r$ where λ_E is the mean free path at Earth (where r = 1 AU).

thus $$\frac{dI}{I} = \frac{1}{\lambda_E} \cdot \frac{dr}{r}$$

Integrating $$\ln I = \frac{1}{\lambda_E} \cdot \ln r + C \qquad (C = \text{constant})$$

now $I = I_o$ when $r = r_s$

thus $$C = \ln I_o - \frac{1}{\lambda_E} \cdot \ln r_s$$

and $$\ln I = \ln I_o + \frac{1}{\lambda_E} \cdot \ln (r/r_s)$$

so $$I = I_o (r/r_s)^{1/\lambda_E}$$

When $r = 1$ AU and $r_s = 10$ AU

$$\frac{I_E}{I_o} = \left(\frac{1}{10}\right)^{1/\lambda_E} = 10^{-1/\lambda_E}$$

Curve B in Figure 3.2 shows the differential response function multiplied by this factor, to give the differential response function for unscattered cosmic radiation. Curve C in Figure 3.2 shows the same function but for the case of $\lambda \propto r^2$, $r_s = 50$ AU.

The weight W_i (see equation 3.2) for energy interval i is obtained by dividing the area under the appropriate section of curve B by the total area under curve A. The weights so calculated and the energy increments used are listed in Table 3.1.

TABLE 3.1

The weights of the sidereal variations calculated using the asymptotic directions at four cosmic ray energies

Energy Interval	Representative Energy	Weight W_i
50 - 87·5 GeV	75 GeV	0·099
87·5 - 150	100	0·191
150 - 300	200	0·278
300 - 600	400	0·182

3.3 Sidereal Variations, Case 1

An anisotropy of the form $J(\varepsilon) = J_o + J_1.\cos\varepsilon$ is now assumed to exist outside the solar cavity. This is sometimes called a "1-way anisotropy". The anisotropy is assumed to be aligned with the interstellar magnetic field (see Davies, 1965) with its maximum

in the direction R.A. = 330°, Dec. = +55°. The countrate on Earth due to the anisotropic component (amplitude J_1) of $J(\varepsilon)$ is calculated at 24 times of day using equation 3.3 (where $G(\varepsilon) = J_1 \cos\varepsilon$), for one day in each month of the year ($\cos\varepsilon$ is calculated according to equation 3.2). A harmonic analysis is performed on the 24 values for each of these 12 days to give the amplitude and phase of the diurnal and semidiurnal components of the variation. The galactic anisotropy is given an amplitude of $J_1 = 1{\cdot}0$ unit and the amplitudes calculated for the sidereal variations on Earth are expressed in the same units. The phases are expressed in degrees east of the R.A. = 0° (0000 hours S.T.) direction.

Figures 3.4 and 3.5 show the diurnal and semidiurnal amplitudes and phases versus month of year for the 1-way anisotropy described above. In Figure 3.4, (a) and (d) show the diurnal and semidiurnal amplitudes for $\Delta = 60°$, (b) and (e) for $\Delta = 30°$, and (c) and (f) for $\Delta = 0°$ (where Δ is as defined in Figure 2.1). Figure 3.5(a) and (b) shows the phases of the diurnal and semidiurnal variations respectively. The dotted line in Figure 3.5(b) indicates the Sun-Earth direction. Several interesting features appear in Figures 3.4 and 3.5.

(i) The sidereal diurnal variation is amplitude modulated at both 1 cycle/year and 2 cycles/year. The average of these monthly amplitudes is 0·22 units.

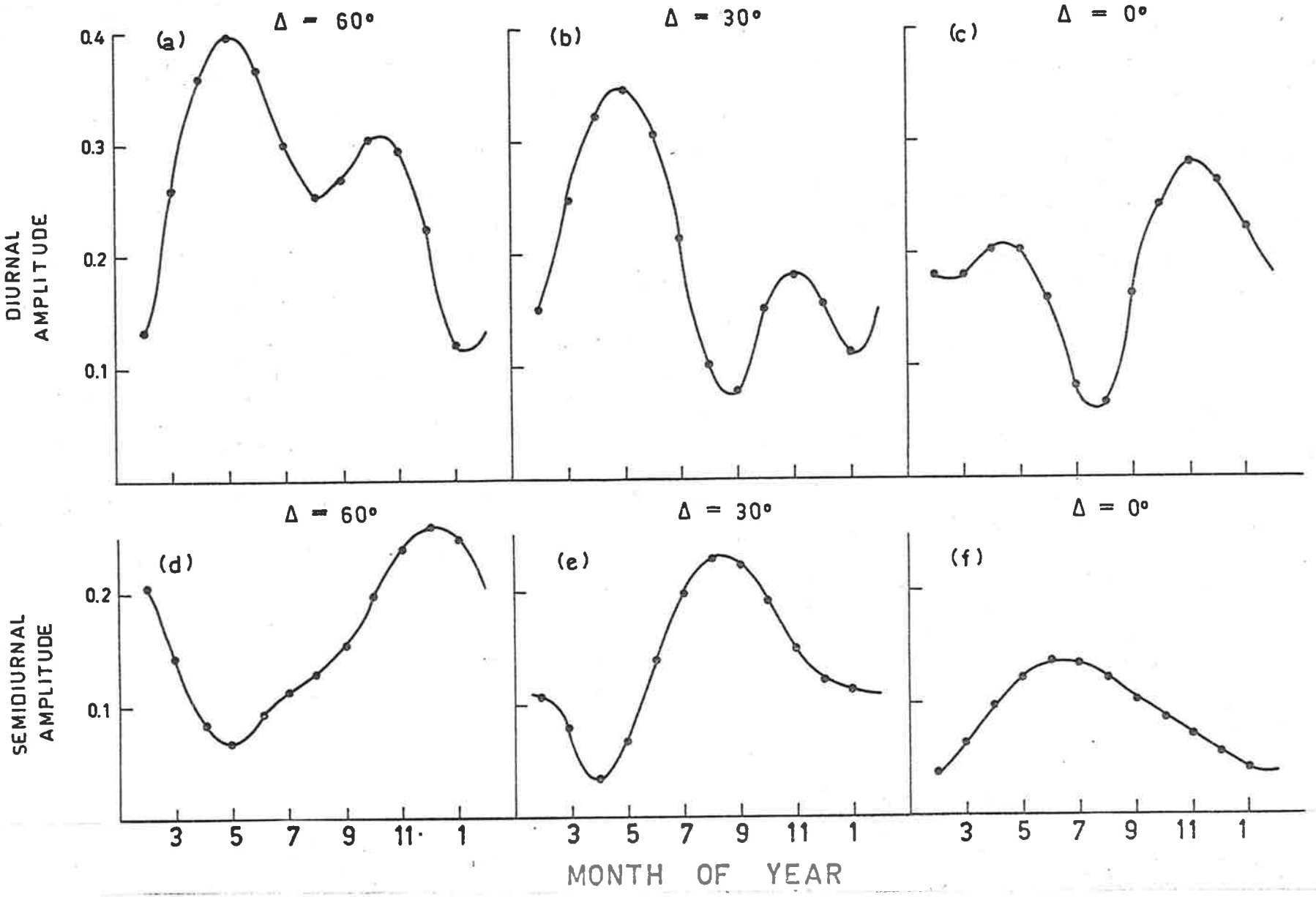

Figure 3.4 Diurnal and Semidiurnal amplitudes for the 1-way anisotropy.

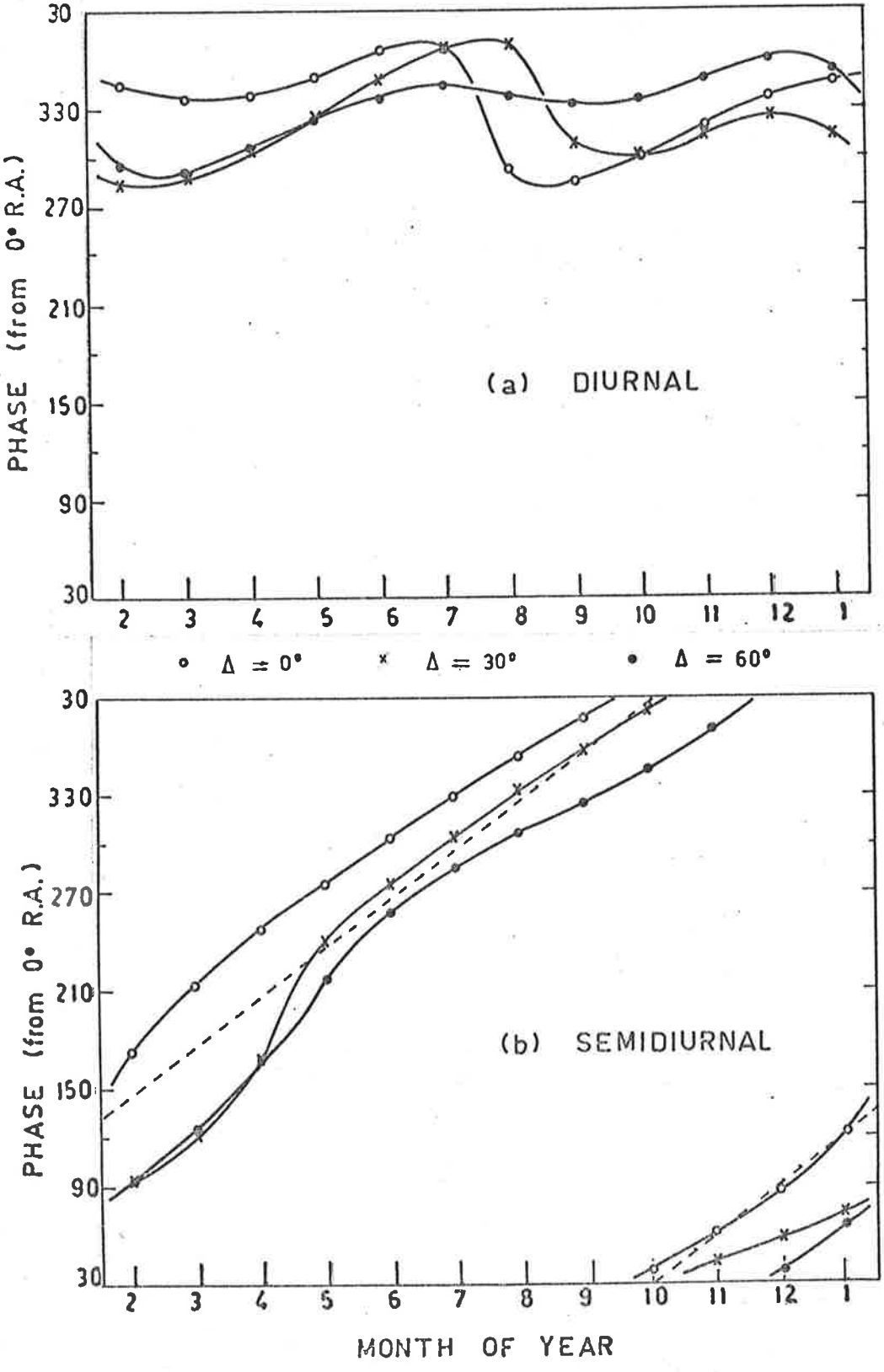

Figure 3.5 Diurnal and Semidiurnal phases for the 1-way anisotropy.

(ii) The phase of the diurnal variation remains close to 330° (the direction of the anisotropy maximum) throughout the year.

(iii) A semidiurnal variation appears which is amplitude modulated at 1 cycle/year. The average of the 'monthly' amplitudes in Figure 3.4(d), (e) and (f) is 0·13 units.

(iv) The phase of this semidiurnal variation changes through 2 complete cycles in 1 year (1 cycle = 180° of R.A.). Hence we have a solar semidiurnal variation (730 cycles/year) which is caused by the 1-way sidereal anisotropy.

(v) The semidiurnal variation has its maximum amplitude when the diurnal variation amplitude is minimum and vice versa.

This last feature supports the suggestion in (iv) that the semidiurnal variation is a solar induced effect. It is proposed that the Sun's magnetic field (which is extended to form the interplanetary magnetic field) distorts the observations of the galactic anisotropy when the detector looks in towards the Sun (see Figure 2.3), and produces this spurious semidiurnal variation, at the expense of the diurnal variation. This can be seen more clearly in Figure 3.6 which shows the actual daily variations for the 12 days considered throughout the

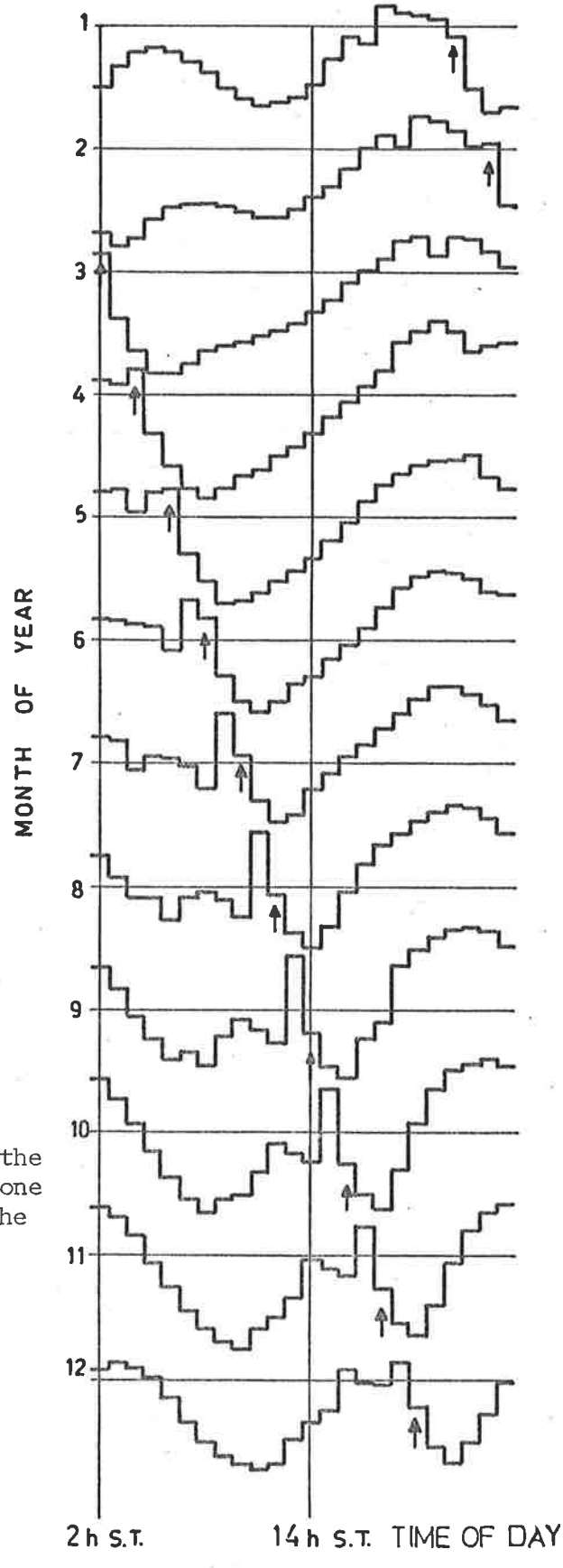

Figure 3.6

The actual daily variations for the 12 equispaced days of the year (one in each month) considered, for the 1-way anisotropy.

year. The small arrows indicate the times of transit of the Sun, and it is seen that near these times there is a perturbation introduced into the diurnal variation. If the cosmic ray trajectories were rectilinear, no semidiurnal variation would be observed.

A simplified model is now discussed to show how the features of Figures 3.4, 3.5 and 3.6 arise. Consider a sinusoidal (cos ε) anisotropy with its maximum at (330°, 0°), i.e. in the equatorial plane. Figure 3.7(a) shows this anisotropy and four idealised orbits which terminate in the asymptotic direction of viewing, for the Earth at 4 equispaced positions around the Sun. The four cosmic ray orbits chosen correspond to 2 arrival directions parallel to the anisotropy axis (1000 and 2200 S.T.), and 2 arrival directions perpendicular to the anisotropy axis (0400 and 1600 S.T.). The four positions of the Earth in its orbit correspond to months 2 and 8 when the Sun-Earth line is parallel to the anisotropy axis and months 5 and 11 when it is perpendicular to the anisotropy axis.

In month 2 at 1000 and 2200 the detector sees the anisotropy minimum, while at 0400 and 1600 it sees the mean (isotropic component) flux level, which therefore appears as the maximum flux level of the daily variation. Consequently the variation is predominantly semi-diurnal with phase (= direction of maximum) = 60°. In month 5 the maximum is seen at 2200, the minimum at 1000 and the mean level at

Figure 3.7 (a) A projection onto the ecliptic showing the asymptotic directions of viewing at 4 representative times of day, at 4 different times of year.

Figure 3.7 (b) A projection onto the meridional plane showing the anisotropy axis and the most closely aligned asymptotic direction of viewing at the two times of year when the anisotropy axis lies in the meridional plane.

(a)

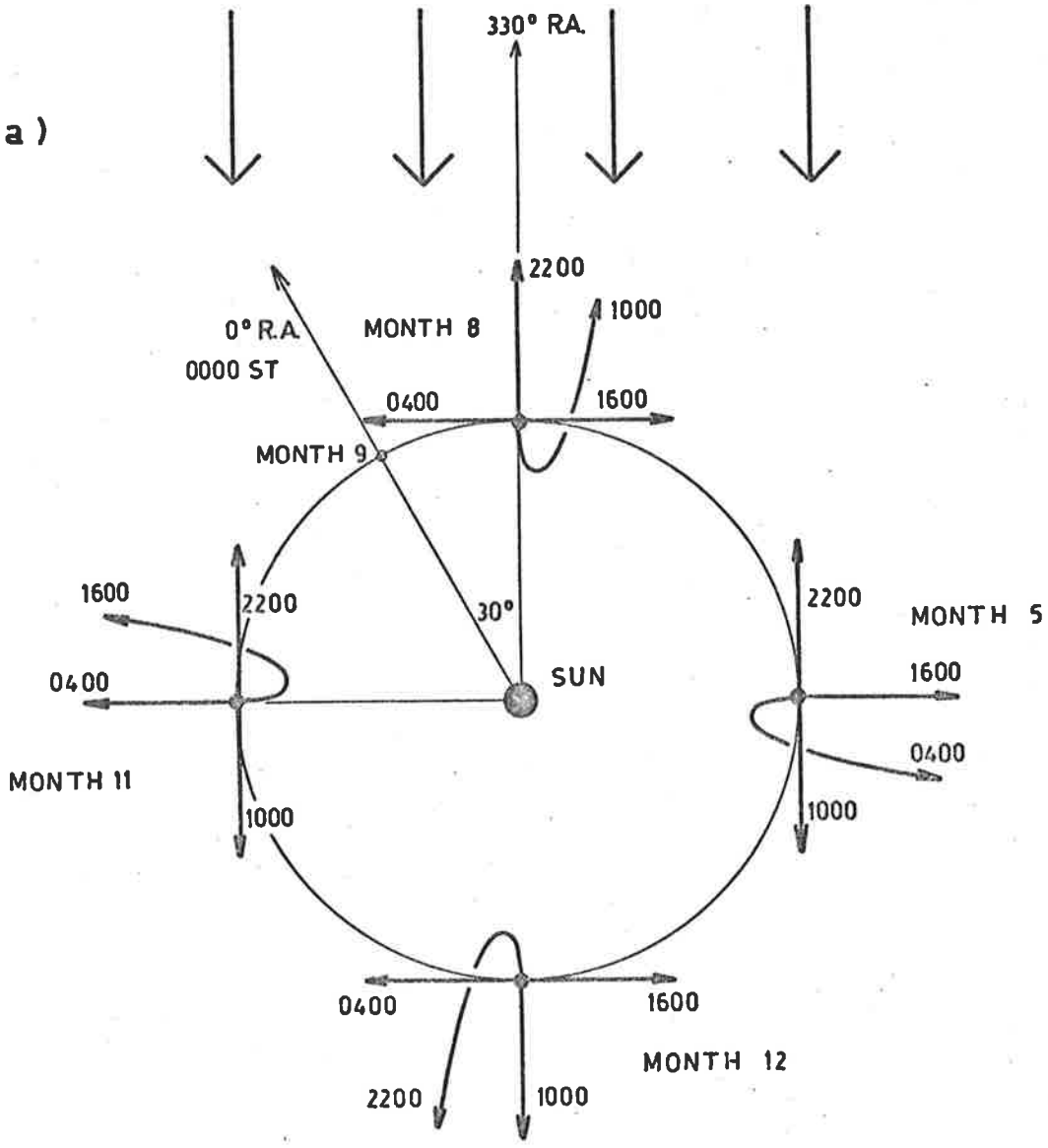
330° RA.
2200
1000
0° R.A.
0000 ST
MONTH 8
0400
1600
MONTH 9
30°
SUN
1600
2200
0400
MONTH 11
1000
2200
MONTH 5
1600
0400
1000
0400
1600
MONTH 12
2200
1000

(b)

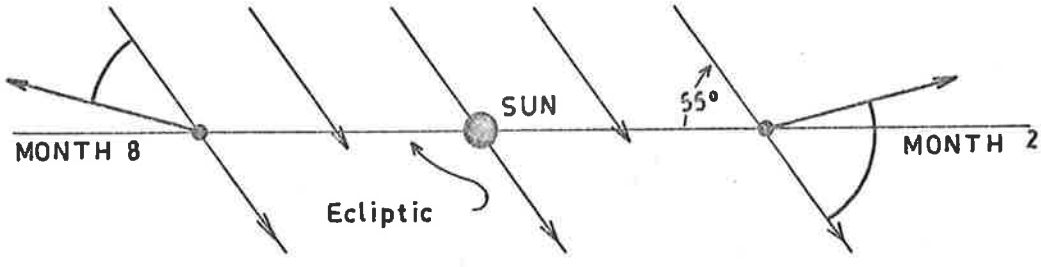
SUN
55°
MONTH 8
MONTH 2
Ecliptic

0400 and 1600; so a strong diurnal variation is observed with phase = 330°. The semidiurnal variation at this time is small. Three months later in month 8 the maximum flux is seen at 1000 and 2200, and the mean level at 0400 and 1600, yielding a strong semidiurnal variation with phase near 150° (or 330°). The diurnal variation here will be small (see Figure 3.4). In month 11 the maximum is observed at 2200, minimum at 1000, and mean level at 0400 and 1600, yielding a strong diurnal variation again with phase 330°.

This approach provides an intuitive understanding of the 2 cycle/year modulation of the diurnal variation and also for the coincidence of the semidiurnal variation maximum amplitude with the diurnal variation minimum amplitude. It also suggests that the phase of the diurnal variation will remain constant (in sidereal time), while the semidiurnal variation phase changes throughout the year. Indeed this approach yields variations in the last six months of the year identical to the variations in the first six months, i.e. a 2 cycle/year modulation of both the diurnal and semidiurnal variations and no 1 cycle/year modulation.

There is a serious discrepancy here, in that all of the variations in Figures 3.4, 3.5 or 3.6 show a 1 cycle/year modulation. This discrepancy is resolved if we remember that both the asymptotic directions of viewing and the anisotropy axis are inclined to the

equatorial plane. Figure 3.7(b) is a projection onto the meridional plane showing the relation between the anisotropy axis and an asymptotic direction with positive latitude for months 2 and 8 when the anisotropy axis lies in the meridional plane (it was noted in section 2.4 that, in a field-out sector, the asymptotic latitudes were predominantly positive). It can be seen from Figure 3.7(b) that the directions of viewing are more closely aligned with the anisotropy axis in month 8 than in month 2, so the semidiurnal variation amplitude is greatest near month 8. Hence a large 1 cycle/year modulation is introduced into the semidiurnal variation. Figure 3.6 shows how the semidiurnal variation increases at the expense of the diurnal variation amplitude (and vice-versa). Consequently a similar 1 cycle/year modulation can be expected in the diurnal variation (but 6 months out of phase with the semidiurnal modulation).

3.4 Sidereal Variations, Case 2

The calculations which yielded the results discussed in section 3.3 were repeated for an anisotropy of the form $J(\varepsilon) = J_o + J_1 \cos 2\varepsilon$, in the cosmic rays outside the solar cavity, with maxima at $(330^\circ, 55^\circ)$ and $(150^\circ, -55^\circ)$. This will be referred to as a "2-way anisotropy". The amplitude of the anisotropy is again $J_1 = 1{\cdot}0$ unit so that in equation 3.3, $G(\varepsilon) = \cos 2\varepsilon$. The behaviour of the amplitude and phase of the diurnal and semidiurnal variations as a function of time of year is shown in Figures 3.8 and 3.9.

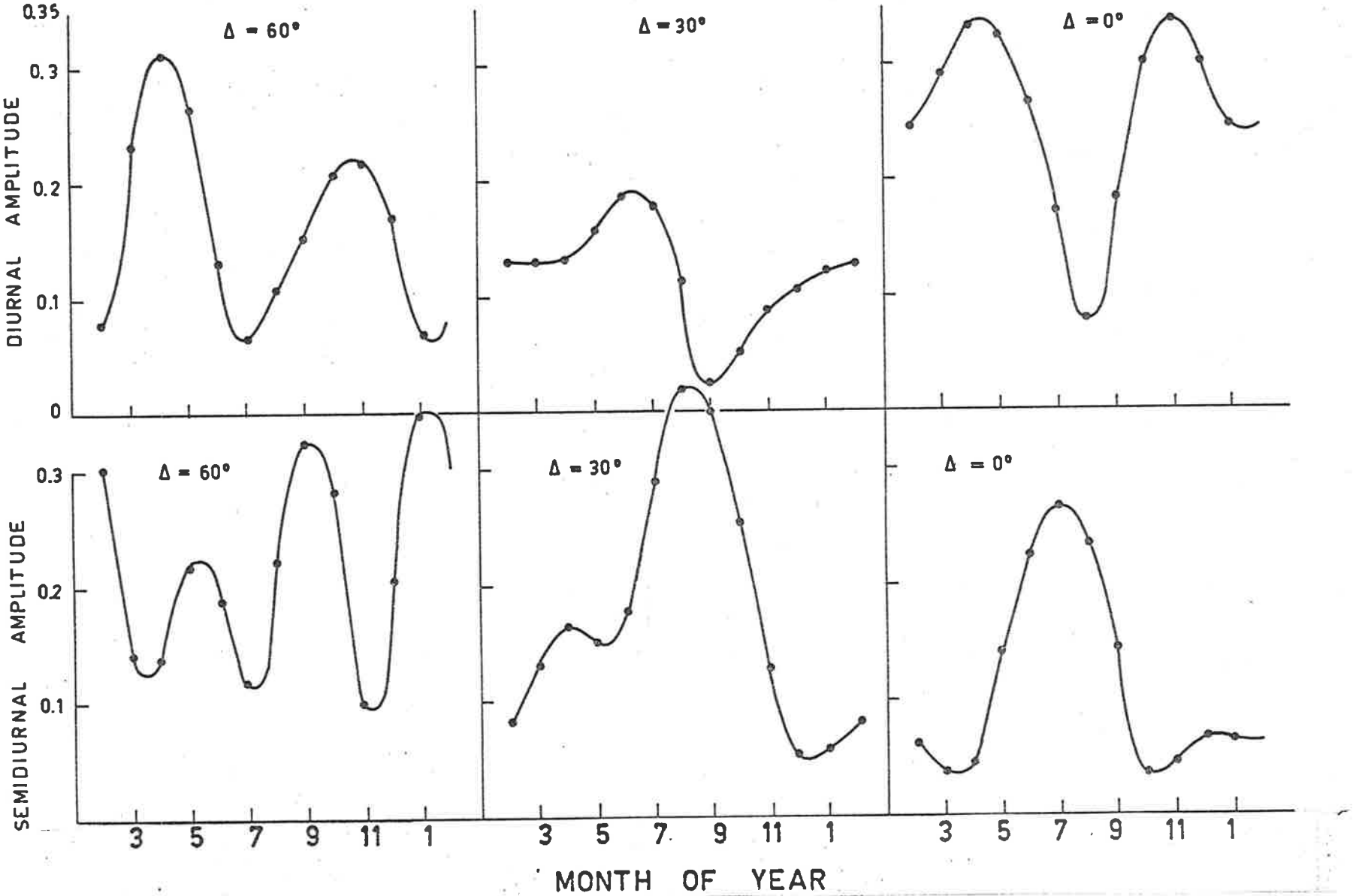

Figure 3.8 Diurnal and Semidiurnal amplitudes for the 2-way anisotropy

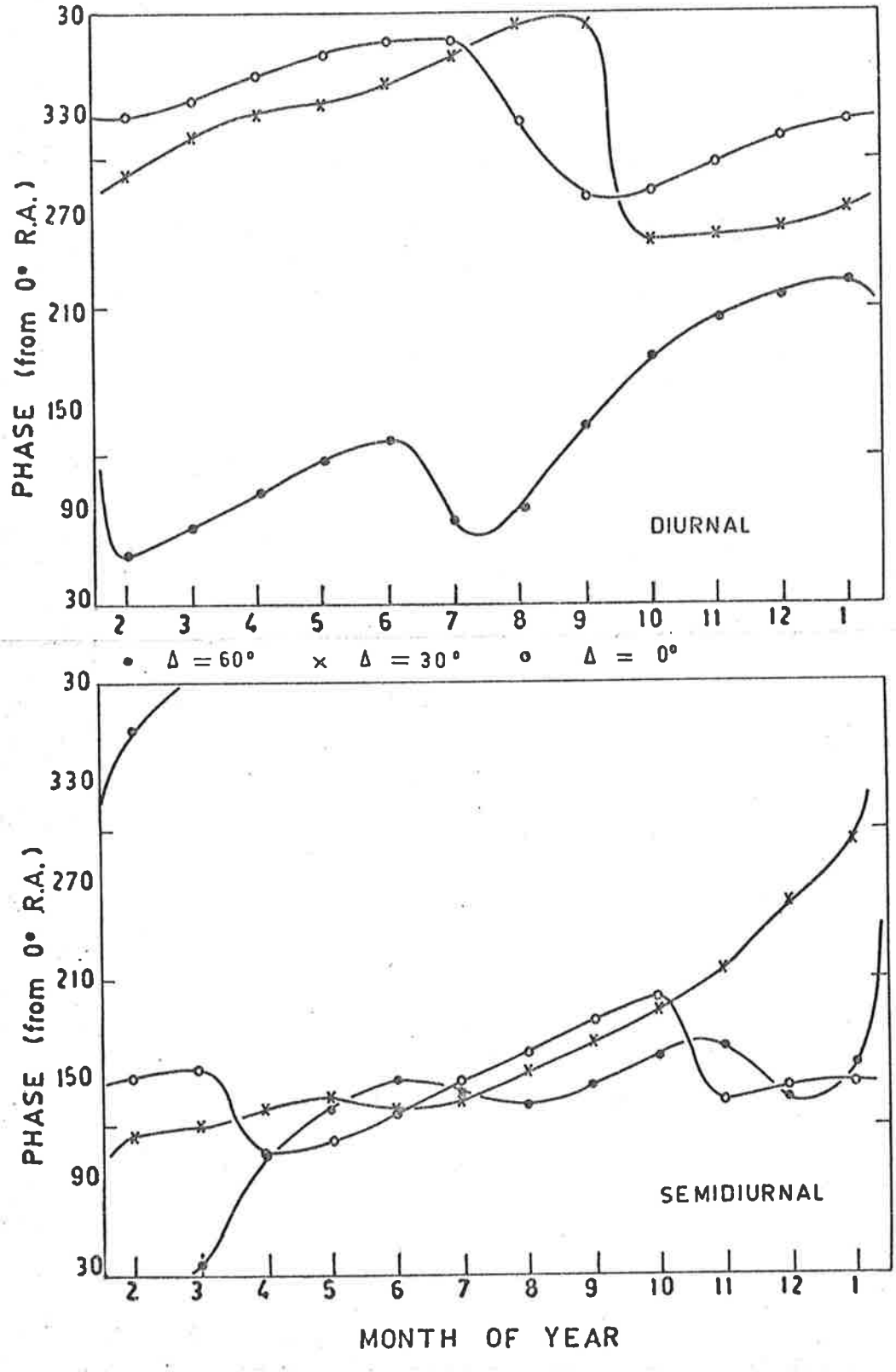

Figure 3.9 Diurnal and semidiurnal phases for the 2-way anisotropy.

Figures 3.8 and 3.9 show that

(i) There is a diurnal variation which is modulated at 1 cycle/year and 2 cycles/year as in the case of a 1-way anisotropy. The average monthly amplitude is 0·18 units.

(ii) The diurnal variation phase changes by up to 140° throughout the year in contrast with the 1-way anisotropy case, where the phases remain constant near 330°. As Figure 3.9 shows, the magnitude of the changes in the diurnal variation phase, and the actual values of the phases are strongly dependent on the Earth's position within the sector structure (i.e. dependent on Δ).

(iii) The semidiurnal variation amplitude in general undergoes a more complex modulation than for the 1-way anisotropy case. For $\Delta = 30^{\circ}$ and $\Delta = 0^{\circ}$ there is a marked 1 cycle/year modulation, but for $\Delta = 60^{\circ}$ a 3 cycle/year component appears in the modulation. The average of the monthly amplitudes is 0·17 units.

(iv) The semidiurnal variation phases approximate to 140° for 9-10 months of the year indicating that this variation is a result of the observation of the

galactic 2-way anisotropy (maxima at 150° and 330°).

(v) For the most part the semidiurnal variation has maximum amplitude when the diurnal variation has minimum amplitude (and vice versa), suggesting that the diurnal variation appears as a consequence of perturbation of the semidiurnal variation.

Figure 3.10 shows the actual daily variations for the 12 equispaced days within a year, for $\Delta = 30^{\circ}$. The arrows in Figure 3.10 indicate the time of transit of the Sun for each day. It can be seen that near this time, there is a deviation from the semidiurnal variation, expected for rectilinear cosmic ray orbits.

It should be noted that it is, at first sight, quite surprising that a diurnal variation should be derived from a semi-diurnal (2-way) anisotropy. The presence of the diurnal variation is in fact due to the diurnal nature of the variation in ε, the separation between the anisotropy axis and the asymptotic direction. This is a result of the anisotropy (with its axis inclined to the equatorial plane) being observed at predominantly positive asymptotic latitudes (see Figure 2.6). This causes the detector to sample maximum intensity (to look closest to the anisotropy axis) once a day only, thereby producing the spurious diurnal component. If the anisotropy axis was in the equatorial plane the generation of the diurnal "sub-harmonic" would be much less pronounced.

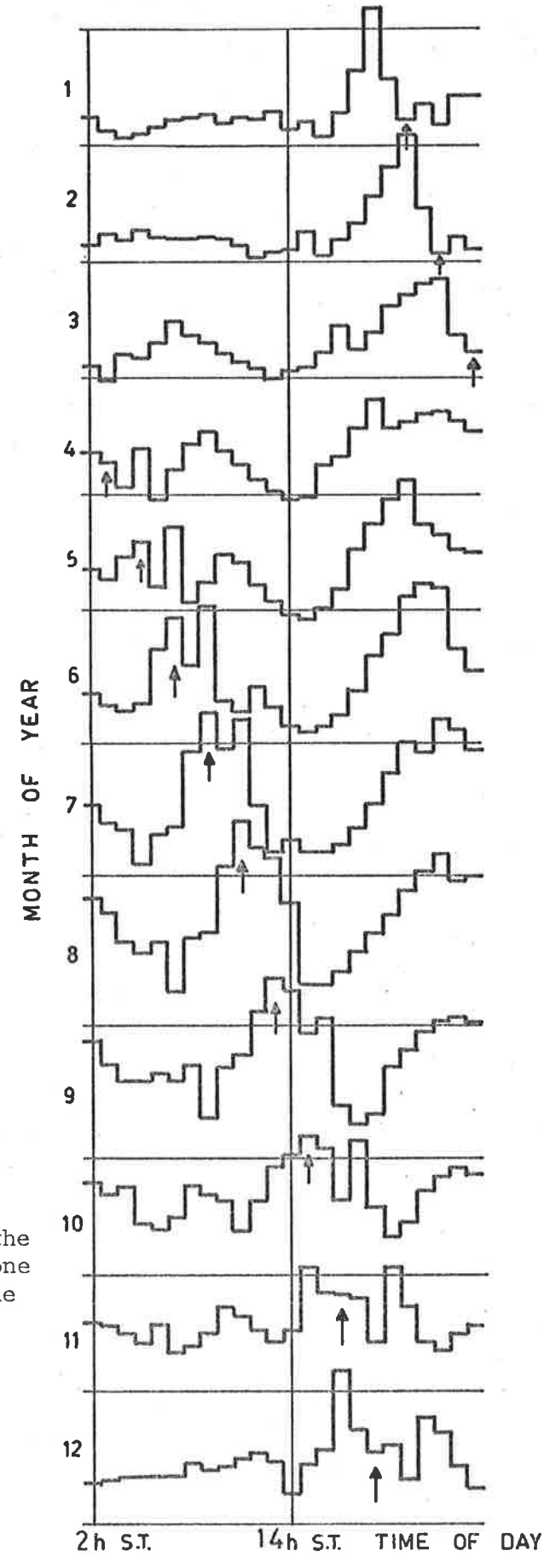

Figure 3.10

The actual daily variations for the 12 equispaced days of the year (one in each month) considered, for the 2-way anisotropy.

In view of the results obtained for the 1-way and 2-way anisotropies it is possible to draw a useful conclusion. The spurious component of the sidereal daily variation (semidiurnal variation for 1-way anisotropy, and diurnal variation for 2-way anisotropy), arises as a direct consequence of the presence of the interplanetary magnetic field. Since the direction of the interplanetary magnetic field changes throughout the year (in celestial co-ordinates), then the phase of the spurious component of the sidereal variation can also be expected to change (in S.T.) in a similar way throughout the year. On the other hand the anisotropy is fixed in space, so that the component of the sidereal variation resulting from direct observation of this anisotropy will have a constant phase (in S.T.) throughout the year.

3.5 Modulation by the Rotating Sector Structure

The behaviour of the amplitudes of the diurnal and semi-diurnal variations through a year can be constructed by plotting the amplitudes for all three values of Δ in the sequence determined by the rotation of the sector structure past the Earth. For sector boundaries separated by 90° of longitude, it takes 6·75 days for a whole sector to pass the Earth. (The solar rotation period is taken to be 27·0 days).

So far, only sidereal variations for the Earth situated within a positive sector (field directed away from Sun) have been considered.

Figure 3.11 shows the modulation calculated for the Earth in the same relative position ($\Delta = 30^{\circ}$) within two sectors of opposite polarity. It can be seen that the modulations are the same except that they are 6 months out of phase. This is not an unexpected result, since the asymptotic directions for these two positions have the same longitudes, but their latitudes have opposite sign.

The rotating sector structure will therefore have a striking effect if there is a 1 cycle/year modulation of the daily variations. For example, in the month when the 1 cycle/year modulation yields a maximum (say) diurnal variation amplitude, there will be a minimum amplitude 6·75 days later in the next sector (where the 1 cycle/year modulation is effectively 6 months out of phase). If the modulation is predominantly at 2 cycles/year however, the passage of the sectors will have little effect since a 6 month phase shift yields the same amplitude value, i.e. there is no change from sector to sector.

The presence of any 1 cycle/year modulation therefore implies that there will also be a modulation of 13·5 days period (27 cycles/year) in the amplitude of the daily variation in question. For a 1-way galactic anisotropy, both the diurnal and semidiurnal variations show a strong 1 cycle/year modulation (see Figure 3.4), and so could be expected to have a strong 27 cycle/year modulation also. In Figure 3.12 the amplitude of the diurnal and semidiurnal variations for a

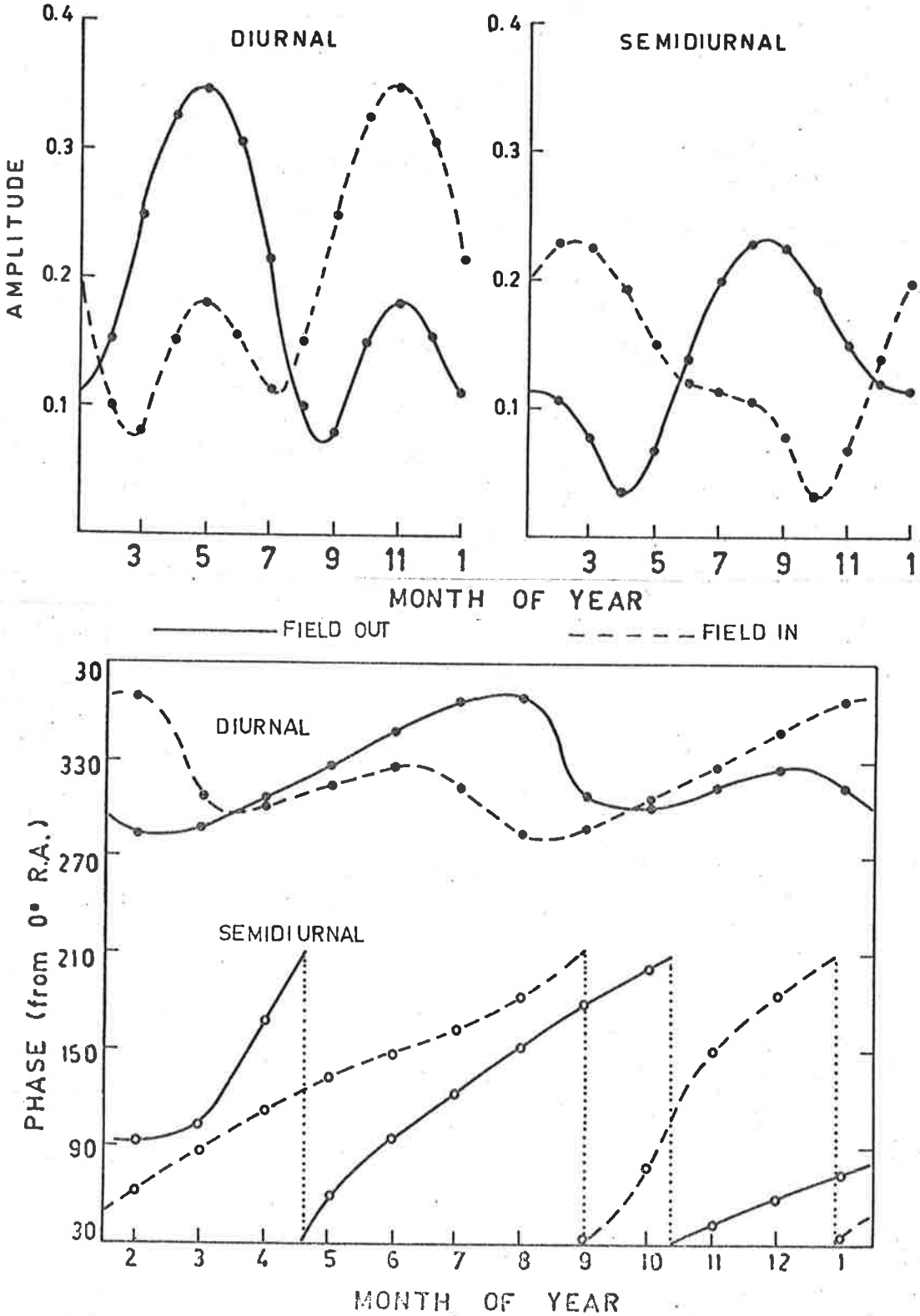

Figure 3.11 The diurnal and semidiurnal variation amplitudes and phases for the Earth at $\Delta = 30^{\circ}$ in a positive sector (full lines) and a negative sector (dashed lines) for the 1-way anisotropy.

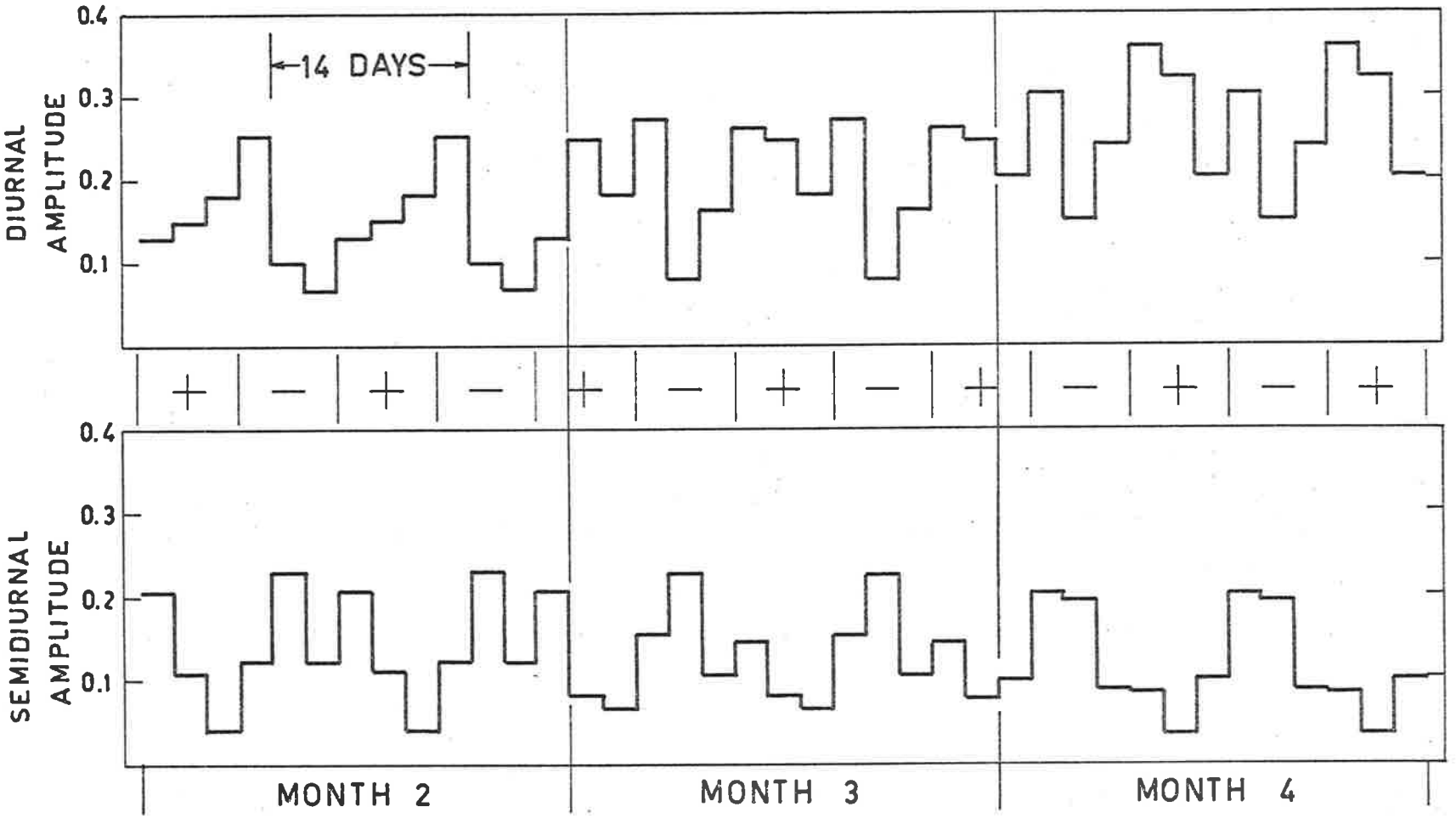

Figure 3.12 The modulation of the diurnal and semidiurnal variation amplitude for 3 months of the year, for the 1-way anisotropy.

1-way galactic anisotropy is plotted at 6·75/3 day intervals for months 2, 3 and 4. (Each sector takes 6·75 days to pass and we consider 3 equispaced positions within each sector). Figure 3.12 clearly shows the presence of a 14 day period (26 cycles/year) modulation.

The Frequency Spectrum of the Sidereal Variations

If we have a wavetrain amplitude a and frequency ω_1, and we amplitude modulate this with another sinusoidal waveform of amplitude b and frequency ω_2, the amplitude A of the resultant waveform is given by

$$A = (1 + b\cos\omega_2 t)\, a\cos\omega_1 t$$

expanding this

$$A = a\cos\omega_1 t + \tfrac{1}{2} ab \cos(\omega_1 + \omega_2)t + \tfrac{1}{2} ab \cos(\omega_1 - \omega_2)t$$

Therefore the product of the two waveforms yields three Fourier components with amplitudes and frequencies (i) a, ω_1 ; (ii) $ab/_2$, $\omega_1 + \omega_2$; (iii) $ab/_2$, $\omega_1 - \omega_2$. In radio terminology, component (i) is the carrier, and components (ii) and (iii) are sidebands.

Table 3.2 lists the principal components of the sidereal variation frequency (or power) spectrum obtained using the above result for the modulations discussed earlier.

TABLE 3.2

The principle frequency components in the variation at Earth associated with a cosmic ray anisotropy outside the solar system

Carrier	Modulation	Frequencies
'Sidereal' Diurnal Variation (366 cycles/year) for 1-way and 2-way	1 cycle/year	365 cycles/year 366 367
	2 cycles/year	364 366 368
	*27 cycles/year	339 366 393
'Solar' Semidiurnal Variation (730 cycles/year) for 1-way	1 cycle/year	729 cycles/year 730 731
	*27 cycles/year	703 730 757
'Sidereal' Semidiurnal Variation (732 cycles/year) for 2-way	1 cycle/year	731 cycles/year 732 733
	*27 cycles/year	705 732 757

* The sector boundary modulation will be centered on 27 cycles/year; however there will be considerable fluctuation. Thus the results for this modulation should be regarded as center frequencies of extended ranges.

These results suggest a method of testing for a component in the sidereal variation due to the presence of a galactic anisotropy, as distinct from a component due to the solar controlled mechanism of Swinson, (1969a). A 2 cycle/year modulation would not be expected in sidereal variations caused by the N-S streaming mechanism of Swinson, so the presence of a 368 (366 + 2) or a 734 (732 + 2) cycle/year component in the data would indicate a galactic anisotropy origin for the sidereal variation. Modulation at 366 $\pm$ 27 and 732 $\pm$ 27 cycles/year would be present in both of these forms of sidereal variation.

To distinguish between the 366 and 368 cycle/year components (or between the 732 and 734 cycle/year components) a power spectrum analysis would be required. However to obtain the necessary frequency resolution and satisfactory stability, many years of data would be required.

3.6 The Yearly Average Sidereal Variations

Most of the observations of the high energy cosmic ray flux ($\geq$ 50 GeV) have been made with detectors with geo-asymptotic directions of viewing near $\theta_A = \pm 40^\circ$ (e.g. Hobart, London, Rome, Huancayo, Freiberg). The observations of the sidereal diurnal variation made with these detectors have suggested that this is a true sidereal effect as distinct from a spurious solar induced effect (Jacklyn, 1966). Strong support was provided for this conclusion

when in 1954 Conforto and Simpson (1957), and in 1961 Jacklyn (1965a,b) observed that as the solar diurnal variation decreased to a minimum, the sidereal diurnal variation increased until it became the predominant effect. The analysis performed here for an equatorially viewing detector is not directly comparable with these results, however.

Recently (Jacklyn and Vrana, 1969), results have been obtained from an equatorially viewing detector at 40m.w.e., which (together with the above results) can be best explained using a bidirectional (2-way) galactic anisotropy. Jacklyn and Vrana give their observations averaged over 1 year, so that a detailed comparison with the monthly averages derived here is not possible at this time. Further observations with equatorially viewing detectors have been made by Swinson (1969a,b ; 1970). In this case the diurnal variations are averaged over $1\frac{1}{2}$ - 3 years for times when the interplanetary magnetic field is (1) directed inwards (2) directed outwards; however no semidiurnal variation results are given.

To facilitate a comparison with such observational results, the theoretical variations described in sections 3.3 and 3.4 are suitably averaged. Firstly the variations for each month of the year are averaged over the 6 Earth-sector structure positions used (3 in + sector, 3 in - sector). These monthly values are then averaged to yield the yearly values. For the two cases of 1-way and 2-way

anisotropies, Figures 3.13 and 3.14 show the diurnal and semidiurnal variation amplitude and phase for each month after averaging over the 6 sector structure positions and performing the harmonic analysis. It is seen that the amplitudes are now modulated at 2 cycles/year only, except in the 2-way semidiurnal case, where there is a small 1 cycle/year component. This is because the 1 cycle/year components for corresponding positions in sectors of opposite polarity are effectively 6 months out of phase (see Figure 3.11 and discussion in section 3.5), and so they cancel when summed (or averaged). Figure 3.13 shows that the diurnal phase varies systematically by 20° about 330° - the direction of the anisotropy, whereas the semidiurnal phase varies through one complete cycle in 12 months. This suggests that the semidiurnal variation would largely cancel if these 12 semidiurnal variations were averaged. On the other hand Figure 3.14 shows that for a 2-way anisotropy, it is the semidiurnal phase which remains nearly constant (near 150° or 330°), while the diurnal phase varies through 360° over the year. In this case the diurnal variation can be expected to cancel when the results are averaged over one year.

Figure 3.15 shows the sidereal daily variation which results from summing the 6 variations (i.e. 3 in a +ve sector, 3 in a -ve sector) for the days chosen to represent each month, and then summing these variations over the 12 months in the year. Figure 3.15(a) is the yearly average variation for a 1-way anisotropy and 3.15(b) for a

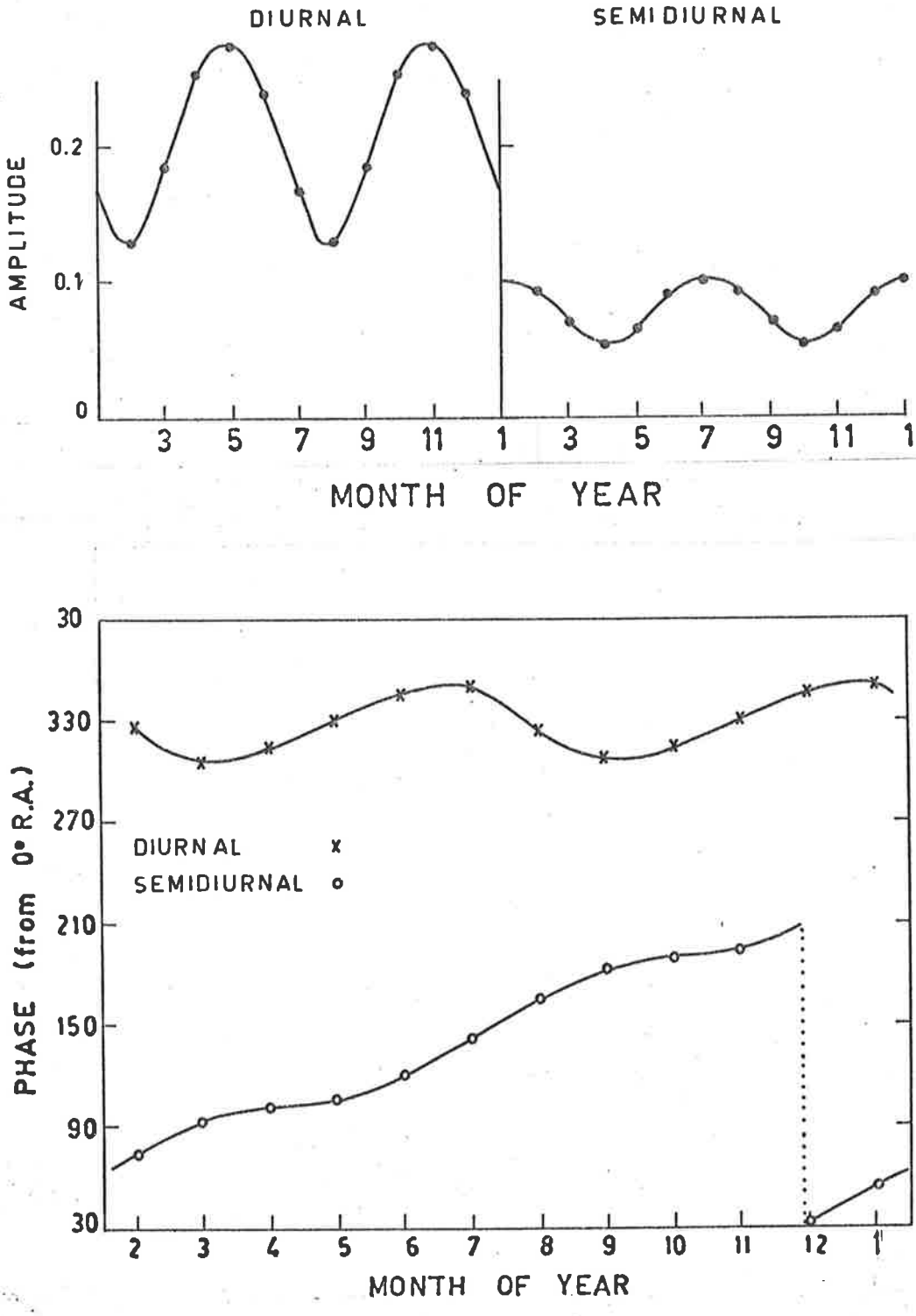

Figure 3.13 The diurnal and semidiurnal variation amplitudes and phases after averaging over 6 sector positions for the 1-way anisotropy.

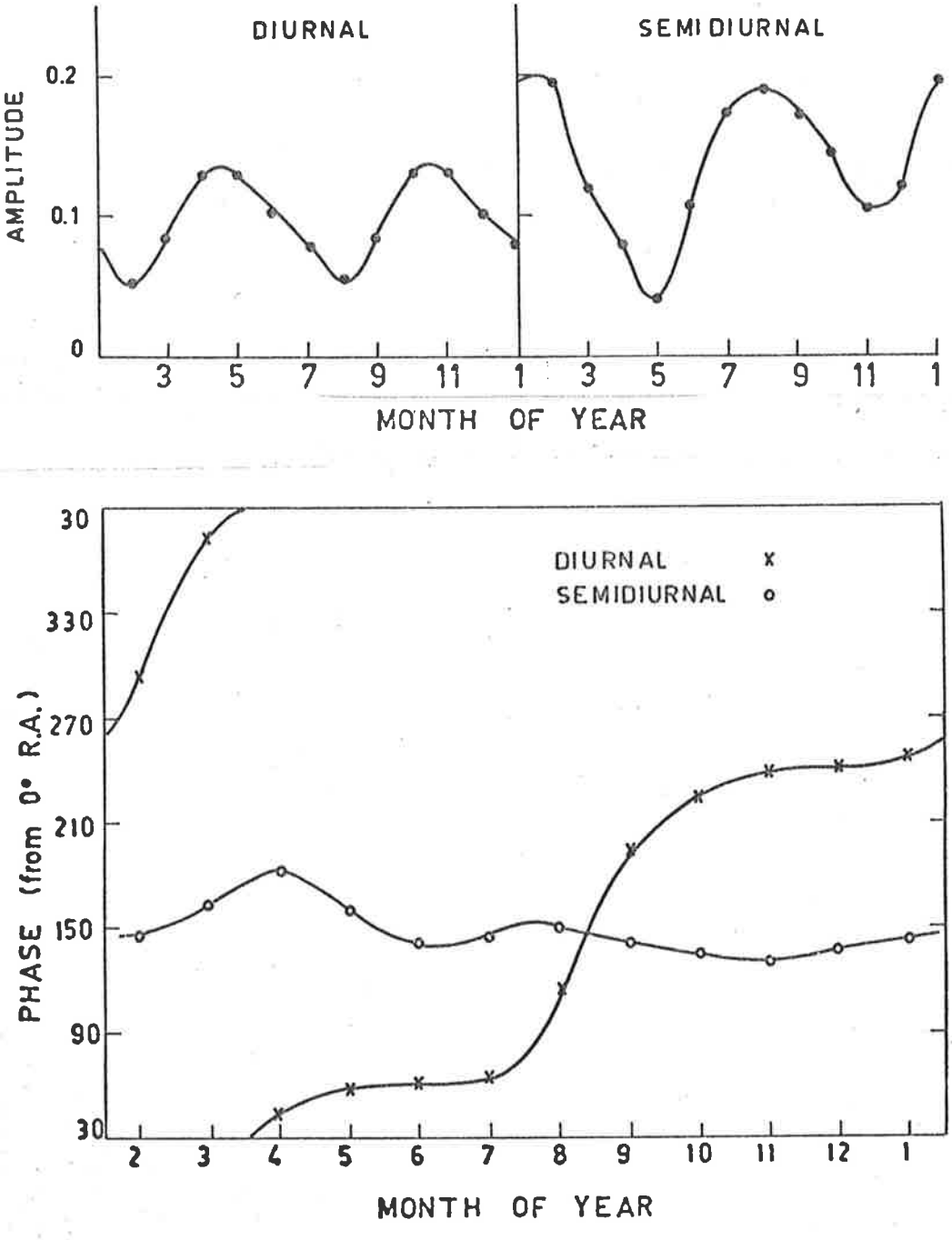

Figure 3.14 The diurnal and semidiurnal variation amplitudes and phases after averaging over 6 sector positions for the 2-way anisotropy.

2-way anisotropy. It can be seen that the 1-way yearly average is a diurnal variation with phase 330° and with no appreciable semidiurnal component, while the 2-way yearly average is a semidiurnal variation with phase 150° (or 330°) and no appreciable diurnal component. These are just the forms which would be expected for straight line trajectories. However, the amplitudes of these yearly variations are smaller than would be expected for the straight line case. The reduction factor

$$= \frac{\text{variation amplitude with real trajectories}}{\text{variation amplitude with straight line trajectories}}$$

is $1/_{2\cdot9}$ for the 1-way case, and $1/_{2\cdot6}$ for the 2-way case. Hence although the phase of the yearly average variation is the same as would be expected for straight line trajectories, the interplanetary magnetic field has the effect of reducing its amplitude by a factor of more than 2·5 (relative to the straight line case). The amplitude reduction factor was also calculated for a 1-way anisotropy with maximum at (270, 30). This is the direction towards which the solar system is moving relative to the interstellar medium. For this case the factor is $1/_{2\cdot8}$. Elliot et al (1969) have estimated that a variation of amplitude ·015% will result from this apparent cosmic ray flow (using a relative velocity of 20 km/sec). The present analysis suggests that an amplitude of $\cdot015/_{2\cdot8}$ = ·0054% could be expected in this case.

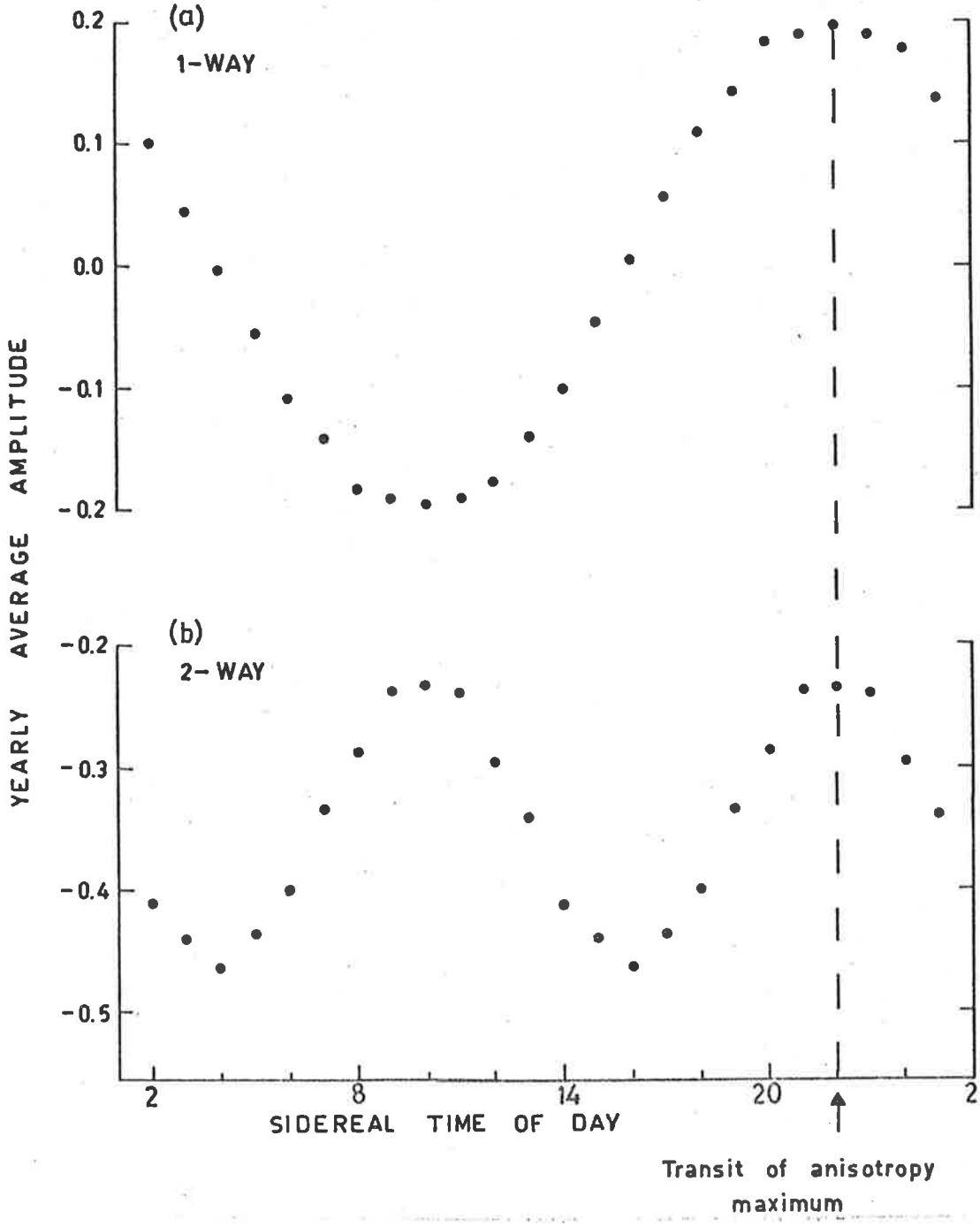

Figure 3.15 The yearly average daily variation in sidereal time for (a) the 1-way anisotropy, (b) the 2-way anisotropy.

It is now possible to summarise these results. Although the analysis was performed using an idealised model, these general conclusions can give a reliable indication of what can be expected under real conditions. The conclusions are

(i) A galactic anisotropy will be observable at Earth, but with a reduced amplitude. The average reduction factor is $1/2{\cdot}9$ for a 1-way anisotropy, and $1/2{\cdot}6$ for a 2-way anisotropy.

(ii) On the short term, spurious harmonics are present in the sidereal daily variation (a semidiurnal variation for a 1-way anisotropy, and a diurnal variation for a 2-way anisotropy).

(iii) The phase of the spurious harmonic varies roughly linearly through 24 hours (in sidereal time) throughout the year. Hence the spurious variations cancel when a yearly average is taken.

(iv) The phase of the yearly average variation is just that expected for straight line trajectories.

(v) The interplanetary magnetic field introduces a 2 cycle/year modulation in both the diurnal and semidiurnal variation amplitude. This should provide

a method of differentiating against the solar induced sidereal effects. For a true galactic anisotropy this effect will introduce a 368 cycles/year variation (for a 1-way anisotropy).

The choice of a different direction for the interstellar magnetic field would not effect these general conclusions, although the values for the amplitudes and phases on a short time scale would differ.

CHAPTER 4

THE ORIGIN OF SCATTER COEFFICIENTS - THEORY

4.1 Introduction

From time to time in the cosmic ray literature attention has been drawn to large amplitude depressions of 3-12 hours duration in the cosmic ray flux centered near 0900 hours Local Time, that is when the detector 'looks' in along the interplanetary magnetic field line (Fenton et al, 1959; Rao and Sarabhai, 1967; Ables et al, 1967; Lockwood and Razdan, 1963). The conclusion drawn from this behaviour is that, at these times, there exists a cosmic ray anisotropy aligned with the interplanetary magnetic field. The interplanetary conditions associated with these events will now be examined in detail, but instead of dealing with anisotropies or bulk effects, a microscopic approach is adopted and the behaviour of selected individual cosmic rays is examined. An important property of the cosmic rays involved, is that they are appreciably scattered in the interplanetary medium, and herein lies the key to our understanding of these phenomena.

If we know the trajectory that a cosmic ray follows through interplanetary space to Earth, then we know that a cosmic ray which is detected on Earth must have been last-scattered at a point on this trajectory. If we also know the scattering properties of the interplanetary medium, and we specify the relative cosmic ray number density to be 1·0 everywhere, then it is possible to calculate the relative

probability of the particle being last-scattered from different regions along the trajectory. The sum of these probabilities is here taken to be 100%. Because the trajectories differ for the same cosmic ray arriving at different times of day, these probabilities change throughout the day for any particular region of space.

These probabilities are here called the "Origin-of-Scatter Coefficients", of the cosmic ray detector in question. These coefficients can be used to calculate how the cosmic ray flux at Earth varies throughout the day when the relative cosmic ray number density is not 1·0 everywhere. The flux arriving at the detector from a given region (at heliocentric radius r) at time of day T, is obtained by multiplying its origin-of-scatter coefficient $\zeta(r,T)$, by the relative number density in that region. The contributions from all possible regions are then summed to give the total flux observed on Earth at time T. This process is repeated for 24 times of day to yield the daily variation for the radial number density gradient in question.

The outcome of this approach is that it is possible to predict the daily variations that will be observed as a consequence of any assumed cosmic ray density gradient. The fluctuations predicted are similar to those observed in practice. Since a number density gradient implies a diffusive streaming or anisotropy in the cosmic rays parallel to the magnetic field lines, this result is a generalisation of the usual diffusive models used to explain the diurnal variation (Parker, 1964; Axford, 1965). It is a generalisation in so

far that situations can be studied that are not tractable using simple diffusive theory.

The application of this origin-of-scatter technique shows that unique interplanetary cosmic ray gradients can be associated with most short term ($\sim$ 1 day) cosmic ray variations. In Chapter 6 details of these gradients and other interplanetary conditions are derived for several classes of cosmic ray intensity variations. In the remainder of this chapter a theoretical expression for the origin-of-scatter coefficient is derived, and in Chapter 5 the calculation procedure used in practice is given and the resulting origin-of-scatter coefficients are presented.

All references to asymptotic directions in these chapters (4, 5 and 6), are in fact to geo-asymptotic directions, or the directions just outside the magnetosphere of the Earth.

4.2 The General Analytical Approach

We require to calculate the probability that a cosmic ray arriving at a detector at time of day T is last-scattered within a given volume of space; or equivalently we require the fraction (expressed in %) of the total cosmic ray flux detected at time T, which was last-scattered within the given volume of space.

Volume elements of interplanetary space are defined, and each of these is regarded as the source of the cosmic rays which are scattered within that volume. The 'strength' of any volume element as

a source of cosmic rays is proportional to the number density of cosmic rays in that volume. The volumes chosen are bounded by concentric spheres centered on the Sun, but because the cosmic rays of interest spiral about the local interplanetary magnetic field line after their last scatter, only that small fraction of the volume near the magnetic field lines which pass close to Earth is an effective source to an observer on Earth. Typical cosmic ray trajectories for 3 arrival times are shown in Figure 4.1. Notice how these orbits spiral about the field lines (which lie in the ecliptic).

The origin of scatter coefficient $\zeta(r,T)$ (in percent) is then given by

$$\zeta(r,T) = \frac{1}{F} \frac{dF}{dr} \cdot 100 \quad \% \qquad (4.1)$$

where F is the total cosmic ray flux arriving at the detector, and dF is that part of F which was last scattered between r and r + dr, and which reaches the detector without being scattered again. $\zeta(r,T)$ is computed assuming that the number density is 1·0 everywhere, and it is assumed that in this situation the total flux F will be the same for all times of day T, so that for any T

$$\sum_r \zeta(r,T) = 100\% \qquad (4.2)$$

The total flux F arrives at a detector from within a solid angle known as the asymptotic cone of acceptance. To estimate the flux which is last scattered between r and r + dr we trace representative cosmic rays back along their orbits from within the cone of

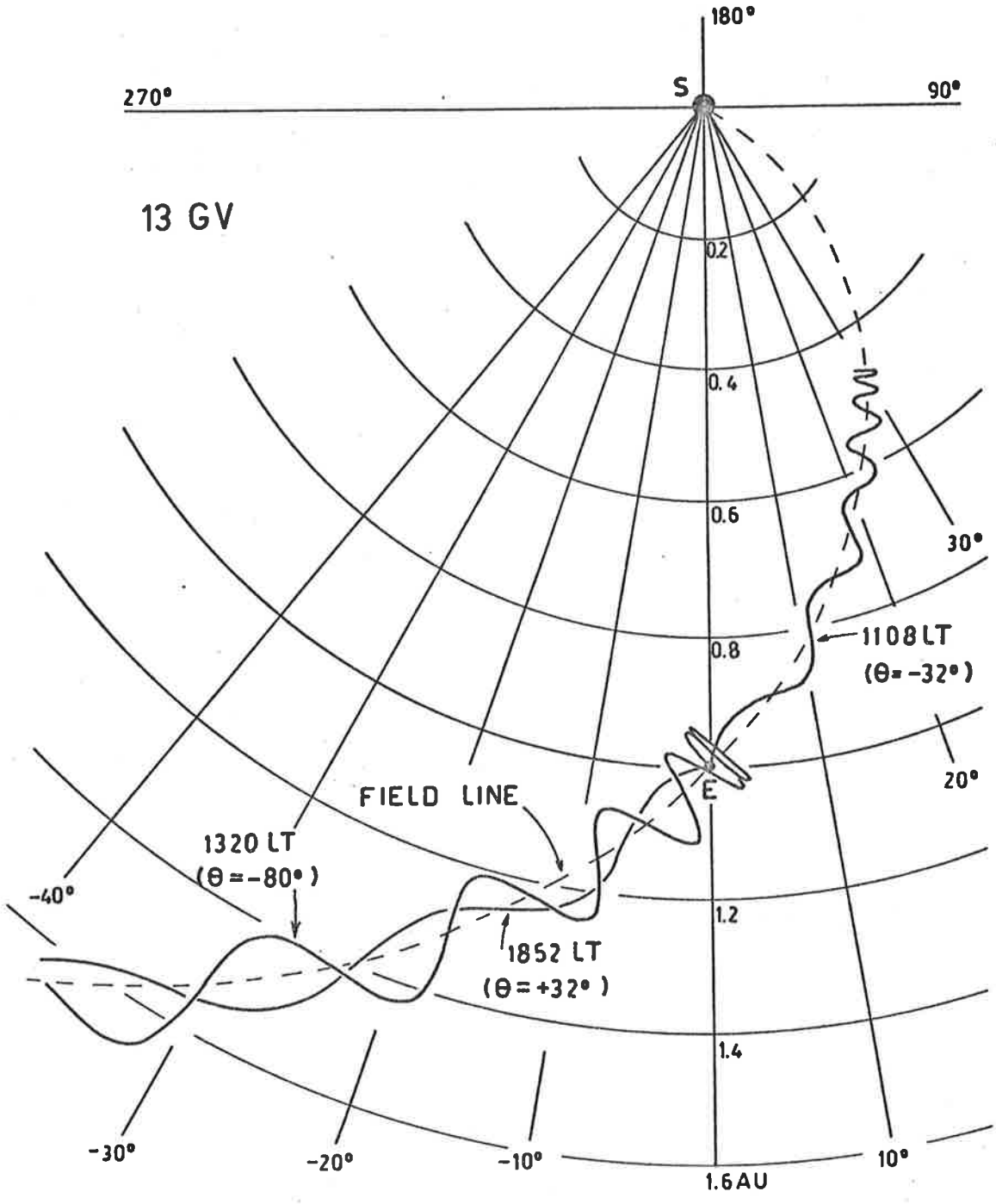

Figure 4.1 Three examples of cosmic ray orbits which terminate at Earth, showing how the orbits spiral about the interplanetary magnetic field. The orbits shown are for 13 GV cosmic rays which arrive with pitch angles of -32°, -80°, and +32°.

acceptance at Earth to calculate the necessary parameters. Now the cone of acceptance changes for different particle rigidities. McCracken et al (1965) give asymptotic directions which define the cone of acceptance at rigidities which can be taken as representative of a series of rigidity increments over the detector differential rigidity response. The total flux at the detector of cosmic rays scattered within dr at r, is then the sum of the fluxes from the separate rigidity intervals. For each representative rigidity, McCracken et al list 9 asymptotic directions. These 9 directions were chosen to represent 9 "subcones" of acceptance which contribute equal fluxes ($\frac{1}{9}$th each) to the total flux within that rigidity interval. This is an important fact because it enables us to normalise the flux from each dr so that the total flux from all r is the same for each subcone.

Let $f_{ij}(r,T)$ be the flux at the detector in the rigidity increment i, which arrived within the subcone of acceptance j from the volume element at r at time of day T. This flux is normalised so that the total flux from all r arriving in subcone j is $\frac{1}{9}$.

$$\text{i.e.} \quad f^*_{ij}(r,T) = \frac{f_{ij}(r,T)}{9 \sum_r f_{ij}(r,T)} \tag{4.3}$$

The flux $F_i(r,T)$ from the volume element at r which arrives at time T through the whole cone of acceptance for cosmic rays in rigidity increment i is then

$$F_i(r,T) = \sum_{j=1}^{9} f^*_{ij}(r,T) \tag{4.4}$$

The earlier normalisation means $\sum_r F_i(r,T) = 1{\cdot}0$. The flux contributions $F_i(r,T)$ from r are now weighted with W_i, the area under the differential response curve for the i^{th} rigidity interval. W_i is normalised so that $\sum_i W_i = 100\%$. Thus

$$\zeta_i(r,T) = W_i F_i(r,T) \qquad (4.5)$$

where $\zeta_i(r,T)$ is the origin of scatter coefficient for rigidity interval i for the volume element at r for time T. The total origin of scatter coefficient $\zeta(r,T)$ is then

$$\zeta(r,T) = \sum_i \zeta_i(r,T) \qquad (4.6)$$

The normalisation procedures used ensure that $\sum_r \zeta(r,T) = 100\%$.

It can be seen that the fundamental quantity required to calculate $\zeta(r,T)$ is the flux $f_{ij}(r,T)$. We now derive an expression for this.

4.3 The Fundamental Flux Increment, $f_{ij}(r,T)$

To find an expression for $f_{ij}(r,T)$ we consider cosmic rays of one rigidity (the representative rigidity of the ith rigidity increment) which arrive within a subcone of acceptance (jth) at time of day T.

Now the cone of acceptance of a detector (for a given rigidity) defines a volume in space inside which all cosmic rays of the chosen

rigidity which reach Earth, are last-scattered. In Figure 4.2 the form of this volume is sketched by extending two trajectories each from opposite edges of a subcone of acceptance. This volume is designated the volume of acceptance in Figure 4.2. $f_{ij}(r,T)$ is the flux of cosmic rays at Earth which were last scattered between r_1 and r_2 within this volume. Because the value for this flux is later normalised, constant factors are not important in the expression derived for $f_{ij}(r,T)$, and can be ignored. Only factors which change with r, the heliocentric radius, need be retained.

Consider the cross-sectional volume element at P within the volume of acceptance (see Figure 4.2). We define the "cone of injection" at P to be the solid angle of cosmic ray directions at P which result in the cosmic rays reaching the detector at Earth (if they are not scattered en-route). It is important to note that the cone of injection at any point P will only be finite if the detector has a finite area; there is only <u>one</u> orbit through any point P in the volume of acceptance which can reach a point detector. The source function S, at P is defined to be the number of cosmic rays scattered into unit solid angle per unit time per unit volume at P. The dimensions of the volume element at P are ΔA_p the area of cross-section of the volume of acceptance at P, and thickness dx, where x is the distance of P along the orbit from Earth (see Figure 4.2). Let $d\Omega_p$ be the average cone of injection for all points across ΔA_p.

The number of cosmic rays $N_p dx$, scattered from within the

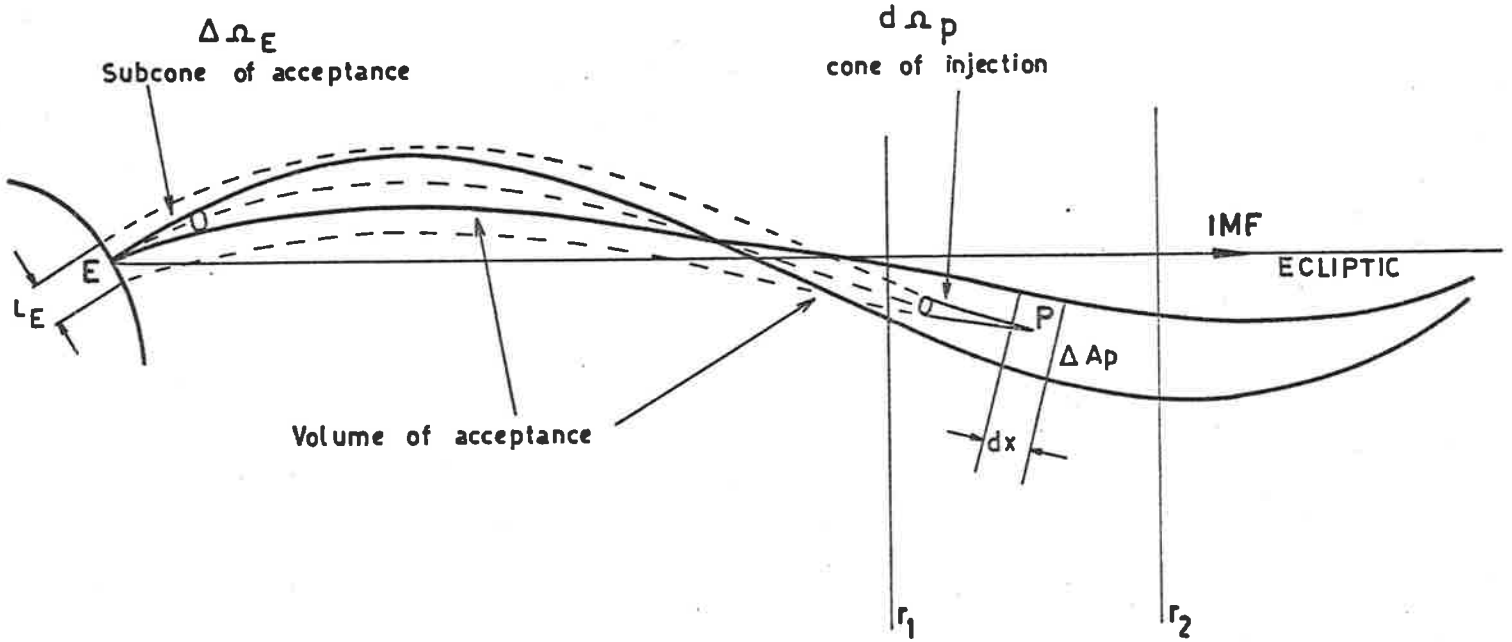

Figure 4.2 Showing the region of space (= volume of acceptance), for a given rigidity, inside which all cosmic rays which reach Earth within the subcone of acceptance shown, are last-scattered. The cone of injection $d\Omega_p$ at point P is defined by the orbits which pass through P and which reach the detector on Earth.

volume element at P per unit time into the cone of injection is therefore $Sd\Omega_p \Delta A_p dx$, and the number of cosmic rays from this volume at P which reach Earth can be written as

$$N_p dx = Sd\Omega_p \cdot \Delta A_p dx \, e^{-x/\lambda} \qquad (4.7)$$

where λ is the scattering mean free path. The term $e^{-x/\lambda}$ is an attenuation factor which accounts for cosmic rays which are scattered again en-route from P to the detector.

In this treatment we have assumed isotropic pitch angle scattering so that the value of S is indepenedent of the orientation of $d\Omega_p$.

The Source Function, S

S is given by the number of cosmic rays scattered into unit solid angle per unit time per unit solid angle. Let λ_i and v_i be the scattering mean free path and the velocity respectively, for cosmic rays within the ith rigidity increment. Now λ_i is the average distance a cosmic ray travels between scatters, and since the cosmic ray travels a distance v_i in unit time, the probability of one cosmic ray being scattered in unit time into unit solid angle is $v_i/\lambda_i \cdot 1/4\pi$. Hence, if the number density of cosmic rays in rigidity interval i is U_i

$$S = \frac{U_i v_i}{4\pi\lambda_i} \quad \text{sec}^{-1} \text{ ster}^{-1} \text{ cm}^{-3} \qquad (4.7A)$$

$$\text{or } S = \frac{I_i}{\lambda_i} \qquad (\text{since } U_i = \frac{4\pi I_i}{v_i}) \qquad (4.7B)$$

where I_i is the cosmic ray intensity in rigidity interval i.

The expression for $f_{ij}(r,T)$, the flux from between r_1 and r_2 or x_1 and x_2 ($x_1 = x(r_1)$, $x_2 = x(r_2)$ as in the adjacent diagram), is therefore given by

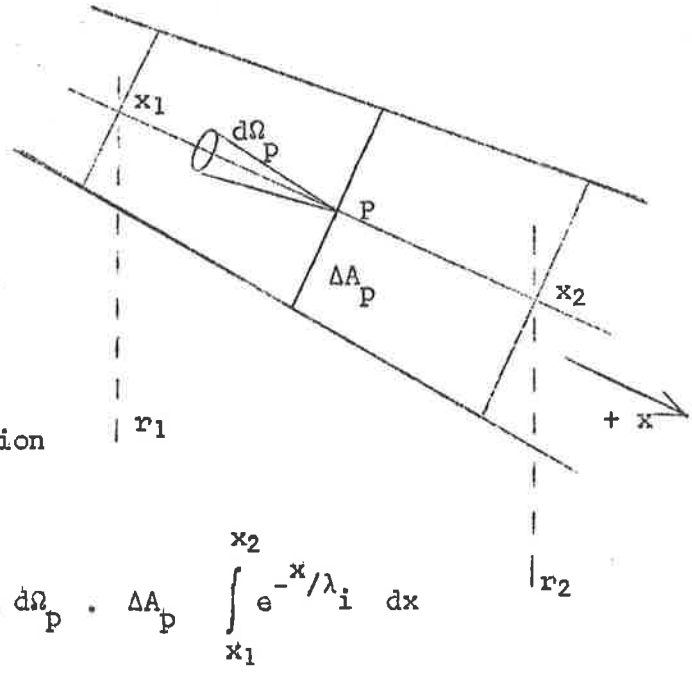

$$f_{ij}(r,T) = \int_{x_1}^{x_2} N_p \, dx$$

and using equation 4.7, and substituting for S from equation 4.7B

$$f_{ij}(r,T) = \frac{I_i}{\lambda_i} \cdot d\Omega_p \cdot \Delta A_p \int_{x_1}^{x_2} e^{-x/\lambda_i} \, dx$$

and integrating

$$f_{ij}(r,T) = I_i \, d\Omega_p \, \Delta A_p \, (e^{-x_1/\lambda_i} - e^{-x_2/\lambda_i}) \qquad (4.8)$$

This assumes $d\Omega_p . \Delta A_p$ can be taken as representative of the whole volume between x_1 and x_2. The parameter x is obtained from the representative orbit calculated for each subcone.

We now require an expression for $d\Omega_p . \Delta A_p$ as a function of r. It is therefore necessary to investigate the properties of a cone

cone of trajectories as we move away from the point from which all the trajectories emerge.

4.4 Properties of a Cone of Directions in Space

We require an expression for $d\Omega_p \Delta A_p$ in equation 4.8. The solid angle (cone of injection) $d\Omega_p$ is dependent on the effective detection area at Earth, while the cross-sectional area ΔA_p is dependent on the size of the subcone of acceptance at Earth (see Figure 4.2). Thus in both cases we require an expression relating the angular dimensions of a cone of directions at a 'starting' point in space to the area of cross-section of the volume defined by this cone of directions in regions away from the starting point. We now derive such an expression.

Consider the cone of directions $d\Omega_y$ at an arbitrary point Y in interplanetary space. It is convenient to represent this cone on the celestial sphere as in the diagram. Each point on the surface of the sphere represents the direction obtained by projecting from the center outwards through that point. Points separated by equal 'distances' around the sphere's surface represent

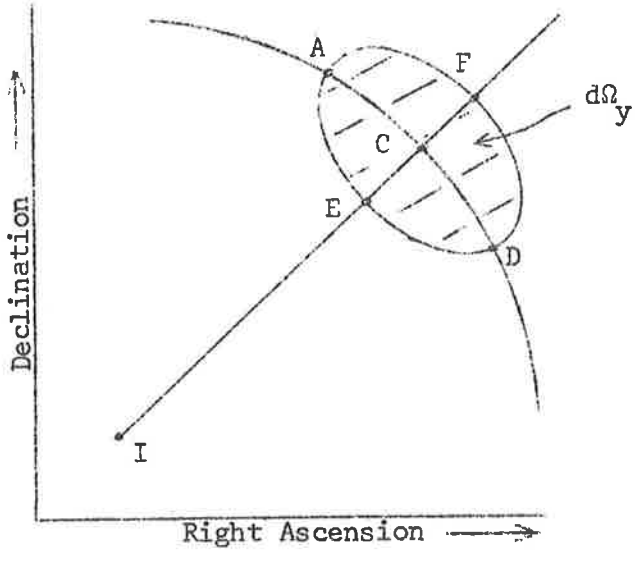

directions with equal angular separations. Thus in the diagram the curve AFDE defines the cone of directions $d\Omega_y$, and C is the central direction of the cone. The point I represents the direction of the interplanetary magnetic field at Y.

We now investigate how the spatial separation of trajectories A and D, and E and F varies as we move away from Y. Points A, C and D are equidistant from I and so represent trajectories with the same pitch angle. Points E, C and F have unequal pitch angles and they represent the full range of pitch angles in $d\Omega_y$ (the cone of directions that connects point Y to the observer on Earth).

The first step in understanding how these trajectories behave relative to each other is to determine how their guiding centers behave. As Figure 4.1 shows, the cosmic ray guiding centers closely approximate to the interplanetary field lines. Hence if we know the separation of the respective guiding centers for the trajectories at Y, it is possible to calculate the separation for the same trajectories away from Y.

We find the position of the guiding center relative to the point Y on the orbit, using

$$\underset{\sim}{\rho} = \frac{m}{qB^2} \cdot (\underset{\sim}{v} \times \underset{\sim}{B})$$

where $\underset{\sim}{\rho}$ is the radius of gyration vector linking Y to the guiding center, $\underset{\sim}{v}$ is the cosmic ray velocity vector and $\underset{\sim}{B}$ is the interplanetary

magnetic field vector (this equation is derived in section 1.5). Thus the guiding centers of all trajectories at Y lie in the plane perpendicular to the interplanetary magnetic field at Y. The magnitude of the radius of gyration ρ is given by

$$\rho = \frac{P \sin\theta}{Bc}$$

where P is cosmic ray rigidity, θ is the pitch angle, B is the magnetic field strength and c is the velocity of light. Therefore trajectories A, C and D have equal gyroradii while $\rho_e < \rho_c < \rho_f$. Figure 4.3(a) shows the cone of directions at Y, the directions of the five representative trajectories ($\underset{\sim}{YC}$, $\underset{\sim}{YA}$, $\underset{\sim}{YD}$, $\underset{\sim}{YE}$ and $\underset{\sim}{YF}$) and the five radius of gyration vectors for these trajectories at Y. These five vectors terminate in the five guiding centers. It is seen that

(i) The guiding centers of trajectories A, D and C lie in the plane perpendicular to the magnetic field direction ($\underset{\sim}{YI}$).

(ii) The guiding centers of trajectories E, C and F also lie in this plane and they are colinear.

It is now possible to produce Figure 4.3(b), a projection onto the plane perpendicular to the magnetic field, which shows how the 5 trajectories evolve as the cosmic rays move away from Y. Points A′, C′, D′, E′ and F′ represent the guiding centers of the five trajectories. The trajectories are shown as circles centered on the appropriate guiding center - this is only so in a constant amplitude

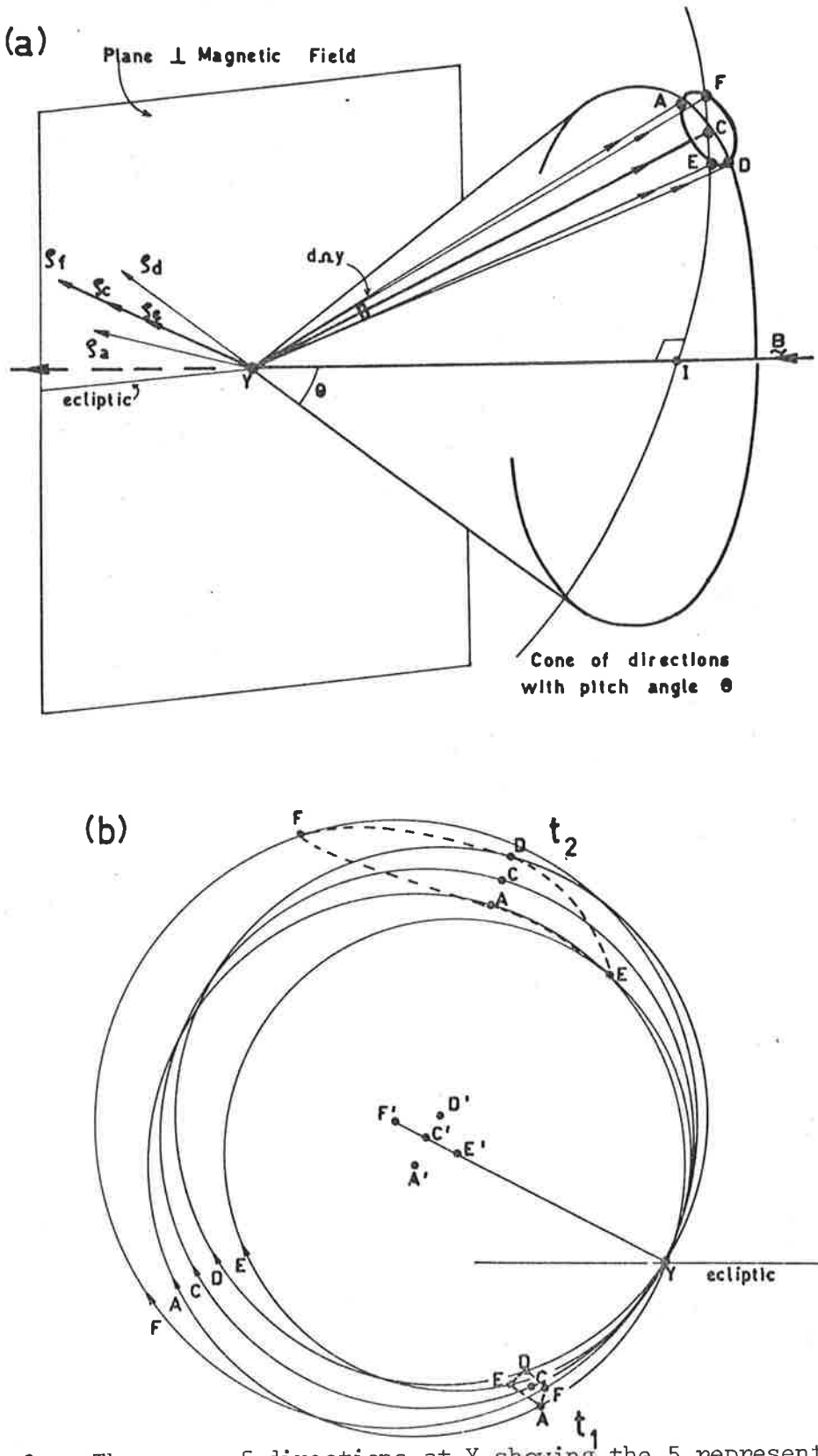

Figure 4.3a. The cone of directions at Y showing the 5 representative directions $\underset{\sim}{YC}$, $\underset{\sim}{YA}$, $\underset{\sim}{YD}$, $\underset{\sim}{YE}$, $\underset{\sim}{YF}$ and their radius of gyration vectors at point Y.

b. A projection onto the plane perpendicular to the interplanetary magnetic field showing how the five trajectories become separated in planes remote from Y.

magnetic field. As B varies Figure 4.3(b) will contract or expand as a whole as the gyroradii change. Trajectories A, D and C have equal ρ and equal periods of gyration, so in any plane removed from Y the phase relation between these three trajectories remains the same as at Y. On the other hand trajectories E, C and F have unequal ρ and unequal periods of gyration, so that as we move our plane (perpendicular to the magnetic field) away from Y, the points on the circles showing the intersections of these trajectories change their phase relationship.

Thus the area of cross-section of the cone becomes extended in one dimension as trajectories E and F increase their separation, while the other dimension (AD) oscillates from a minimum near zero to a maximum related to the separation of the guiding centers of A and D. In figure 4.3(b) two examples of the cross-sectional area are shown at different distances away from Y.

We now develop a quantitative expression for the dimension of the cross-sectional area of the cone of directions as we move away from Y. The two dimensions of this cross-sectional area mentioned above are considered separately, i.e. we investigate the separation of two trajectories

(i) with equal pitch angles (A and D)

(ii) with different pitch angles (E and F)

Before proceeding however, it is necessary to derive a relation for the

separation of two guiding centers, as we change r.

4.4.1 The Variation with r of the Separation between Two Guiding Centers

The guiding centers are assumed to follow the interplanetary magnetic field lines. Consider the two extreme situations: case 1 when both guiding centers lie in the plane perpendicular to the ecliptic (diagram A), and case 2 when the two guiding centers lie in the plane of the ecliptic (diagram B). The two adjacent field lines considered in each case are formed by the radial outflow of plasma from two adjacent points on the Sun. In case 1 the points are separated in heliolatitude by $d\lambda$, and in case 2 are separated in heliolongitude by $d\phi$. Consider the separations s_y and s_z, perpendicular to the field lines.

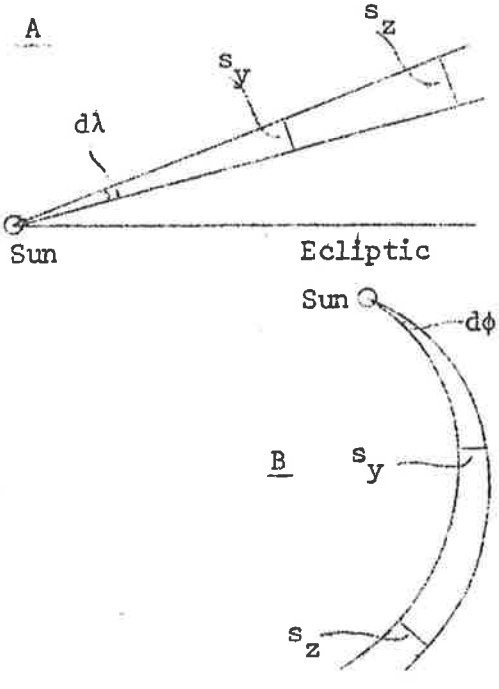

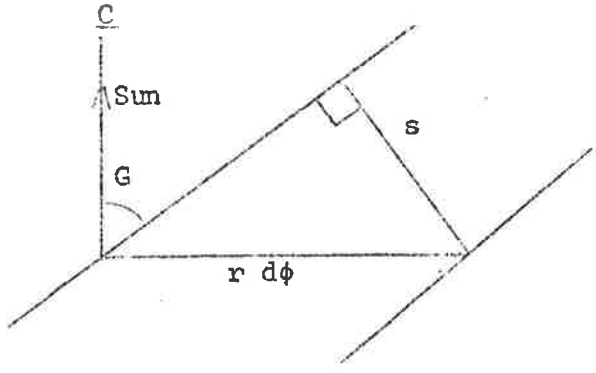

In case 1 diagram A shows that

$$\frac{s_z}{s_y} = \frac{r_z d\lambda}{r_y d\lambda} \qquad \text{so} \qquad s_z = s_y \frac{r_z}{r_y} \tag{4.9}$$

In case 2 diagrams B and C show that

$$s = r d\phi \cos G$$

$$\text{so that} \qquad s_z = s_y \frac{r_z \cos G_z}{r_y \cos G_y} \tag{4.10}$$

The average of case 1 and case 2 is taken after the final expression for each has been established.

4.4.2 The Separation of Two Trajectories with Equal Pitch Angles

Consider two trajectories A and D with equal pitch angles which both pass through point Y (Figure 4.4a) where they have an angular separation α_y. We require the spatial separation L_{1z} of these two trajectories in the plane perpendicular to the magnetic field line at Z (on the guiding center of the central trajectory C).

We first calculate the separation of the guiding centers of trajectories A and D at Y. The angular separation α_y' of the gyroradius vectors ρ_a and ρ_d at Y is shown in Figure 4.4(b), in which all directions on the cone have equal pitch angles θ_y. We are interested in the two directions YA and YD and the relationship between α_y and α_y'. Now in Figure 4.4(b) $\angle AID = \alpha_y'$, so we can use triangle AID to relate α_y and

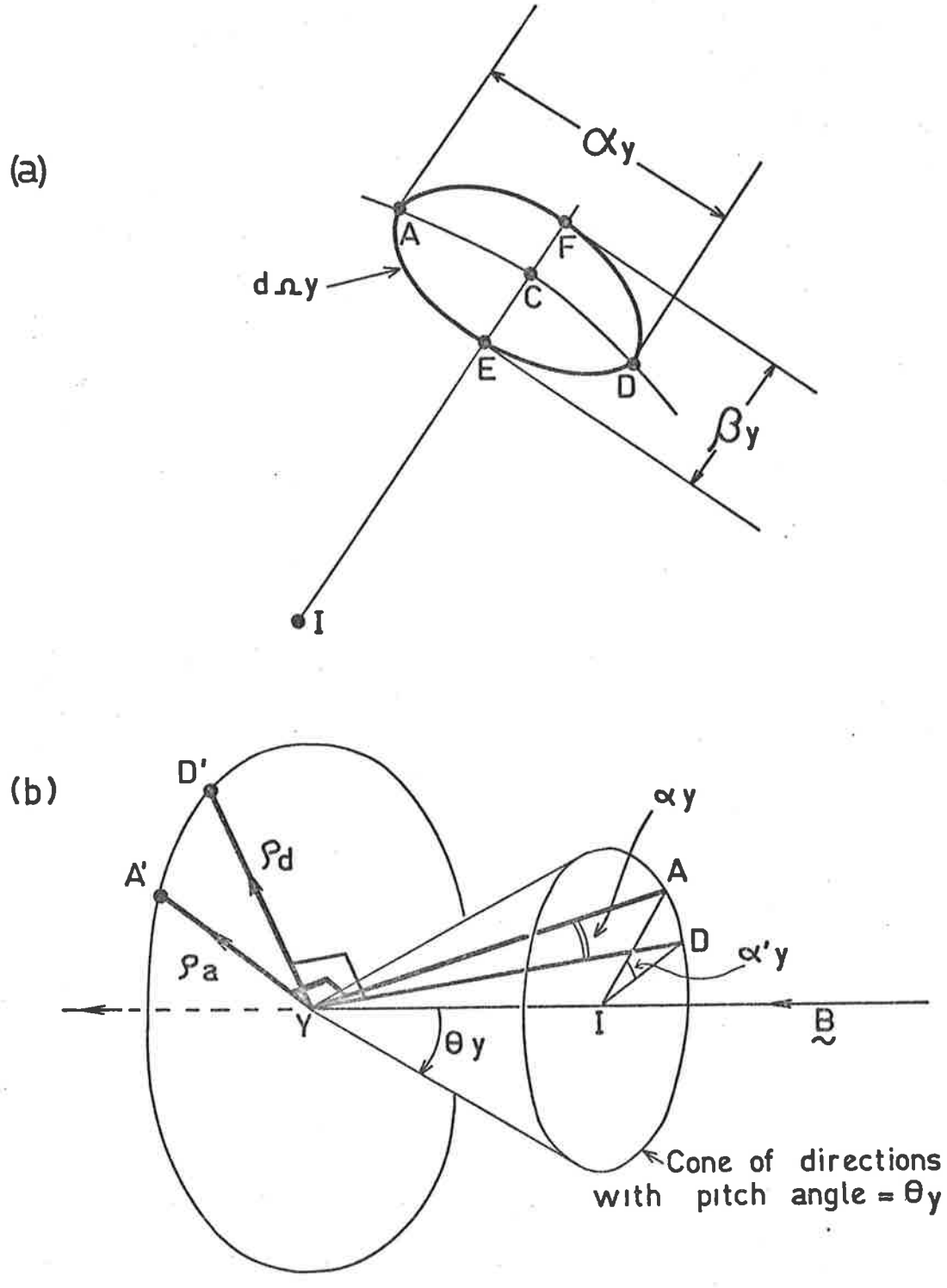

Figure 4.4a. The cone of injection at Y projected onto the celestial sphere (see text), showing the angular dimensions α_y and β_y.

b. The geometry used to calculate the angular separation ($\angle A'YD' = \alpha'_y$) of two gyro-radii when the orbits have equal pitch angles.

α_y' (AD can be considered a straight line for small α_y and α_y').

$$\text{Now} \quad AD = YA \cdot \alpha_y$$

and in triangle AID

$$AD = YA \sin \theta_y \cdot \alpha_y'$$

$$\text{Hence} \quad \alpha_y' = \frac{\alpha_y}{\sin \theta_y}$$

Thus from Figure 4.4(b) the distance $A'D'$ between the two guiding centers at Y is simply

$$A'D' = \rho_y \cdot \alpha_y' \qquad \text{where} \quad \rho_y = \rho_a \text{ (at Y)} = \rho_d \text{(at Y)}$$

$$\text{so} \quad A'D' = \rho_y \frac{\alpha_y}{\sin \theta_y} \tag{4.11}$$

In section 4.3.1 the relation between the separation s, of two guiding centers at points Y and Z at different distances from the Sun is found to be

$$s_z = s_y \cdot \frac{r_z}{r_y} \cdot \left(\frac{\cos G_z}{\cos G_y} \right) \tag{4.12}$$

where the term inside the brackets is omitted for case 1 (equation 4.9) and included for case 2 (equation 4.10). Now $A'D'$ in equation 4.11 is s_y for two trajectories with equal pitch angles. At a point Z removed from Y equations 4.11 and 4.12 yield

$$s_z = \alpha_y \frac{\rho_y}{\sin \theta_y} \cdot \frac{r_z}{r_y} \cdot \left(\frac{\cos G_z}{\cos G_y} \right) \qquad (4.13)$$

The separation L_{1z} of the actual trajectories at Z is related to the guiding center separation by a phase factor $f(\psi_{cz} - \psi_{cy})$ where $\psi_{cz} - \psi_{cy}$ is the phase difference in the central orbit C between points Y and Z (i.e. the angular separation of $\underset{\sim}{\rho}$ at Y and Z)

$$\text{i.e.} \quad L_{1z} = f(\psi_{cz} - \psi_{cy}) \cdot s_z$$

$$\text{or} \quad L_{1z} = \alpha_y \frac{\rho_y}{\sin \theta_y} \cdot \frac{r_z}{r_y} \cdot \left(\frac{\cos G_z}{\cos G_y} \right) f \qquad (4.14)$$

This is the required relation between L_{1z} and α_y.

4.4.3 The Separation of Two Trajectories with Unequal Pitch Angles

Consider now the trajectories E and F at point Y in Figure 4.3(a). Their angular separation at Y is β_y, the second dimension of the cone of directions at Y. We require to know how the spatial separation of these two trajectories changes as we move away from Y.

Figure 4.5 shows the projection of trajectories E, C and F onto the plane perpendicular to the guiding center locus. It can be seen that at Y trajectories E and F are coincident and in phase. As we move the plane away from Y, the points E and F in Figure 4.5 (the intersection points of trajectories E and F) become further and further

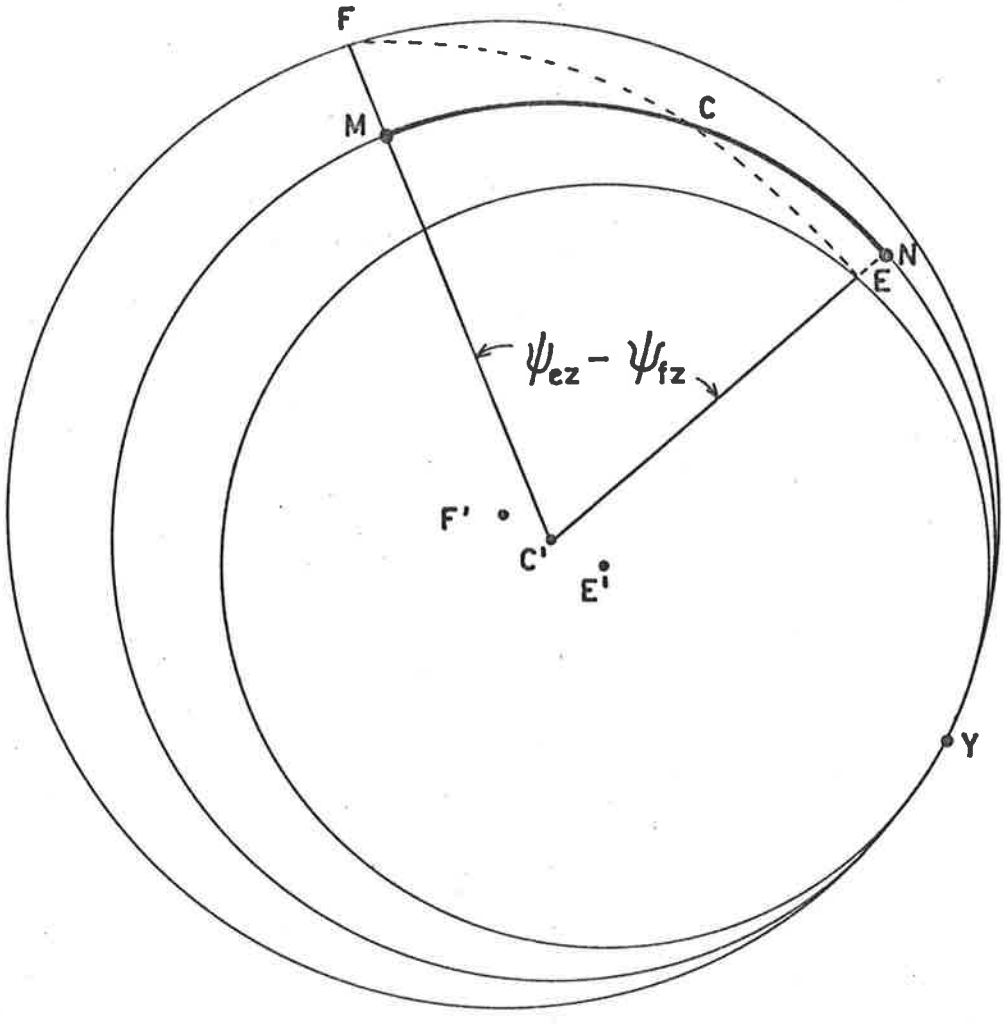

Figure 4.5 The geometry used to estimate the spatial separation of two orbits with unequal pitch angles.

out of phase. The phase difference when the plane is at point Z on the central trajectory C is $\psi_{ez} - \psi_{fz}$.

In appendix 3 it is shown that

$$\psi_{ez} - \psi_{fz} \quad \alpha \quad \beta_y$$

$$\text{or} \qquad \psi_{ez} - \psi_{fz} = \beta_y \, g(r_y, r_z) \tag{4.15}$$

where $g(r_y, r_z)$ is the factor which relates the phase difference between trajectories E and F at Z, to β_y, the angular separation of E and F at Y.

Then from Figure 4.5, when β_y is small L_{2_z} (i.e. EF) can be approximated by MN

$$\text{i.e.} \quad L_{2_z} = \rho_z \cdot (\psi_{ez} - \psi_{fz})$$

$$\text{so} \quad L_{2_z} = \rho_z \cdot \beta_y \cdot g \tag{4.16}$$

This is the required expression between β_y and L_{2_z}.

4.3.4 Summary

We now have a relation between the angular dimensions α_y and β_y of a cone of dimensions at a point Y, and the corresponding spatial dimensions L_{1_z} and L_{2_z}, of the area of cross-section of the cone at same point Z along the cone from Y. These are given by equations

4.14 and 4.16, in which f and g are unknown factors of the orbital motion. Using these two equations we can now relate the solid angle $d\Omega_y$ at Y to the area of cross-section ΔA_z at Z.

$$\Delta A_z = L_{1_z} L_{2_z} = \alpha_y \beta_y \frac{\rho_y \rho_x}{\sin \theta_y} \cdot \frac{r_z}{r_y} \cdot \left(\frac{\cos G_z}{\cos G_y} \right) \cdot fg$$

$$\text{i.e. } \Delta A_z = d\Omega_y \frac{\rho_y \rho_x}{\sin \theta_y} \cdot \frac{r_z}{r_y} \cdot \left(\frac{\cos G_z}{\cos G_y} \right) \cdot fg \qquad (4.17)$$

The term in brackets is removed when the guiding centers of the trajectories with equal pitch angles lie in a plane perpendicular to the ecliptic (see section 4.3.2).

4.5 The Equation for the Origin-of-Scatter Coefficient

In section 4.2 we developed an expression (equation 4.8) for the basic element $f_{ij}(r,T)$ required to calculate the origin-of-scatter coefficient $\zeta(r,T)$. In this equation $d\Omega_p$ and ΔA_p are unknowns. $d\Omega_p$, the cone of injection is defined by the effective detector area at Earth, and ΔA_p is defined by the subcone of acceptance at Earth (see Figure 4.2).

We will now use the relation (equation 4.17) between the angular dimension of a cone of directions at a point Y and the spatial dimension of the same cone at another point Z, to obtain $d\Omega_p \Delta A_p$ in a usable form. Equation 4.17, however, contains the two unknown factors f and g. A closer examination of the geometry involved in this

problem reveals a method which removes these factors.

Figure 4.6 shows the effective detection area at Earth (dimension L_E) and the subcone of acceptance $\Delta\Omega_E$. The four orbits arriving at the edge of the detection area are the orbits which define the cone of injection at P. Also shown in Figure 4.5 is a cone of directions $d\Omega_E$ at Earth defined by the four orbits from P which intersect the edge of the effective detector area at E. It can be seen that it is possible to define the element dA_p of the cross-sectional area ΔA_p at P, which is bounded by orbits from $d\Omega_E$ at E, using orbits which are "parallel" to the orbits to the edge of the effective detector area which define $d\Omega_p$ at P. In this way $d\Omega_p$ and dA_p can be calculated using the same sets of orbits (except that they are displaced slightly in space), and the unknown factors f and g will be the same in each case. The cross-sectional area ΔA_p at P is then given by

$$\Delta A_p = \frac{\Delta\Omega_E}{d\Omega_E} \cdot dA_p$$

We now use this approach to write the expression required for $d\Omega_p, \Delta A_p$ in equation 4.8.

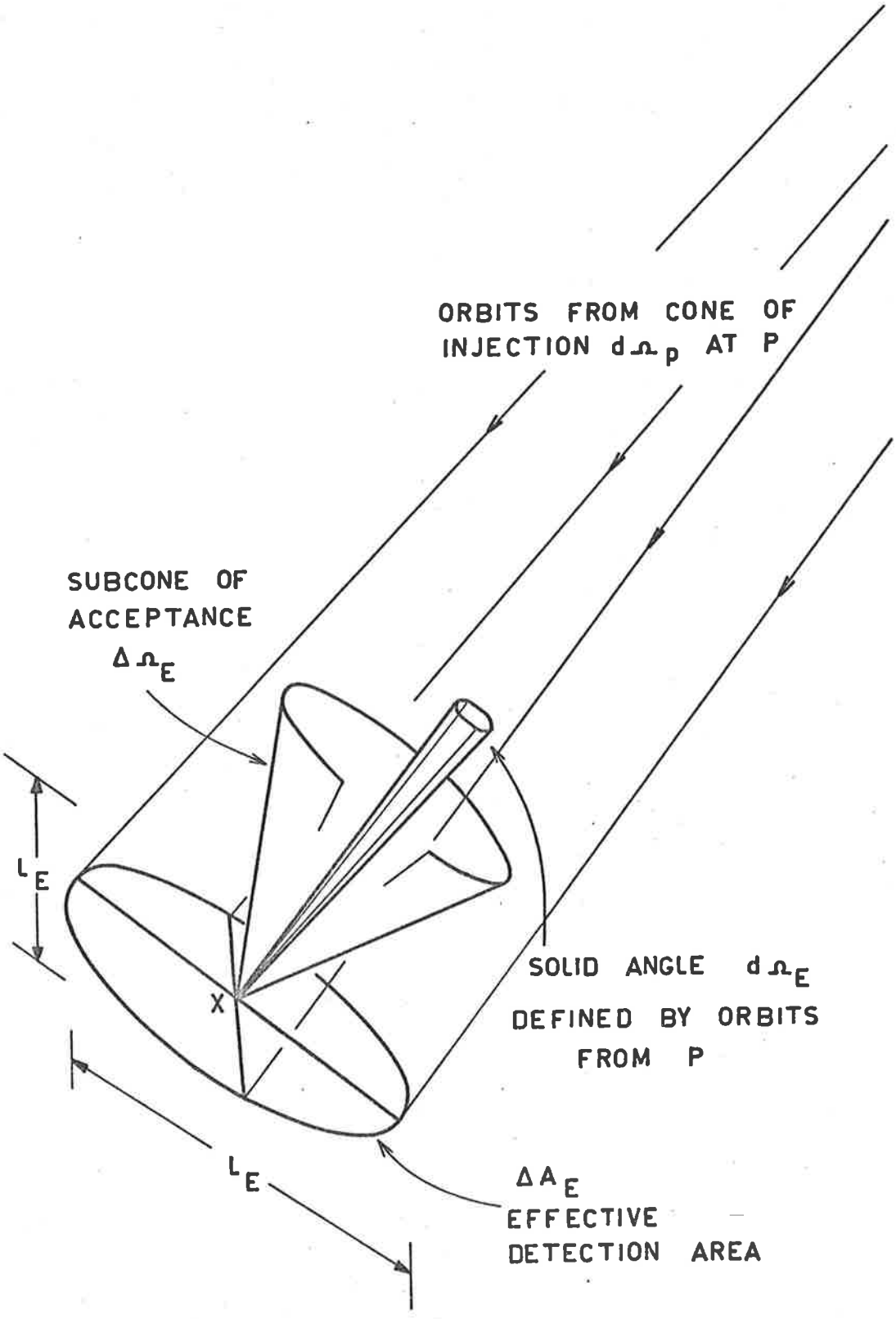

Figure 4.6 Showing the effective detection area ΔA_E at Earth, the subcone of acceptance $\Delta\Omega_E$ and the cone $d\Omega_E$ defined by the directions of orbits arriving at ΔA_E from point P.

Using equation 4.17 $d\Omega_p$ is found by substituting p for y and E for z (ie for the case of points P and E in Figure 4.2)

$$\text{i.e.} \quad d\Omega_p = \Delta A_E \frac{\sin\theta_p}{\rho_p \rho_E} \frac{r_p}{r_E} \left(\frac{\cos G_p}{\cos G_E} \right) \frac{1}{fg}$$

Similarly dA_p is obtained by substituting E for y and p for z

$$\text{i.e.} \quad dA_p = d\Omega_E \frac{\rho_p \rho_E}{\sin\theta_E} \frac{r_p}{r_E} \left(\frac{\cos G_p}{\cos G_E} \right) fg$$

Using the above three equations we obtain

$$d\Omega_p \cdot \Delta A_p = \Delta\Omega_E \Delta A_E \frac{\sin\theta_p}{\sin\theta_E} \frac{r_p^2}{r_E^2} \left(\frac{\cos^2 G_p}{\cos^2 G_E} \right)$$

Now the term within the brackets is removed for one extreme case and included for the other (see section 3.4.2). We now take the average of these two cases, so that

$$d\Omega_p \cdot \Delta A_p = \Delta\Omega_E \Delta A_E \frac{\sin\theta_p}{\sin\theta_E} \frac{r_p^2}{r_E^2} \frac{1}{2} \left(1 + \frac{\cos^2 G_p}{\cos^2 G_E} \right) \qquad (4.18)$$

We can now write the final expression for $f_{ij}(r,T)$ by substituting equation (4.18) in equation (4.8). Because this expression is later normalised we omit the constant terms. In addition subscript p is replaced by r, the heliocentric radius of the point P.

$$f_{ij}(r,T) = I_{ir} \sin\theta_r \cdot r^2 \left(1 + \frac{\cos^2 G_r}{\cos^2 G_E} \right) \cdot \left(e^{-x_1/\lambda_i} - e^{-x_2/\lambda_i} \right) \qquad (4.19)$$

where θ_r is the orbit pitch angle and G_r is the garden hose angle at heliocentric radius r (the central radius of the element of the volume of acceptance between r_1 and r_2, see Figure 4.2). Since at a given r, $U_{ir} = \frac{4\pi I_{ir}}{v_i}$, and since $v_i \approx c$ for all i, I_{ir} and U_{ir} are interchangeable in equation 4.19. (U_{ir} is the number density in rigidity interval i at r).

The parameters θ_r, x_1 and x_2 are obtained using the orbital calculations described in section 1.5. Equation 4.19 can then be used to calculate the origin-of-scatter coefficient $\zeta(r,T)$ using equations 4.3, 4.4, 4.5 and 4.6.

CHAPTER 5

THE ORIGIN-OF-SCATTER COEFFICIENTS - THE CALCULATIONS

5.1 Introduction

In Chapter 4 the theory for the calculation of the origin-of-scatter coefficients $\zeta(r,T)$ of a cosmic ray detector on Earth was given. In this chapter the details of implementing this theory are described and the resulting origin-of-scatter coefficients are presented.

Origin-of-scatter coefficients are here calculated for neutron monitors only. For any particular neutron monitor station $\zeta(r,T)$ are computed for 24 times of day T. The times chosen are 0030, 0130, 0230 ... etc. hours UT so that the cosmic ray variations predicted with this technique (in chapter 6) are directly comparable with the data from the world-wide net of stations. This data is given for hour 1 UT, hour 2 UT etc., where hour 1 UT extends from 0000 - 0100 hours UT etc. Consequently the origin-of-scatter coefficients calculated for 0030 hours UT can be used to estimate the flux at hour 1 UT and so on.

The basic volume elements for which $\zeta(r,T)$ are calculated are bounded by spherical surfaces, centered on the Sun, whose heliocentric radii differ by $^1/_{25}$ AU. $\zeta(r,T)$ are calculated for such radial increments out to $r \leq 3$ AU. The calculations are not extended to $r = 3$ AU if the contribution from the radial increments to the flux at

Earth (and therefore $\zeta(r,T)$) becomes negligible. Hence for every time of day T, up to 75 origin-of-scatter coefficients are computed.

The orbital parameters required for these calculations are calculated using the methods described in sections 1.3 and 1.5 for an interplanetary magnetic field model with field strength 5·0γ, and garden hose angle 45° at 1 AU.

Section 2 describes a simplification, concerned with the calculation of the necessary orbital parameters, which is used to make these calculations feasable. Section 3 discusses the details of the non-orbital factors, i.e. the spectral weights W_i and the mean free paths λ_i, which must be specified to compute $\zeta(r,T)$. In section 4 the origin-of-scatter coefficients for several stations for various mean-free-path values are presented and discussed.

5.2 The Standard Set of Orbits

In chapter 4 it was shown how the origin-of-scatter coefficients are derived from $f_{ij}(r,T)$, the parameter which is expressed in equation 4.19. It should be noted that although equation 4.19 was derived from a consideration of a cone of directions, it is sufficient to calculate the orbital parameters θ and x (pitch angle and orbit length) for one representative orbit only. This is because equation 4.19 is not an exact relation. Terms which remain constant for any one orbit are omitted, because the $f_{ij}(r,T)$ are later normalised as

in equation 4.3.

The cone of acceptance for rigidity interval i is divided into 9 subcones of acceptance. The representative (or central) asymptotic direction of each subcone is known (McCracken et al, 1965), so that the orbital parameters can be calculated for 9 arrival directions for each rigidity interval i. Now 10 rigidity intervals are considered. Hence to calculate $\zeta(r,T)$ for 24 times of day $9 \times 10 \times 24 = 2160$ interplanetary orbits would be needed for each cosmic ray station. In terms of computing time this is out of the question for even one station. The method of avoiding this difficulty arises out of the following discussion.

Consider the orbits A and B which arrive at the Earth with equal pitch angles θ, but 90° out of phase (see adjacent diagram). Now the behaviour of any one orbit tends to obey the relation $\frac{\sin^2\theta}{B} = k$, where k is a constant of that orbit, θ is the pitch angle and B is the magnetic field strength at any point along the orbit.

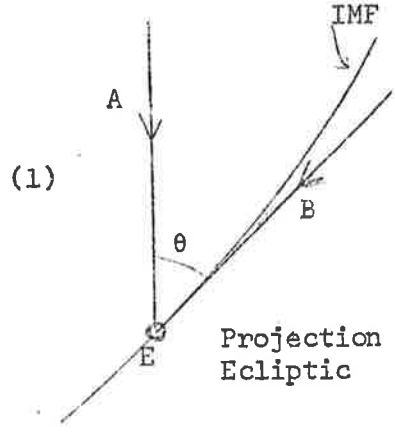

Projection onto Ecliptic

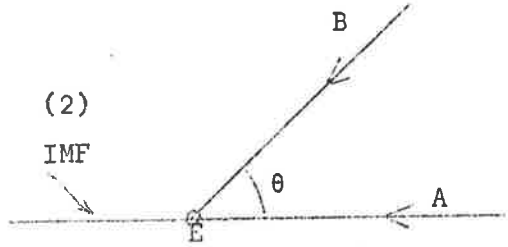

Projection onto meridional plane containing IMF at E.

This adiabatic relationship is most accurate at low rigidities, and becomes increasingly inaccurate at higher energies. It is useful to illustrate the reasoning used here however.

For the two orbits in the above diagram, k is the same ($= \sin\theta_E/B_E$), where the subscript E denotes values for r = 1 AU. Both orbits will mirror when $\sin^2\theta = 1$ i.e. $B = {}^1/_k$, and because B = B(r) they both mirror at the same heliocentric radius. Thus these two orbits can be expected to be similar along their complete length. Figure 5.1 shows a projection onto the ecliptic of these two orbits to the points where they mirror; the dotted lines show their guiding centers.

This result suggests that one orbit of pitch angle θ_E at Earth can satisfactorily (although not rigorously) represent all orbits arriving with this pitch angle. Furthermore it is now clear that the best way to minimise the number of orbits to be calculated is to define (arrival) pitch angle intervals, and to approximate an orbit with an arrival pitch angle within a given interval, to the representative orbit calculated for the pitch angle at the center of that interval. These representative orbits are called the standard orbits.

To reduce the errors which this approach may introduce, the length x along the orbit to the boundary of a volume element is taken to be the length along the orbit to the point which has its guiding center on the $r = \frac{N}{25}$ AU surface (rather than where the orbit itself

crosses this surface). The necessity for this can be understood from Figure 5.1.

Consider the volume element between r = $^{23}/_{25}$ AU and r = $^{22}/_{25}$ AU. The difference between the orbit lengths to these two surfaces (i.e. between x_1 and x_2) influences the flux estimated to originate in this volume element (see equation 4.19). It is clear from Figure 5.1 that the difference between these two lengths depends strongly on the phase of the cosmic ray orbit. On the other hand the difference between the orbit lengths to the two heavy dots on each of these orbits (the points where the guiding centers cross the surface of the volume element) are almost equal. Hence the guiding center criterion of determining when an orbit reaches a volume element, minimizes the errors which are introduced into the origin-of-scatter coefficients using the standard orbits.

The pitch angle intervals $\Delta\theta_E$ (and their central values $\bar{\theta}_E$) are chosen such that the increase in heliocentric radius Δr of an orbital point at a fixed distance x_D from Earth, is the same for each increase $\Delta\theta_E$. Thus the values of $\Delta\theta$ were chosen to give constant 'resolution' with respect to r, since the ultimate use of the orbits is to investigate the effects of an r-dependent quantity. The way $\frac{\Delta r}{\Delta\theta_E}$ (at a point x_D along the orbit from Earth) varies with θ_E was found empirically by calculating orbits for pitch angles at 10° intervals from 0° to 90° for 15 GV cosmic rays. Δr was calculated by taking the

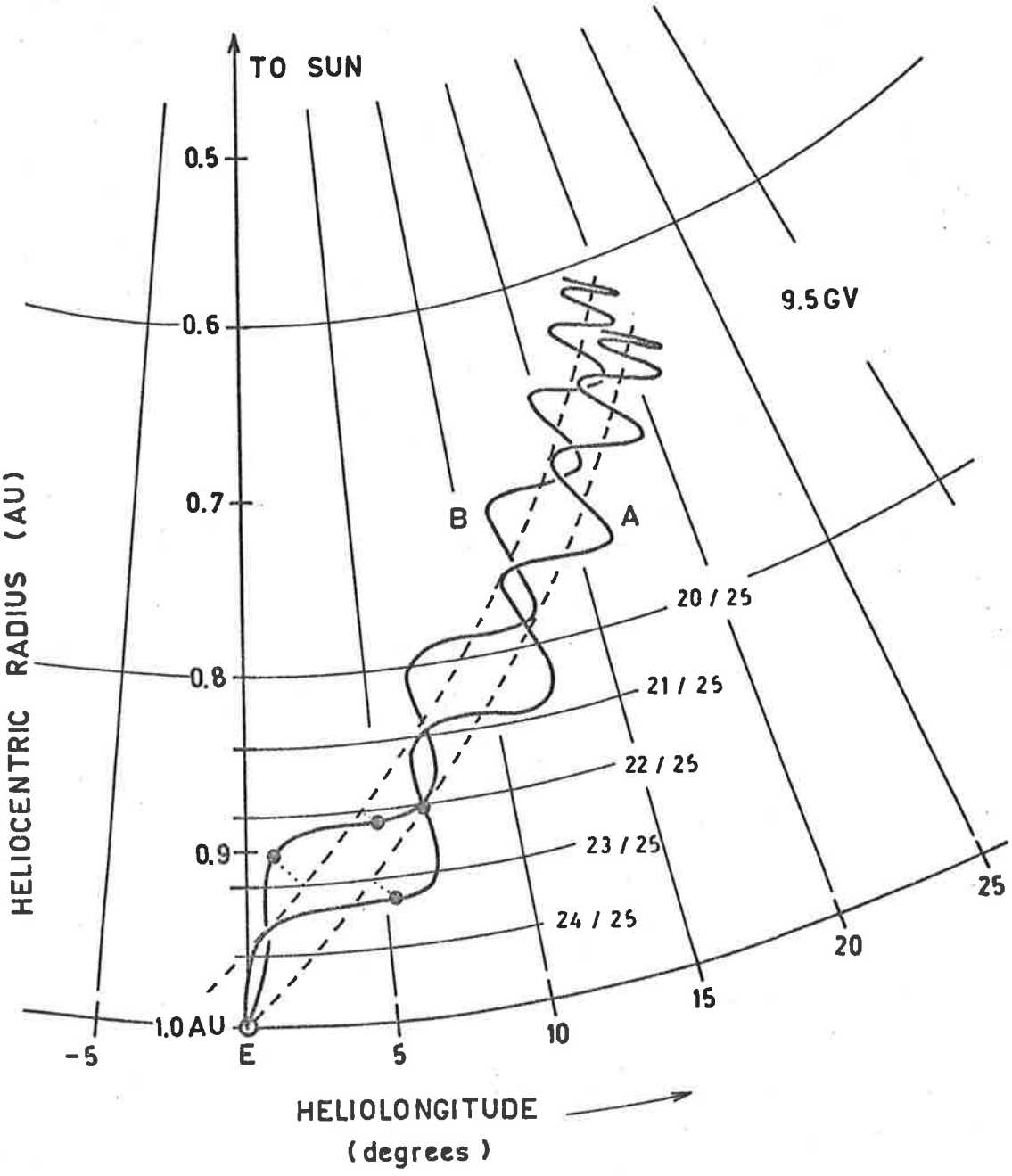

Figure 5.1 Two 9·5 GV cosmic ray orbits which have the same arrival pitch angle ($\theta_A = -42^\circ$) at Earth, but which are 90° out of phase.

difference in the values of r at x_D = ·55AU, i.e. 2 mean-free-paths (of MFP set 1) for orbits with 10° difference in θ_E. The result is shown in Figure 5.2(a). It is seen that $\Delta r/\Delta\theta_E$ is approximately proportional to $\sin\theta_E$ (dashed curve). Using this curve, 9 pitch angle intervals were chosen (each corresponding to $\Delta r \simeq 0{\cdot}06$ AU at $x_D = 0{\cdot}55$AU).

These 9 intervals apply to cosmic rays projected from Earth so that their guiding centers (initially) follow field lines in towards the Sun. Such pitch angles are given a negative sign. Another 9 pitch angle intervals are used for cosmic rays projected from Earth so that their guiding centers move away from the Sun. These positive pitch angle intervals take the same values as their negative counterparts.

The 18 pitch angle intervals, their representative pitch angles and the actual arrival directions used to calculate these representative (standard) orbits are listed in Table 5.1.

It is seen that the arrival directions of all the standard orbits have $\theta_A = 90°$, that is, they all lie in the ecliptic. Figure 5.2(b) shows these arrival directions relative to the interplanetary magnetic field direction.

Hence for each rigidity interval i, the orbital parameters are known at points along the orbit where the guiding center crosses $r = \frac{N}{25}$ AU surfaces, for 18 standard orbits. Thus orbital parameters are known along the length of a total of 180 standard orbits (10 rigidity intervals are utilized). This data can therefore be used

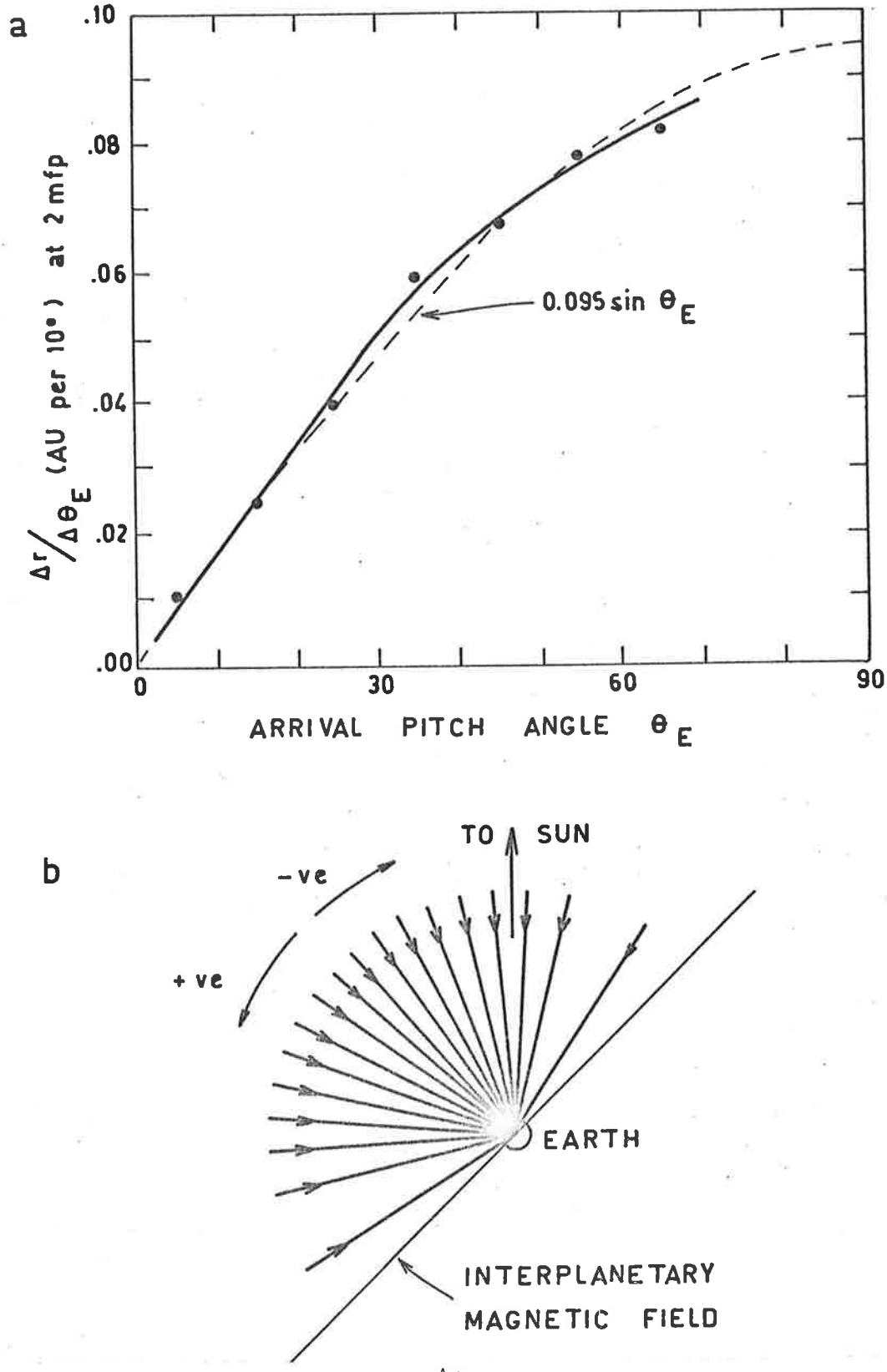

Figure 5.2(a) The variation of $\frac{\Delta r}{\Delta\theta_E}$ with θ_E at x = 0·55 AU for 15 GV cosmic rays; (b) The arrival directions of the 18 standard orbits.

TABLE 5.1

THE STANDARD PITCH ANGLES

Pitch Angle Increment	Representative Pitch Angle	Actual (θ_A, ϕ_A) of standard orbit
0 - 26	13	90°, 302°
26 - 37	32	90 , 283
37 - 46	42	90 , 273
46 - 54	50	90 , 265
54 - 62	58	90 , 257
62 - 69	66	90 , 249
69 - 76	73	90 , 242
76 - 83	80	90 , 235
83 - 90	87	90 , 228
0 - -26	-13	90 , 148
-26 - -37	-32	90 , 167
-37 - -46	-42	90 , 177
-46 - -54	-50	90 , 185
-54 - -62	-58	90 , 193
-62 - -69	-66	90 , 201
-69 - -76	-73	90 , 208
-76 - -83	-80	90 , 215
-83 - -90	-87	90 , 222

(via the equations in Chapter 4) to calculate the origin-of-scatter coefficients for any cosmic ray detector on Earth, for which the required geo-asymptotic directions are known.

Orbits are not calculated to beyond the point where the guiding center crosses the r = 3 AU surface. The flux at Earth last-scattered from regions beyond 3 AU is estimated using x_1 = 3·0 AU and $x_2 = \infty$, and the values of U, θ, r and G at 3 AU, in equations 4.19 etc.

In practice the 9 asymptotic directions for each of the 10 representative rigidities are read into the computer and each direction is converted to an arrival pitch angle for the particular time of day T in question. Each arrival pitch angle is subsequently allotted to one of the 18 intervals in Table 5.1, and the orbital data for the appropriate standard orbit, which is stored on magnetic tape, can then be used in the origin-of-scatter calculations as described in chapter 4.

In addition to the geo-asymptotic directions other input parameters are required. In particular the spectral weights W_i, and the scattering mean free paths λ_i for each of the 10 rigidity increments. The values used for these parameters are discussed in the next section.

5.3 Non Orbital Parameters

5.3.1 The Spectral Weights of the 10 Rigidity intervals

The origin-of-scatter coefficients have been calculated for neutron monitors only. The differential response function of a super neutron monitor at sea level is shown in Figure 5.3 (Lockwood and Webber, 1967).

To derive the origin-of-scatter coefficients for a particular detector, this response function is divided into 10 rigidity intervals such that the representative rigidity of each interval is a value for which the geo-asymptotic directions of arrival are known.

The rigidity intervals chosen and their representative values are tabulated in Table 5.2. In Figure 5.3 these intervals are indicated by vertical lines and their representative values by the small triangles.

TABLE 5.2

Spectral Weights W_i and Mean Free Path λ_i for the 10 Rigidity Intervals

i	ith Rigidity Interval	W_i %	ith Repr. Rigidity	λ_i (AU) for MFP set 1	2	3
1	0.0 - 2.5 GV	3·29	1·5 GV	·027	·036	·051
2	2·5 - 4·5	7·24	3·5	·064	·085	·110
3	4·5 - 6·5	8·77	5·5	·100	·147	·242
4	6·5 - 8·5	8·84	7·5	·136	·215	·437
5	8·5 - 11·25	10·63	9·5	·173	·294	·685
6	11·25- 15·0	9·61	13·0	·236	·445	1·242
7	15·0 - 21·0	9·43	17·0	·309	·623	2·068
8	21·0 - 30·0	8·12	25·0	·455	1·035	4·303
9	30·0 - 40·0	5·40	35·0	·636	1·620	8·156
10	40·0 - 60·0	6·19	45·0	·818	2·500	13·147
	>60·0	22·46				

It can be seen (Table 5.2 and Figure 5.3) that an appreciable contribution to the counting rate of a neutron monitor arises from primaries beyond 60 GV, the upper limit of the tenth rigidity interval. It is assumed that the scattering of these cosmic rays (P > 60GV) is negligible (i.e there is no contribution to the origin-of-scatter coefficients), but this fraction of the counting rate is included in the total when calculating the relative weights W_i of the 10 rigidity

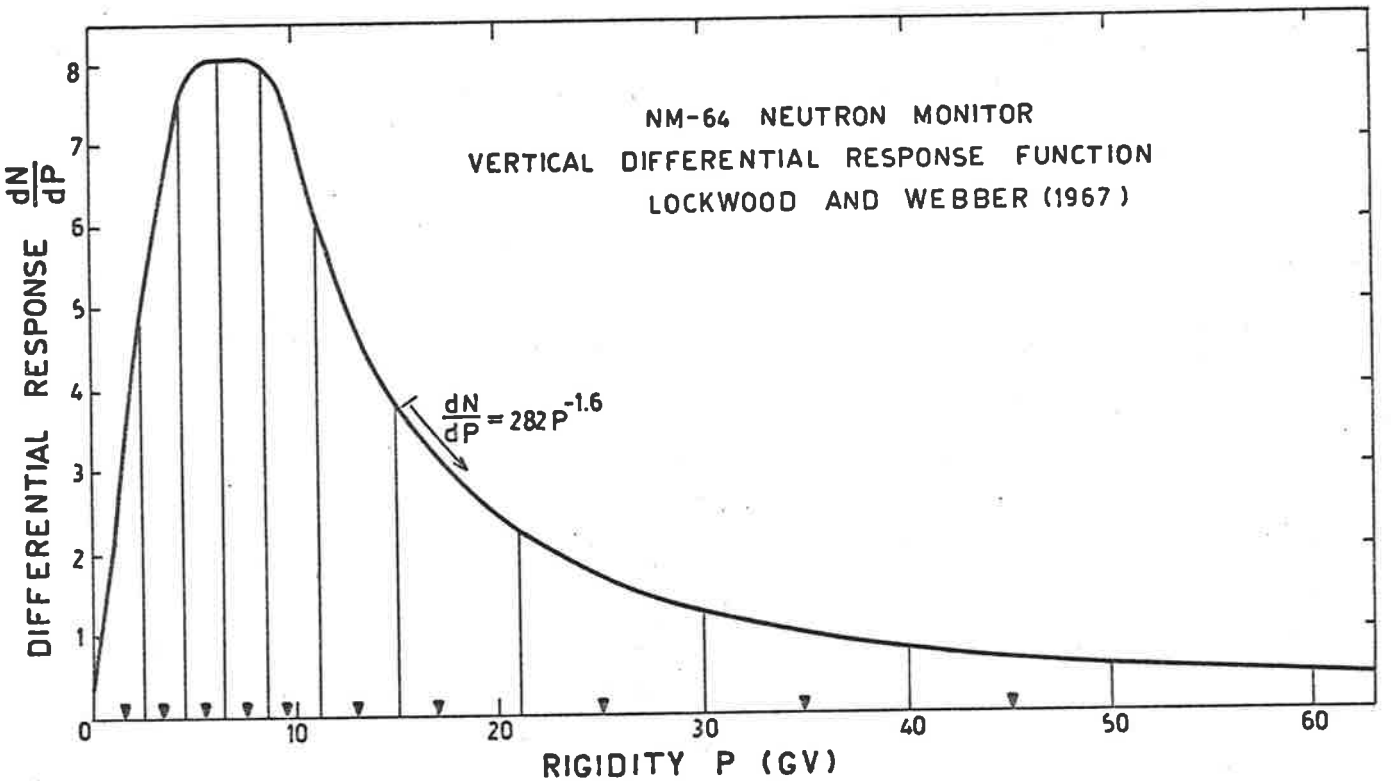

Figure 5.3 The vertical differential response function for an NM-64 neutron monitor (Lockwood & Webber, 1967), showing the rigidity intervals and the representative rigidities (small triangles) used in the present study.

intervals with P < 60GV. The weights W_i are obtained by evaluating the relative area beneath the response curve in rigidity interval i. These values are also given in Table 5.2.

The weights W_i in Table 5.2 apply to a neutron monitor station with geomagnetic cut-off rigidity P_c = 0·0GV. For most stations this is not so, and the weights for the rigidity intervals are different from those in Table 5.2. Table 5.3 lists W_i for the neutron monitors at Deep River, Inuvik, Alert and Chacaltaya, along with other details of these stations.

For high altitude stations the differential response curve of Figure 5.3 cannot be used. In Figure 5.3 the curve for $P \gtrsim 15GV$ can be described by a power law of the form $\frac{dN}{dP} \sim P^{-1\cdot6}$. It has been found however that the power law index changes significantly with altitude (e.g. Lockwood and Webber, 1967). The spectral weights W_i in table 5.3 for the station on Mt. Chacaltaya, Bolivia (550 gm cm^{-2}), were obtained using a power law index of -1·85.

5.3.2 The Scattering Mean Free Paths

Figure 5.4 shows scattering mean free paths λ, deduced from spacecraft observations of the interplanetary magnetic field near 1AU. The curves in Figure 5.4 which are labelled MFP set 1 (Wibberenz et al 1969, from Mariner 2 data), MFP set 2 (Wibberenz et al 1969, from Mariner 4 data), and MFP set 3 (Jokipii and Coleman 1968, from Mariner 4 data) yield the values used herein to calculate the origin-of-scatter

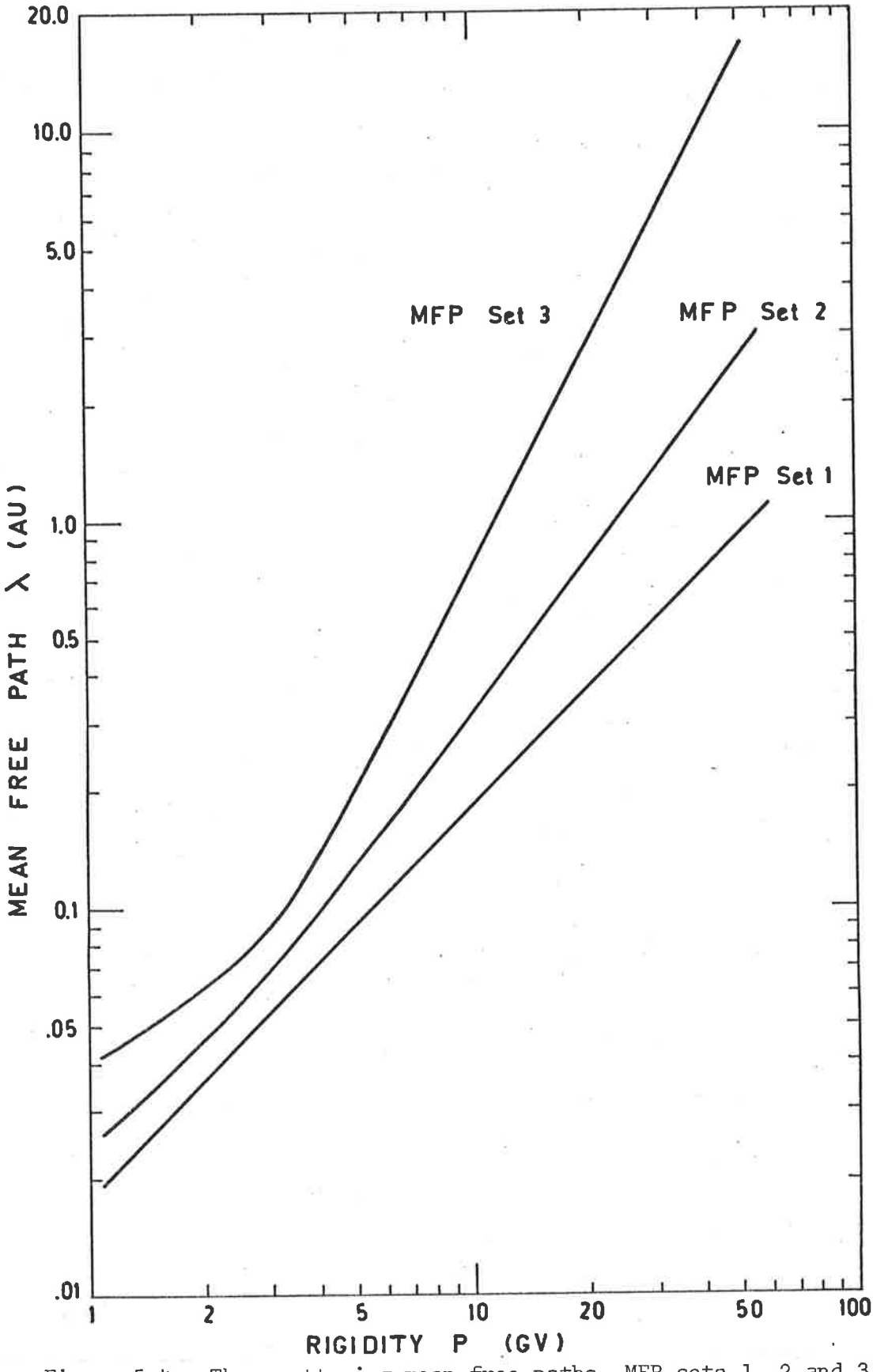

Figure 5.4 The scattering mean free paths, MFP sets 1, 2 and 3.

coefficients.

TABLE 5.3

Characteristics of the Neutron Monitor Stations considered

Station	Geographic Lat.	Lon.	Cut-off Rigidity GV	Spectral Weights W_i (%) i= 1	2	3	4	5	> 60
				6	7	8	9	10	
Deep-River	46·1	-77·5	1·02	2·8	7·3	8·8	8·9	10·7	
				9·7	9·5	8·2	5·4	6·2	22·6
Inuvik	68·4	-133·7	<·18	3·3	7·2	8·8	8·9	10·6	
				9·6	9·4	8·1	5·4	6·2	22·5
Alert	82·5	-62·3	<·05	as for Inuvik					
Chacal-taya	-16·3	-68·2	13·10	-	-	-	-	-	
				5·9	21·4	19·0	11·6	12·3	29·8

Beyond 10GV the curves in Figure 5.4 are extrapolations of the curves given in the references. The actual values used for λ_i are tabulated in Table 5.2. The mean free paths shown in Figure 5.4 are the values at 1 AU. It has been suggested that these scattering mean free paths may show an r-dependence (e.g. Jokipii and Coleman, 1968). Thus origin-of-scatter coefficients are calculated for the two cases.

(a) λ independent of r ($\lambda \sim r^0$)

(b) λ r-dependent ($\lambda \sim r^1$)

5.4 The Origin-of-Scatter Coefficients

In this section the origin-of-scatter coefficients $\zeta(r,T)$ for several stations are presented and their most interesting features are discussed. For the purpose of appreciating the variation of the magnitude of $\zeta(r,T)$ with heliocentric radius r and time of day T, it is best to consider them as the relative flux which originates in (is last-scattered in) the volume element of space at r, at time of day T. From this point of view $\zeta(r,T)$ can be regarded as indicative of the spatial response or the remote sensing capability of the detector.

The first station considered is the Deep River neutron monitor (see Table 5.3 for details). The asymptotic cone of acceptance of the Deep River detector is shown in Figure 5.5(a) which shows 5 directions for each of the 10 representative rigidities (Table 5.2). These asymptotic directions (McCracken et al, 1965) apply at 0000 hours U.T. It is seen that the cone of acceptance at Deep River is centered near 0° latitude, -40° longitude, which is 175° west of $(0^{\circ}, 135^{\circ})$, the direction which looks in along the interplanetary magnetic field. Hence at 1200 UT Deep River will look in the direction parallel to the interplanetary magnetic field and towards the Sun.

Figure 5.6 shows the Deep River origin-of-scatter coefficients for r = 0·0 to r = 2·0 AU for every second hour of the day. Each of the 12 individual histograms is a plot of percent of total flux at Earth which originates within $\Delta r = {}^{1}/_{25}$ AU at r, versus heliocentric

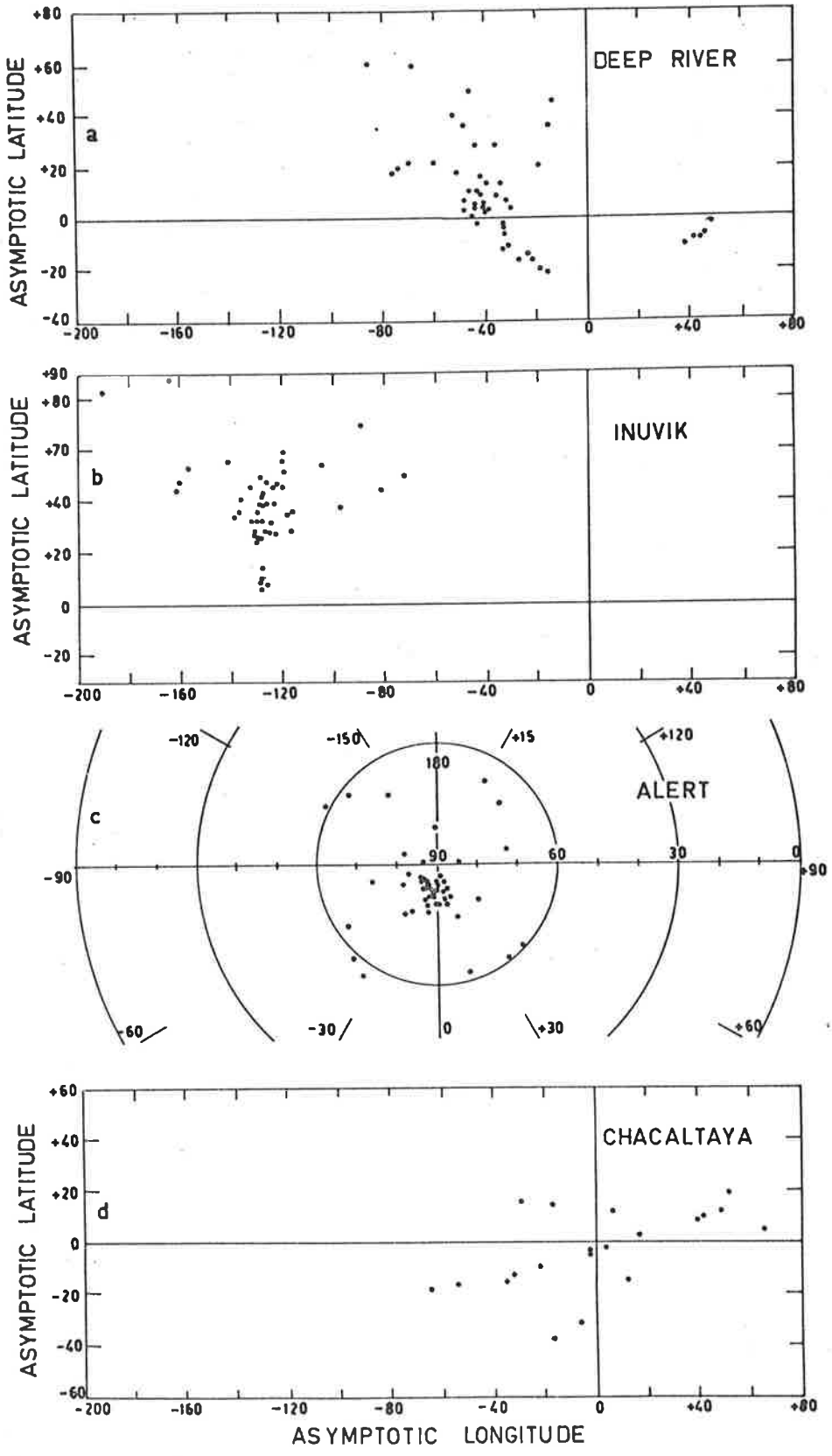

Figure 5.5 The asymptotic cones of acceptance at Deep River, Inuvik, Alert and Chacaltaya at 0000 UT. Five directions for each of 10 rigidities (see Table 5.2) are plotted (for vertical, 32°N, 32°E, 32°S and 32°W arrival).

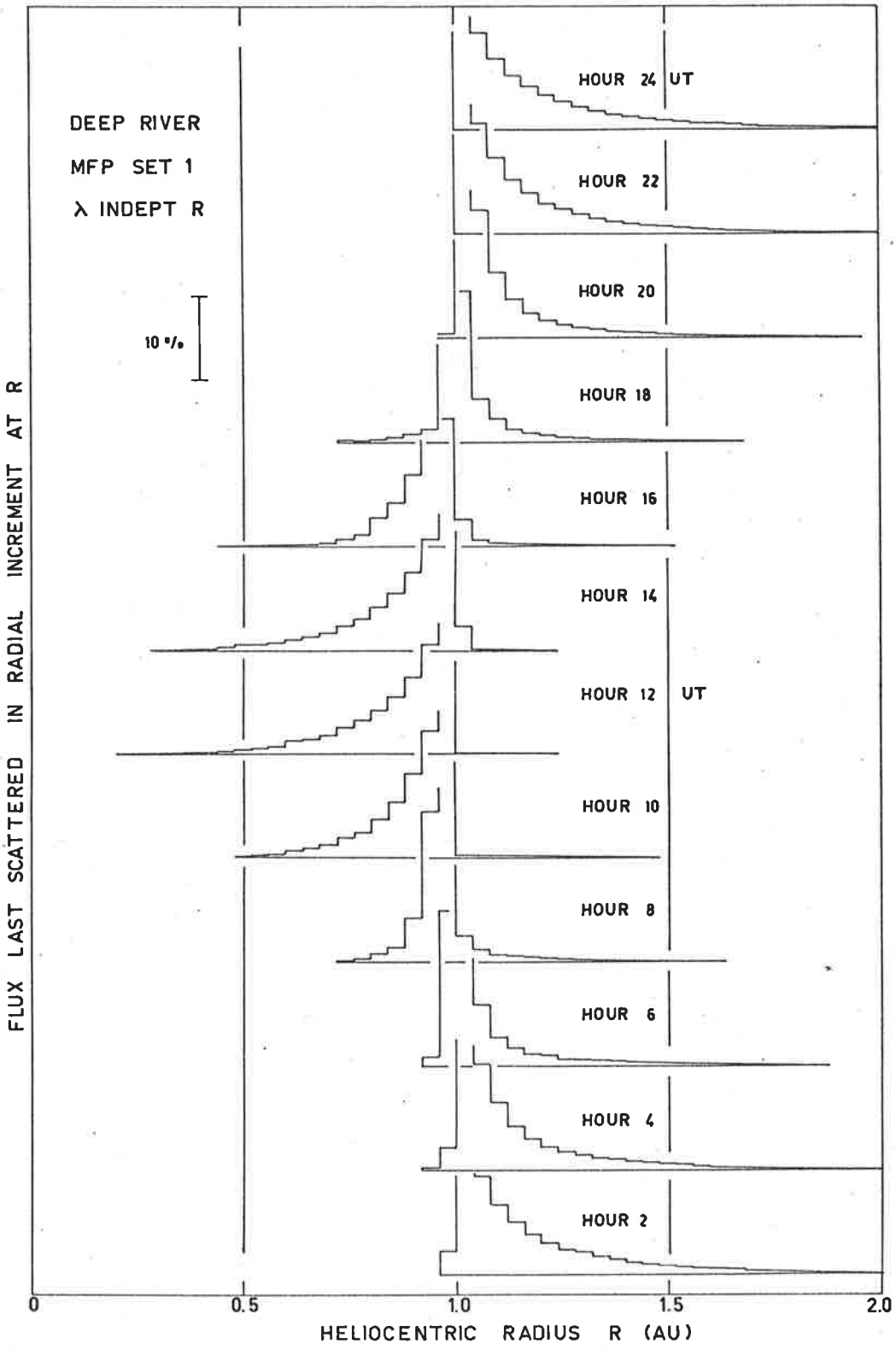

Figure 5.6 The origin-of-scatter coefficients $\zeta(r,T)$ for 12 times of day at Deep River when the scattering mean free paths are given by MFP set 1 (λ independent of r).

radius r. The points where $\zeta(r,T) < 0{\cdot}1\%$ are not plotted. The results in Figure 5.6 were calculated for MFP set 1 (with λ independent of r).

An intuitive understanding of these results can be obtained by referring to Figure 5.7. This Figure shows (9·5 GV) cosmic ray orbits for 6 different arrival pitch angles (θ_A). For $\theta_A = -13^\circ$ and -42° the orbits are plotted until they mirror, while the other four orbits are plotted to points beyond 1 AU. The points on each orbit which are 1, 2, 3 and 4 mean free paths (MFP set 1) from the Earth are marked with heavy dots. These 9·5 GV orbits also indicate the regions of space which are traversed by different rigidity cosmic rays with the same arrival pitch angles.

Consequently at hours 12 and 14 in Figure 5.6 when most orbits within the cone of acceptance at Earth have small θ_A (i.e. the orbits are similar to Figure 5.7a), a significant flux originates as far away as r = 0·6 AU, which is 3 mean free paths from Earth (at 9·5 GV). As we advance towards hour 19 and θ_A approaches 90°, the orbits mirror closer to the Earth (Figure 5.7 a, b, c, d), and progressively more of the cosmic ray flux originates between 24/25 and 26/25 AU in Figure 5.6. The minute flux which originates from outside 1 AU at hours 12 and 14 is due to high energy (large mean free path) cosmic rays which reach the detector after mirroring near the Sun. Beyond hour 19 the arrival pitch angles θ_A, are positive (Figure 5.7 e, f) and they decrease from $+90^\circ$ ($\equiv -90^\circ$) to $+0^\circ$ near hour 24. As θ_A

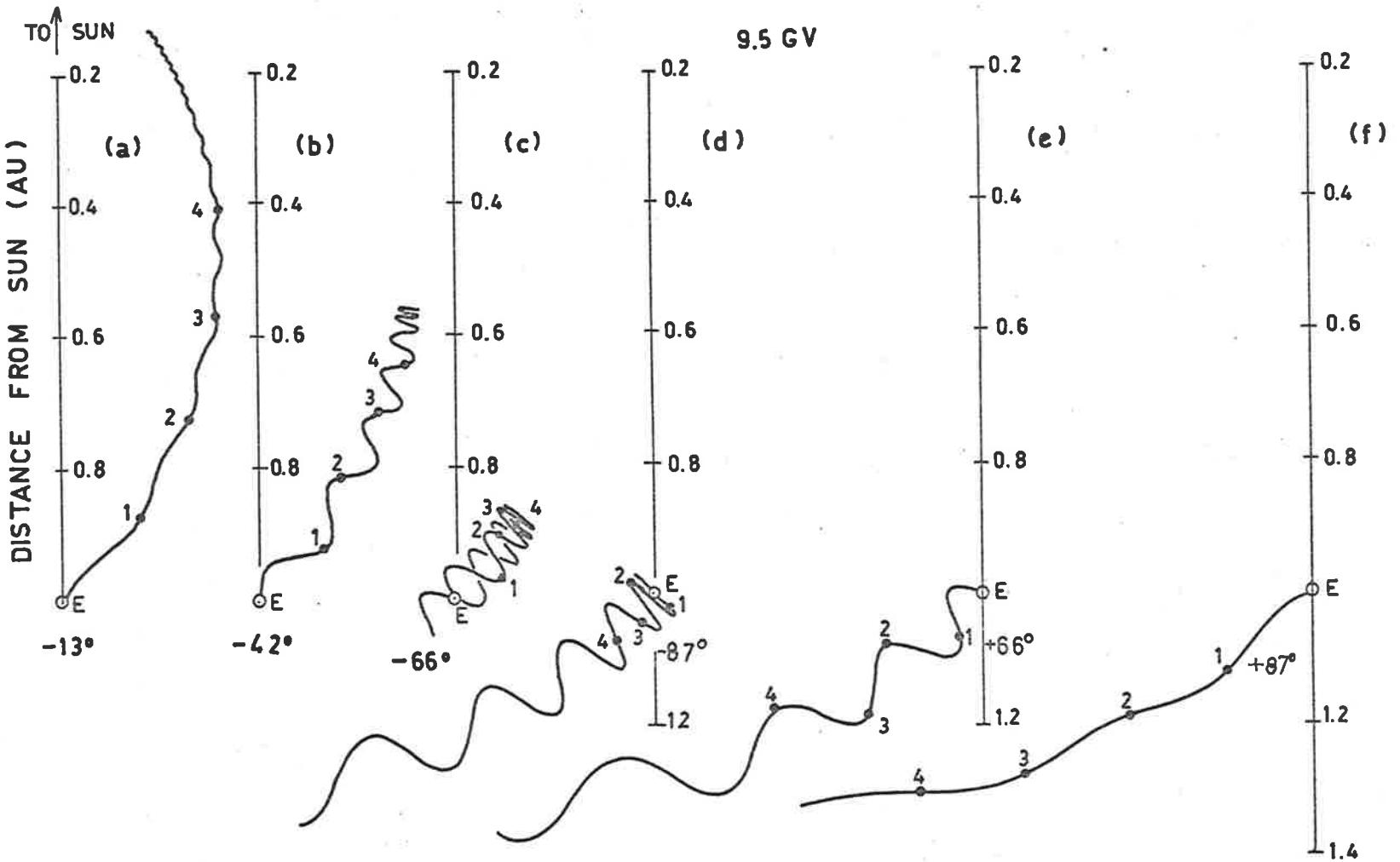

Figure 5.7 Orbits for 9·5 GV cosmic rays which arrive at Earth with pitch angles θ_A = -13°, -42°, -66°, -87°, +66° and +13°. The points on the orbits which are 1, 2, 3 and 4 mean free paths from Earth are shown (for MFP set 1).

ADELAIDE LIBRARY UNIVERSITY

decreases from $+90^{\circ}$, more of the flux at Earth originates from progressively further outside 1 AU, until at hour 24 and hour 1 more than 7% originates beyond 1.5 AU. From hour 1 to hour 13 in Figure 5.6 the above sequence is reversed.

Figures 5.8 and 5.9 are plots of $\zeta(r,T)$ for the Inuvik and Alert stations (see table 5.3 for details of these stations) for MFP set 1, λ independent of r. The cones of acceptance for these stations are shown in Figure 5.5(b) and (c). The cone of acceptance of Inuvik is narrow and centered near latitude $+40^{\circ}$, longitude -130° (at 0000 hours UT). Hence the average θ_A at Inuvik will be a minimum ($= 40^{\circ}$) at 1800 UT (towards Sun), and 0600 UT (away from Sun). The cone of acceptance of Alert is also quite narrow but it is centered near latitude $+83^{\circ}$ (note the Figure 5.5c is a polar plot), so that the central θ_A of the Alert cone of acceptance will only vary from $+83^{\circ}$ to $+90^{\circ}$ throughout the day.

These features are reflected in the behaviour of $\zeta(r,T)$ in Figures 5.8 and 5.9, which together with Figure 5.6 show that the bulk of the observed flux originates closer to the Earth as we go to higher latitude stations.

Deep River, Inuvik and Alert are all low cut-off rigidity stations. We now consider the high cut-off rigidity station (P_c = 13.10 GV) at Chacaltaya. Figure 5.5(d) shows that this station has a broad cone of acceptance centered near (0,0) at 0000 UT. We

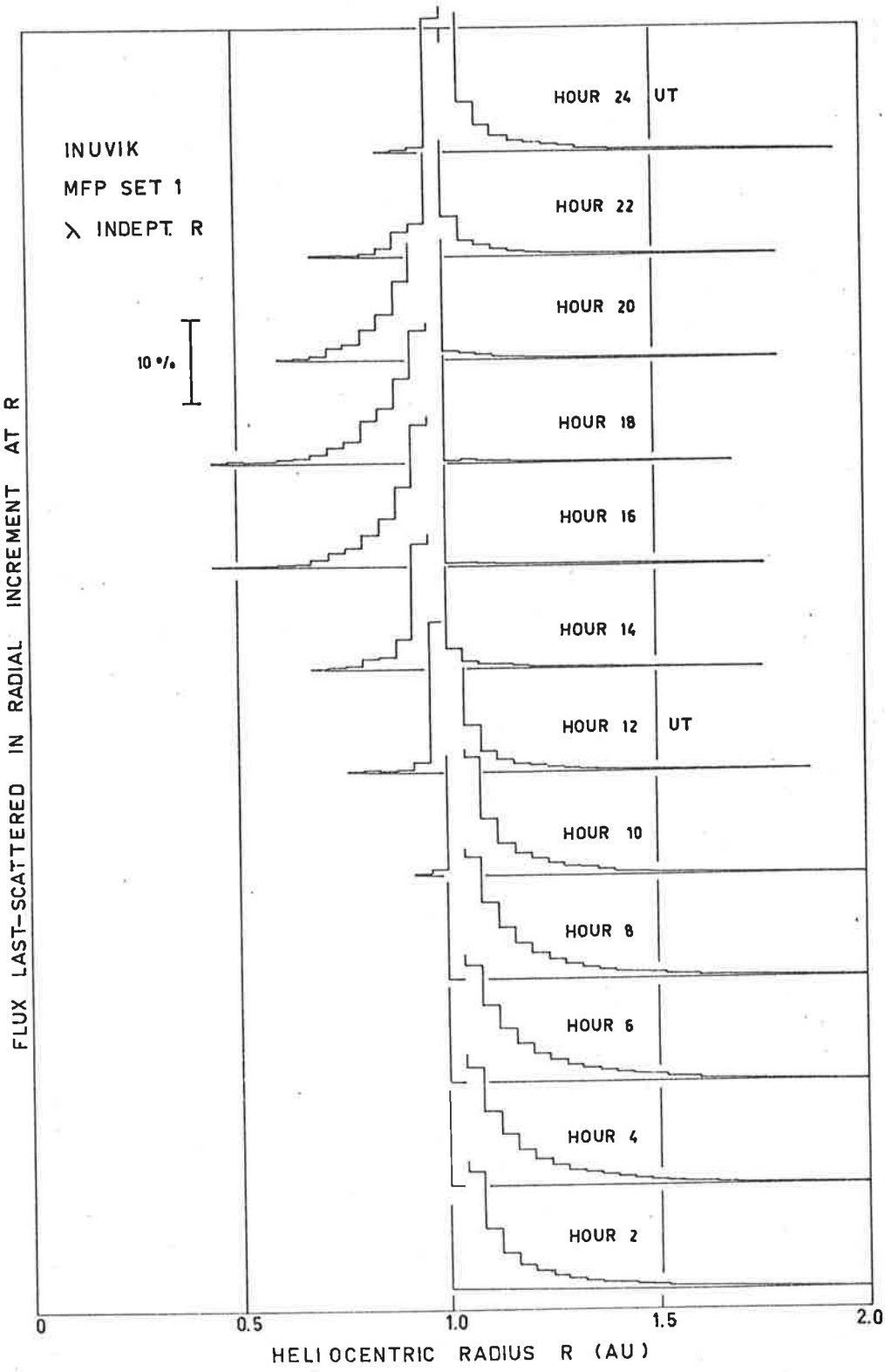

Figure 5.8 The origin-of-scatter coefficients $\zeta(r,T)$ for 12 times of day at Inuvik for MFP set 1 (λ independent of r).

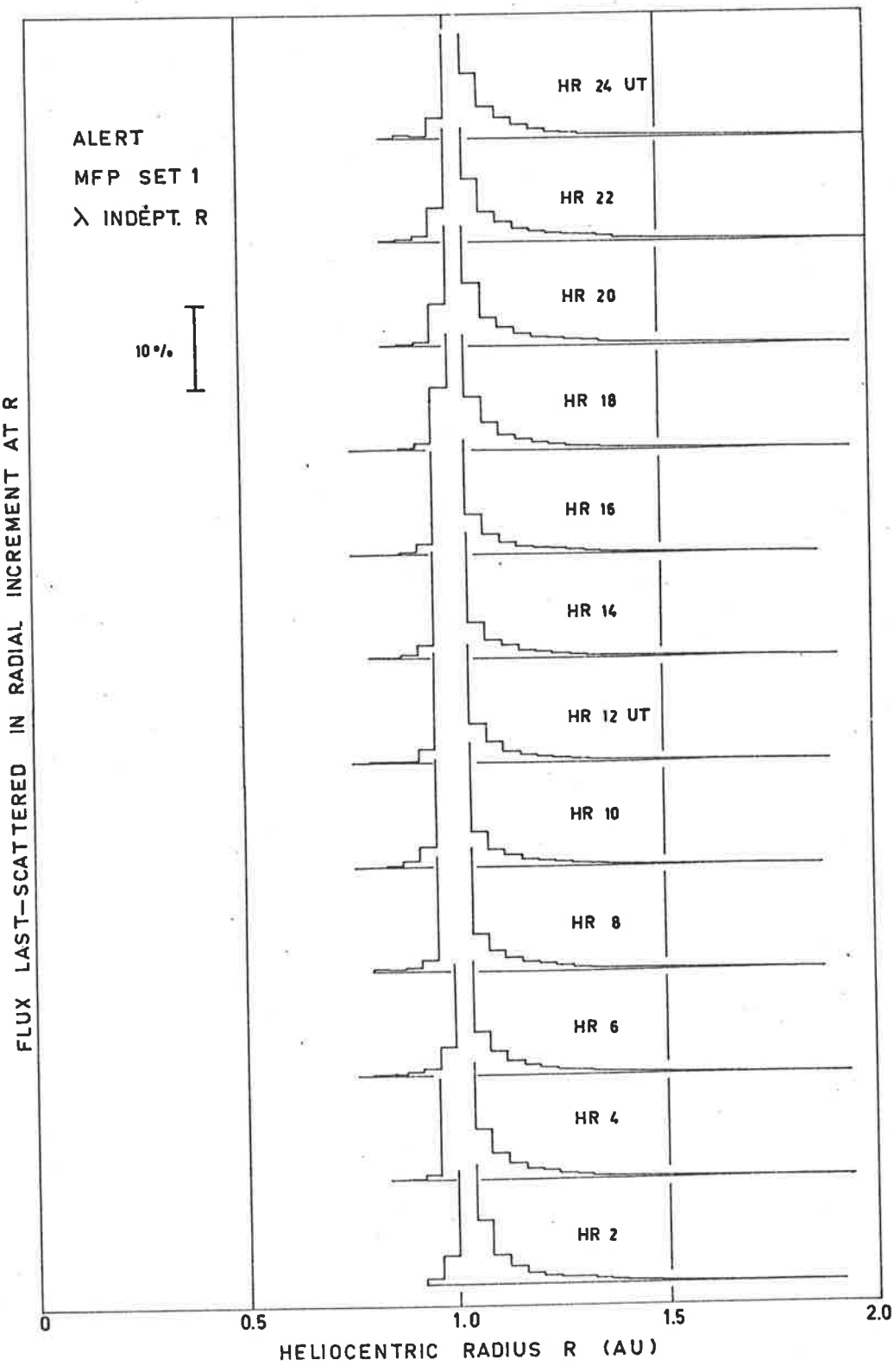

Figure 5.9 The origin-of-scatter coefficients $\zeta(r,T)$ for 12 times of day at Alert for MFP set 1 (λ independent).

would therefore expect the average θ_A to be a minimum near 0900 UT (towards Sun) and 2100 UT (away from Sun).

The origin-of-scatter coefficients for Chacaltaya (for MFP set 1, λ independent of r) are shown in Figure 5.10. This indicates that in general this station detects cosmic rays from a more extended region of space than the low cut-off rigidity stations. The broad cone of acceptance of this station causes it to sense deep into the solar system over a period of 11 hours (centered near 0900 UT), compared with about 5 hours for Deep River.

The enhanced remote sensing ability of the Chacaltaya detector arises because all of the cosmic rays it detects have rigidities > 13 GV, whereas the flux of cosmic rays > 13 GV arriving at Deep River is largely masked by the very large flux at lower rigidities. From Figure 5.3 it can be seen that the average rigidity detected at Deep River is $\sim$ 9·5 GV, while at Chacaltaya it is $\sim$ 25 GV. Now the mean free path at 25 GV is $\sim$ 2·5 times larger than the mean free path at 9·5 GV (for MFP set 1). Referring to Figure 5.7, it would be expected that such an increase in mean-free-path would increase the flux of cosmic rays from regions further from the Earth.

Figures 5.11, 5.12 and 5.13 show the origin-of-scatter coefficients for Deep River, Inuvik and Chacaltaya for MFP set 3 (λ independent of r). For the two low cut-off rigidity stations the longer mean free paths have the effect of increasing their remote

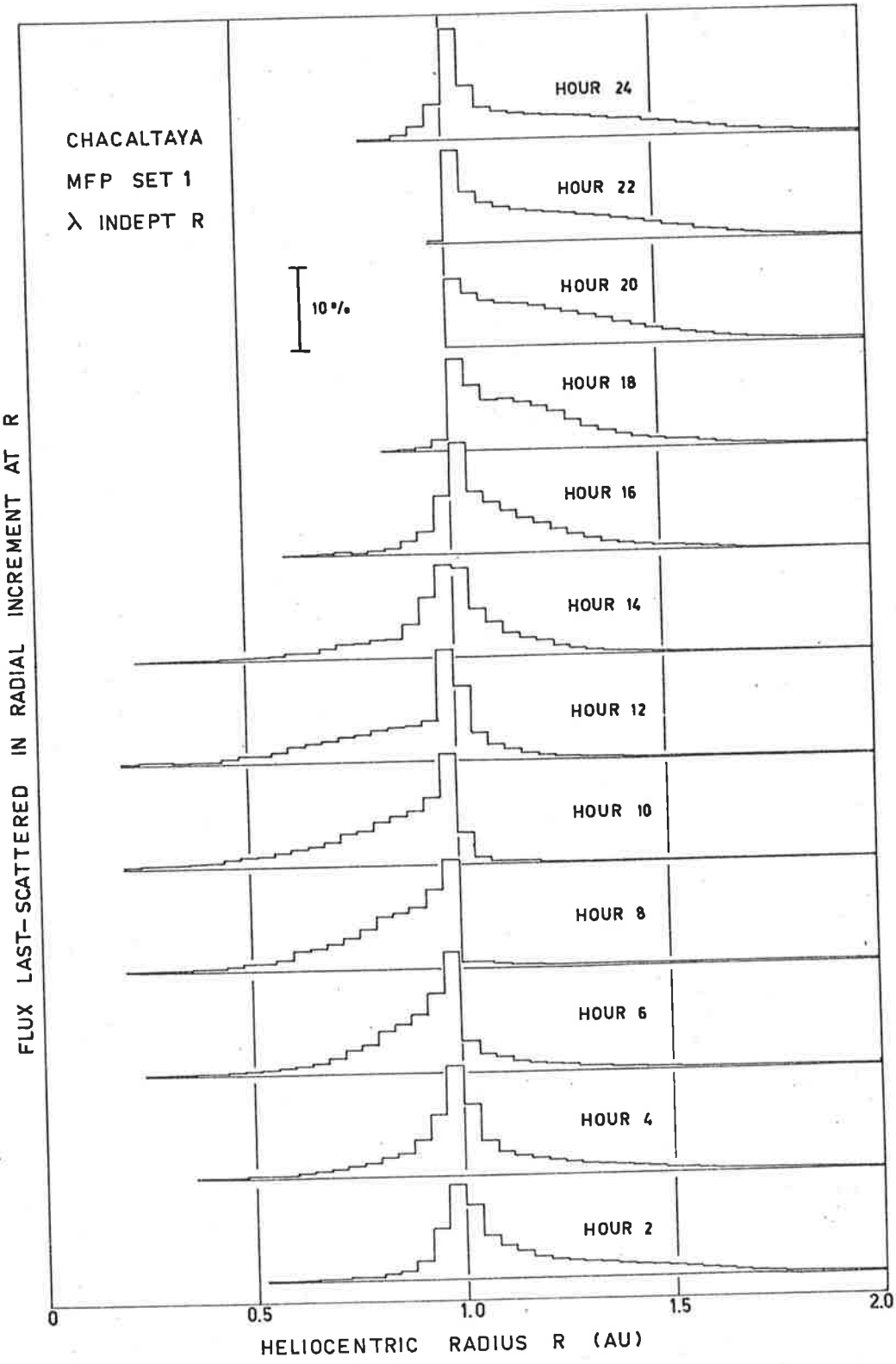

Figure 5.10 The origin-of-scatter coefficients $\zeta(r,T)$ for 12 times of day at Chacaltaya for MFP set 1 (λ independent).

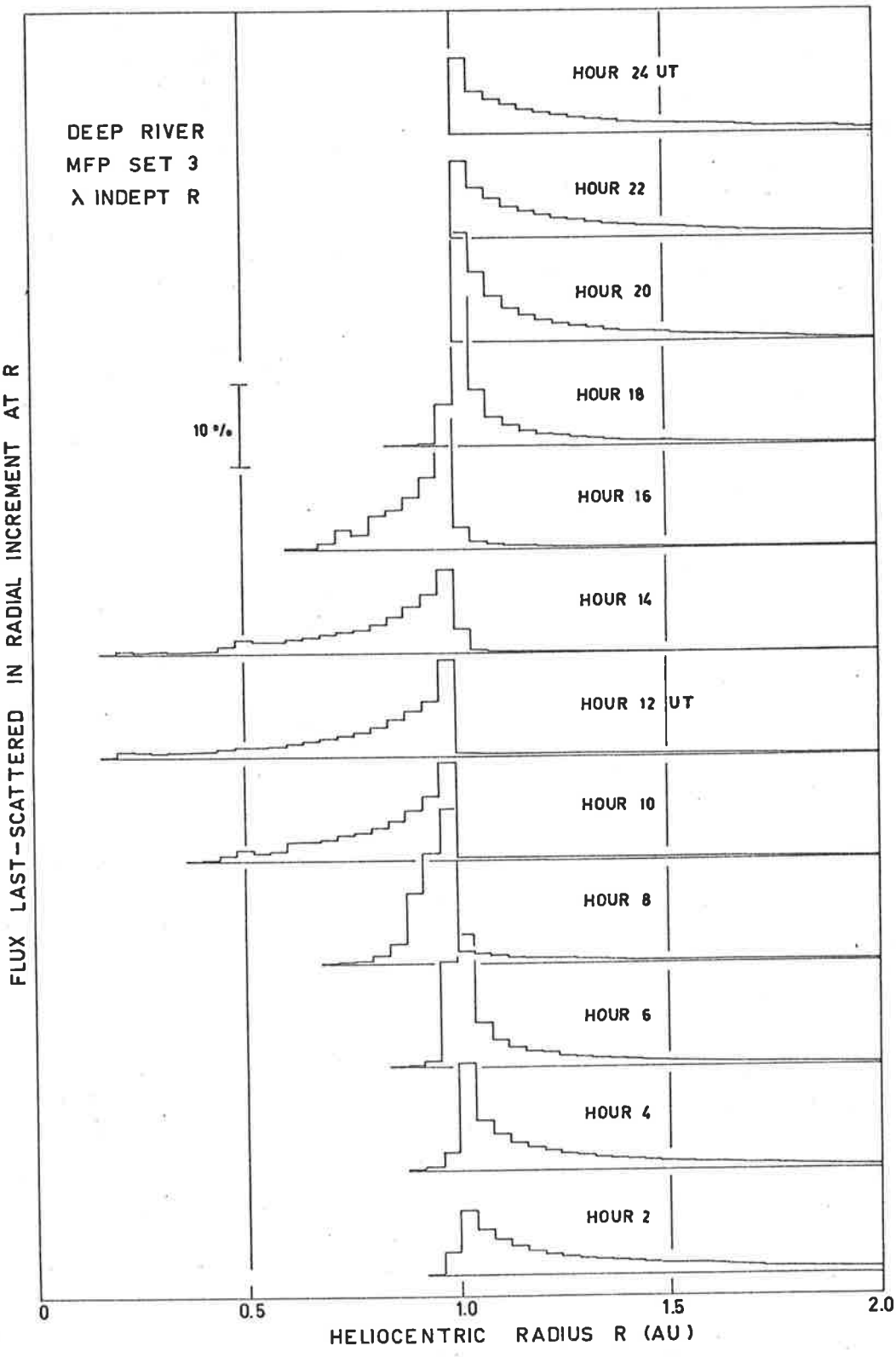

Figure 5.11 The origin-of-scatter coefficients $\zeta(r,T)$ for 12 times of day at Deep River for MFP set 3 (λ independent).

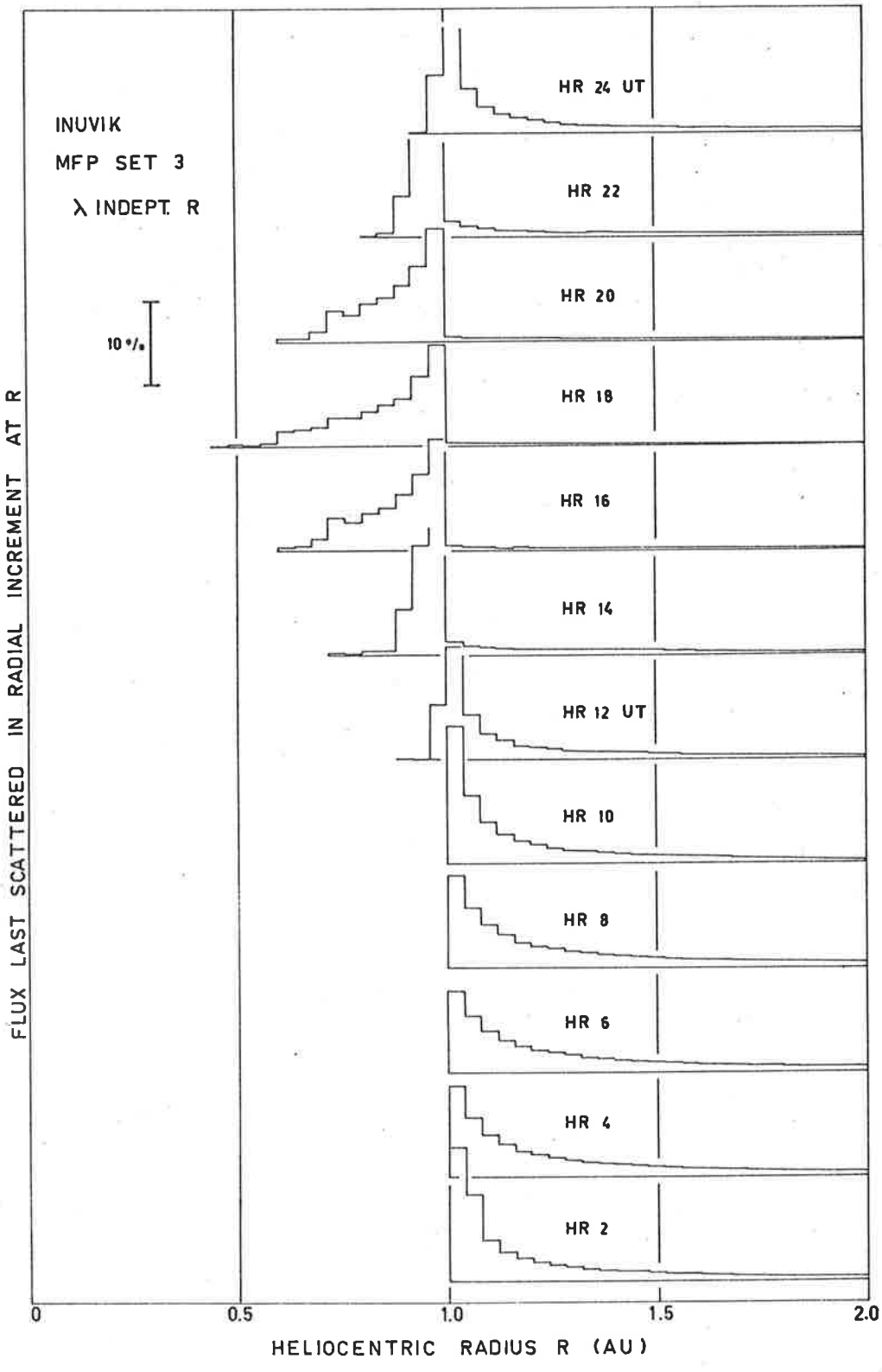

Figure 5.12 The origin-of-scatter coefficients $\zeta(r,T)$ for 12 times of day at Inuvik for MFP set 3 (λ independent).

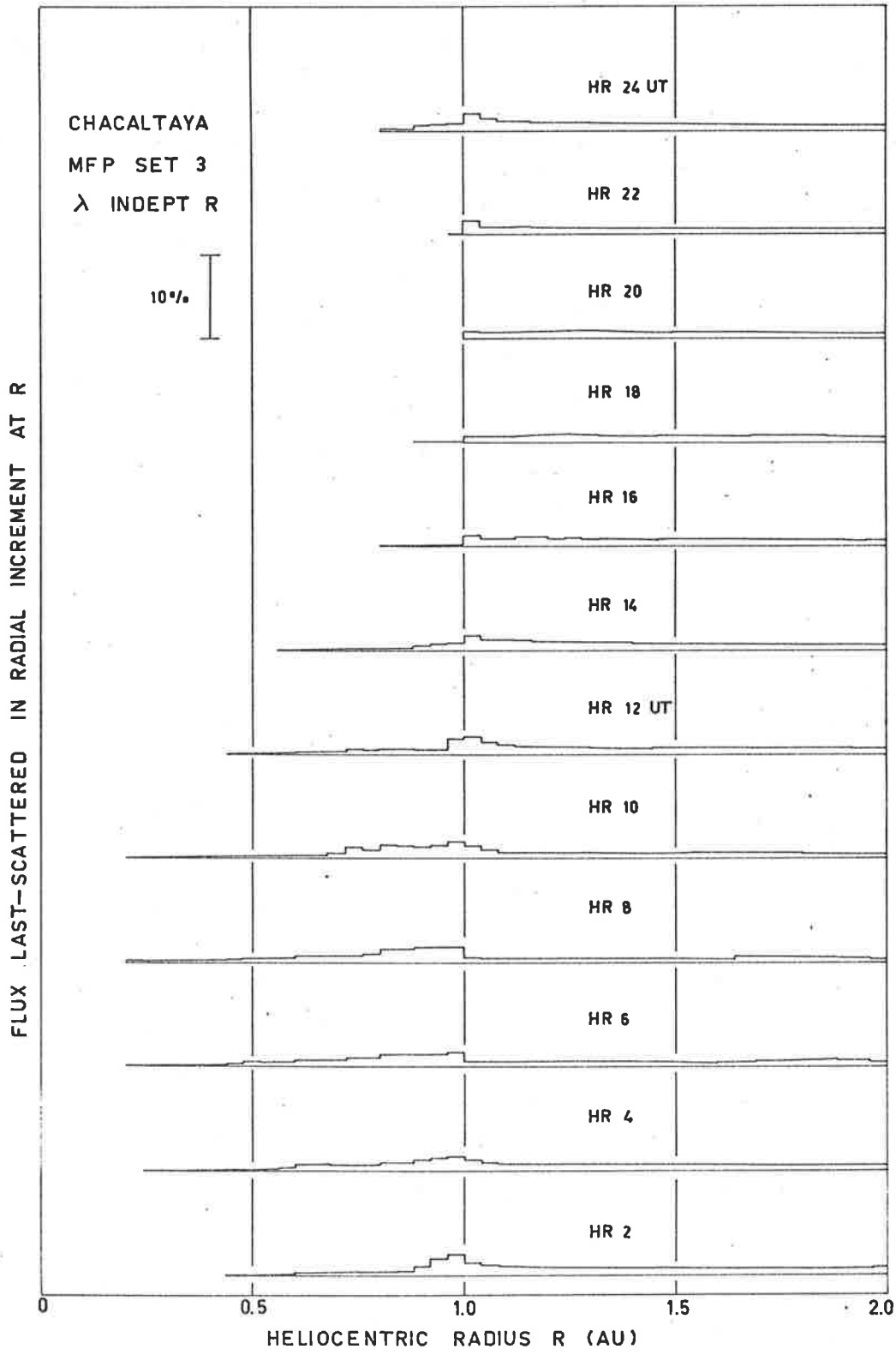

Figure 5.13 The origin-of-scatter coefficients $\zeta(r,T)$ for 12 times of day at Chacaltaya for MFP set 3 (λ independent).

sensing ability (at 9·5 GV the mean free path is increased by a factor of $\sim$ 4 relative to the value for MFP set 1). However the high cut-off rigidity station at Chacaltaya shows the opposite effect. At 25 GV the mean free path is increased by a factor of $\sim$ 10 relative to the MFP set 1 value. With such large mean free paths (25 times those indicated in Figure 5.7) only a small fraction of the flux observed on Earth is scattered inside 2 AU (for all times of day). The origin-of-scatter coefficients for Chacaltaya for the intermediate mean free paths of MFP set 2 (λ independent of r) are shown in Figure 5.14.

Origin-of-scatter coefficients were also calculated for the case when the mean free path λ varies as a function of heliocentric radius r, i.e. $\lambda = \lambda_E\, r$, where λ_E is the mean free path at 1 AU (for the rigidity in question) and r is given in AU. It was found that the change in the values $\zeta(r,T)$, relative to the λ independent of r case, was generally small. This r-dependence causes the greatest change in the mean free path at points furthest away from the Earth (where the values of $\zeta(r,T)$ are smallest). As a consequence the greatest difference between the r-independent $\zeta(r,T)$ and the r dependent $\zeta(r,T)$ occur for stations which detect appreciable fluxes of cosmic rays from regions distant from the Earth. Examples of the largest changes are given in Figure 5.15. which shows $\zeta(r,T)$ at Deep River and Chacaltaya for the two times of day when these detectors sense furthest away from the Earth. MFP set 3 was used to derive Figure 5.15. The differences for MFP set 1 between the r-independent and r-dependent values of $\zeta(r,T)$

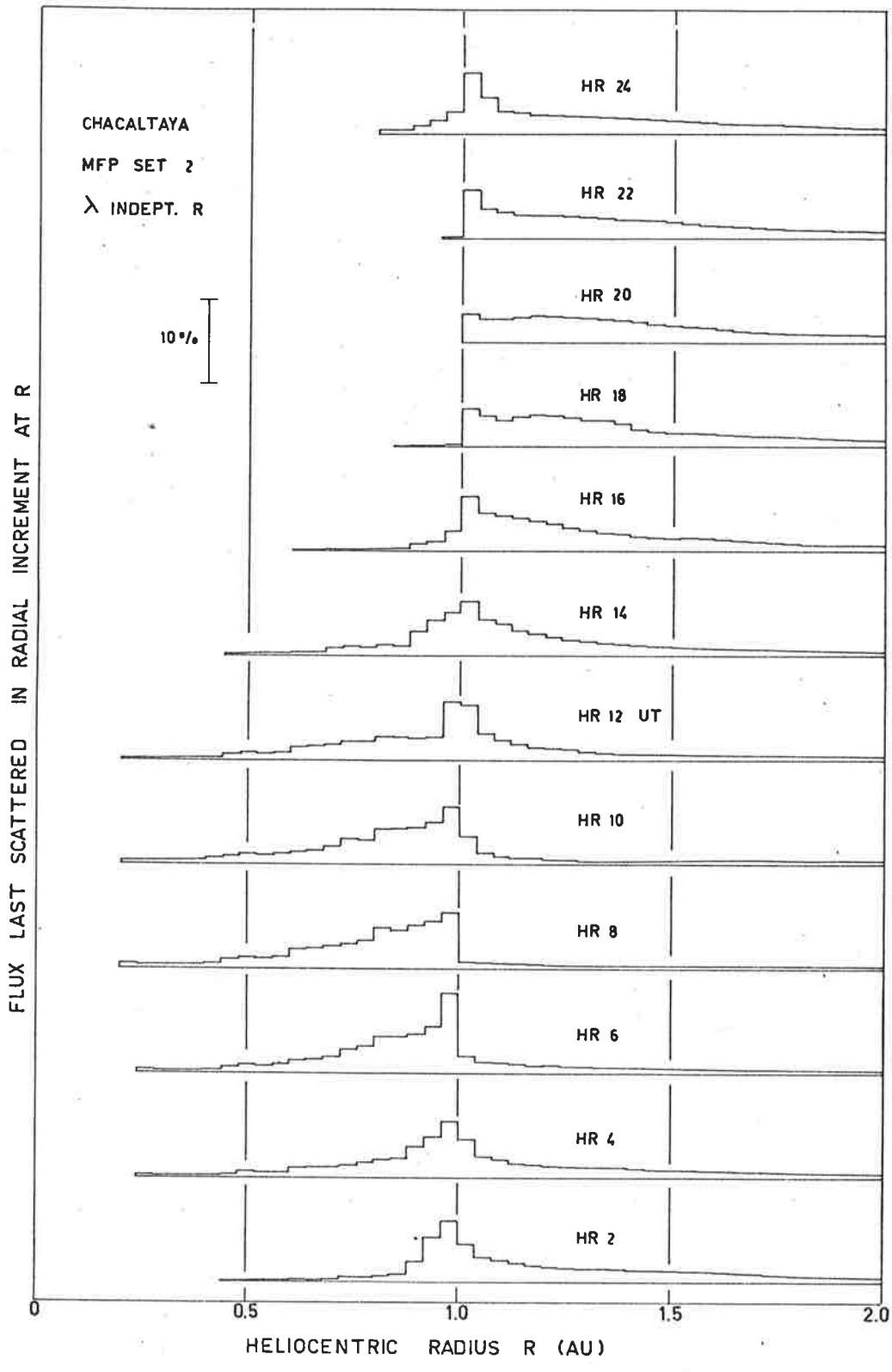

Figure 5.14 The origin-of-scatter coefficients $\zeta(r,T)$ for 12 times of day at Chacaltaya for MFP set 2 (λ independent).

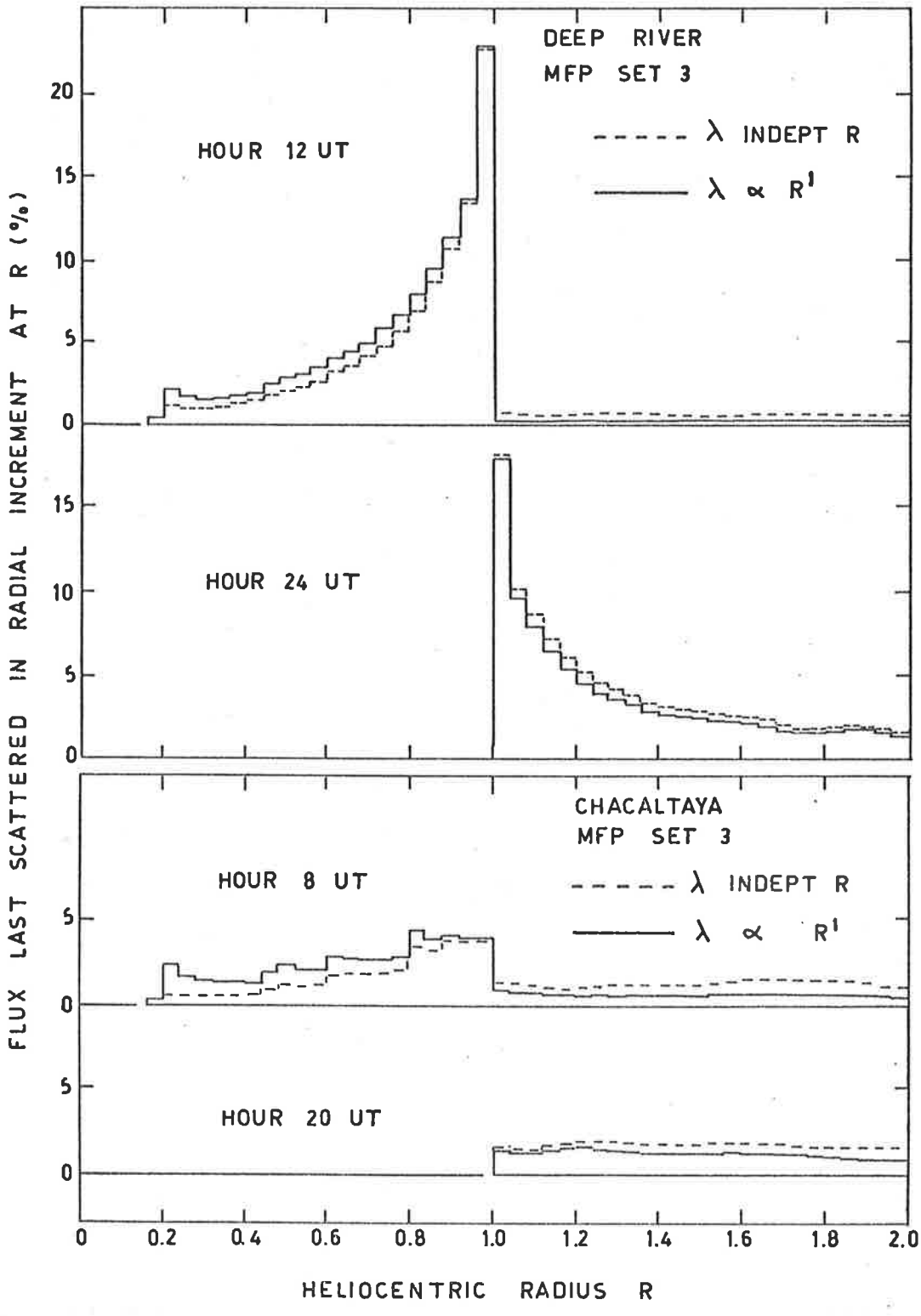

Figure 5.15 The variation in the origin-of-scatter coefficients for scattering mean free paths with different r-dependence.

are considerably smaller.

5.5 The Energy Dependence of $\zeta(r,T)$

Section 4.3 described how the origin-of-scatter coefficient $\zeta(r,T)$, i.e. the relative flux last-scattered within Δr at r, was the result of summing $\zeta_i(r,T)$ over all the rigidity intervals used (see equation 4.6). $\zeta_i(r,T)$ is the origin-of-scatter coefficient for the ith rigidity interval, i.e. the relative flux of cosmic rays in rigidity interval i, which was last-scattered within Δr at r.

The energy dependence of $\zeta(r,T)$ can therefore be shown by plotting the individual $\zeta_i(r,T)$ as in Figure 5.16. Although 10 rigidity intervals were used in the calculation of $\zeta(r,T)$, for the present purpose 5 rigidity intervals (each one of sum of 2 original intervals) are used (see Table 5.4). Figure 5.16 shows the five histograms (one for each rigidity interval) obtained using both MFP set 1 and MFP set 3 (r-independent), at hour 12 and hour 24 UT at Deep River. The points where $\zeta_i(r,T) < 0{\cdot}05\%$ are not plotted in Figure 5.16.

Figure 5.16 shows that as we go to high rigidities a progressively smaller fraction of the flux originates (is last-scattered) from the immediate vicinity of Earth; that is at higher rigidities, regions further away from Earth become more important flux 'sources' relative to the regions close to the Earth. This effect is seen as a

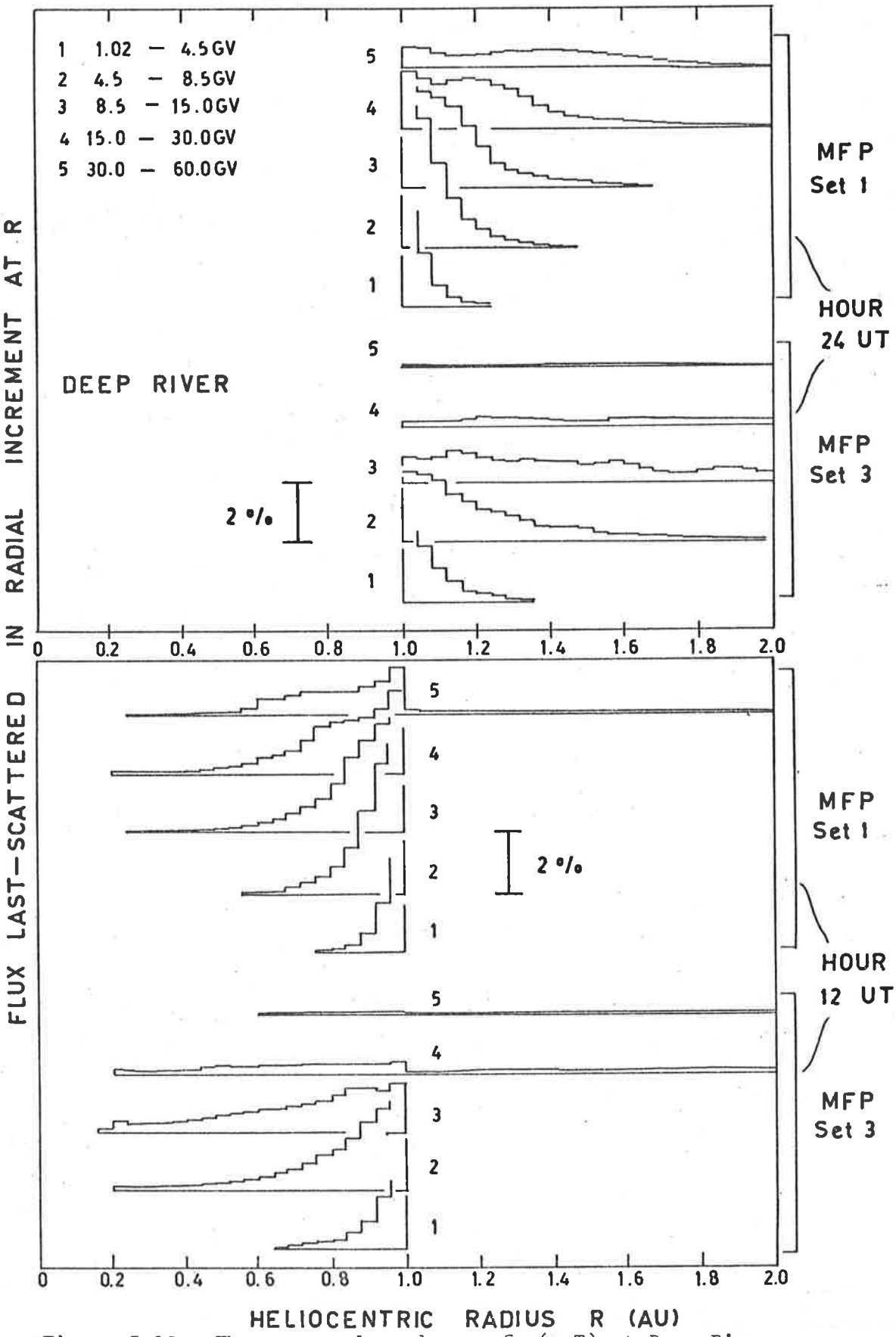

Figure 5.16 The energy dependence of $\zeta(r,T)$ at Deep River.

TABLE 5.4

The 5 Rigidity Intervals used in the Application of the Origin-of-Scatter Coefficients

Interval No.	Rigidity Range	Spectral Weight % (for P_c = 0 GV)
1	0·0 - 4·5 GV	10·53
2	4·5 - 8·5 GV	17·61
3	8·5 - 15·0 GV	20·24
4	15·0 - 30·0 GV	17·55
5	30·0 - 60·0 GV	11·59
	> 60·0 GV	22·46

flattening out of the curves in Figure 5.16 at the higher rigidities. This effect of extending the region from which the flux originates is also noticed as we go to longer mean free paths (compare corresponding curves for MFP set 1 and MFP set 3 in Figure 5.16).

For rigidity intervals 1, 2 and 3, the total flux which originates inside 2 AU (i.e. which is shown in Figure 5.16) is approximately the same for both mean free path sets (i.e. the area under the curves is about the same). However for rigidity intervals 4 and 5 there is a much reduced total flux from within 2 AU for MFP set 3. At these rigidities the mean free paths become so long (for MFP set 3) that the scattering of cosmic rays is beginning to become unimportant. This effect has already been seen in Figure 5.13, the origin-of-scatter coefficients for Chacaltaya at MFP set 3 (Chacaltaya's rigidity

response covers rigidity intervals 5, 4, and part of 3).

Some of the curves presented in this chapter show small scale fluctuations (e.g. Figure 5.15, HOUR 24, MFP set 3, curve 3). These are introduced by the approximation and quantization procedures which have been necessary to make these calculations possible (see first 3 sections of this chapter). Therefore a more realistic picture is obtained if such small scale fluctuations are smoothed out.

The origin-of-scatter coefficients for the 5 rigidity intervals and for the total rigidity range, for the Deep River station are listed in appendix 4 (for MFP set 2, $\lambda \sim r^1$).

CHAPTER 6

COSMIC RAY VARIATIONS ASSOCIATED WITH RADIAL NUMBER DENSITY GRADIENTS

6.1 Introduction

The origin-of-scatter coefficients $\zeta(r,T)$ were calculated by assuming that the cosmic ray number density, $U(r)$ was 1·0 for all r (in equation 4.19). That is, they are quantitative measures of the probability that cosmic rays reaching a given observer at time T were last-scattered at (sampled from) a distance r from the Sun. These $\zeta(r,T)$ are now used to calculate the variations in the flux at Earth when various radial gradients exist in the cosmic ray number density in interplanetary space, that is the number density varies as a function of r.

Since the values of $\zeta(r,T)$ are calculated for radial volume elements of space it is only possible to consider radial gradients. However results can be obtained for any arbitrary radial gradient. Now the total origin-of-scatter coefficient $\zeta(r,T)$ is obtained by summing the components $\zeta_i(r,T)$ over the rigidity intervals (i = 1 - 10) of the total rigidity range. Therefore by using $\zeta_i(r,T)$, the origin-of-scatter coefficients for rigidity interval i, it is possible to evaluate the effects of rigidity dependent gradients. The rigidity intervals used in these applications are the 5 listed in table 5.4 (each of these is a combination of two of the original intervals in table 5.2).

The flux at Earth of cosmic rays in rigidity interval i, which is last-scattered in Δr at r at time of day T is given by $U_i(r).\zeta_i(r,T)$, where $U_i(r)$ is the number density of cosmic rays in the i^{th} rigidity interval at r. The total flux at time T is given by

$$N(T) = \sum_{i=1}^{5} \sum_{r} U_i(r)\ \zeta_i(r,T) + N(>60) \qquad (6.1)$$

where N(>60) is the flux of cosmic rays with P > 60GV which we assume is not scattered, but which must be included to obtain the total flux. It is possible to calculate N(T) at the 24 times of day T for which $\zeta(r,T)$ are known.

This procedure is carried out to derive the daily variations which are associated with selected radial gradients in the cosmic ray number density. Furthermore, by adjusting the gradient until the variation predicted using equation 6.1 agrees with the observed variation (e.g. diurnal variation, Forbush decreases), it is possible to investigate the gradient which is associated with a particular event. A brief discussion of some of these results is given by Barnden,(1971); Barnden and McCracken,(1971).

In section 2 we consider the variations which are predicted for linear gradients. These variations approximate to a sine wave of 24 hours period. An estimate of the gradients associated with the average observed diurnal variation is obtained. Although this is not a new result, it provides an interesting comparison with the results

obtained using other methods. Moreover, several stations with different characteristics are considered, and the gradients associated with the average diurnal variation are calculated for each station using MFP sets 1, 2 and 3 for (a) λ independent of r, and (b) $\lambda \propto r^1$. Then the average scattering mean free paths (i.e. associated with the average diurnal variation) are taken to be those values for which the gradients predicted for each station are most closely the same.

6.2 The Long Term Average Diurnal Variation

The results of applying the above origin-of-scatter technique to linear gradients in the cosmic ray number density are now discussed. A linear gradient is a number density distribution of the form

$$U(r) = 1{\cdot}0 + (r - 1)\frac{dU}{dr} \qquad (6.2)$$

where r is heliocentric radius in AU, and $\frac{dU}{dr}$ is the amplitude of the gradient (i.e. the change in number density per AU). For a linear gradient $\frac{dU}{dr}$ is constant. We only consider positive gradients here, for which the number density increases as r increases.

The first application of this technique is to obtain an estimate of the gradient which is associated with the average diurnal variation (assuming this gradient to be linear). The long term average diurnal variation is observed (McCracken and Rao, 1965) to have an amplitude of 0·4% with its maximum 90° east of the Earth-Sun line. These are the free-space characteristics of the anisotropy.

Rao et al (1963) have shown that a free-space anisotropy of the form $\frac{\Delta N(T)}{N} = \xi \cos(15T - \theta)$ (ξ is amplitude = 0·4% here, θ is direction of maximum = 270° east of Sun-Earth line, T is local time), is observed by a detector on Earth as the anisotropy

$$\frac{\Delta N_E(T)}{N_E} = \xi B \cos(15T - \theta - \gamma)$$

The attenuation factor B, and the phase factor γ have been calculated (McCracken et al, 1965) and are listed in Table 6.1 for Deep River, Inuvik, Chacaltaya and Alert (γ is given in hours).

The parameters of the free-space anisotropy were thus calculated (McCracken and Rao, 1965) from the anisotropy observed on Earth using the correction factors, B and γ. Thus the amplitude A of the anisotropy (diurnal variation) observed on Earth is given by

$$A = \xi B \qquad (6.3)$$

The long term average daily variation amplitudes on Earth (A = 0·4B) are also listed in table 6.1. We now wish to use the origin-of-scatter coefficients to calculate the gradients associated with the above average diurnal variations observed by these stations.

Before we can do this however, it is necessary to establish the significance of the variation which is derived using the origin-of-scatter technique. The following discussion briefly describes the origin of the diurnal variation and indicates where the results of the origin-of-scatter technique fit into the framework of this theory.

TABLE 6.1

The long term average diurnal variation amplitude A at 4 stations, and the parameters relating this to the anisotropy in free-space

Station	Attenuation factor B	Phase Change γ (hours)	Average Amplitude A
Deep River	0·8448	2·33	0·338%
Inuvik	0·6446	0·62	0·258
Chacaltaya	0·6514	3·64	0·265
Alert	0·0990	2·01	0·040

The fundamental cause of the diurnal variation is the radially expanding solar corona or solar wind. This highly conductive plasma carries "frozen in" with it, the Sun's magnetic field, which in turn convects the bulk cosmic ray population outwards with the solar wind velocity. This is the so-called convective flow usually described by the differential current density

$$\underset{\sim}{S}_c = CU\underset{\sim}{V} \qquad (6.4)$$

where C is the Compton Getting factor, U is the number density and V is the solar wind velocity (Gleeson, 1969). Such a flow tends to remove cosmic rays from the inner solar system and therefore to produce a radial gradient in the cosmic ray population. The presence

of a density gradient immediately results in a diffusive flow $\underset{\sim}{S}_d$ which tends to cancel the gradient and repopulate the inner solar system. Under equilibrium conditions (no net radial flow) $\underset{\sim}{S}_c$ is balanced by the radial component of the inward diffusion flow $\underset{\sim}{S}_d$. $\underset{\sim}{S}_d$ can be written

$$\underset{\sim}{S}_d = -\kappa_{\parallel} \left(\frac{\partial U}{\partial \underset{\sim}{r}}\right)_{\parallel} - \kappa_{\perp} \left(\frac{\partial U}{\partial \underset{\sim}{r}}\right)_{\perp} \qquad (6.5a)$$

where $\kappa_{\parallel}$ and $\kappa_{\perp}$ are the diffusion coefficients for diffusion parallel to and perpendicular to the interplanetary magnetic field (Forman and Gleeson, 1971). Similarly $\left(\frac{\partial U}{\partial \underset{\sim}{r}}\right)_{\parallel}$ and $\left(\frac{\partial U}{\partial \underset{\sim}{r}}\right)_{\perp}$ are the parallel and perpendicular components of the radial density gradient. The diffusion flow $\underset{\sim}{S}_d$ can therefore be divided into two flows, one parallel and one perpendicular to the interplanetary magnetic field.

$$\text{i.e.} \qquad \underset{\sim}{S}_d = \underset{\sim}{S}_{d\parallel} + \underset{\sim}{S}_{d\perp} \qquad (6.5b)$$

The relative directions of these three flows are shown in Figure 6.1. The relative amplitude of $\underset{\sim}{S}_c$, $\underset{\sim}{S}_{d\parallel}$ and $\underset{\sim}{S}_{d\perp}$ in Figure 6.1 were chosen to satisfy the equilibrium condition of no <u>net</u> radial flow.

A cosmic ray flow $\underset{\sim}{S}$ will produce an anisotropy of amplitude $\underset{\sim}{\xi}$ where

$$\underset{\sim}{\xi} = \frac{3\underset{\sim}{S}}{vU} \qquad (6.6)$$

where v is the cosmic ray velocity. Such an anisotropy will appear as a diurnal variation in the records of an Earth-based detector. Thus,

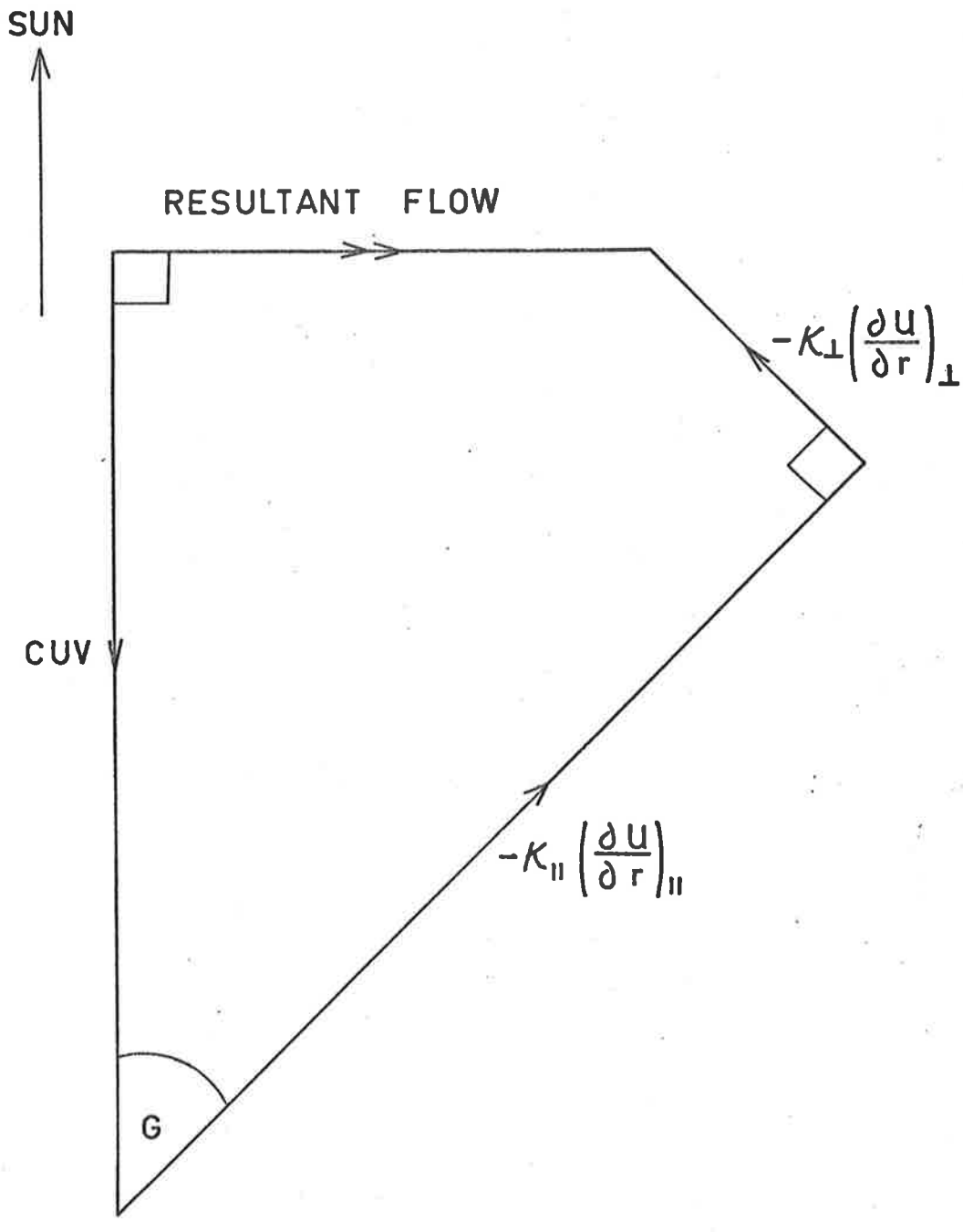

Figure 6.1 The three components $\underset{\sim}{S}c = CU\underset{\sim}{V}$, $\underset{\sim}{S}_{d_{\parallel}} = -\kappa_{\parallel}\left(\frac{\partial U}{\partial r}\right)_{\parallel}$ and $\underset{\sim}{S}_{d_{\perp}} = -\kappa_{\perp}\left(\frac{\partial U}{\partial r}\right)_{\perp}$ of the cosmic ray flow which causes the diurnal variation. The long term average directions are shown here.

just as the net flow of cosmic rays in space can be regarded as the sum of 3 component flows, the resulting daily variation can be regarded as the sum of three daily variation components. These three components of the diurnal variation have amplitudes A_c (produced by $\underset{\sim}{S}_c$), $A_{d_\parallel}$ (produced by $\underset{\sim}{S}_{d_\parallel}$), $A_{d_\perp}$ (produced by $\underset{\sim}{S}_{d_\perp}$). Each of these amplitudes is reduced from the free space anisotropy amplitude by the factor B in table 6.1.

Similarly the maximum of each of the daily variation components at Earth is phase shifted by γ (see Table 6.1) relative to the corresponding free space anisotropies. However the relative directions of these components are the same, so that the geometry of Figure 6.1 can be used to find relations between them.

Now the daily variation component calculated for a given gradient by the origin-of-scatter technique is the variation <u>at</u> the station caused by the diffusive (gradient induced) flow $\underset{\sim}{S}_{d_\parallel}$ of cosmic rays parallel to the interplanetary magnetic field. Thus the origin-of-scatter technique yields the amplitude $A_{d_\parallel}$.

The amplitude of the observed daily variation A_o is known, (see Table 6.1) and the amplitude of the convective component A_c can be calculated. Thus from the geometry of Figure 6.1 the amplitude $A_{d_\parallel}$ associated with the observed diurnal variation is

$$A_{d_\parallel} = A_o \cos G + A_c \sin G \qquad (6.7a)$$

also $$A_{d_\perp} = A_c \sin G - A_o \cos G \qquad (6.7b)$$

where G is the garden hose angle. The origin-of-scatter technique is then used to find the gradient which yields this value of $A_{d\parallel}$. This is the gradient which is associated with the average diurnal variation.

The amplitude ξ_c of the free-space anisotropy caused by the convective flow $\underset{\sim}{S}_c$ is now calculated. From equations 6.4 and 6.6

$$\xi_c = \frac{3CV}{v}$$

For the high energy cosmic rays involved here the Compton-Getting factor C in this equation is given by

$$C = \frac{2 + \mu}{3} \qquad \text{(Gleeson and Axford, 1967)}$$

where μ is the cosmic ray number density differential spectrum index (i.e. $U(P) \sim P^{-\mu}$). Two solar wind velocities are considered here, namely 400 km/sec ($G = 47{\cdot}4^{\circ}$) and 435 km/sec ($G = 45{\cdot}0^{\circ}$), and μ is taken to be 3·0 (i.e.. intensity differential spectrum index = 2·5). For these velocities, ξ_c (the free-space anisotropy amplitude) is 0·667% and 0·725% respectively. The amplitude of the anisotropy observed on Earth is $A_c = B\xi_c$ (B is given in table 6.1).

Table 6.2 lists the diurnal variation amplitudes $A_{d\parallel}$ deduced using the origin-of-scatter technique for a gradient of 10% per AU (at 6·5GV). Results are given for 4 different stations for various mean free paths. These gradients are given a P^{-1} rigidity dependence. Since the amplitudes $A_{d\parallel}$ are proportional to the gradient (equation 6.1), the gradient associated with any given $A_{d\parallel}$ can be calculated using the

TABLE 6.2

The amplitude (in %) of the diurnal variation component $A_{d_\parallel}$ calculated using the origin-of-scatter technique for a radial gradient of 10% per AU at 6·5 GV.
The gradient is linear and $\sim P^{-1}$.

MFP \ Station		Deep River	Inuvik	Chacaltaya	Alert
set 1	λ indept. r	0·587	0·476	0·407	0·120
set 2	"	0·846	0·675	0·552	
set 3	"	1·103	0·918	0·418	0·125
set 1	$\lambda \sim r^1$	0·643	0·512	0·514	0·125
set 2	"	1·011	0·781	0·848	0·137
set 3	"	1·480	1·158	0·737	

values in table 6.2. The value of $A_{d_\parallel}$ associated with the average diurnal variation was found using equation 6.7a.

The radial gradients associated with a free space anisotropy of 0·4% with its maximum 90° east of the Earth-Sun line are given in table 6.3 for a solar wind velocity of 400 km/sec (i.e. ξ_c = ·667%), for 4 stations for various mean free paths. Similarly table 6.4 gives the gradients for a solar wind velocity of 435 km/sec (ξ_c = ·725%). The rigidity dependence of the mean free paths used to obtain these gradients is shown in Figure 5.4. These gradients (in percent per AU)

are the gradients at 6·5 GV. All gradients are given a P^{-1} rigidity dependence for these calculations.

TABLE 6.3

The Radial Gradients (at 6·5GV) in percent per AU associated with the average diurnal variation for V = 400 km/sec, when the gradients are linear and $\sim P^{-1}$.

MFP	Station / $A_{d\parallel}$	Deep River ·630%	Inuvik ·481%	Chacaltaya ·493%	Alert ·076%
set 1	λ indept. r	10·7	10·1	12·1	6·3
set 2	"	7·5	7·1	8·9	
set 3	"	5·7	5·2	11·8	6·1
set 1	$\lambda \sim r^1$	9·8	9·4	9·6	6·4
set 2	"	6·2	6·2	5·8	5·6
set 3	"	4·3	4·1	6·7	

It can be seen in Tables 6.3 and 6.4 that the gradient estimates from the four different stations are in closest agreement for MFP set 2, $\lambda \sim r^1$. This indicates that these are the average mean-free-paths associated with the observed long term average diurnal variation. That is, these are the values of the long term average scattering mean free paths in interplanetary space. It appears that even better agreement between these four stations would be achieved for mean free paths slightly shorter than MFP set 2 ($\lambda \propto r$).

TABLE 6.4

The Radial Gradients (at 6·5 GV) in percent per AU associated with the average diurnal variation for V = 435 km/sec, when the gradients are linear and $\sim P^{-1}$.

MFP \ Station $A_{d\parallel}$		Deep River ·672%	Inuvik ·512%	Chacaltaya ·526%	Alert ·079%
set 1	λ indept. r	11·4	10·8	12·9	6·6
set 2	"	7·9	7·6	9·5	
set 3	"	6·1	5·6	12·6	6·3
set 1	$\lambda \sim r^1$	10·5	10·0	10·2	6·3
set 2	"	6·7	6·6	6·2	5·8
set 3	"	4·5	4·4	7·1	

It can be seen that the gradients calculated for Alert are about the same for all mean free paths used. Since the gradients calculated for the other stations vary strongly with mean free path, the Alert value effectively determines the mean free path set which we associate with the long term diurnal variation. That is the long term average mean free paths are those for which the gradients at Deep River, Inuvik and Chacaltaya are closest to the (almost) constant gradient at Alert.

It is important to realise therefore, that the reduction factor B which is used to determine $A_{d\parallel}$ at Alert (which then defines the

gradient), is very sensitive to small changes in the asymptotic directions of viewing. In fact $B \sim \cos \Lambda$, where Λ is the average asymptotic latitude of viewing at Alert. For these calculations $\Lambda \simeq 83^{\circ}$. If this was 3° in error, i.e. if the true Λ was 86° the error in B would be $\frac{\cos 83}{\cos 86}$, i.e. a factor of 1·75.

Hence it can be seen that the results in Tables 6.3 and 6.4 for Alert must be regarded with some caution, and for this reason there is some uncertainty in the mean free path set which gives a constant gradient for all stations.

Clearly more work is needed to resolve this uncertainty (e.g. it would be more accurate to use the actual observations at Alert to find A_o and thence $A_{d\parallel}$). However this is not attempted in this thesis. Most of the discussion which follows uses the extreme mean-free-path values (MFP sets 1 and 3).

Assuming the results for Alert to be correct however, Tables 6.3 and 6.4 also show that the amplitude (at 6·5 GV) of the radial gradient associated with the long term average diurnal variation is

(i) 6·0% per AU, for $\overline{V}$ = 400 km/sec

(ii) 6·3% per AU, for $\overline{V}$ = 435 km/sec

where $\overline{V}$ is the average solar wind velocity. These are the results for linear gradients with amplitudes which vary as P^{-1}. The above values were obtained by averaging the MFP set 2 ($\lambda \propto r$) gradients over the

4 stations in Tables 6.3 and 6.4.

The actual daily variation (due to the parallel diffusion flow) for a gradient of 10·3% per AU (at 6·5 GV), calculated using the origin-of-scatter technique for Deep River for MFP set 1 ($\lambda \propto r$), is shown in Figure 6.2a.

The time scale used in Figure 6.2 is asymptotic time T_a, where

T_a = Local Time + correction for geomagnetic deflection of cosmic rays.

$$= LT + \gamma$$
$$= UT + \frac{\phi_s}{15} + \gamma \qquad (6.8)$$

where ϕ_s is station longitude (for Deep River T_a = UT - 2·84 hours). The longitude of viewing Ψ of the cone of acceptance is simply $\Psi = 15T_a$ degrees (T_a in hours). For a garden hose angle of 45° (V = 435 km/sec) an equatorial detector looks parallel to the interplanetary magnetic field at 0900 AT (into Sun) and 2100 AT (away from Sun).

Figure 6.2a shows a daily variation with maximum near 2100 hours AT, and minimum near 0900 AT. Thus the minimum is observed when the cone of acceptance views parallel to the magnetic field and into the Sun. In terms of cosmic ray flows, the minimum is observed when the detector looks in the direction of the parallel diffusion flow $\underset{\sim}{S}_{d\parallel}$. It must be stressed that Figure 6.2 does not contain the convective or the perpendicular diffusion component of the diurnal variation.

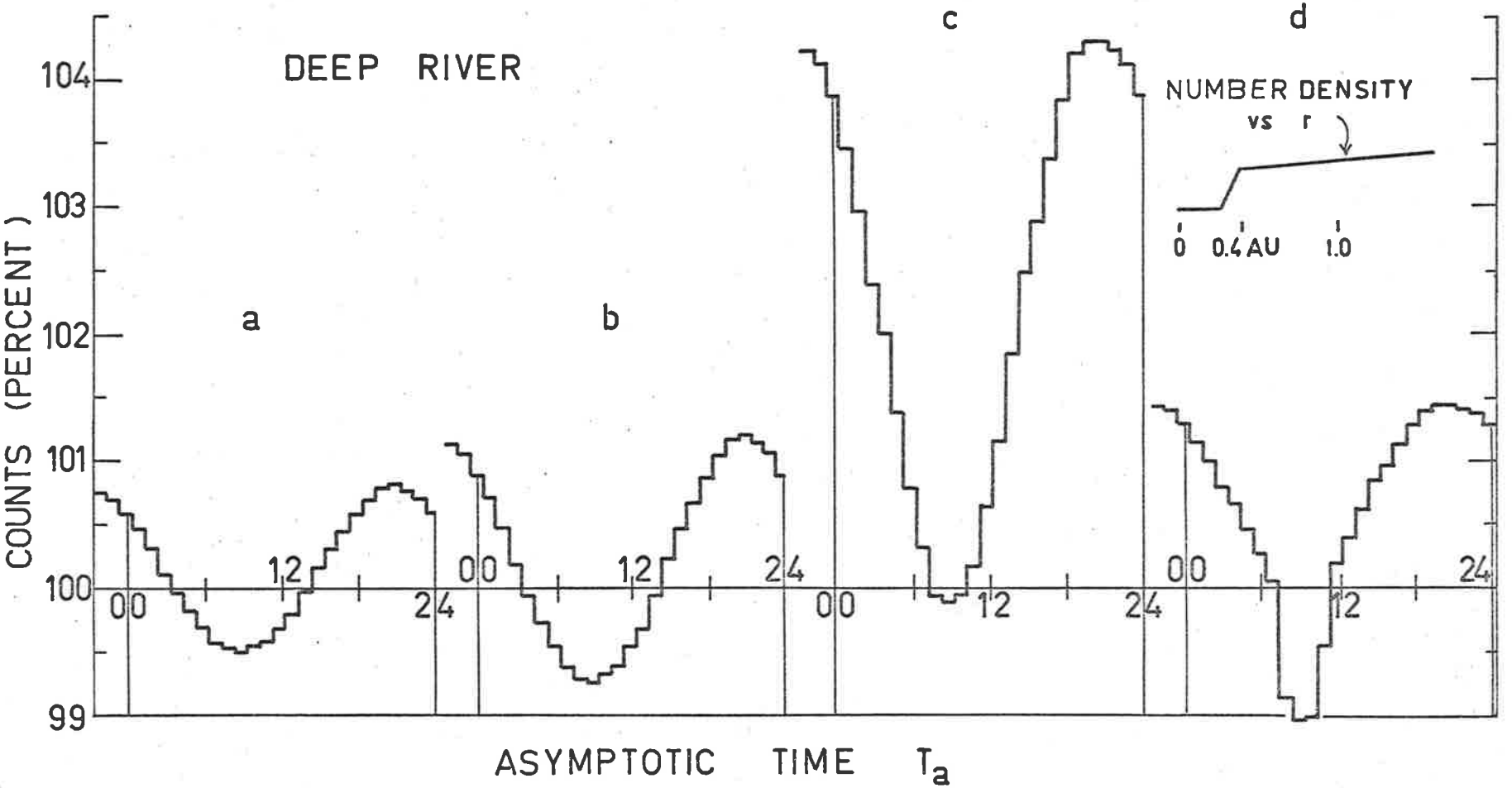

Figure 6.2 The daily variation component (due to the parallel diffusion flow $S_{d\parallel}$) as calculated by the origin-of-scatter technique for the Deep River station. (a) For a gradient of 10·3% per AU (at 6·5 GV) for MFP set 1 ($\lambda \propto r$). (b) For a gradient of 15% per AU (at 6·5 GV) for MFP set 1 ($\lambda \propto r$). (c) For a gradient of 15% per AU (at 6·5 GV) for MFP set 3 ($\lambda \propto r$). (d) For a gradient of the form shown, i.e. 5% per AU + 300% per AU inside 0·4 AU (until the number density is half its value 0·4 AU) for MFP set 3 ($\lambda \propto r^1$).

6.2.1 The Second Harmonic in the Theoretical Daily Variation

Harmonic analysis of the daily variation component calculated by the origin-of-scatter technique for linear gradients indicates the presence of a small second harmonic or semidiurnal variation. Table 6.5 gives the phase of this semidiurnal component at Deep River and Inuvik for various scattering mean free paths. This phase was estimated by using the γ_2 of McCracken et al (1965) to allow for the geomagnetic effects. (γ_2 is the semidiurnal analogue of the γ on p.110). The phase, or direction of maximum is expressed in degrees east of the Sun-Earth line. In addition table 6.5 gives the semidiurnal variation amplitude (in %) for the gradient which produces the long term average diurnal variation.

TABLE 6.5

The theoretical semidiurnal variation associated with the linear gradient which yields the average diurnal variation.

Mean free path	Deep River amplitude	Deep River phase	Inuvik amplitude	Inuvik phase
set 1	·020%	44·3°	·017%	45·1°
set 2 λ indept. r	·016	41·2	·019	47·5
set 3	·005	-30·0	·017	50·5
set 1	·008	-46·3	·001	32·7
set 2 $\lambda \alpha r^1$	·003	74·9	·007	45·2
set 3	·049	47·4	·021	47·6
Average	·014	22·0	·013	45·3

It can be seen from this table that the amplitude varies considerably for different mean free paths, but when it exceeds 0·01%

the phase is very close to 45°. This is the phase of the observed semidiurnal variation (Rao and Agrawal, 1970), although the observed amplitude is greater ($\sim$ 0·04%). Clearly there is a distinct possibility that a component of the observed semidiurnal variation is a radial gradient induced effect.

6.3 Short Term Effects in the Diurnal Variation

It is well known that the diurnal variation amplitude and phase vary strongly from the long term average values on a day to day basis. In this section we use results obtained with the origin-of-scatter technique to investigate the effects on the diurnal variation of

(i) a change in the amplitude of the (linear) number density gradient.

(ii) a change in the rigidity dependence of the number density gradient.

(iii) a non linear gradient, chosen to simulate the situation when there is a blast wave close to the Sun which, although it may not ultimately reach the Earth, is 'connected' to the Earth by the interplanetary field lines.

Now the origin-of-scatter technique yields the daily variation component $A_{d\parallel}$. To find the amplitude and phase of the resultant free space anisotropy ξ_o, the following procedure is used.

a. The convective component A_c, and the garden hose angle G are assumed to be unchanged by any change in the radial gradient.

b. The perpendicular diffusion component $A_{d_\perp}$ is assumed to change from its long term average value, by the same factor as $A_{d_\parallel}$.

c. The vector sum of $\underset{\sim}{A}_c$, $\underset{\sim}{A}_{d_\parallel}$ and $\underset{\sim}{A}_{d_\perp}$ is then taken to yield the resultant $\underset{\sim}{A}_o$.

d. The free space amplitude ξ_o of the anisotropy associated with A_o is calculated using equation 6.3.

e. The phase of the free space amplitude is found from the angular separation of $\underset{\sim}{A}_o$ and $\underset{\sim}{A}_c$. This angle gives the direction of ξ_o relative to the Earth-Sun line.

This procedure may not be rigorously correct in all cases, (e.g. changing the gradient rigidity dependence as in section 6.3.2 may imply a change in the number density spectral index μ on p114) but it serves to indicate the type of behaviour which will occur. The following results were calculated for V = 400 km/sec, G = $47{\cdot}3^{\circ}$.

6.3.1 The effect of changing the amplitude of the gradient

Figure 6.2b shows the daily variation component $A_{d_\parallel}$ at Deep River for a gradient of 15% per AU (at 6·5 GV) for MFP set 1 ($\lambda \propto r^1$). For the longer mean free paths of MFP set 3 the origin-of-scatter

technique shows that this gradient (15% per AU at 6·5 GV) yields the variation in Figure 6.2c. Applying the procedure described above, the amplitude and phase of the free space anisotropy under these conditions are 0·7% and 120° (for MFP set 1, $\lambda \propto r$) and 2·0% and 141° (for MFP set 3, $\lambda \propto r$). These features are typical of the enhanced diurnal variation (Mathews et al, 1969; Hashim and Thambahpillai, 1969). The vector diagram used to calculate A_o (which then gives ξ_o) for these two cases is shown in Figure 6.3a.

6.3.2 The Effect of Changing the Rigidity Dependence of the Gradient

In the analysis so far, we have used a P^{-1} rigidity dependence for the gradient amplitude. We now consider cases of a $P^{-\eta}$ rigidity dependence when η varies from 0·4 to 1·6. Such changes in η will occur if the distribution of scale size of the magnetic field irregularities changes, since a cosmic ray is most strongly 'scattered' by an irregularity whose scale size is comparable to its gyroradius.

For the present purpose the amplitude of the (linear) gradient at rigidity P is given by

$$\frac{dU(P)}{dr} = \frac{dU(6{\cdot}5GV)}{dr} \left(\frac{P}{6{\cdot}5} \right)^{-\eta} \qquad (6.9)$$

i.e. the gradients are calculated from the gradient at 6·5GV which has the same value for all η. The amplitude of the daily variation component $A_{d\parallel}$ is calculated using the origin-of-scatter technique for

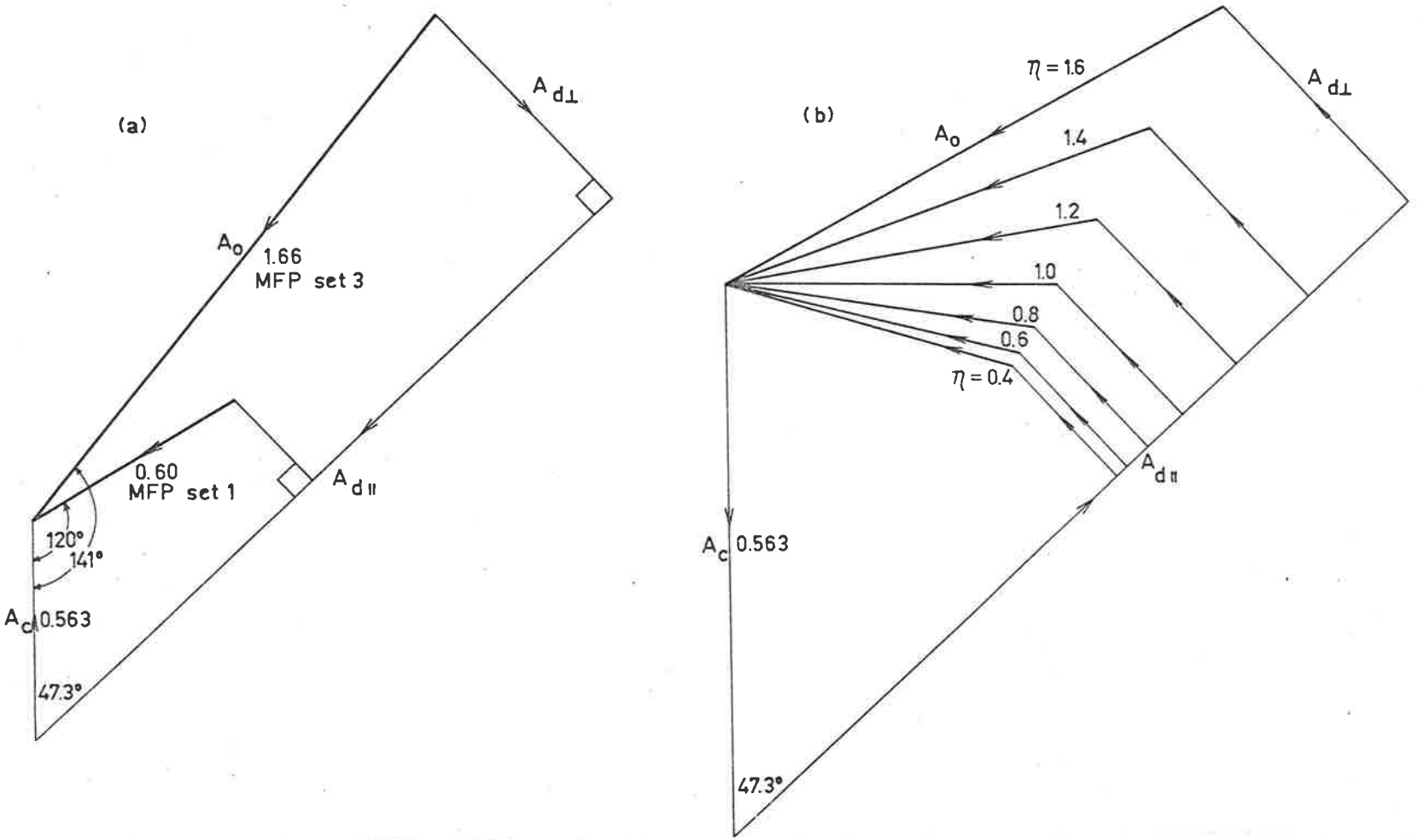

Figure 6.3 Illustrating the manner in which a transient variation in the cosmic ray density gradient will alter the phase and amplitude of the diurnal variation. (a) $\frac{dU}{dr}$ = 15% per AU (at 6·5 GV, $\frac{dU}{dr} \propto P^{-1}$) with MFP set 1 and MFP set 3 ($\lambda \propto r^1$).

(b) $\frac{dU}{dr} \propto P^{-\eta}$ for MFP set 1 ($\lambda \propto r^1$). 7 values of η were considered. Note that (a) and (b) are not drawn on the same scale.

each value of η. From $A_{d\parallel}$ the amplitude and phase of the free space anisotropy ξ_o, are calculated using the procedure given on page 122.

Table 6.6 lists the amplitude and phase, as would be deduced at Deep River, of ξ_o for gradients with different rigidity dependence (for MFP set 1, $\lambda \propto r$). These values were calculated using

$$\frac{dU(6{\cdot}5GV)}{dr} = 10\% \text{ per AU, in equation 6.9.}$$

TABLE 6.6

The free space diurnal variation as observed from Deep River when the gradients have a $P^{-\eta}$ rigidity dependence (equation 6.9)

η	0·4	0·6	0·8	1·0	1·2	1·4	1·6
Amplitude %	·358	·364	·373	·397	·452	·532	·682
Phase (degrees)	73°	76°	81°	90°	99°	110°	119°

Table 6.6 shows that the diurnal variation changes strongly as η varies, especially for $\eta > 1{\cdot}0$ (the assumed long term average index). Figure 6.3b shows the vector diagrams used to calculate the amplitude and phase of A_o (which then gives ξ_o) for the values of η listed in Table 6.6. It is seen that as η increases the amplitude increases and the phase swings anticlockwise. It should be noted that these results will differ if a different rigidity is used (instead of 6·5GV in equation

6.9) for the value where $\frac{dU}{dr}$ is constant as we change η.

The range of daily variations which is shown in Figure 6.3a and b is similar to that observed in practice.

6.3.3 The Effect of a non-linear gradient

The daily variation component ($A_{d\parallel}$) calculated for a non-linear gradient is shown in Figure 6.2d. This was calculated for Deep River with MFP set 3, $\lambda \propto r$ (see figure 5.11). The gradient which is also shown in Figure 6.2d, represents a region of depleted number density close to the Sun. It is a summation of a 5% per AU gradient and (inside 0·4AU) a 300% per AU gradient which drops the number density to half that at 0·4 AU. The resulting modulation shows a marked decrease at 0900 AT superimposed on the sinusoidal variation. If the other components of the diurnal variation (A_c and $A_{d\perp}$) were added to this, the result would have its maximum 90° east of the Sun-Earth line and its minimum 45° west of the Sun-Earth line. This is the type of observation reported by Rao and Sarabhai (1964). Their results together with the above calculations suggest that strongly non-linear gradients are common occurrences in the inner solar system.

6.3.4 Changes in the Daily Average with Different Mean Free Paths

The change in $A_{d\parallel}$ as the mean free path changes can be seen in Table 6.2 (for a 10% per AU gradient at 6·5GV). In addition to this effect it is found that the average daily level of the cosmic

ray flux also changes with mean free path. Table 6.7 lists the average daily level for a 10% per AU gradient (at 6·5GV) of the form expressed in equation 6.2, for Deep River, Inuvik and Chacaltaya. In all cases the average level increases as we go to longer mean free paths.

TABLE 6.7

The Theoretical Daily Average Flux Level (in %)

Mean Free Path	Deep River	Inuvik	Chacaltaya
set 1	100·08	100·08	100·13
set 2 λ indept. r	100·33	100·32	100·59
set 3	101·25	101·22	102·07
set 1	100·14	100·13	100·22
set 2 $\lambda \alpha r^1$	100·47	100·46	100·80
set 3	101·51	101·55	102·30

This effect can be understood by comparing the origin-of-scatter plots for MFP set 1 and MFP set 3 for Deep River, say. In Figures 5.6 and 5.11 it can be seen that an appreciable flux originates outside 1AU at all times of day, but this is not the case for the flux inside 1AU. Furthermore the flux from outside 1AU originates from regions 2-3 AU distant from the Earth, whereas the flux from inside 1AU originates from regions less than 1AU from Earth. Consequently when a linear gradient is present, the decrease produced by observing

regions inside the Earth (number density < 1·0) is smaller than the increase produced when regions outside 1AU are observed (number density > 1·0). Thus the average daily flux is greater than the flux in space at 1AU, because the mean sampling point is outside 1AU.

This effect is much more pronounced for longer mean free paths, (the mean sampling point moves further out from the Earth) so that a higher average flux level results. This effect is very noticeable at high cut-off rigidity stations such as Chacaltaya, where, for MFP set 3, $\lambda \propto r^1$, more than 30% of the flux (apart from the 30% > 60GV) originates outside 3AU. In the calculation of the daily variation this 30% was assumed to originate from a region where the number density was the same as at r = 3·0AU. Hence the average fluxes in Table 6.7 are lower limits only. The errors for the shorter mean free paths are much smaller (only $\sim$ 2% originates outside 3AU for Chacaltaya MFP set 1, $\lambda \propto r$). However the average level for Chacaltaya MFP set 3, $\lambda \propto r$ is probably greater than 105%.

Hence if the scattering mean free paths in interplanetary space increase, the level of the daily average flux will also increase. This effect will be most pronounced at high cut-off rigidity stations. This effect can be seen in Figure 6.2c which is the daily variation (parallel diffusion component) at Deep River for MFP set 3 ($\lambda \propto r$) for a 15% per AU gradient. In this case the average flux is 102·1% which should be compared with 100·2% for the same gradient (Figure 6.2b)

for MFP set 1.

This mechanism would explain increases in the daily average, lasting for ∿ 10 days, which sometimes appear in the data, and which are clearly not Forbush decrease recoveries.

6.4 The Step Gradient - The Forbush Decrease

We now apply the origin-of-scatter technique to calculate the variation on Earth due to a non-linear density gradient in interplanetary space. The basic non-linear gradient used is a step gradient, that is a region of depleted number density is imposed on the solar system. In addition this depletion region moves outwards from the Sun with a radial velocity component V_r in the ecliptic (see Figure 6.4a).

This type of cosmic ray density distribution is expected at times of solar activity when blast waves or shocks (e.g. Parker, 1963) propagate outwards from the Sun. The effects of such depletion regions have been observed on Earth in the form of Forbush decreases in the cosmic ray flux. However the profiles of these decreases show unexpected variation from event to event, and also from station to station for one particular event (Fenton et al, 1959; Lockwood and Razdan, 1963). Spacecraft observations show that there is usually an abrupt increase in the magnetic field intensity as the blast wave passes. However the arrival at Earth of these enhanced magnetic fields

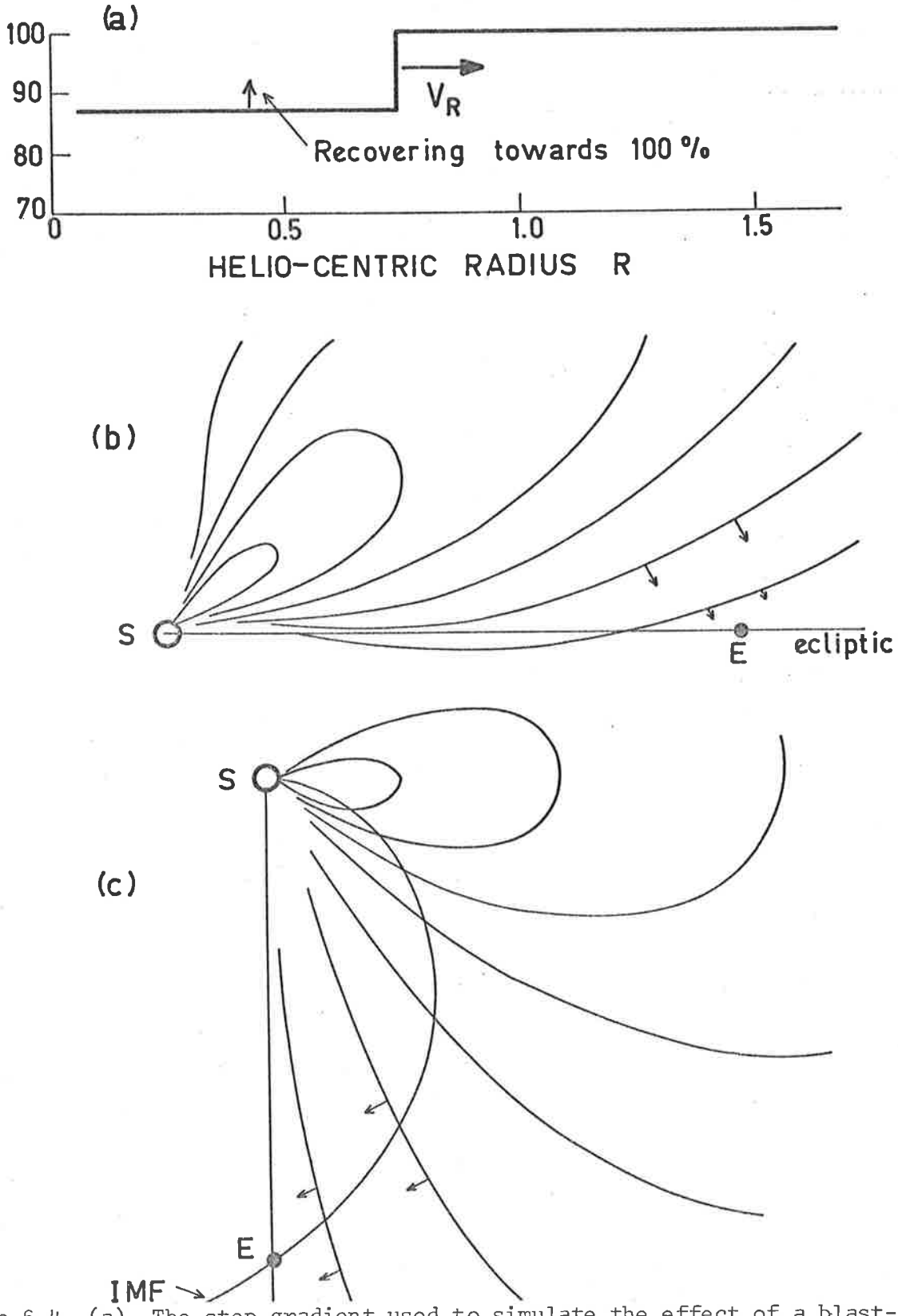

Figure 6.4 (a) The step gradient used to simulate the effect of a blast-wave in interplanetary space. V_R is the effective radial approach velocity of the step. (b) and (c) The type of blast-wave geometry which would yield a low value for V_R, for shock originating at high solar latitude, and for shock originating near 90°W.

seldom coincides with the onset of the Forbush decrease. The suggestion is, that the opacity of the shock and therefore its ability to sweep cosmic rays, is the result of an enhanced scattering capability in the form of very turbulent magnetic fields associated with the shock.

In the present treatment the only effect of the blast wave is taken to be a simple step in the cosmic ray number density, which moves with the velocity of the shock. At first sight this may appear to be an over-simplification. However it is shown that the origin-of-scatter technique, when applied to this number density 'gradient', yields most of the anisotropic features observed during Forbush decreases. Thus most of the complexity observed in Forbush decrease profiles arises as a natural consequence of the remote sensing properties of an Earth-bound detector, and therefore need not indicate complexity in the gradients in interplanetary space.

Because the origin-of-scatter technique effectively allows for the varying spatial response of an Earth-bound detector, it can be used to deduce information about certain interplanetary conditions, from observations made on Earth. These interplanetary parameters exist within the framework of the origin-of-scatter technique and can be varied to obtain a best fit between theoretical and observational results. The approach here however, is to take representative values of these interplanetary parameters and illustrate how the family of

Forbush decrease profiles emerges. We now consider the effect of changing (i) V_R, the radial component (in the ecliptic) of the blast wave approach velocity, and (ii) the position of the station on Earth.

In these investigations the depth of the number density depletion inside the shock is given a $P^{-\frac{1}{2}}$ rigidity dependence. In addition, in order to simulate the real situation more accurately, the depth of the number density depletion inside the shock is taken to be decreasing with time, that is the number density inside the shock is slowly approaching 100%. This recovery is here taken to be linear. Examples of Forbush decreases calculated without this recovery are shown in Figure 4 of Barnden, (1971).

In the following subsections, frequent examples are given for blast waves which approach the Earth with a radial velocity component which is no greater than the local solar wind velocity. This situation does not necessarily infer that the plasma inside the shock is travelling this slowly.

It has been pointed out (see Figures 4.1 and 5.7) that a detector on Earth senses cosmic rays from close to the spiral field line which intersects the Earth. If the geometry of the shock envelope is such that its intersection with this field line moves towards the Earth with an effective radial velocity V_R, then the Forbush decrease profile will be the same as for a blast wave expanding spherically with velocity V_R.

Recent observations have suggested that some shocks have a form which is very different to the ideal expanding hemisphere. Greenstadt et al (1970), using observations from three widely separated spacecraft, deduced that the shock associated with the proton flare of 7 July 1966 arrived at the Earth with its normal directed 65-70^{o} below the ecliptic and towards 165^{o} solar ecliptic longitude. Since the parent flare was at N34W48 the suggestion is that the shock was an elongated envelope of the form depicted in Figures 6.4(b) and (c), and that it was predominantly a lateral expansion which was observed near Earth. A similar oblique shock has been observed by Hirshberg et al (1970).

Figure 6.4(b) is a projection onto the plane perpendicular to the ecliptic which contains the Sun and Earth, while Figure 6.4(c) is a projection onto the ecliptic. In both cases it can be seen that if the lateral expansion of the shock envelope is slow, then the effective radial approach velocity of the shock is also slow even though the plasma within the envelope is travelling many times faster. Greenstadt et al (1970) suggest that this non-uniform expansion may be a result of the influence of coronal structure, such as is observed in coronal streamers. Similarly Lazarus and Binsack (1969) have suggested that sector boundaries may influence shock propagation. Dorman et al (1969) note that near to the Sun the energy density of the magnetic field may exceed the kinetic energy density of the plasma, so that initially the plasma flow would be largely controlled by the magnetic

field. In this case lateral expansion of the shock envelope is restricted until the shock moves out to a region where the energy density of the magnetic field is smaller.

Thus any of these mechanisms could support the behaviour shown in Figure 6.4(b) and (c), and would effectively cause a shock (which originates from a suitable area on the Sun) to have a very slow radial approach velocity.

6.4.1 The Effect of Different Approach Velocities V_R

Figure 6.5 shows the Forbush decrease profiles calculated for Deep River for radial approach velocites of 400, 800 and 1600 km/sec. Figure 6.5 a, b and c show the results for a shock arriving at 0000 UT, while Figure 6.5 d, e and f is for arrival at 1200 UT. The depth of the depletion region was 10% at 6·5 GV (varying as $P^{-\frac{1}{2}}$) and the scattering mean free paths in interplanetary space were taken to be those of MFP set 1 (λ indept. of r). The dashed lines show the shock arrival time.

Figure 6.5 shows that both the depth of the preliminary Forbush decrease and the height of the peak which occurs during the recovery stage, increase as we go to lower radial approach velocities. It will be noticed that the time from maximum flux to minimum flux (i.e. the fall time) is about 6 hours in all cases in Figure 6.5, that is the fall times are reasonably slow for shock arrival times of 0000 and 1200 hours UT. This can be understood in terms of the origin-of-scatter coefficients in Figure 5.6. In the six hours after 0000 UT an appreciable part of the flux at Deep River 'originates' from <u>beyond</u>

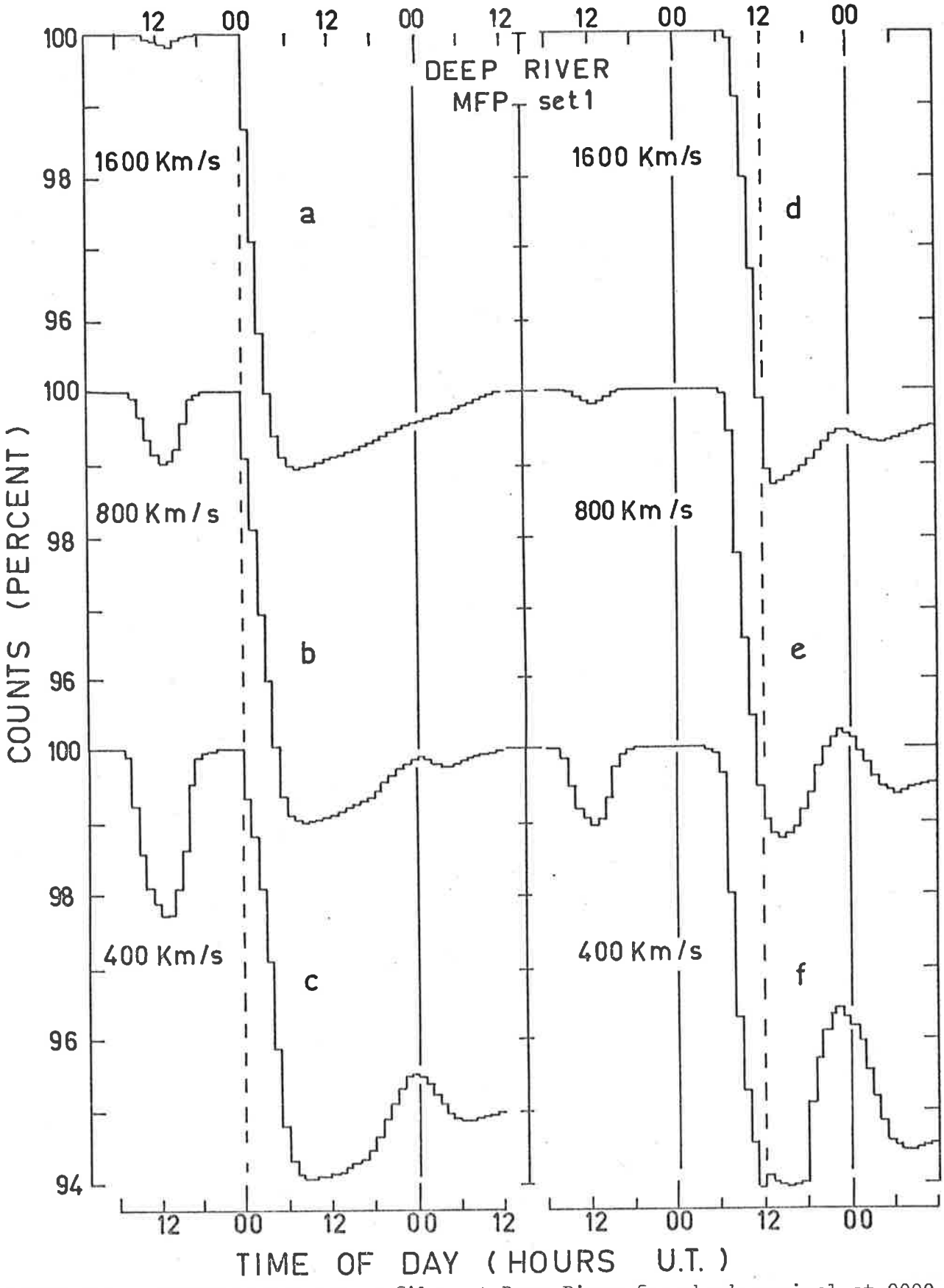

Figure 6.5 Forbush decrease profiles at Deep River for shock arrival at 0000 and 1200 UT for V_R = 1600, 800 and 400 km/sec.

1 AU and outside the shock. Thus although the Earth is completely enveloped in the depletion region, it still has access to cosmic rays from beyond the shock. Similarly for several hours before 1200 UT Deep River senses from well inside 1 AU, so that the depleted number density behind the shock is observed before the shock reaches Earth. However the full depth of the Forbush decrease is not recorded until 1200 UT when the total flux originates inside the shock.

This discussion suggests however, that these curves would be very different if the shock arrived near 0600 UT say, when nearly all of the flux (at Deep River) originates from closer than 0·1 AU from Earth. The way the Forbush decrease profiles change as the shock arrival time changes is discussed in the next subsection.

The preliminary Forbush decrease occurs because the detector is able to sense the region of depleted cosmic ray number density before it reaches Earth. The Deep River station senses deepest into the solar system near 1200 UT (i.e. 0900 asymptotic time), when the detector looks in parallel to the interplanetary magnetic field, so that this is when preliminary decrease is observed. In Figure 6.5, when the shock is sampled (at 1200 UT) on the day before its arrival at Earth, it is at $r = 0{\cdot}875$ AU (400 km/sec), at $r = 0{\cdot}77$ AU (800 km/sec), and at 0·50 AU (1600 km/sec). Thus the depletion region is sensed most strongly for the slowest velocity.

6.4.2 The Profiles at Different Geographic Longitudes

We first consider detectors on Earth with the same latitude,

but separated in longitude. This is achieved by calculating results for six detectors equispaced in geographic longitude. It is assumed that each of these detectors has a cone of acceptance which is the same as Deep River's (except for the displacement in longitude). Deep River is typical of a family of stations, each with a low cut-off rigidity and with its cone of acceptance centered on the equatorial plane.

This method is used because of the equivalence which exists between Forbush decrease profiles at (i) the same station for different arrival times of the shock, and (ii) sister stations separated in longitude which view the same shock. Consider the adjacent diagram in which two stations A and B, with identical cones of acceptance are separated by H hours of longitude. Clearly the Forbush decrease recorded by station B at longitude L + H (in hours) for a shock which passes 1AU at time T UT, is the same as the Forbush decrease recorded by station A at longitude L for the same hypothetical shock which passes 1AU H hours later at T + H UT (by T + H UT, station A rotates to the position occupied by station B at T UT). Thus for identical stations

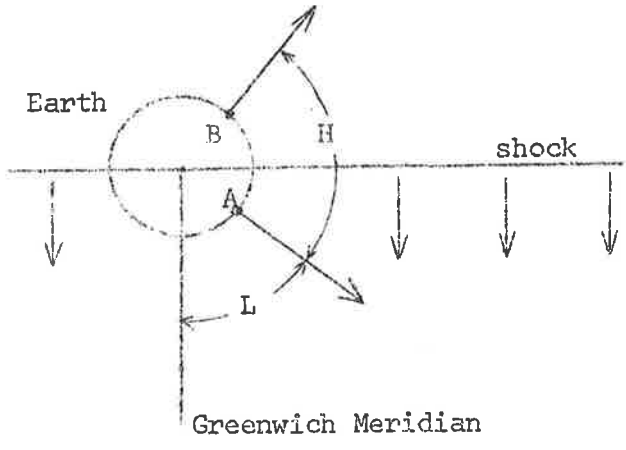

$$FD\ (L + H,\ T) = FD\ (L,\ T + H) \qquad (6.10)$$

Thus by calculating the Forbush decrease profiles at Deep River for a hypothetical shock with arrival times separated by 4 hours, the profiles for stations separated by 60° in longitude are obtained. To simulate a single event as observed by 6 equispaced detectors (in longitude), the profiles are shifted until the time of arrival (UT) in each profile is aligned.

The Forbush decreases expected around the world for a shock with a radial velocity component V_R = 400 km/sec, which reaches 1AU at 00UT. are shown in Figure 6.6A. The vertical dashed line shows the arrival time of the shock. The profile for the station at longitude = DR + 60, is also the profile for Deep River when the arrival time is 04 UT. Similarly the profile for longitude DR + 120 is the Deep River profile for arrival at 08 UT, ...etc.

Figures 6.6B and 6.6C show the Forbush decrease profiles at 60° intervals around the world for V_R = 800 km/sec and V_R = 1200 km/sec. Again the shock arrival time at Earth is 00UT as shown by the vertical dashed lines. Figures 6.6A, B and C all show a strong station dependence for the Forbush decrease profile. In particular the apparent onset time varies from 16 UT at DR + 240° to 00 (or 24) UT at DR. This feature is normally interpreted as a large anisotropy parallel to the interplanetary magnetic field (Fenton et al, 1959).

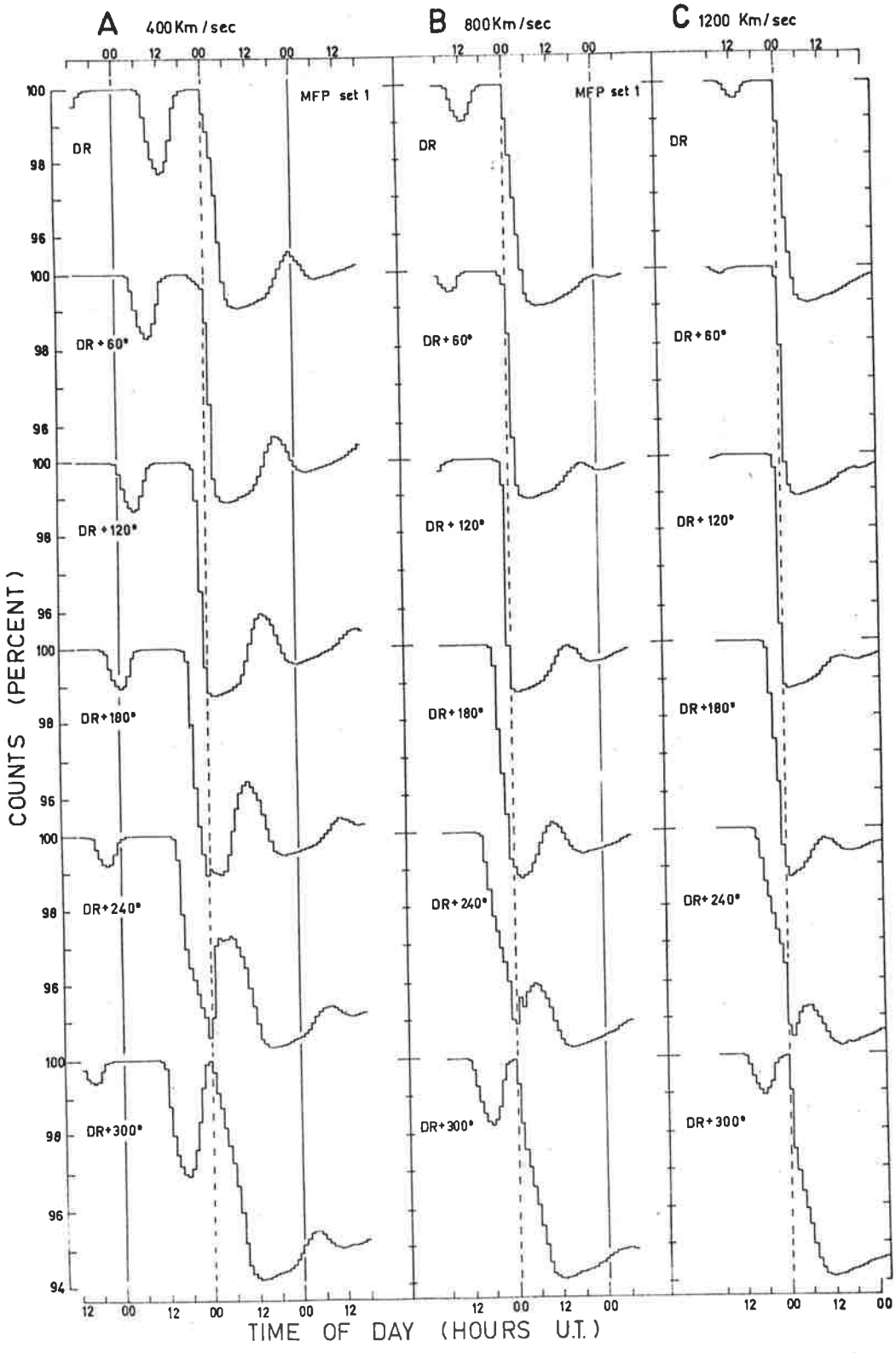

Figure 6.6 Illustrating the theoretical predictions of the origin-of-scatter theory for the Forbush decreases seen by 6 stations equispaced in longitude for a shock which reaches Earth at 0000 UT with A. V_R = 400 km/sec, B. V_R = 800 km/sec, C. V_R = 1200 km/sec, for MFP set 1 (λ indept. r).

The present theory enables us to take this explanation one step further because it shows in detail how this anisotropy arises. It has been shown that a simple step decrease in number density which moves outwards past the Earth produces an anisotropic flow of the form which yields the general features of the world wide modulation observed in practice.

The origin-of-scatter technique, which yields this conclusion, takes the detailed cone of acceptance of the detector, determines the regions of space traversed by the cosmic rays which arrive within this cone, and for a given (radial) number density distribution it computes the flux which will arrive at the detector (for a given time of day). Thus this technique essentially estimates the total anisotropic flux at Earth arriving within the cone of acceptance at any given time when there is a radial number density gradient in interplanetary space.

The origin-of-scatter coefficients, when displayed as in Figure 5.6 etc. suggest an alternative (but equivalent) way of interpreting the difference in onset times in Forbush decreases observed at different localities on Earth. Figure 5.6 shows that a station (Deep River here) effectively samples cosmic rays from regions of space which change from predominantly outside 1AU to predominantly inside 1AU in the course of a day. Equally, at any one time, detectors in the world-wide net of stations, when combined, are sampling from this whole region of space.

Thus an early onset is seen by those stations looking in parallel to the spiral field line (e.g. Deep River in hour 12 UT) a few hours before the shock reaches Earth. These detectors effectively sample from deep inside Earth at this time and can sense the region of depleted number density, so that they record their main phase Forbush decrease well before the shock reaches Earth (see DR + 240° in Figure 6.6). Similarly the late onset times occur at stations which are looking away from the Sun, and so do not sense the depleted number density to record their main phase decrease, until the shock actually passes the Earth (e.g. DR in Figure 6.6).

Preliminary Forbush decreases occur if a detector senses the depleted number density when the shock is so far from the Earth that the station has time to rotate (with the Earth) by 90°, say, so that it reverts to the situation of sampling from beyond 1AU before the shock reaches Earth. In this case the countrate returns to its undisturbed level and the decrease which was observed is not considered to be the Forbush decrease onset (i.e. the main phase decrease).

The profiles presented in Figure 6.6 were calculated using the origin-of-scatter coefficients for MFP set 1 (λ indept. of r). Figure 6.7 shows the Forbush decrease profiles calculated using $\zeta(r,T)$ for MFP set 3 (λ indept. r). The six profiles correspond to six Deep Rivers equispaced in longitude. The number density depletion is 10% behind a shock which arrives at 00UT with A. V_R = 400 km/sec and B. V_R = 1200 km/sec.

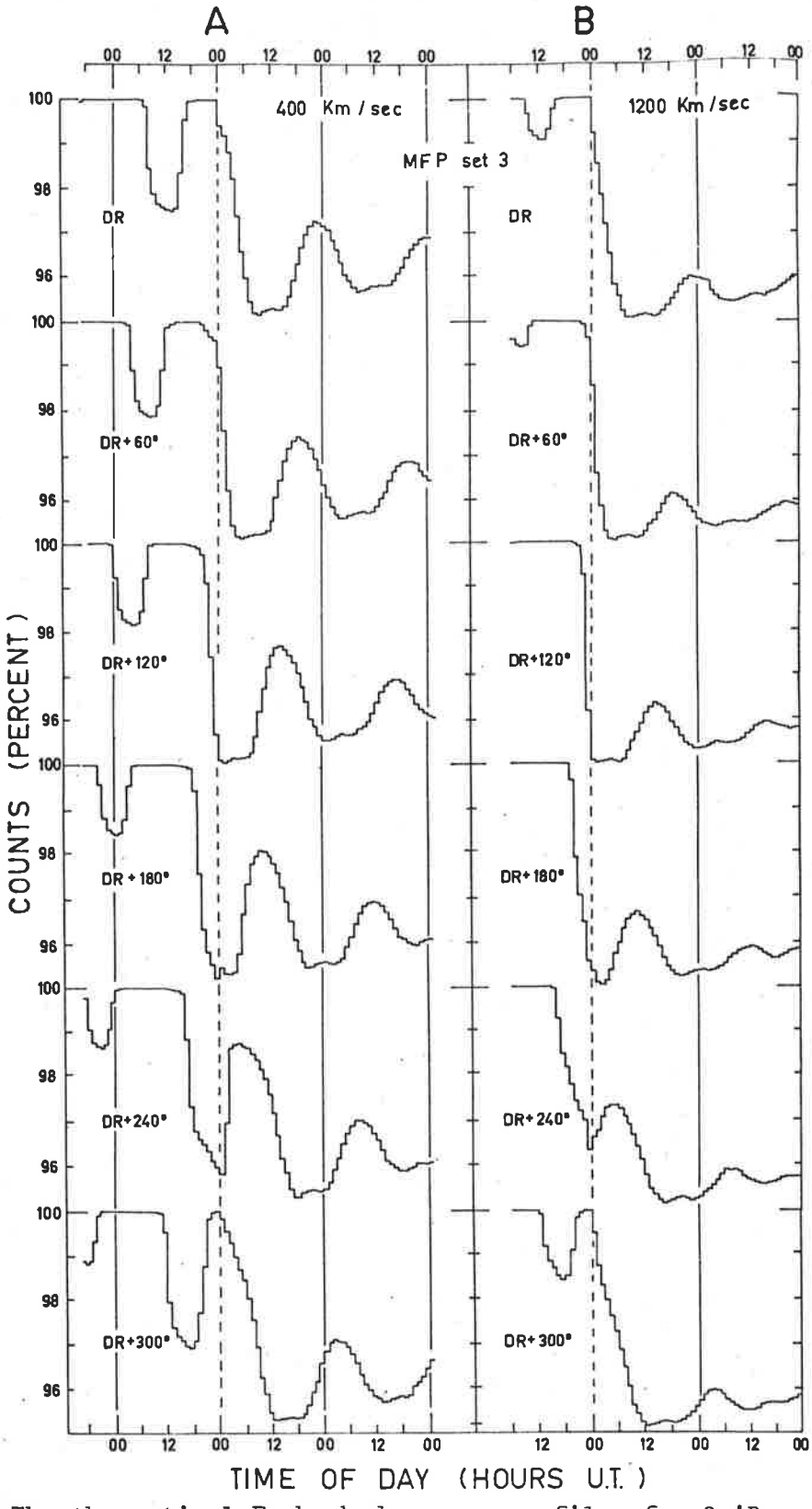

Figure 6.7 The theoretical Forbush decrease profiles for 6 'Deep Rivers' which are equispaced in longitude for a shock which arrives at 0000 UT with A. V_R = 400 km/sec, B. V_R = 1200 km/sec. for MFP set 3 (λ indept. of r).

Figure 6.7 shows that in general the preliminary decreases and the increases which occur after the passage of the shock (marked with a dashed line) are larger than for the corresponding MFP set 1 profiles in Figure 6.6. This result suggests that when the scattering mean free paths are longer the remote sensing capability of a low cut-off rigidity station is enhanced. This is indeed the case as can be seen from a comparison of Figures 5.6 and 5.10.

6.4.3 The Profiles at Different Geographic Latitudes

We now consider the case of detectors at different geographic latitudes. We consider an equatorial station with high cut-off rigidity (Chacaltaya), a mid-latitude station with low cut-off rigidity which views equatorially (Deep River), and two high latitude (low cut-off rigidity) stations, one which views $\sim 40^{\circ}$ from the ecliptic (Inuvik) and one which views $\sim 83^{\circ}$ from the ecliptic (Alert).

To show latitude effects only, two of these stations have been displaced in geographic longitude until their cones of acceptance are aligned in longitude. The four stations used are Alert, Inuvik + 120°, Deep River + 30°, and Chacaltaya. The amplitudes of these longitude shifts were judged using Figure 5.5. Figure 6.8 shows the Forbush decrease profiles at these stations for a 10% depletion region (at 6·5GV), with A. V_R = 400 km/sec, and B. V_R = 1200 km/sec, which arrives at 00 (=24) UT.

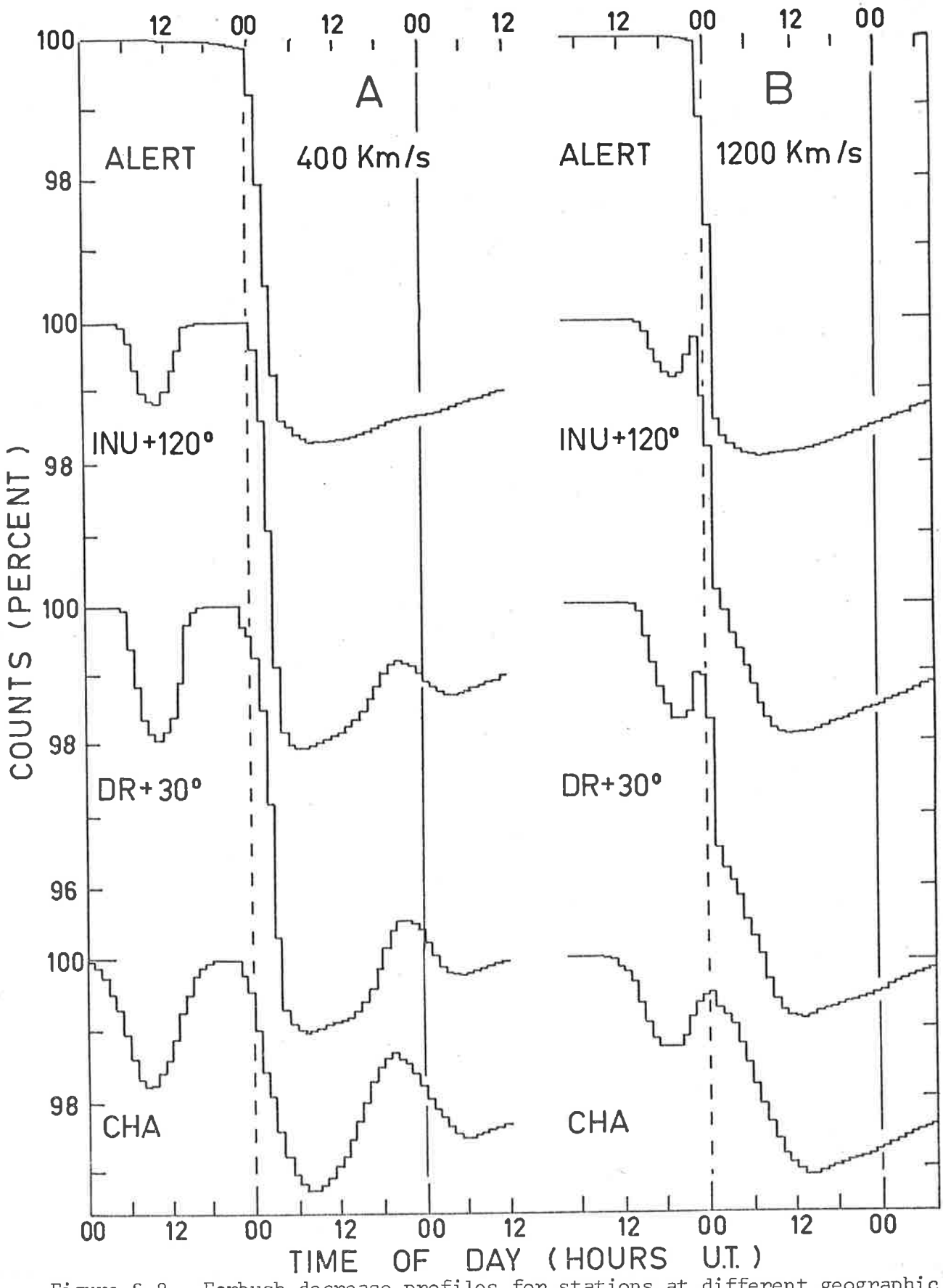

Figure 6.8 Forbush decrease profiles for stations at different geographic latitudes, but with the same longitude.

It can be seen that the remote sensing ability increases from Alert to Inuvik to Deep River, as expected from Figures 5.9, 5.8 and 5.6. Chacaltaya shows even more pronounced remote sensing than Deep River (see Figure 5.10). In addition the broad cone of acceptance of Chacaltaya results in smoother features in its Forbush decrease profile, and the depth of the decrease (3%) is smaller than the 6% of the low cut-off rigidity stations (due to the $P^{-\frac{1}{2}}$ rigidity dependence of the gradients). All of these features are observed in practice.

Figure 6.9 shows how the Forbush decrease profile at Chacaltaya varies for different shock arrival times, or equivalently, how 6 stations identical to Chacaltaya and equispaced in longitude respond to a 10% (at 6·5GV) depletion region moving at A. V_R = 400 km/sec, B. V_R = 1200 km/sec.

6.4.4 Simulation of an Observed Event

This technique is now used to produce a close fit to the Forbush decrease profile observed over July 7, 8 and 9,1966. The shock associated with this event was very oblique when it arrived at Earth (see P.131). Hence it is reasonable to use very low values of V_R, the effective radial approach velocity of the shock.

Figure 6.10 shows the observed Forbush decrease at Deep River (heavy lines) and a close fit calculated using the origin-of-scatter technique (light lines). The parameters used were

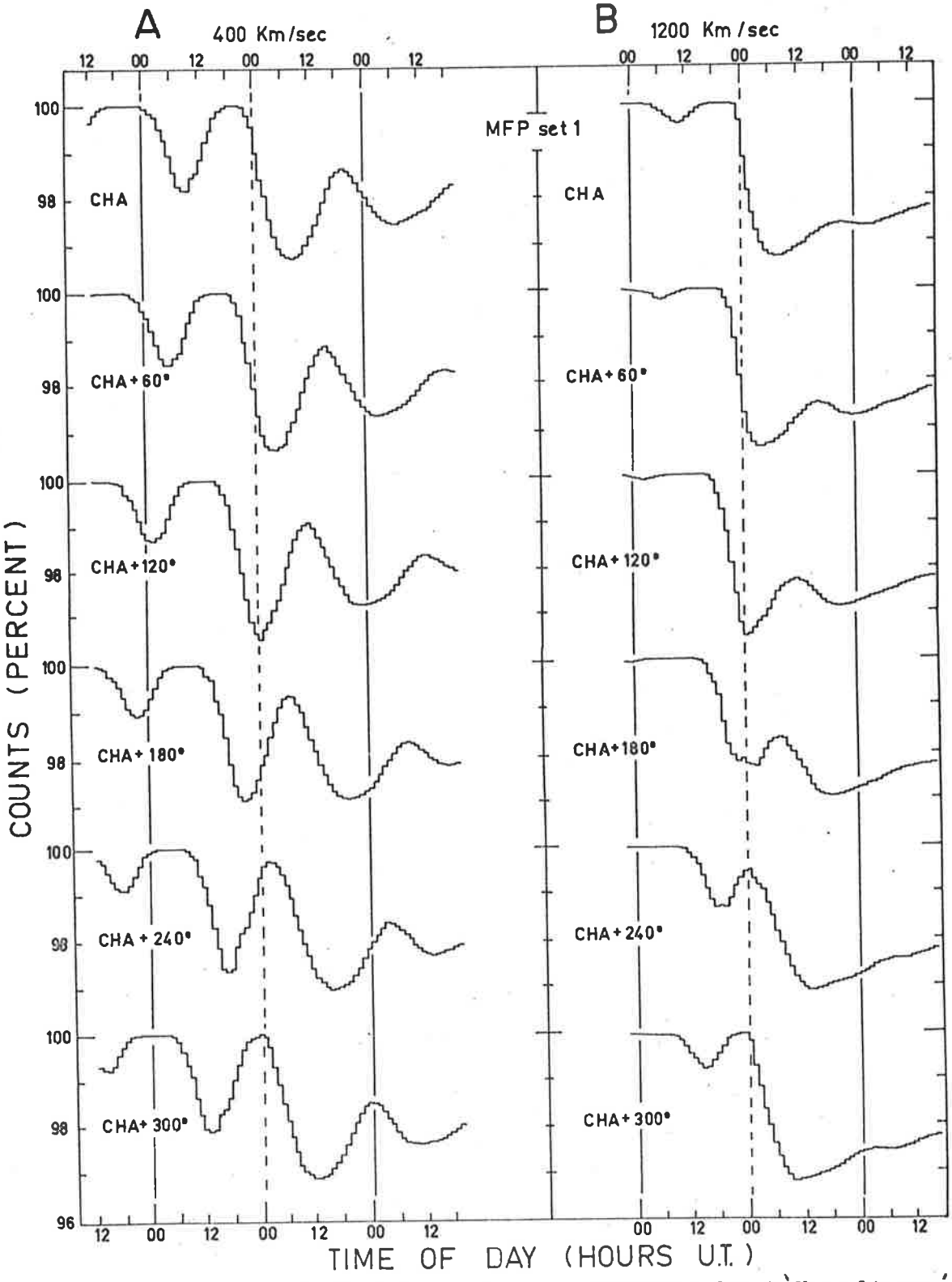

Figure 6.9 The theoretical Forbush decrease profiles for 6 'Chacaltayas' which are equispaced in longitude, for a shock which arrives at 0000 UT with A. V_R = 400 km/sec., B. V_R = 1200 km/sec.

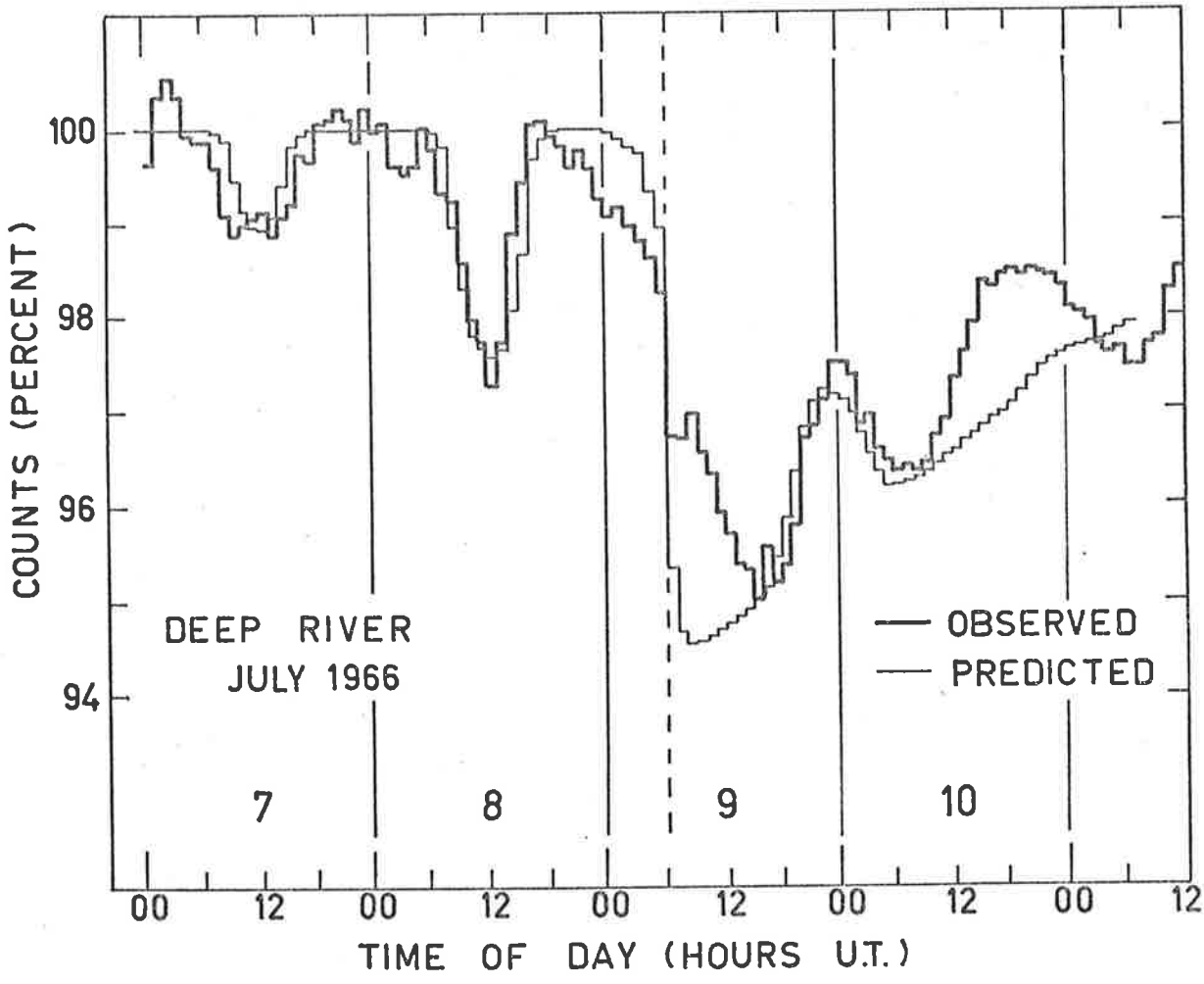

Figure 6.10 The Forbush decrease observed at Deep River on July 9, 1966, and the profile predicted for Deep River when V_R = 260 km/sec; depletion depth = 9% at 6·5 GV ($\sim P^{-\frac{1}{2}}$) at 1 AU, which decreases linearly towards 0% at 0·1% per hour; shock arrival time = 0600 UT; scattering mean free paths = MFP set 1 (λ independent of r).

mean free path	:	MFP set 1, independent of r
effective V_R	:	260 km/sec
number density depletion	:	9% at 6·5GV ($\propto P^{-\frac{1}{2}}$) and recovering at 0·1% per hour.
shock arrival time	:	0600 UT

The discrepancies just before and just after 0600 UT may be the result of the extreme obliquity of this shock. The origin-of-scatter theory assumes that a detector senses in the ecliptic only. However cosmic ray orbits move above and below the ecliptic in their spiralling motion. Hence an oblique shock can be sensed at a heliocentric radius r along the local field line where the shock has not yet reached the ecliptic. In a similar way although the shock may have just passed the Earth, this 'latitudinal sensing' will enable the shock to be reached by orbits with guiding centers at 1AU. While these off-ecliptic effects are no doubt significant, we judge them second order compared to the first order effects discussed earlier, and we will not discuss them further at this time.

6.4.5 Increases Prior to Forbush Decreases

Some Forbush decrease events show a distinct increase in countrate just before the arrival of the shock, e.g. the Jan 26-27, 1968 event (Lockwood and Webber, 1969). It has been suggested that this effect is the result of a number density build up just in front

of the shock, caused by the sweeping of cosmic rays by the shock (e.g. Palmeira et al, 1969; Dorman et al, 1967). Isolated examples of this effect may be the result of a decrease in the threshold rigidity for stations with cut-off rigidity near 4GV (Wolfson and Nobles, 1970).

We now use the origin-of-scatter technique to investigate the result of a number density build up in front of the shock. Figure 6.11A shows the radial variation in number density used for this study. The build up is 0·8 x depletion depth, and it falls to e^{-1} at $^{1}/_{25}$ AU from the shock. The Forbush decrease profiles at Deep River equivalent stations separated by 60° in longitude are shown in Figure 6.11B for a shock with V_R = 400 km/sec which arrives at Earth at 2000 UT. These profiles show a close resemblance to the observed profiles of the January 26-27, 1968 event (see Lockwood and Webber, 1969), although no attempt was made to obtain a best fit to this event.

6.5 The Rigidity Dependence of the Forbush Decrease

The contributions to the total Forbush decrease from each of the five rigidity intervals in table 5.4 are now presented for the Deep River station. Figure 6.12A shows the modulation within each rigidity interval for a 10% depletion region (at 6·5GV) behind a shock which arrives at Earth at 00 UT with V_R = 800 km/sec. Figure 6.12B shows the sum of these variations. These are the results when the depth of the number density step at the shock varies as $\left(\frac{P}{6\cdot5}\right)^{-\frac{1}{2}}$, as is shown by the η = 0·5 curve in Figure 6.12C.

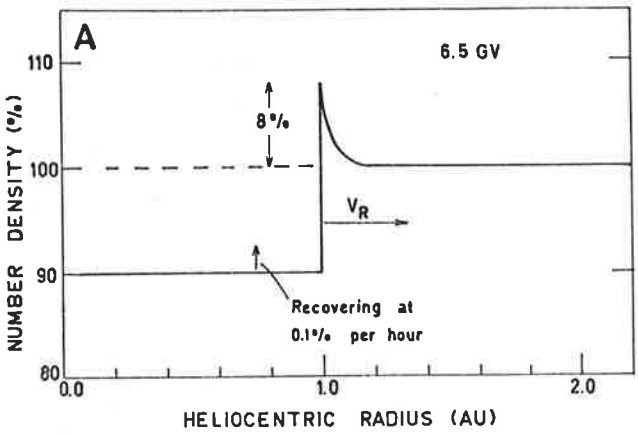

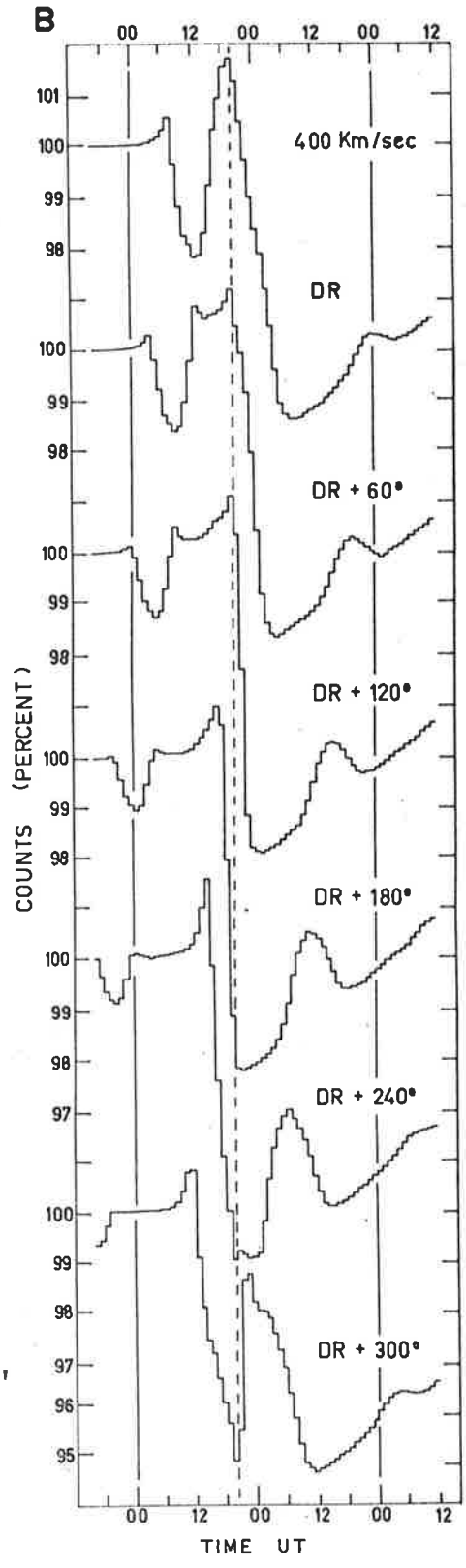

Figure 6.11

A. The number density distribution used to investigate the increases sometimes observed just before Forbush decreases.

B. The theoretical Forbush decrease profiles for 6 equispaced 'Deep Rivers' when the number density in A. arrives at 0000 UT with V_R = 400 km/sec.

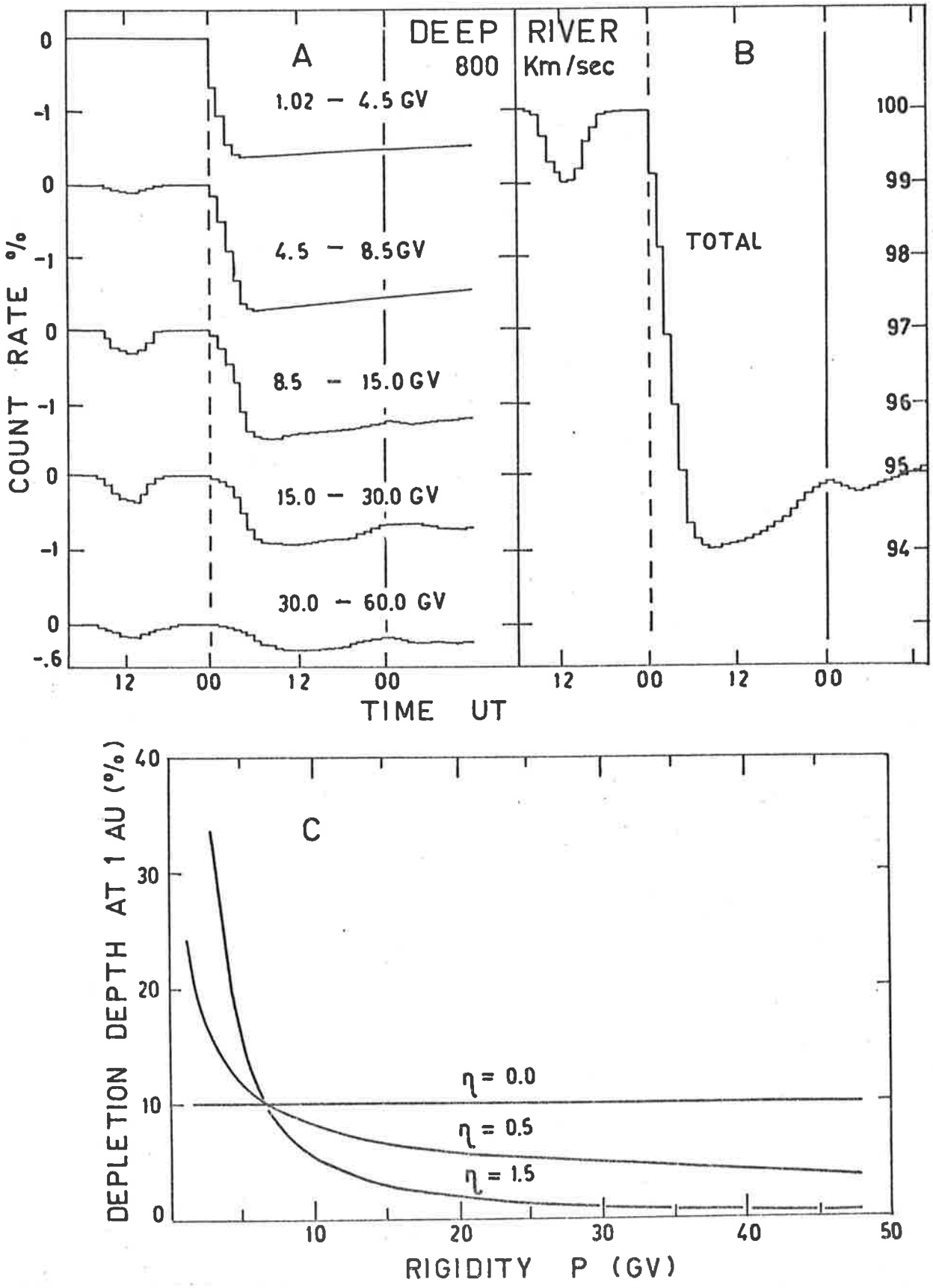

Figure 6.12 A. the theoretical Forbush decreases in the 5 rigidity intervals; B. their total; C. depletion depth vs rigidity for η = 0·0, 0·5 and 1·5.

It can be seen that the relative amplitude of the preliminary decrease and the increase following the shock, increase as we go to higher rigidities. This is expected from Figure 5.16 which indicates that the remote sensing ability of a detector is greatest at high rigidities.

The effect of a different rigidity dependence for the depletion depth behind the shock can be judged from Figure 6.13. This shows the Forbush decrease profiles when the depletion depth varies as $\left(\frac{P}{6{\cdot}5}\right)^{-\eta}$ for $\eta = 0{\cdot}0$ and $\eta = 1{\cdot}5$ (as in Figure 6.12C).

For $\eta = 0{\cdot}0$ the step depth at high rigidities is relatively deeper than for $\eta = 0{\cdot}5$ or $\eta = 1{\cdot}5$. Hence the remote sensing is strongest for $\eta = 0{\cdot}0$ and therefore the preliminary decrease and the post-shock increase are largest for $\eta = 0{\cdot}0$, as is shown in Figure 6.13. Similarly these features are smallest for $\eta = 1{\cdot}5$.

6.6 The Effects of Departures from the Ideal Magnetic Field

The origin-of-scatter coefficients used here were calculated for an interplanetary magnetic field of $5{\cdot}0\gamma$ at 1AU and directed 45° west of the Earth-Sun line ($G = 45^{\circ}$). As was stated in chapter 1, the observed magnetic field varies in strength and direction about these average values. A qualitative discussion is now given on the effects such departures from the ideal magnetic field will have on the origin-of-scatter coefficients $\zeta(r,T)$, and the cosmic ray variations calculated

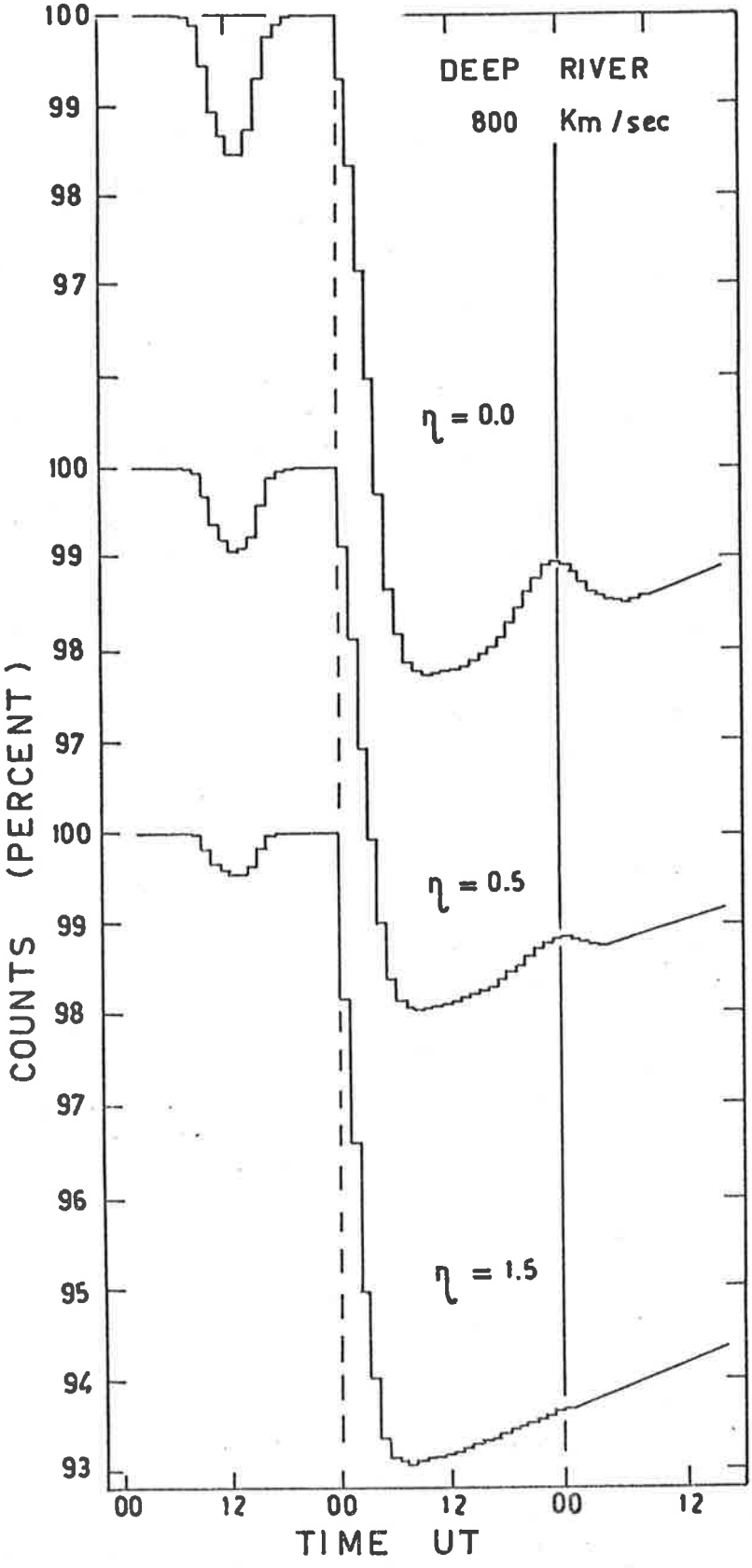

Figure 6.13 The change in the modulation associated with Forbush decreases as we change η.

using them.

An increase in field strength B has the effect of decreasing the gyroradius ρ and increasing the gyrofrequency ω. These effects cancel with the result that the distance travelled along an orbit corresponding to a given guiding center distance is independent of B. Consequently the $\zeta(r,T)$ will be independent of B (for given mean free paths).

A change in solar wind velocity V produces a change in the direction of the magnetic field given by $\tan G = \frac{r\Omega}{V}$. The magnetic field lines which intersect the Earth will still lie in the ecliptic however. An increase in V causes the magnetic field lines to straighten (G decreases), and vice versa. Hence an increase in V means that a (negative) cosmic ray will travel a shorter distance x around its orbit in reaching a given r from Earth (whether $r < 1AU$, or $r > 1AU$). Thus all values of x will be shorter and the values of $\zeta(r,T)$ smaller. However the relative values of $\zeta(r,T)$ for different r will be much the same. Thus the cosmic ray variations in this case will have the same general form but with slightly smaller amplitude, and will be displaced in time corresponding to the angular displacement of the magnetic field. A slower V (and larger G) will produce the reverse effect.

Direct observations of the interplanetary magnetic field indicate that it is often directed away from the ecliptic plane for extended periods. This factor could be expected to have a profound

effect on the remote sensing characteristics of a particular detector. Let us consider the case when the magnetic field at Earth is inclined at 45° to the ecliptic, but with the longitude (135°) of the ideal case.

The Deep River detector which views equatorially will now view with an average pitch angle of $\sim 45^{\circ}$ when its cone of acceptance is most closely aligned with the magnetic field. Hence its remote sensing characteristics will now resemble those of Inuvik (for the ideal magnetic field situation). The Inuvik station which views at about 45° from the equator will now look parallel to the magnetic field, but once a day only; 12 hours later it will look perpendicular to the magnetic field. Hence Inuvik would have enhanced remote sensing characteristics at one time of day only, unlike any detector under normal conditions. The Alert station which essentially looks in a fixed direction (due North) would have an average pitch angle of 45° throughout the day. Thus Alert would have quite good remote sensing ability, either in towards the Sun or away from the Sun (depending whether the field was directed below or above the plane of the ecliptic), and these would remain essentially constant throughout the day.

6.6.1 North-South Anisotropies Associated with Forbush Decreases

A comparison of the Forbush decrease profiles recorded at polar stations which look north and south, often indicates a N-S anisotropy. That is there is a delay in the N and S onset times, and at any one time in the next 1-2 days the decrease at one station is

greater than at the other (e.g. Duggal and Pomerantz, 1970). The discussion above suggests a mechanism which would account for such N-S anisotropies.

If the interplanetary magnetic field is inclined to the ecliptic then one polar station will sense from inside the orbit of Earth, while the other senses from outside the orbit of Earth, and this situation will be essentially invariant with time of day. Hence, depending on the magnetic field inclination, one detector will see the Forbush decrease before, and the other after the shock reaches Earth. That is one detector will observe the ambient flux level while the other observes a reduced flux level due to the region of depleted number density. Hence a N-S anisotropy is detected. This N-S anisotropy will persist even after the shock has passed Earth, because while the detector looking in samples cosmic rays from the depleted regions only, the detector which looks out can still sample cosmic rays from outside the shock, and so will record a higher flux level.

This N-S anisotropy therefore appears because the anisotropy which is normally present in the ecliptic (when the field is in the ecliptic) as discussed on pages 136 and 137, will have a N-S component when the field is inclined to the ecliptic (i.e. the anisotropy is aligned with the interplanetary magnetic field). If the field is inclined to the ecliptic in front of the shock only, then we would only expect to see a N-S anisotropy before the shock reaches Earth,

and vice versa.

It should be noted that even when the interplanetary magnetic field lies in the ecliptic a small N-S gradient will be associated with a Forbush decrease at most times of the year. This is because the axis of rotation of the Earth is inclined at $23{\cdot}5^{\circ}$ to the plane of the ecliptic so that in mid-winter a polar station will have an average pitch angle near $+66{\cdot}5^{\circ}$ (90-23·5), and the detector will sense from regions outside 1AU. In mid summer the average pitch angle will be near $-66{\cdot}5^{\circ}$ and the detector will sense from inside 1AU. Hence a N-S anisotropy can be expected with most Forbush decreases. Indeed its magnitude and duration will indicate the inclination of the large scale interplanetary magnetic field in the vicinity of Earth.

6.7 Conclusions

The application of the origin-of-scatter technique has shown that

(i) The average scattering mean free paths in interplanetary space approximate to those of MFP set 2 with $\lambda \propto r^{1}$.

(ii) The amplitude of the radial gradient associated with the long term average diurnal variation is 6·0% per AU (at 6·5GV when gradient $\sim P^{-1}$) for $\bar{V}$ = 400 km/sec. This estimate assumed the gradient to be linear, and used the result in (i) above.

(iii) A component of the observed semidiurnal variation may be a radial gradient induced effect.

(iv) Short term deviations from the average diurnal variation amplitude and phase will occur if the amplitude of the radial gradient changes or if the rigidity dependence of the gradient amplitude changes.

(v) The minimum of the diurnal variation will occur later if there is a region of strong number density depletion close to the Sun ($\sim$ 0·4AU).

(vi) For a given gradient, an increase in the scattering mean free paths in interplanetary space results in an increase in the average daily flux level.

(vii) The Forbush decrease profiles observed on Earth are strongly dependent on the effective radial approach velocity of the shock.

(viii) Pronounced preliminary decreases occur when V_R is slow ($\sim$ 400 km/sec).

(ix) The general features of the world-wide variation in the Forbush decrease profiles for a given event can be accounted for in terms of a simple step decrease in number density which is moving outwards from the Sun. The complexity of the profiles occurs because the ability of any one station to sense the shock (before or after it reaches Earth) changes strongly with time of day, and the sensing abilities of different stations are out of phase according to the difference in their asymptotic

longitudes of viewing.

(x) Increases which occur just prior to the onset of the main phase decrease of a Forbush decrease can be explained by a region of increased number density just in front of the shock.

(xi) N-S anisotropies will be associated with Forbush decreases if the large scale interplanetary magnetic field in the vicinity of Earth is inclined to the Earth's equatorial plane.

PART B

CHAPTER 7

INSTRUMENTATION FOR TWO EXPERIMENTS TO OBSERVE CELESTIAL X-RAYS

7.1 Introduction

This part of the thesis discusses the design, preparation and results of two rocket-borne X-Ray astronomy experiments. These two experiments were the third and fourth in a continuing program conducted by the Universities of Adelaide and Tasmania (UAT). To be consistent with other UAT publications these flights are henceforth referred to as flight III and flight IV. The detectors were proportional counters sensitive to X-Rays in the 2-10 keV energy range. Both experiments were launched from the Woomera rocket range in South Australia.

The flight III experiment with a total sensitive area of 150 cm^2 was launched on December 1, 1967 on Skylark SL422A. This flight, although only partially successful, yielded evidence for a new X-Ray source at high galactic latitude in the constellation Cetus (Barnden and Francey, 1969), and an upper limit to the flux from the variable Cen XR-2. The analysis methods and complete results of flight III are given in Chapter 8.

Flight IV carried an experiment (total area 2100 cm^2) as sensitive as any flown before its launch on January 21, 1969 on

PLATE 1A

The Flight IV Launch

PLATE 1B

The Break-up of the Flight IV Vehicle

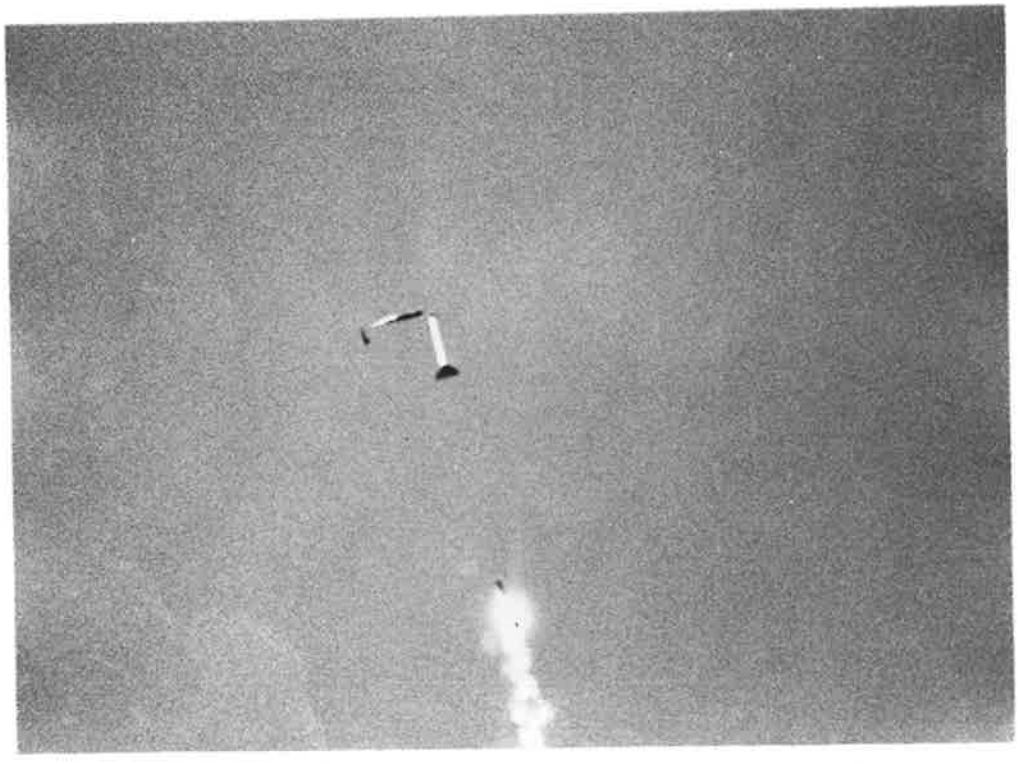

Skylark SL781. However, due to a vehicle malfunction 3 seconds after launch the rocket broke up (see Plate 1) and the experiment was destroyed (Plate 2B).

At the time of the flight IV launch, some 6 years after the discovery of the first cosmic X-Ray source, there was still an urgent need for a complete survey of the Southern X-Ray sky. The results of X-Ray Astronomy at that time are described in the reviews of Giacconi and Gursky (1965), Hayakawa et al (1966), Giacconi (1967), Gould (1967) and Morrison (1967). Dolan (1970) gives a recent catalogue of confirmed and probable X-Ray sources. Reviews of contemporary X-Ray Astronomy instrumentation have been given by Boyd (1965) and Giacconi et al (1966).

In this chapter an account is given of the instrumentation used on UAT flights III and IV, together with a discussion of the factors influencing their design and of the procedures used in their preparation. Section 7·2 gives a brief general description of the Skylark vehicle. Section 7.3 discusses the instrumental parameters which were important in the design of these rocket borne experiments and indicates how these were varied from detector to detector to achieve different aims. The flight III design and preparation is given in section 7.4. Sections 7.5, 7.6 and 7.7 deal with the large flight IV experiment. Section 7.5 gives an overall description of the aims and instrumentation, section 7.6 goes into some detail of the new

PLATE 2A

The Flight III vehicle on recovery. The UAT experiment is attached to the Nose-Cone in the foreground.

PLATE 2B

The Flight IV UAT experiment on recovery

SERIAL 675
TRIAL BS145
MISSILE SL422A
DATE 1 12 67

SERIAL 009
TRIAL BS158
MISLE SL781
DATE 21 1 69

on-board data analysis system, and section 7.7 describes the flight preparation of the integral experiment.

7.2 The Skylark Vehicle

Skylark is an unguided upper atmosphere research rocket with solid propellant motors capable of carrying a headweight of some 200 kg to 200 km or higher for a flight time above 80 km of about 350 seconds. The Skylark head consists of several cylindrical sections called "rings", stacked one above the other. Each ring is a magnesium alloy casting with an outside diameter of 43·8 cm and an average wall thickness of 0·5 cm. In addition to the rings housing the experiments, the head contains rings which carry power supplies, the telemetry unit(s), aspect sensors, a program motor for timing in-flight events, and various other performance monitors not of direct interest to the experimenter. The aspect sensors consist of three orthogonal fluxgate magnetometers, three orthogonal accelerometers, two orthogonal rate gyroscopes, and four pairs of crossed sunslits. The manner in which the flight III attitude solution was derived from the outputs of these devices is described in section 8.2.

The Skylark telemetry unit transmits information to the ground via an FM/AM system with time division multiplexing which gives 24 primary data channels. The first channel is used to carry a synchronisation pulse which signifies the start of each telemetry frame. Multiplexing is achieved by a mechanical commutator with 24

inputs, each of which is sampled every $^{1}/_{80}$ second. The telemetry sender (on the single output of the commutator) accepts analogue voltages between - 3·0 and + 3·0 volts. The stability of the overall system enables resolution on the final records corresponding to about 120 millivolts of input voltage, so that each sample can carry a five bit binary word (after conversion in a D-A converter to one of 32 analogue voltage levels).

Experiments can be situated either in a ring or in the space beneath an ejectable nosecone. Accelerations of 10g and 1g in the longitudinal and lateral directions respectively, may be experienced during ascent. The standard instrumentation ring and most experiment rings are sealed so that a pressure of 1 atmosphere is maintained inside the round throughout the flight. Split nose cones are not sealed, but are vented to allow a gradual decrease in pressure during ascent.

Flights III and IV were flown on "engineering vehicles" with reconditioned components, to test new flight systems, motors etc. This has implications for the overall reliability.

7.3 Experiment Design Considerations

A simplified analytical expression for the sensitivity of an X-ray astronomy experiment is now derived to isolate the factors which must influence the design of a particular experiment. The criterion adopted here is that it is desirable to maximise the statistical

significance of the observations made of an X-ray source. The "sensitivity" is therefore expressed in terms of the number of standard deviations n above background that the flux from a given X-ray source produces in the countrate records.

Consider a flux of S photons cm^{-2} sec^{-1} above the atmosphere from a celestial X-ray source. We only consider X-rays in the energy range (1-10 keV) where conventional detectors (gas counters) have an appreciable response. There are another two sources of radiation which will contribute to the countrate of this detector. Firstly there is a diffuse X-ray 'background' flux, which is assumed here to be isotropic, of B_x photons sec^{-1} cm^{-2} $ster^{-1}$, and secondly a charged particle or cosmic ray flux represented here by B_c counts sec^{-1}.

Consider an experiment which looks directly at the source for T seconds, and then looks in another direction long enough to establish the background level (we ignore statistical errors in the measurement of the background). The number of counts recorded by a detector of area A cm^2 with angular response Ω, and X-ray detection efficiency ε, over the time T of source observation, is

$$C = SA\varepsilon T + B_x A\varepsilon T . \Omega + B_c T$$

One standard deviation for this number is

$$\sigma = \sqrt{C} = \sqrt{T} . \sqrt{(S + B_x\Omega)A\varepsilon + B_c}$$

From the independent observation of the background only, the counts recorded during time T due to the source can be deduced to be SAεT (above background). Therefore the statistical precision of an X-ray source measurement is

$$n = \frac{SA\varepsilon T}{\sigma} = \frac{SA\varepsilon\sqrt{T}}{\sqrt{(S + B_x\Omega)A\varepsilon + B_c}} \qquad (7.1)$$

This is unrealistic however, because the sophisticated pointing systems necessary to look directly at a source for an extended period were not available to UAT.

Consequently our experiments were designed for spinning rockets. These are either "spin-stabilized" (spin period $\lesssim$ 0·5 secs) so that their spin axis remains essentially fixed in inertial space, or unstabilized (spin period $\sim$ 10s) so that their spin axis describes a precession cone about a direction fixed in space. Both flights III and IV were carried on unstabilized rockets.

Consider a spin stabilized experiment with the detectors viewing sideways (perpendicular to the spin axis) so that they scan around the sky as the rocket spins. In this case the source (taken to be in the plane normal to spin axis) is only observed for that fraction of the useful flight time T_f corresponding to the fraction of each spin for which the source is within the detector's angular response. For a detector whose angular response is θ_1 in rocket

azimuth and θ_2 in rocket declination (see Figure 7.1a) the source will be in view for $T_s = \frac{\theta_1}{2\pi} \cdot T_f$ seconds. However for most of time T the detector does not look directly at the source, but at any instant the source flux which reaches the detector window is given by $R(\theta).S$ where $R(\theta)$ is the angular response of the detector ($0 \leq R(\theta) \leq 1$) when the source is θ off axis. The angular response is normally triangular (see Figure 7.1b) so that the average flux reaching the detector window in time T_s is $S/2$. Using the approximation $\Omega = \theta_1.\theta_2$ the statistical precision of the source measurement is

$$n = \frac{SA\varepsilon\sqrt{\frac{\theta_1}{2\pi} \cdot T_f}}{2\sqrt{(\frac{S}{2} + B_x\theta_1\theta_2)A\varepsilon + B_c}} \qquad (7.2)$$

When the rocket also precesses as in unstabilized motion the source observation time may be further restricted. Consider the rocket spin axis to define a precession cone of half angle β as in Figure 7.1c. In the case of the rocket describing one complete cone in T_f the detector axis will scan a band of sky 2β wide and the fraction of time that a source within this band is observed can be approximated by $\frac{\theta_2}{2\beta}$. Allowing for the change in angular response over the observing time, the average flux which reaches the detector in this time is reduced by a further factor of two to $S/4$ so that the statistical precision of the source measurement will be

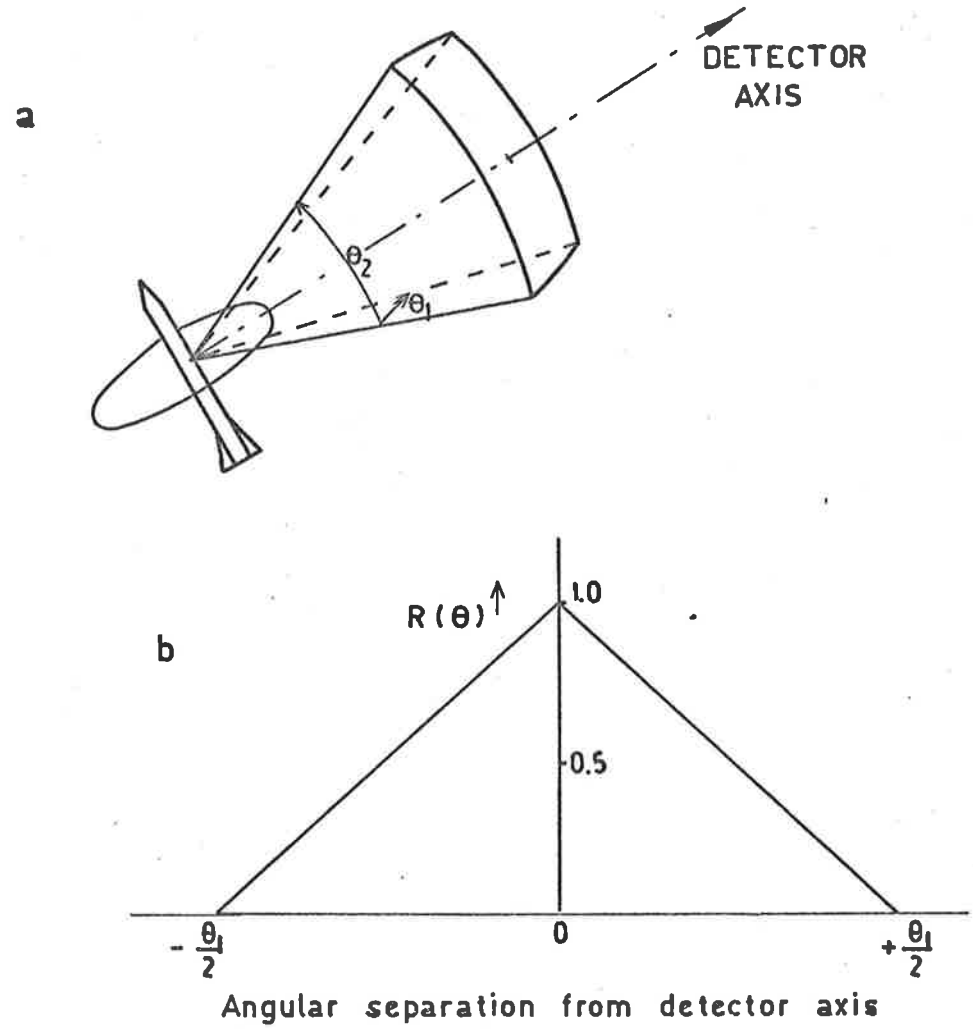

Figure 7.1 a. The dimensions of the angular response. b. Angular response R(θ) vs θ for a slot collimator. c. The precession of the +0X axis and the resulting change in the detector viewing direction.

$$n = \frac{SA\varepsilon \sqrt{\frac{\theta_1\theta_2 T_f}{2\pi.2\beta}}}{4\sqrt{(\frac{S}{4} + B_x\theta_1\theta_2)A\varepsilon + B_c}} \qquad (7.3)$$

There is of course no guarantee that the rocket will complete one precession cone. For a partially completed cone the source could be scanned many times at either high or low angular response, or not at all. The average flux reaching the window during the observation period would be $> \frac{S}{4}$ for observations at high angular response (or $< \frac{S}{4}$ for low angular response), resulting in values of n greater (or less) than that given by equation 7.3.

It can be seen from equations 7.1, 7.2 and 7.3 that four factors influence n in the same way in each case. These are area A, efficiency of detecting X-rays ε, flight duration T_f and charged particle background B_c (S and B_x are constants here). It is clearly desirable to maximise A, ε and T_f, and to minimise B_c. Indeed $n \sim \sqrt{T_f}$ and, when B_c is small, $n \propto \sqrt{A\varepsilon}$.

A casual examination of these expressions for n may suggest that as we increase A (and ε), B_c becomes insignificant and may be ignored. This is not so however: a single term has been used to represent the charged particle countrate, partly to keep the expressions simple and partly because the exact form of B_c is not well known. In fact B_c has a dependence on the incident flux of charged particles and on a geometric factor for the detector which Fisher and Meyerott (1966)

suggest is proportional to the area of the walls surrounding the counter gas (rather than the detector volume or average cross-sectional area of the detector). This indicates that a major component of the charged particle contamination arises from the interaction of high energy primaries with the detector walls. Any increase in window area or counter depth (increases ε) will inevitably increase B_c, so that the charged particle background will also increase as A is increased. Hence the experiment sensitivity (n) is greatly improved if the charged particle countrate is reduced.

A large fraction of the charged particle background can be removed by discriminating between charged particle and X-ray photon events in the detector. These events differ because charged particles lose their energy along the whole length of their path through the gas, whereas photons dissipate their energy within a localised volume of the stopping gas. There are two methods of rejecting charged particle events.

(1) The X-ray sensing counters are surrounded with 'guard' counters, and events which occur in coincidence (within $\lesssim$ 1 microseconds) in both counters are rejected.

(2) A pulse shape discriminator circuit rejects pulses with slow rise times. These are produced by charged particles because their ionization is deposited over a wider range of distances from the counter anode.

Thus for each rocket motion it is desirable to minimise B_c and maximise A, ϵ and T_f. The situation with regard to the choice of θ_1 and θ_2 is not so straightforward however.

The experiments under consideration here were carried on unstabilized vehicles. The sensitivity for this type of motion is expressed in equation 7.3. It will be noticed that θ_1 and θ_2 occur in both the numerator and denominator ($\Omega \sim \theta_1\theta_2$), so that when S and B_c are small, n is almost independent of θ_1 and θ_2. Hence the choice of θ_1 and θ_2 are more strongly influenced by experimental requirements different from the need to maximise n. Equation 7.3 is now considered together with these other flight requirements.

The nature of an unstablized motion is such that while there is no guarantee that a particular source will be scanned, it is also possible that the whole sky may be scanned in the one flight. The situation with UAT flights III and IV was that there were areas of sky which had not been observed before at all, and areas which had only been observed with low sensitivity. The requirements of these early survey experiments were therefore

(1) maximum sky coverage

(2) the ability to derive a reliable position for the sources observed.

(3) statistically reliable observations (maximum n) for the derivation of the source strength and spectrum.

Hence although requirement (3) indicates the desirability of maximising both θ_1 and θ_2 (see equation 7.3), requirements (1) and (2) call for a small θ_1 and a large θ_2. Since the spin period is considerably less than the precession period for an unstabilized round, decreasing θ_1 does not decrease the area of sky scanned (for a given θ_2), but it does give considerable directional sensitivity. Moreover it reduces the probability of observing two sources at once and enhances the probability of observing empty regions of space long enough to establish the background countrate. This requirement for small θ_1 and large θ_2 is achieved with the so-called slat collimator. This is the collimator configuration which yields the best compromise between the statistical reliability (n) and the directional resolution of a source observation, for a single detector.

If more than one detector is available on a given flight there are advantages in using other collimator configurations. A second detector is normally given a collimator with small θ_1 and small θ_2. Observations with this detector enable a much more accurate source position to be found. This collimator type allows measurements with both high countrate sensitivity (n), and high directional accuracy, to be made in a narrow band of sky in the situation when the coning angle is small or when only a small fraction of the precession cone is completed throughout the flight (there is a high scan density over one particular region).

Therefore in UAT flights III and IV two basic collimator types were used, one with small θ_1 and large θ_2 (typically $\theta_1 = 6^\circ$ and $\theta_2 = 80^\circ$, ie 3° x 40° FWHM) and the other with small θ_1 and small θ_2 ($\theta_1 = \theta_2 = 9^\circ$, ie $4{\cdot}5^\circ$ x $4{\cdot}5^\circ$ FWHM). FWHM is the full width of the angular response at half maximum response, that is $\frac{\theta_1}{2}$ (or $\frac{\theta_2}{2}$) in Figure 7.1b. These experiments also carried a pair of detectors with crossed collimators (see Plate 3B) to assist in determining source positions.

7.4 The Flight III Experiment

The flight III experiment (see Plate 3A) was given ancillary status on the recovered round SL422A. This was an engineering round designed to prove a parachute recovery system and test a rocket spin-up system to reduce impact dispersion. UAT were allotted a standard base ring which has three apertures each of about 100 cm^2 area. As with earlier UAT flights there were no ejectable covers available for these apertures, so the detector windows were separated from the outside environment during ascent by the collimators alone. Because only 6 months were available to prepare the experiment it was decided to use existing electronic hardware as used on flights I and II (Harries, 1968), and also two surplus 11·7 cm^2 area LND* counters of the type used on these earlier two flights. Both of these counters

---

* Constructed by LND Inc., Oceanside, Long Island, N.Y. to specifications supplied by J.R. Harries for UAT flights I and II.

PLATE 3A

The UAT Flight III Experiment

PLATE 3B

The Flight III Detector System C

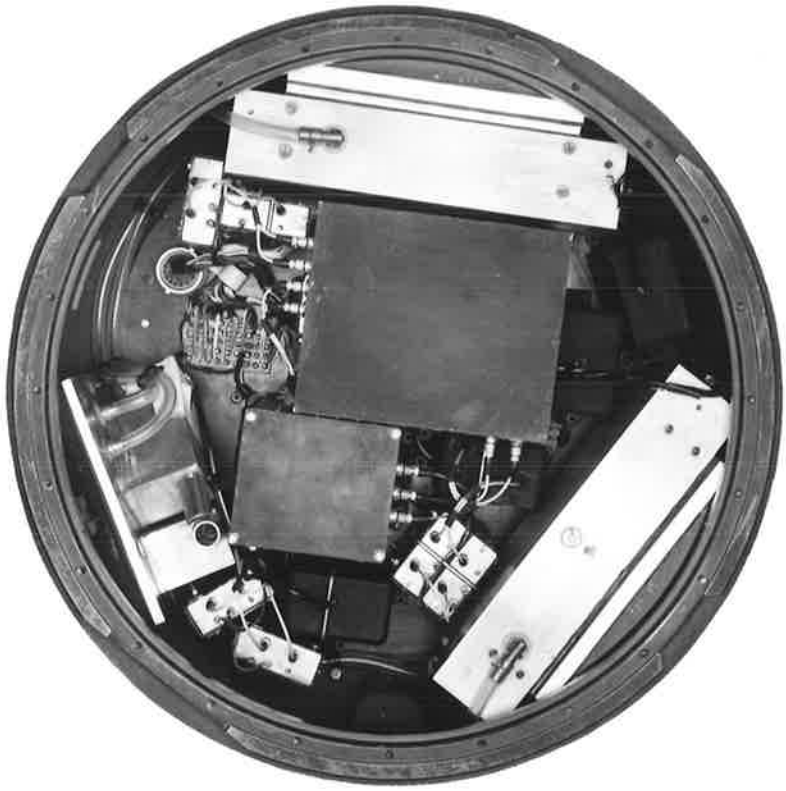

(shown in Plate 3B and Figure 7.2a) were mounted to view through one of the apertures as system C. The counters (A and B) for the other two apertures were newly developed. Mr. Francey was responsible for the basic mechanical design of these counters (Francey, 1970) while the testing of the counters, their integration with the electronics, and the experiment calibration was a joint project.

Counters A and B were fabricated from 10 cm wide extended aluminium channel, which formed the side walls and back, with two aluminium plates araldited in place for the ends (see Figure 7.2b). These were called '4-series' counters. Figure 7.2b shows how the window was pulled down onto a rubber gasket via bolts through a plate aluminium collar, which in turn was mounted to the side of the base ring (Plate 3A). Glazed ceramic insulators araldited into the end walls supported tungsten anodes. Both 4-series counters were divided in cross-section, using sheet aluminium partitions into four chambers each with its own anode. The two larger chambers directly beneath the window were used to monitor the X-ray flux while the rear two chambers served as guard counters to discriminate against charged particles. The end compartments (outside the end walls) of the counters housed EHT filters for each anode, and the load resistors and coupling capacitors for the main and guard anodes.

Detector A had a 0·005 cm (23 mgm cm^{-2}) beryllium window of 44 cm^2 area. An aluminium slat collimator defined a field of view

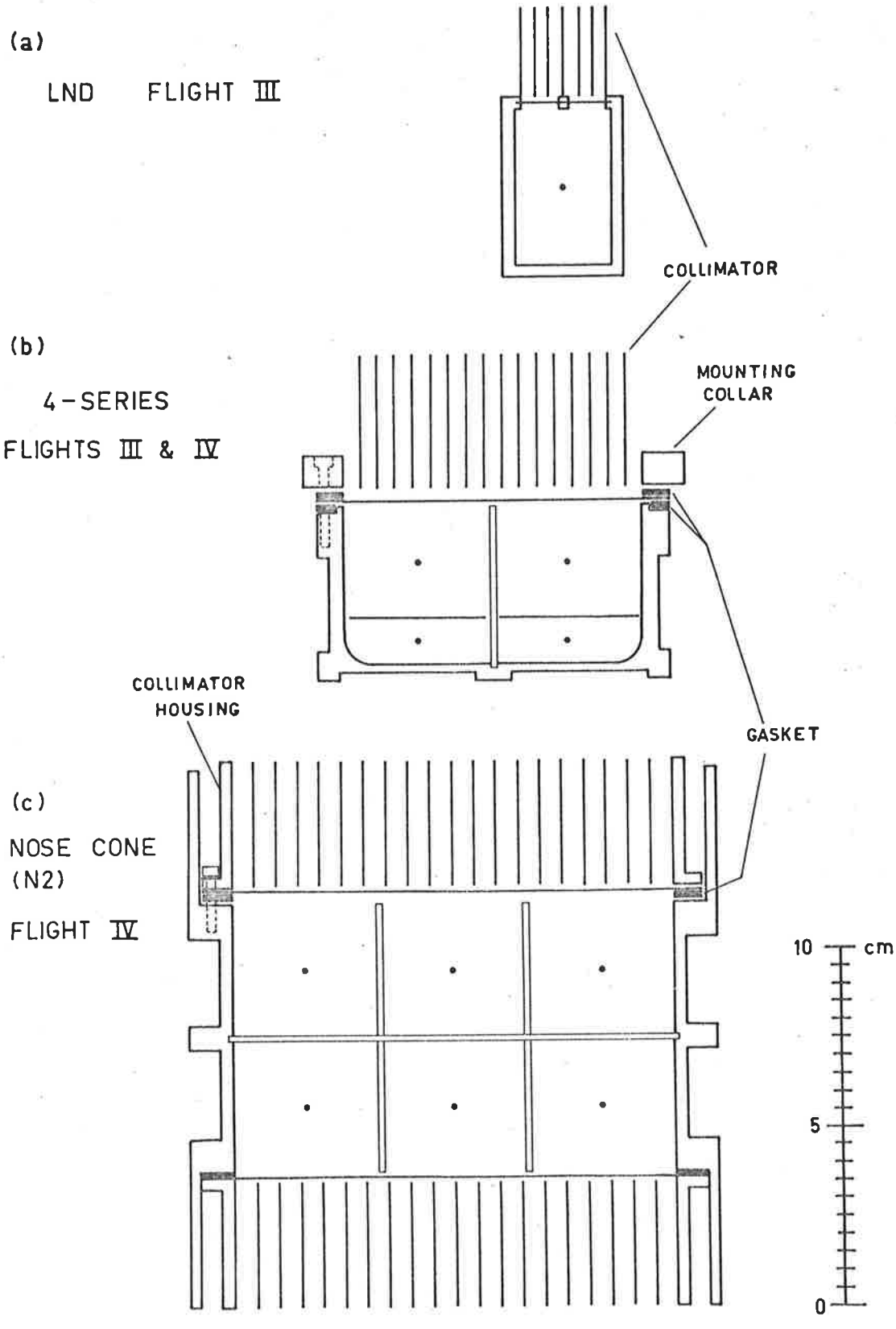

Figure 7.2 A cross-sectional view of the 3 types of proportional counter used on flights III and IV.

of 4° x 37° FWHM ($\theta_1 = 8^{\circ}$, $\theta_2 = 74^{\circ}$). Detector B had a 0·0013 cm (1·77 mgm cm^{-2}) mylar window of 87 cm^2 area with an aluminium 'honeycomb' collimator which defined a hexagonal field of view of $4{\cdot}5^{\circ}$ FWHM ($\theta_1 = \theta_2 = 9^{\circ}$). Laboratory tests indicated that this honeycomb (3·75 cm deep with cell width $\sim$ 3 mm) could provide sufficient insulation from the heat and turbulence generated at the skin of the rocket during ascent, and also contain the window against the 1 atmosphere pressure differential at altitude. Both counters A and B were filled with P10 (90% Argon, 10% Methane) and the depth of the main chambers was 2·9 cm (4·8 mg cm^{-2}). The X-ray detection efficiency ε, for counters A and B is shown in Figure 7.3a and b. These curves were derived using

$$\varepsilon = \exp(-\mu_w x_w)\left[1-\exp(-\mu_g x_g)\right] \qquad (7.4)$$

where μ_w and μ_g are the mass absorption coefficients for the window and the gas, and x_w and x_g are the thicknesses of the window and gas respectively (in gm cm^{-2}).

The gains of counters A and B changed significantly over several hours, so to maintain the gain near the required level it was necessary to periodically flush them with pure P10 gas. This was achieved through shrader valves in aperture C which were connected via nylex tubing to an inlet and outlet on the counters (see Plate 3A and B). The two flushing systems were independent so that a leak

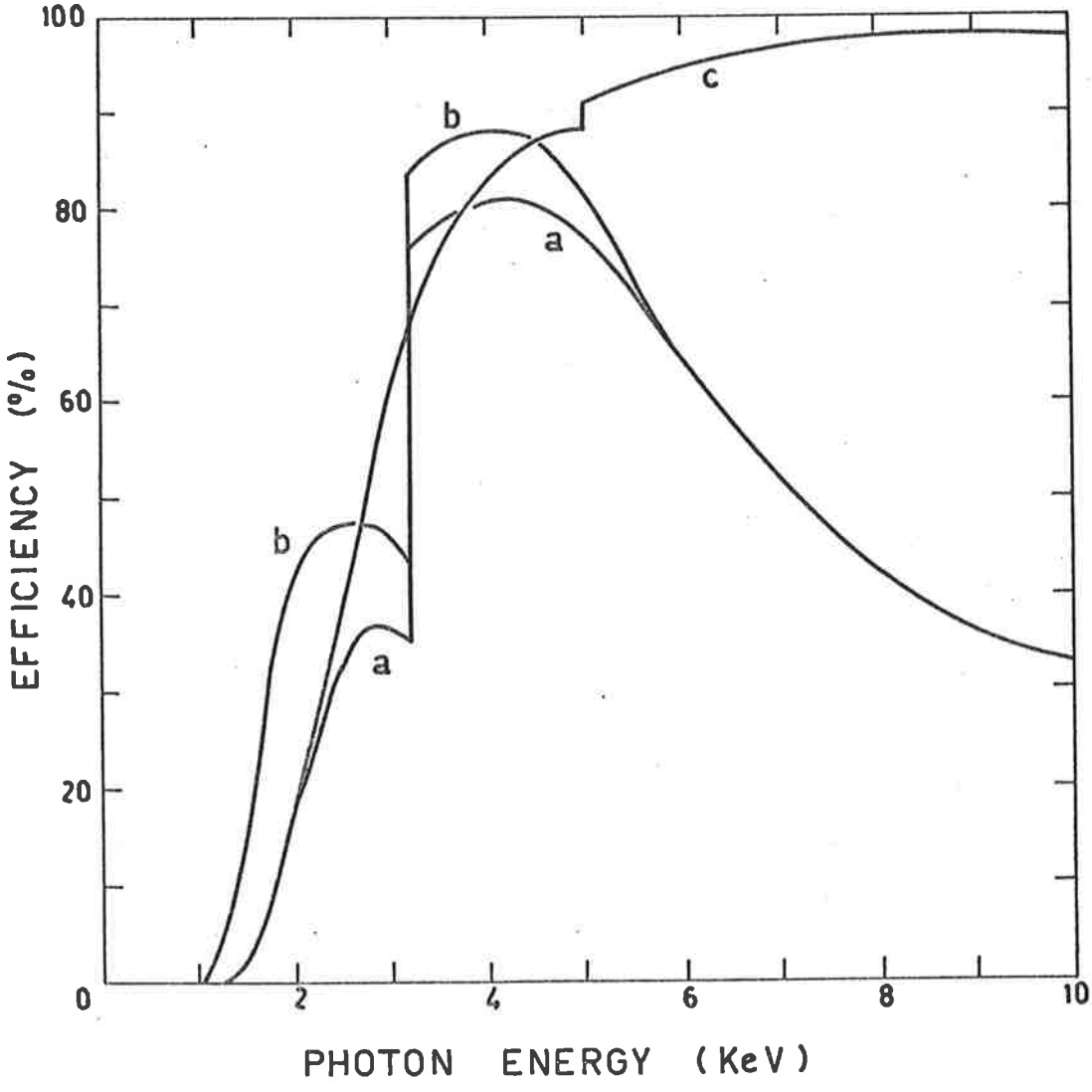

Figure 7.3 The efficiency of the 3 Flight III Detector Systems

a. System A: 23 mg cm^{-2} beryllium window + 4·8 mg cm^{-2} P10 gas.
b. System B: 1·77 mg cm^{-2} mylar window + 4·8 mg cm^{-2} P10 gas.
c. System C: 23 mg cm^{-2} beryllium window + 29 gm cm^{-2} xenon (90%) - methane (10%) gas.

in one counter would not effect the performance of the other.

The two counters of system C each had 0·005 cm (23mg cm^{-2}) beryllium windows of 11·7 cm^2 area and were filled with 29 mg cm^{-2} of 90% Xenon -10% Methane. These counters had no guard chambers. Aluminium slat collimators restricted their fields of view to 4° x 35° FWHM ($\theta_1 = 8^{\circ}$, $\theta_2 = 70^{\circ}$), and these two collimators were inclined at 45° to each other as shown in Plate 3B to aid in the determination of source positions. The efficiency ϵ of system C is shown in Figure 7.3c.

Four channel pulse height analysis was carried out for detector systems A and B only. The independent counters of system C monitored the total countrate of pulses corresponding to photon energies between 2 and 8 keV. The voltage pulses from counters A and B were fed via amplifiers into the signal conditioner. There the pulses in the pulse height range of interest (corresponding to 2-8 keV), which were not vetoed by coincident events in the guard counter, were sorted into the appropriate pulse height channel and fed to a scaler chain with an associated D to A digital to analogue) converter. The output of the D to A converter for each PHA (pulse height analyser) channel was one of 32 (PHA channels 1 and 2) or 16 (PHA channels 3 and 4) voltage levels, and was sampled periodically by the telemetry. The time history on the final records appears as a staircase, the number of steps jumped between successive points being equal to the

number of X-rays counted in that PHA channel per sampling period. Each 4-channel pulse height analyser consisted of 5 input comparators with reference levels which defined the extremities of the four pulse height channels, followed by a system of gates which fed a pulse into the appropriate scaler chain (unless vetoed by a coincident guard event).

Calibration of the experiment was achieved by feeding the input to the on-board 4-channel PHA to a commercial 400 channel PHA when the counter was being irradiated with 5·9 keV X-rays from an Fe^{55} source. The amplifier gain was then adjusted until the peak of the pulse height distribution, ie the pulse height associated with a 5·9 keV photon, occurred at 5·9 volts. The comparator reference levels which were set to 2, 3·2, 4·5, 6 and 8 volts then defined energy channels with extremities at 2, 3·2, 4·5, 6 and 8 keV. The amplifier gain was set slightly high so that in the time between the last flush and launch, the gain would fall to the required level.

System B carried in-flight calibration in the form of an Fe^{55} source which permanently irradiated the guard counter. When the rocket was below 70 km, both during ascent and descent, the guard counter was switched into the 4-channel PHA so that the gain could be calculated from the relative number of counts in each pulse height channel. The countrate of 400 sec^{-1} from this source resulted in only 0·3% random rejection of the main counter pulses. The gain of Detector A was monitored in a similar way by observing the output of

the 4-channel PHA when the counter was exposed to Fe^{55} radiation 15 minutes before launch.

A power converter provided the voltages required for the digital electronics and amplifiers, from the 28V internal rocket supply. The power converter also provided 500V a.c. which was fed to Cockcroft-Walton circuits to provide the high voltage 2400V necessary for the proportional counters.

7.5 The Flight IV General Design

Flight IV, like flight III was an engineering round the main purpose of which was to test a new, more powerful, boost motor (Goldfinch). The UAT experiment was given primary status on this round which meant availability of the nose cone site and a major share of the telemetry space. A nose cone array of three detector systems with total area 1700 cm^2 and the three detector systems in the recovered base ring (total area 200 cm^2), was flown (see Plate 4).

The basic aim was to conduct a comprehensive survey of celestial X-rays in the Southern sky with particular interest in the galactic center region and to confirm the existence of an X-ray source in the constellation Cetus which was reported (Barnden and Francey, 1969) from the results of flight III (see Chapter 8). In addition to its survey capability this experiment was expected to obtain information on the diffuse X-ray background and on the soft X-ray flux

PLATE 4

A and B

Two Views of the UAT Flight IV
X-Ray Astronomy Experiment

1. Nosecone Detector System N1
2. " " " N2
3. " " " N3
4. Nosecone Electronics Ring
5. Base Ring Experiment
6. Calibration Ledex Switches
7. Copper Tubing for EHT lines
8. Flushing Block with Shrader valves
9. Copper Tubing for Flushing
10. Tensioned Mounting Rods
11. Mounting Brackets
12. Auxiliary Sun-slits
13. Sun-Horizon 1-shot Cameras
14. Access ports to amplifier O/P's
15. Base Ring Flushing Port
16. Base Ring Detector B
17. Base Ring Detector A
18. Pre-amp, sunslit and calibration command lines.
19. University of Tasmania Electron Experiment
20. Crash Padding.

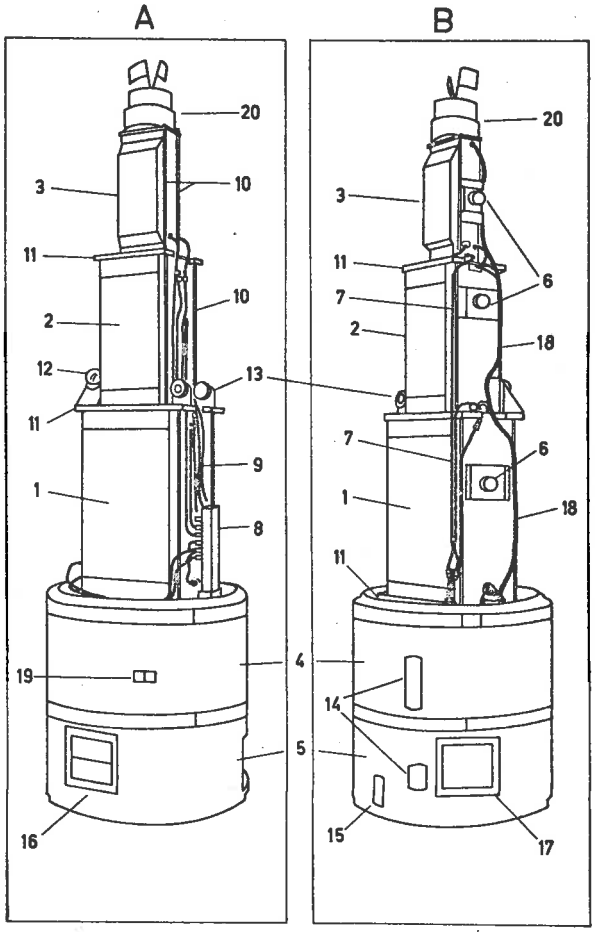

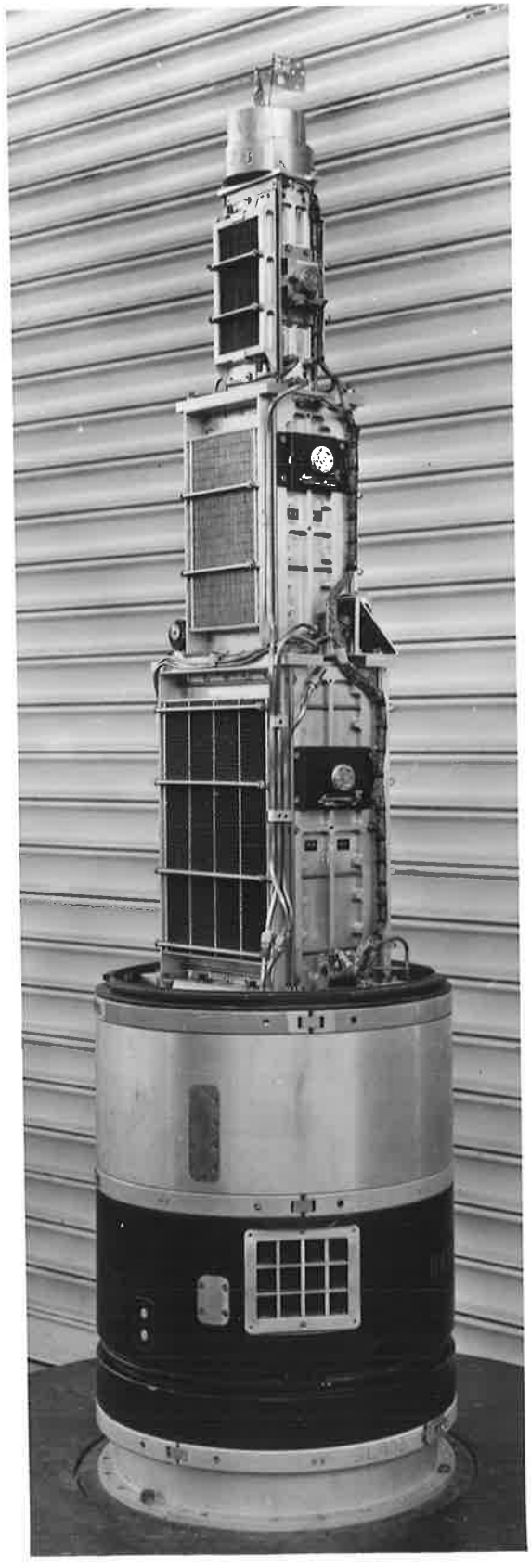

below 1 keV.

In the early stages, the preparation of the instrumentation proceeded in two different localities. Mr. Francey at the University of Tasmania was responsible for the basic design and construction of the nose cone detectors (Francey, 1970),while at the University of Adelaide the author was responsible for the design specifications and preparation of a new on-board data analysis unit, and with Mr. Tuohy for the improvements to the recovered flight III base-ring experiment. After the detectors were brought to Adelaide, their integration with the electronics, their testing and the mounting of the experiment to the rocket was a joint project between Mr. Francey, Mr. Tuohy and myself.

Two views of the total experiment are shown in Plate 4. The three nose cone detector systems were mounted one atop the other to form an array which fitted snugly inside the split nose cone. The three systems were designated N1, N2 and N3 from the bottom upwards. The electronics for these detectors was housed in the 8 inch ring directly beneath the nose cone. This ring was sealed by a pressure bulkhead which also served as the platform on which the nose cone detectors were mounted. Each of N1, N2 and N3 consisted of two back to back detectors with independent gas filling and signal conditioners.

Spectral information was provided by pulse height analysis with 8 channels for each of the N1 counters, 4 channels for both N2

counters, and 3 channels for both N3 counters. Charged particle rejection for each system was provided by anticoincidence logic between the two back-to-back counters. The recovered base ring experiment was located below the 8" nose cone electronics ring. The features of each detector on the flight IV experiment are summarised in Table 7.1.

TABLE 7.1

THE FLIGHT IV DETECTORS

Detector		Collimator °FWHM	Area cm^2	Window mg cm^{-2}	Gas Depth mg cm^{-2}	Bias Levels keV	Energy Res. at 5.9 keV
Nose Cone							(FWHM)
N1	A	4·5 hexag.	570	0·9 M*	7·6	1,2,3,4,5,6	17%
	B	"	570	1·45 P†	"	7,8,12	
N2	A	2·7 x 33	220	0·9 M	6·0	1,2.5,4,6,10	17%
	B	"	220	1·45 P	"		
N3	A	5 x 36	60	0·89 P	3·8	·25,·30,1·50,	17%
	B	"	60	0·89 P	"	3·0	
Base Ring							
	A	4 x 37	65	12·5 Be	4·8	2,3.2,4.5,6,8	17%
	B	4·5 hexag.	87	1·77 M	4·8	2,3.2,4·5,6,8	17%
	C1	3 x 35	30	23 Be	4·8	2,8	20%
	C2	3 x 35	25	23 Be	4·8	2,8	20%

* Mylar $(C_{10}H_8O_4)_n$ † Polypropylene $(CH_2)_n$

The base ring electronics on flight IV remained essentially the same with 4-channel pulse height analysis on systems A and B, but only 1 pulse height channel for each of the system C detectors. The two LND counters of system C on flight III were replaced by a third

4-series detector for flight IV. The collimators of detector A and detector B are seen in plates 4A and B. The upper and lower chambers of C were given crossed collimators and were monitored independently. Neither of the 4-series detectors on flight III operated satisfactorily (Chapter 8.1) and in the light of this experience several modifications were made to these systems. The most important improvement was in the flushing system where the plastic tubing which had been used for internal connections (see Plate 3A) was replaced by $^{3}/_{16}$ inch copper tubing which was connected with very reliable compression type gas fittings. The tubing again terminated at shrader valves located this time in a build-up in the base-ring wall, and accessible from outside by removing a small cover plate. This type of plumbing was also used in the nose cone experiment.

The nose-cone detector systems were mounted using tensioned steel rods between mounting brackets beneath N1, between N1 and N2, between N2 and N3 and above N3 as shown in Plate 4 (and diagram opposite). The mounting brackets beneath N1 were bolted to the bulkhead. The nose cone detectors were fabricated from plate aluminium which, after the necessary machining, was bolted and araldited together. Sealing of the gas volume was again achieved by means of a rubber gasket between the window and the counter walls. The gasket was compressed by pulling down the collimator housing onto the window and gasket with bolts through to the walls. A cross-sectional view of the N2 counter is shown in Figure 7.2c. The nose cone flushing tubing terminated at a flushing

block (Plate 4A) mounted on the bulkhead. A 10 cm diameter hole in the nose cone allowed access to this after the round was assembled and in the launcher. All nose cone counters were equipped for in-flight calibration. Fe^{55} sources were mounted outside small beryllium windows in the side of each detector. A metal screen operated by a ledex switch was rotated to allow X-rays to reach these windows at times below 70 km and for 5 seconds near apogee. These calibration systems are seen mounted to the sides of the detectors in Plate 4B.

The end compartments of N1, N2 and N3 carried EHT filters, load resistors, coupling capacitors and preamplifiers. The power lines to the preamplifiers, the command lines to the calibration ledex switches, and the signal lines from the preamplifiers were fed inside copper braiding down the side of the detector array. The EHT lines for N1, N2 and N3 were fed from three independent Cockcroft-Waltons in the 8" electronics bay, via ¼ inch O.D. copper tubing, again using compression type gas fittings, to the end compartments of the respective detector systems (see Plate 4B).

The window materials used in the nose-cone detectors were either mylar or polypropylene and two basic collimator types were employed to give the best compromise coverage for an unstabilized round (see Section 7.3).

7.6 Flight IV Electronics

A completely new signal conditioner for the nose-cone experiment was required because

(a) There was a need for pulse height analysis with more channels on more detection systems namely

N1: 8 channel pulse height analysis for both sides with charged particle rejection.

N2: 4 channel pulse height analysis for both sides with charged particle rejection.

N3: 3 channel pulse height analysis for both sides with charged particle injection.

The use of flight III type hardware would have required an impossibly large number of printed circuit boards.

(b) The much higher countrates expected from the larger detectors demanded faster electronics.

(c) The total of 30 pulse height analysis channels (information channels) implied the necessity for electronic subcommutation by UAT of the available telemetry channels.

It was desirable that the telemetry accommodate countrates varying from the background rate to that of SCO X-1, the most intense source in the sky. For each N1 detector (area 570 cm^2) the countrate

from the SCO X-1 flux of 20 sec^{-1} cm^{-2}, is 11,400 counts sec^{-1}. On an equal counts per PHA channel basis this is $\sim$ 18 counts per $\frac{1}{80}$ second per PHA channel for N1. Each N2 counter with about half this area (220 cm^2) and half the number of PHA channels would have about 14 counts per $\frac{1}{80}$ second per PHA channel. The stability of the overall TM system allows reliable resolution of 32 analogue levels on the records. Table 7.2 shows dynamic range required on the records to accommodate SCO X-1 for different degrees of sub-commutation.

TABLE 7.2

Subcommutation	Sampling Period	Dynamic Range
x 1	$^1/_{80}$ sec	16
x 2	$^1/_{40}$ sec	32
x 4	$^1/_{20}$ sec	64

Table 7.2 indicates that with 2 x subcommutation the dynamic range required to accommodate SCO X-1 can just be achieved. A sufficient number of telemetry channels was made available to UAT to enable the total of 40 information channels to be telemetered to ground when 2 x subcommunication was used for the nose-cone experiment.

Integrated circuits (ICs) were used wherever possible to achieve space economy. After a review of the performance and cost of different types of pulse height analysers it was decided to depart

from the old type, where an N-channel analyser required N + 1 comparators, each a fairly expensive item, and use a design that needed only two comparators. The remaining requirements were a number of gates and flip-flops - relatively cheap items.

A block diagram for a 4-channel PHA is given in Figure 7.4 and its operation can be followed using Figure 7.5. The voltage pulse from the detector is amplified and then fed firstly to a threshold comparator to test whether the pulse height is greater than the minimum level of interest, and secondly to a sample-and-hold circuit which samples the pulse at its peak and holds that voltage level until it is reset. If the threshold level is exceeded a 1 μsec pulse is fed to a veto circuit which only produces an output if there is a coincident pulse (within 1 μsec) from the oppositely viewing counter.

If there is no coincidence a reference staircase is initiated. The timing for this circuit was supplied by a 1·3 MHz clock so that every 0·77 μsec, its output is incremented to the voltage corresponding to the top level of the next pulse height channel. Thus the reference staircase, originally at 0V, first increases to V_1 volts, then to V_2 volts, V_3 volts and so on, where V_1 is the voltage at the top of pulse height channel 1 (= bottom of pulse height channel 2) etc. The bottom of channel 1 is defined by the threshold comparator reference level. The reference staircase is fed into the reference input of the main comparator and is incremented until it exceeds the pulse height (from

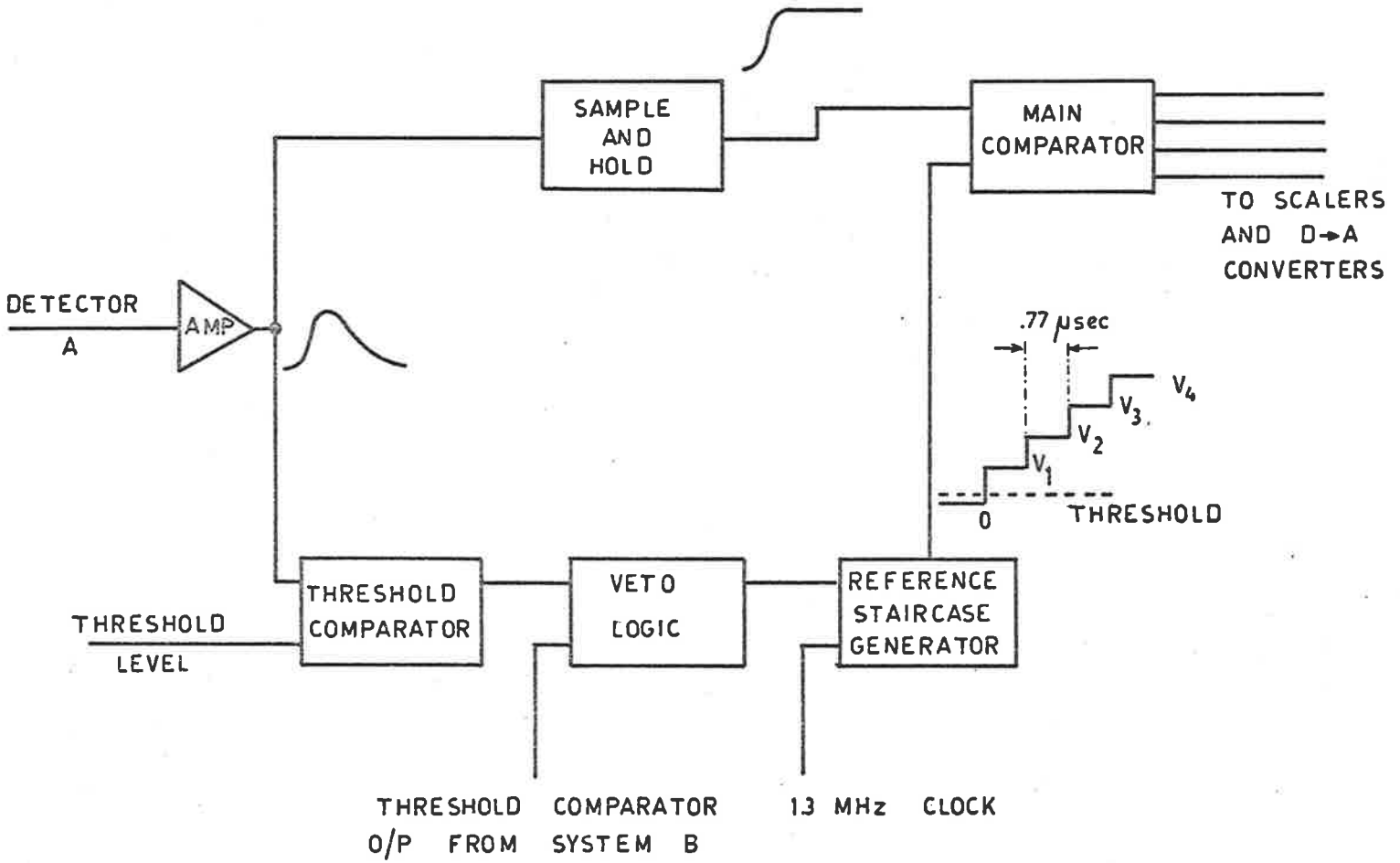

Figure 7.4 A block diagram of a flight IV nose-cone experiment 4-channel pulse-height-analyser.

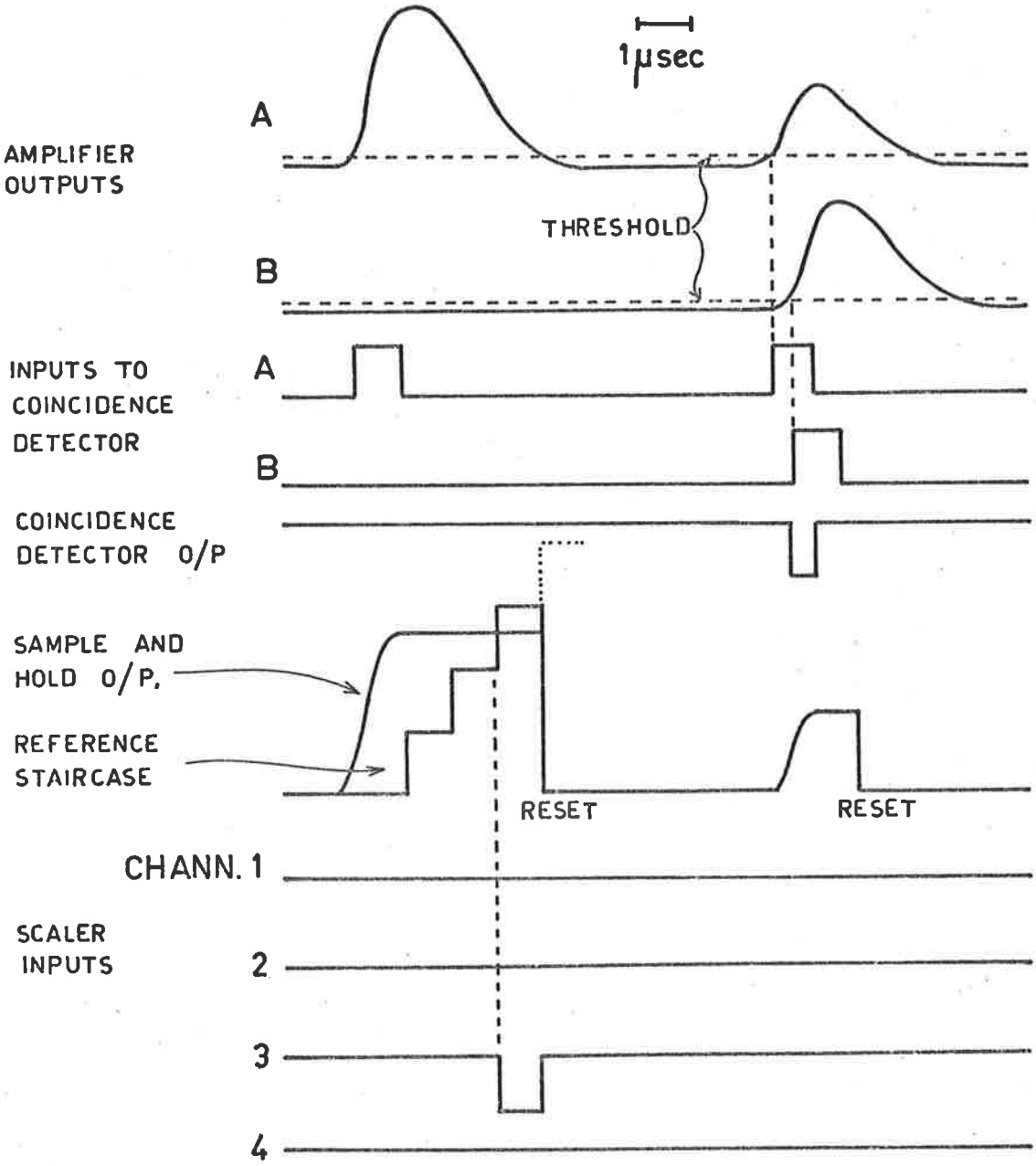

Figure 7.5 The voltage pulses at various points in Figure 7.4 for a pulse which is analysed and found to be in pulse height channel 3, and a pulse which is vetoed by a coincident pulse from the adjacent counter.

the sample-and-hold circuit) at the other input, causing the comparator to feed a pulse to the scalar chain of the appropriate pulse height channel. This also causes the whole system to reset in readiness for the next pulse.

For each pulse height channel there is a 5 element scaler chain. The contents of this chain are periodically (every $\frac{1}{40}^{th}$ sec) transferred into a buffer with a 32 level digital-to-analogue converter which is in turn sampled by the telemetry. 0·77 μsec after its contents were transferred the chain is reset to begin counting for the next $\frac{1}{40}^{th}$ second (= $2{\cdot}5 \times 10^4$ μsec). This mode of operation relies on the availability of the synchronization pulse which signifies the beginning of each telemetry frame and can therefore be used (after scaling by 2) to time the transfer-reset events for each scaler chain.

The resulting records from any telemetry channel appear as a series of points at one of 32 voltage levels, which alternatively give the number of X-rays counted per $\frac{1}{40}^{th}$ sec from the two pulse-height channels on that telemetry channel. This is called picture telemetry because it shows the actual countrate profiles. To expedite the search for sources in the photographic records, the total countrate from each side of N2 was telemetered on a 'picture' channel in this way.

To enable the two independent information streams on each telemetry channel to be separated, the scaled (by 2) synchronization

pulse representing the beginning of the telemetry frame for one of the two sets of information channels, was telemetered to ground on a full telemetry channel.

7.7 Flight IV Preparation

The environmental testing of the flight IV experiment was performed in the 1·2 meter diameter vacuum chamber at the University of Adelaide. The experiment performance during these tests was monitored by a ground unit which also simulated the rocket power supply.

These tests showed several faults associated with the vacuum environment (high voltage discharge and minor proportional counter leaks). After improving the vacuum seals in question, the final environmental test showed that the experiment would operate as required in a vacuum environment, and therefore was ready for final calibration.

The flight IV calibration was similar to that for flight III. The commercial 400 channel analyser was again used so that both the rocket pulse height channel levels and the spectrum peak of the calibration sources (Fe^{55}), could be expressed in terms of channel number. Then because the calibration peak was known to be centered on 5·9 keV, the rocket pulse height channel levels could also be expressed in keV. The final calibration was checked 15 minutes before launch by taking a calibration spectrum from each counter with the 400 channel analyser.

The experiment gain in flight was to be monitored during the three periods when the detectors were irradiated with 5·9keV calibration X-rays. The pulse height levels were to be determined (in keV) from the ratio of the calibration source countrates in adjacent pulse height channels.

CHAPTER 8

THE RESULTS OF THE ROCKET X-RAY EXPERIMENTS

8.1 Introduction

In this chapter the data analysis methods and the results of the UAT flight III X-Ray astronomy experiment are described. There were no results from the flight IV experiment - a vehicle malfunction caused the rocket to break up during ascent and the experiment was destroyed.

Flight III was launched at 0608UT on December 1, 1967 and reached an apogee of 181·5km 220 seconds later (T = +220 seconds). Only one of the three detector systems operated satisfactorily. This was system C, which consisted of the two small detectors, one vertical and one diagonal, shown in Plate 3B. Their summed area was 23 cm^2 out of an experiment total of 150 cm^2. Data was received from detector systems A and B but this was of unknown reliability. The data from these two detectors was nevertheless analysed, but no useful results were obtained.

The system A guard chamber appeared to be in continuous discharge throughout the flight and this resulted in a large fraction of the counts due to X-rays in the main counter being rejected. There was no in-flight calibration on this detector, and since neither the Sun nor any strong source was scanned during the flight, it is not

known if the gain decreased since the last gas flush at -15 minutes. The countrate from system A stopped abruptly at payload separation (+329 seconds). It is puzzling that the small shock associated with payload separation (separation of payload from motor) should produce this effect, since the detector worked satisfactorily after recovery (after flushing with P-10).

The gain of system B (monitored using the in-built calibration source) decreased by a factor of more than 2 in the 15 minutes between its last gas flush and launch. However, due to the ancillary status of the experiment, it was not possible to rectify this fault. The plumbing connections inside the (sealed) ring were the most probable cause. In addition this detector did not operate correctly after the microphonics associated with the motor thrust phase had died out. There were intermittent periods, of up to 10 seconds duration, when no counts at all were recorded. It was not possible to see the calibration source near +60 seconds due to this effect. These cut-outs seemed to disappear by about +150 seconds and the calibration at +340 seconds showed the 5·9keV X-rays to be in pulse height channel 1, indicating that the threshold was $\geq$ 4keV instead of 2keV. The data from +150 to +340 seconds was examined, but no useful results were obtained.

8.2 The Flight III Attitude Solution

The attitude solution for a Skylark rocket is normally derived

using the three orthogonal magnetometers and the 4 pairs of crossed sunslits (each pair has a vertical and a diagonal slit). In addition the rate gyroscopes provide a check on the rocket spin direction.

The rocket axes which are used in this analysis are shown in Figure 8.1a. The OX axis is directed forwards along the rocket spin axis, while the OY and OZ axes lie in the rocket's transverse plane. The three magnetometers yield an analogue voltage proportional to the cosine of the angular separation between the local magnetic field direction and the +OX, +OY and +OZ axes respectively. The 4 pairs of sunslits are mounted on the side of the rocket with the centers of their effective $4^{\circ} \times 120^{\circ}$ (full width) angular responses aligned with the +OY, +OZ, -OY, -OZ axes.

The initial requirement for an attitude solution is to define the direction of the OX axis in space as a function of time. Once this is known it is a relatively simple matter to define the directions of viewing of a sideways viewing detector as it scans in the rocket's transverse plane. The principle behind the calculation of the OX direction in space is illustrated in Figure 8.1b. This figure is drawn on the surface of the celestial sphere so that each point represents the direction in space defined by the line from the center of the sphere through the point in question. Similarly, the separation of any two points on this diagram is in reality an angular separation, since each point represents a direction.

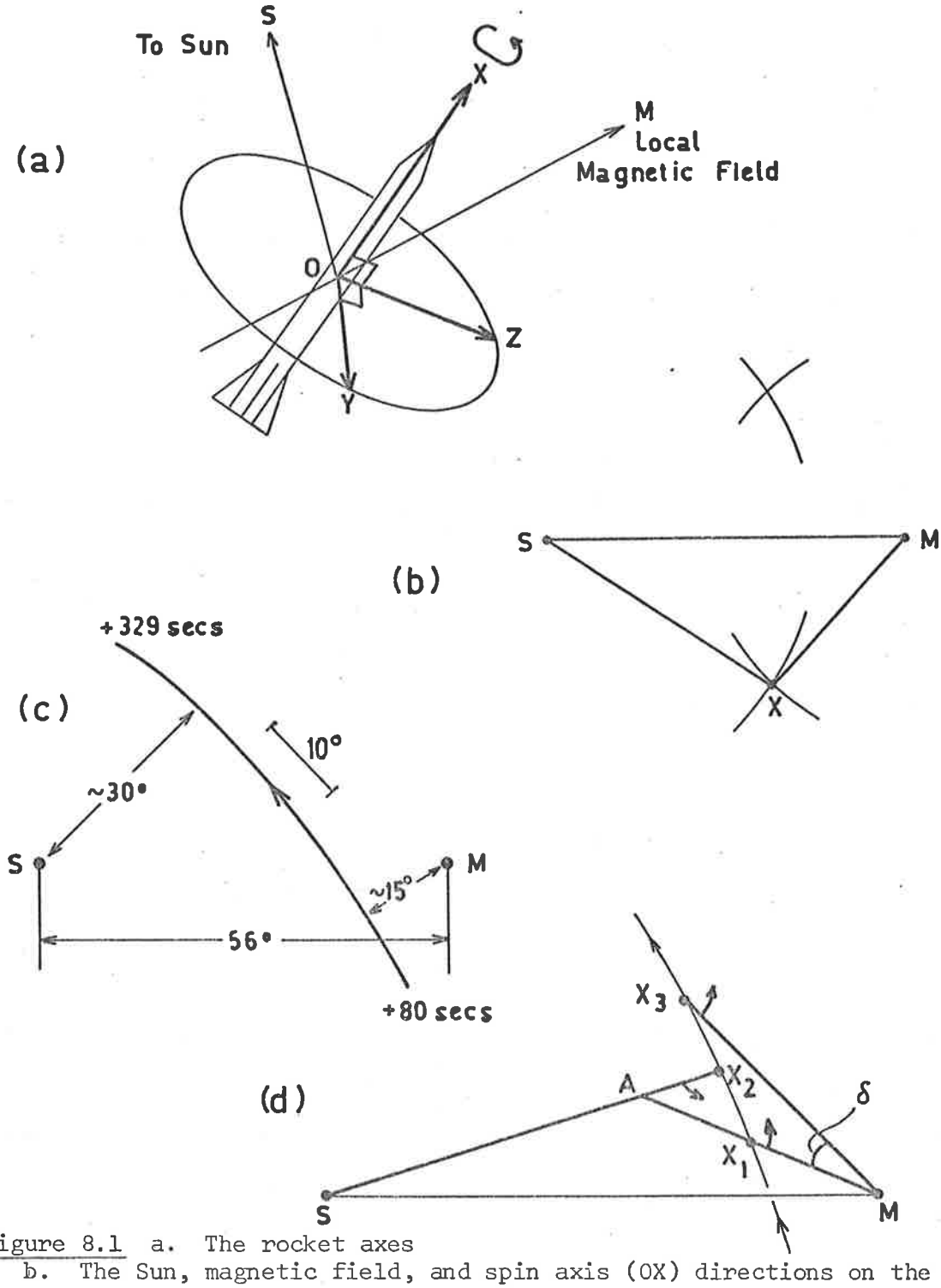

Figure 8.1 a. The rocket axes
b. The Sun, magnetic field, and spin axis (OX) directions on the celestial sphere.
c. The rough attitude solution for OX.
d. The geometry used to calculate $\lfloor MXS$.

In Figure 8.1b the point M represents the direction of the Earth's magnetic field in the vicinity of the rocket, point S shows the direction of the Sun, and point X is the direction of the rocket OX axis. We now describe how the direction OX is found relative to the direction OS and OM (points S and M in Figure 8.1b) using the magnetometer and sunslit records.

At any time during the flight $\angle MOX$ is found as follows. Let the components of the magnetic field $\underset{\sim}{M}$ in the OX, OY and OZ directions be M_x, M_y, M_z respectively.

$$M_x^2 + M_y^2 + M_z^2 = M^2$$

Now $$M_x = M \cos \angle MOX$$

Thus $$M_y^2 + M_z^2 = M^2 \sin^2 \angle MOX \qquad (8.1)$$

The rocket spin causes M_y and M_z to oscillate from positive to negative values (90° out of phase), as is shown in Figure 8.2a. When M_y is a maximum (most closely aligned with $\underset{\sim}{M}$) or minimum, M_z is zero (perpendicular to $\underset{\sim}{M}$), so that from equation 8.2

$$M_{ymax} = \pm M \sin \angle MOX \qquad (8.2)$$

By reading the peak to peak deflection from the OY magnetometer records (see Figure 8.2a) any zero shift errors are eliminated. If $\angle MOX$ is 90° at any time during the flight then the peak to peak value $(M_{ymax} - M_{ymin})$ will pass through a maximum value. If all values of

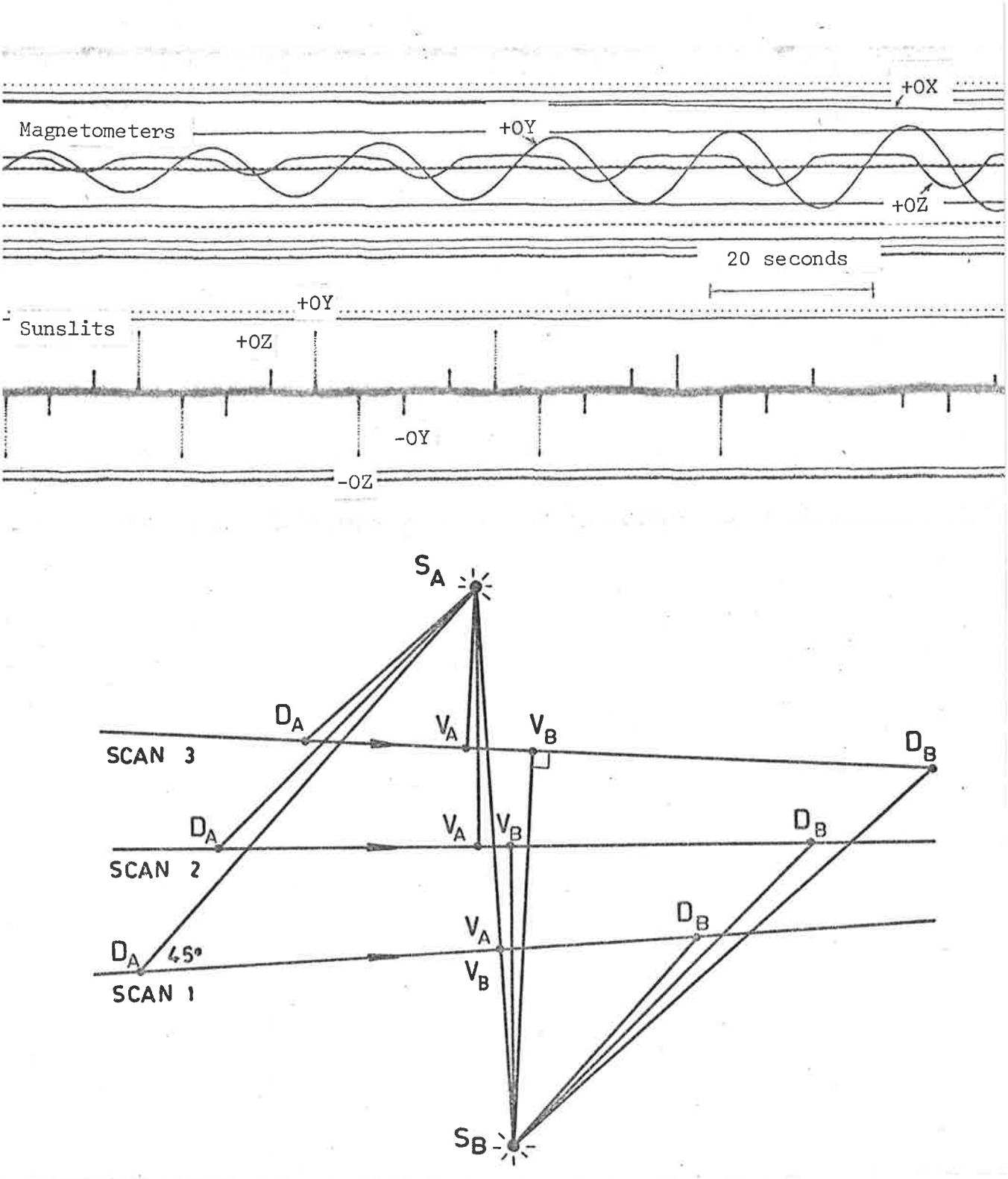

Figure 8.2 a. Flight III magnetometer and suncell records.
b. The observation times of two test sources (S_A and S_B) by the vertical and diagonal detectors on 3 consecutive scans.

$M_{ymax} - M_{ymin}$ are normalised so that this maximum value equals 1·0, then they define the value of sin |MOX throughout the flight.

The value of $M_{ymax} - M_{ymin}$ during flight III did not reach its maximum, that is |MOX did not reach 90° before +329 seconds when payload separation (from the motor casing) changed the rocket motion. However at about +350 seconds |MOX appeared to pass through +90° and it was possible to obtain an estimate for $M_{ymax} - M_{ymin}$ at this time. It is possible that the magnetometer sensitivity was changed at payload separation due to the removal of the stainless steel motor casing, although there was no sudden change apparent in the magnetometer records. The values of $M_{ymax} - M_{ymin}$ were therefore normalised so that this maximum value was 1·0, and then used to deduce |MOX throughout the flight. These values were also corrected to allow for changes in the magnetic field strength during the flight.

Normally |SOX (SX in figure 8.1b) is obtained from the delay between the Sun sightings of the vertical and diagonal sunslits (e.g. Harries, 1968). The sunslit angular response prevents the vertical sunslits from seeing the Sun when $|SOX \lesssim 30^{\circ}$, and the diagonal sunslits when $|SOX \lesssim 50^{\circ}$. The flight III motion was such that at no time during the flight did the diagonal sunslits see the Sun so that the above method of calculating |SOX could not be used. Furthermore the Sun was beginning to move out of the vertical sunslit field of view at payload separation (see Figure 8.2c and 8.3a).

A rough attitude solution indicated, as is shown in Figure 8.1c, that the OX axis only moved about 60° throughout the whole flight (before payload separation) and that it passed between the OM and OS directions (which were separated by 54°). This motion enabled a method to be used which yielded good estimates for $\angle MXS$, which were then used to derive $\angle SOX$. The method of estimating $\angle MXS$ was based on the delay between the sightings of the Sun and magnetic field by the sunslit and magnetometer aligned with the +OY axis (or equivalently for the pair of sensors aligned with the +OZ axis).

Consider Figure 8.1d. This is the situation for *case 1* when the directions OX_1, OX_2 and OX_3 correspond to the times: t_1 when the rotating OXY plane contains OM (the +OY axis is most closely aligned with OM), t_2 when the OXY plane contains OS (the vertical +OY sunslit sees the Sun), and t_3 when the OXY plane again contains OM. These times are easily read from the OY magnetometer and sunslit records. Between t_1 and t_3 the OY axis rotates 360-δ degrees (the rocket spun anticlockwise looking aft). Thus assuming $X_1X_2X_3$ to be a straight line, between t_1 and t_2 the OY axis rotates through $\angle SAM$ where

$$\angle SAM = \frac{t_2 - t_1}{t_3 - t_1} \quad (360 - \delta)$$

Now $$\angle SX_2M = \angle SAM - \angle AMX_2$$

and $$\angle AMX \simeq \frac{t_2 - t_1}{t_3 - t_1} \cdot \delta$$

Thus $$\angle MX_2S \simeq \frac{t_2 - t_1}{t_3 - t_1} (360 - 2\delta) \qquad (8.3)$$

The angle δ will be small when OX moves slowly (x_1x_3 is small) and when $\angle MOX$ is large.

In *case 2* $X_1(t_1)$ is a Sun sighting point, $X_2(t_2)$ is a magnetic field sighting, and $X_3(t_3)$ is the next Sun sighting. Using the same method we find

$$\angle MX_2S \simeq \frac{t_2 - t_1}{t_3 - t_1} (360 + 2\delta) \qquad (8.4)$$

Equations (8.3) and (8.4) were approximated by

$$\angle MX_2S = \frac{t_2 - t_1}{t_3 - t_1} 360$$

For *case 1*, this is an over estimate, and for *case 2* it is an underestimate. The curves for *case 1* and *case 2* were plotted throughout the flight, and the true value of $\angle MXS$ was taken to be the average value. The $\angle MX_2S$ curves for the two methods were separated by $< 3^\circ$ throughout the flight, indicating that the maximum error in $\angle MXS$ was $< 1'5^\circ$ for the whole flight.

These values of $\angle MXS$ were then used in the following spherical triangle relation to find $\angle SOX$

$$\cos\angle SOM = \cos\angle MOX \cos\angle SOX + \sin\angle MOX \cos\angle MXS \sin\angle SOX \qquad (8.5)$$

where $\angle SOM$, $\angle MOX$ and $\angle MXS$ are known.

The positions of the Sun and magnetic field were marked on a 12 inch celestial globe and the path of the OX axis was obtained by swinging arcs corresponding to the angles SOX and MOX at 10 second intervals throughout the flight.

The viewing directions of the detectors in the OXY plane were then obtained from the times when the vertical sunslits observed the Sun. If the viewing direction of the detector at +OY at time T was required, and the preceding +OY sun sighting was at T_1 and the next +OY sun sighting at T_2, then the +OY detector viewed at an angle of

$$\theta = \frac{T - T_1}{T_2 - T_1} \cdot 360 \qquad (8.6)$$

around from the Sun.

A frame was constructed to fit over the celestial sphere at the zenith which indicated the plane of the horizon and which was marked with 360° of azimuth. When placed on the position of the OX axis it defined the OYZ plane on the celestial sphere, and it was possible to find the position corresponding to a sun sighting, and then find the position corresponding to the detector direction of viewing at time T.

The direction of viewing of the system 3 detectors during the flight, as calculated by the above method, is shown in Figure 8.3.

An attitude solution for this flight was received several

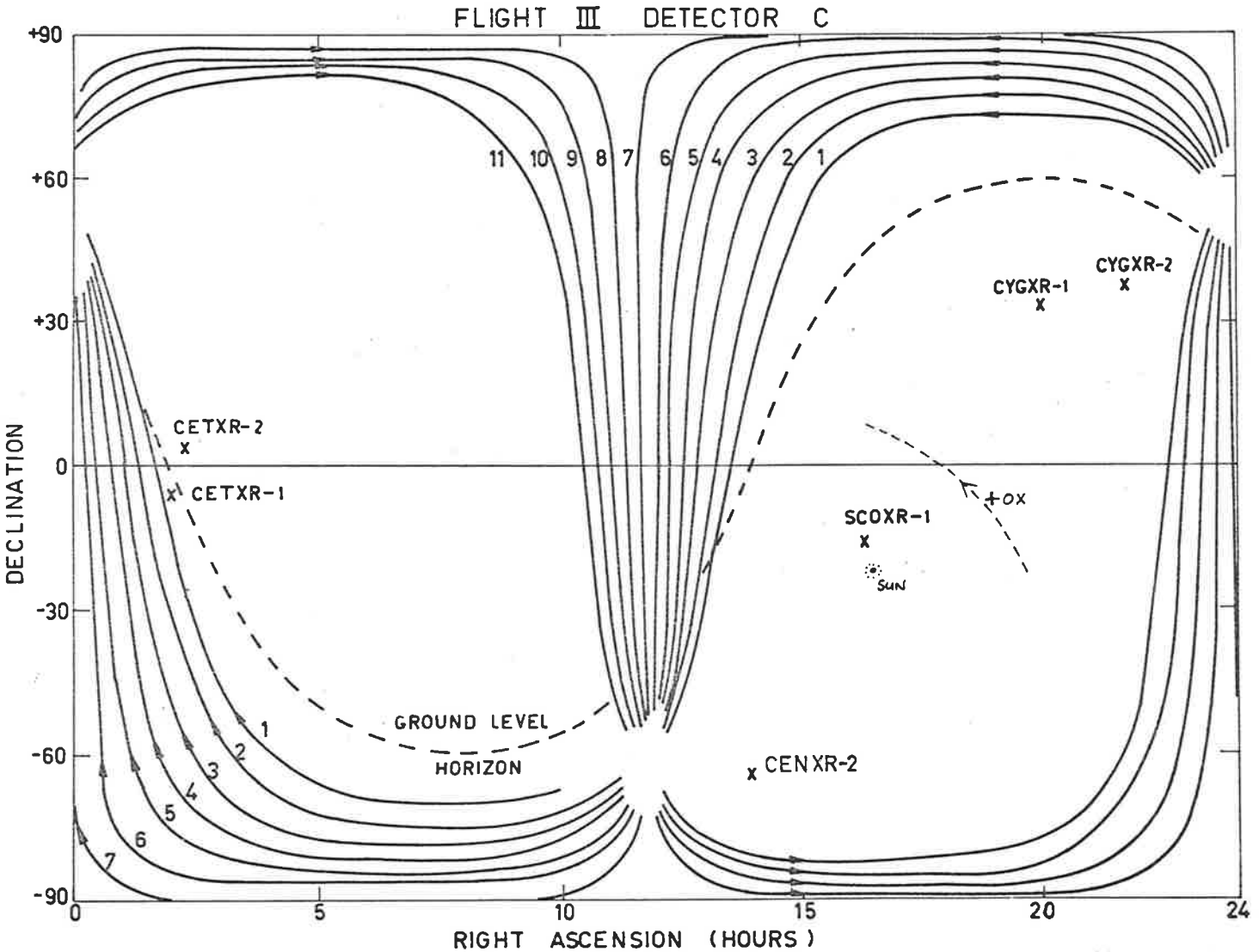

Figure 8.3 The regions of sky scanned by detector system C (flight III). The ground level horizon is shown together with the positions of several sources.

months after the completion of the above analysis from the rocket subcontractor BAC. This solution was calculated on the assumption that the precession cone half angle was 90°, although from my solution it appeared that this was closer to 65°. Nevertheless, because only a small section of the cone was completed, the two solutions were in substantial agreement (to within 5°). My solution would be even closer to the BAC solution (would yield a 90° precession cone) if the magnetometer calibration was changed to yield slightly smaller values for $|\underline{MOX}|$. However there is no more reason for doing this than for assuming a 90° precession cone.

8.3 Countrate Analysis

System C was the only detector system on flight III which yielded reliable countrate data, and this is the only flight III data used herein. System C was made up of a pair of detectors (Plate 3B) whose total area was 23·4 cm^2. With such a small area and with the flight III spin period, it would not be possible to detect sources weaker than about 5 photons.$cm^{-2}sec^{-1}$ from the counts recorded on any one scan (for a countrate peak 3 standard deviations above background). Since no known strong sources were scanned and no new strong sources were evident in the data it was necessary to superpose successive scans over any given region to look for weaker sources.

The flight III motion was particularly suited for the use of the superposed epoch analysis technique. The spin period was $\sim$ 22·5

seconds and in that time the OX axis moved only $\sim 6^{\circ}$ across the sky so that adjacent scans were separated by at most 6°. Consequently it was possible for the vertical collimator (3° x 35° FWHM) to make at least 6 scans of any one position with a response > 0·5 (full response = 1·0).

The counts in 0·1 second intervals were read from the records and plotted for 22·5 second periods (the spin period). These 22·5 second sections of data were arranged one above the other and a search was made for countrate increases which were approximately aligned in successive scans. From the time of the strongest countrate increase the direction of viewing of the detector axis was calculated using the reverse of the procedure given in the previous section (8.2). Various test-positions for the source were then chosen within the collimator response at that time, and the times of viewing that position were calculated for the other scans. This was repeated until the observation times of the test position corresponded to the times of the countrate increases in each scan. If it was possible to achieve alignment for a given test position then this was taken to be the position of a source - if the superposition of the scans yielded a significant peak in the countrate.

The way in which the observation times change for different test positions can be seen in Figure 8.2b. Let point V (= V_A = V_B) on scan 1 be the central direction of viewing for the detector with the

vertical collimator at the time of observation of a countrate increase in the scan 1 records. Two test positions S_A and S_B within the vertical collimator response at this time are considered. It can be seen that the observation times in scans 2 and 3 are earlier for position S_A than for position S_B. This effect is particularly marked for the diagonal collimator detector (observations by this counter are marked by D_A and D_B) and this shows how sensitive the diagonal observation times are to the rocket declination of the source position.

Hence for weak sources where the countrate increases in individual scans are very small, the position of the source in rocket azimuth is well defined by the vertical collimator detector, but an accurate estimate of the source position in rocket declination can only be obtained from the diagonal collimator detector. Figure 8.2b also illustrates how the diagonal response decreases more rapidly than the vertical response as the scans move away from the source positions. For scans separated by 6° only 4 scans will observe a given source of more than half response (compared with 6 for vertical collimator).

The geometry of Figure 8.2b can also be used to calculate the observation times for the scans of a source in a known position.

8.4 The Source in Cetus

The procedure described in section 8.3 was successful in a search for weak sources in the data of the vertical and diagonal

viewing detectors of system C. A series of countrate increases in 5 scans of detector V (vertical) and detector D (diagonal) was discovered and the best alignment was obtained for the position R.A. 2·0 hours, Dec. - 6° (ℓ^{II} = 165°, b^{II} = -63°) in the constellation Cetus.

The total peak is 3·9 standard deviations above background (this is greater than the value of 3·6σ given by Barnden and Francey (1969) because the background level used for that estimate was too large). Allowing for the collimator response of these observations, this peak corresponds to an X-ray flux of about 1·5 photons sec^{-1} cm^{-2} in the 2-8 keV energy range.

The individual scans, the vertical and diagonal scans, and their total are are shown in Figure 8.4. This shows how insignificant the sightings appear on individual scans, and how the superposed epoch analysis reveals a source after summing these scans. The numbers at the right hand end of each scan are the collimator response and the distance (in degrees) of this position above the 80km horizon for that sighting. The collimator response values (and Figure 8.3) indicate that this position was observed most directly on scan 1. This is also suggested by the individual scan plots, although for scan 1 when the rocket was only at 98km for a source near the horizon there may have been significant atmospheric absorption.

At the time of this analysis (1968) no survey of greater sensitivity had been made of this region of the sky. This position was

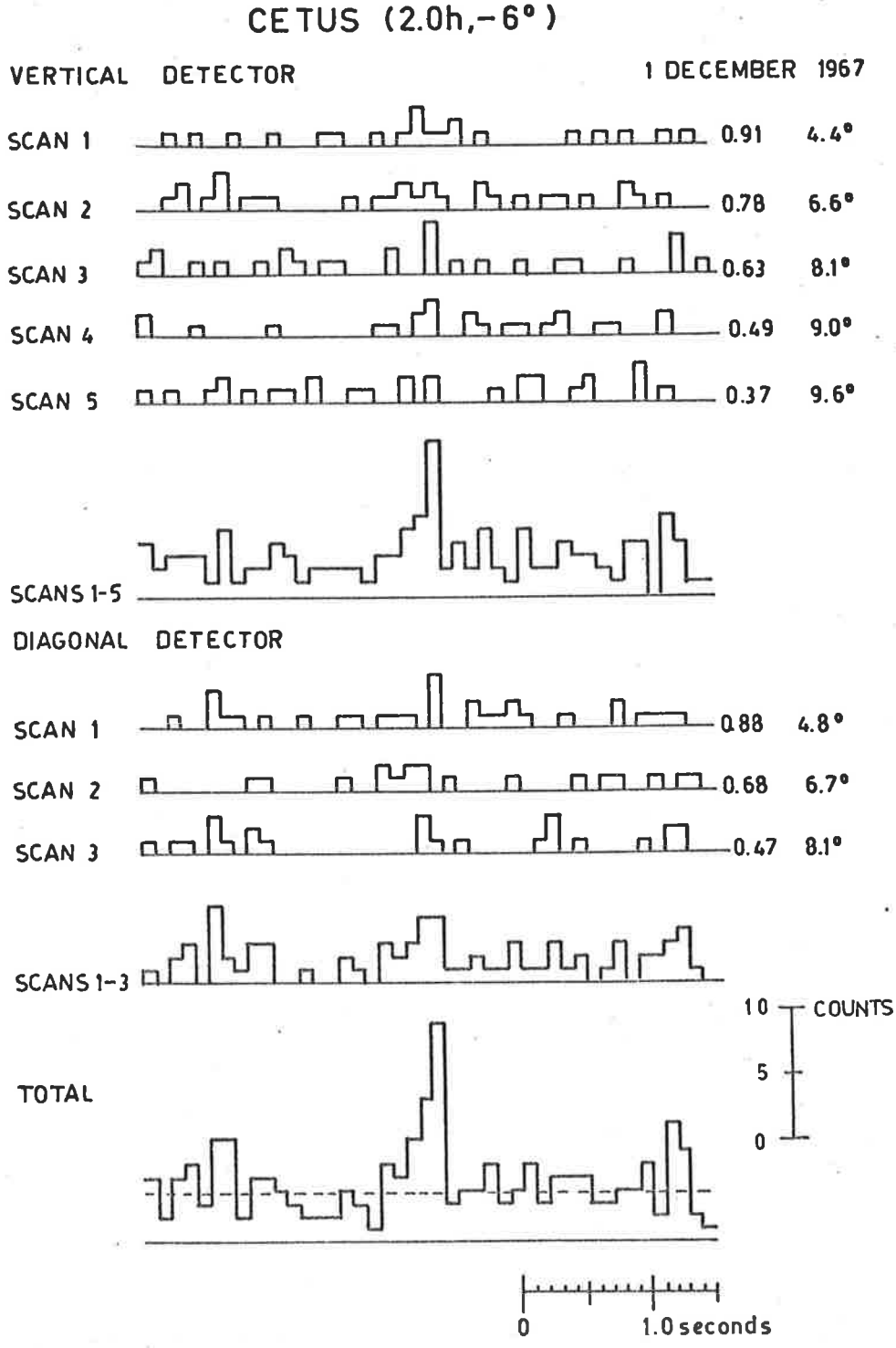

Figure 8.4 The Cetus XR-1 observation on Flight III, showing the counts recorded on five scans of the vertical detector and their sum, and on three scans of the diagonal detector and their sum, and also the total of the 5 vertical scans and 3 diagonal scans. The collimator response and the distance above the 80km horizon of the position (2·0h, -6°) are given for each scan.

however scanned by the earlier UAT experiments, flights I and II, launched in April 1967. During the first flight, the $10{\cdot}5^{\circ}$ FWHM angular response of the collimators meant that the Sun was observed at the same time as the above source position. Consequently any X-rays from this position were obscured by the large flux from the Sun. During the second flight the detectors were able to resolve the Sun and this position. Superposition of four scans revealed a peak $2{\cdot}7$ standard deviations above background which implies a source intensity compatible with that from flight III (the detector areas were identical for both flights).

This source, called Cet XR-1, is of special interest because it is located so far from the galactic equator (galactic latitude $b^{II} = -63^{\circ}$). In the catalogue of Dolan (1970), only 8 of the 59 sources listed (including Cet XR-1) are further than 25° from the galactic equator, and three of these are "unconfirmed". Two of these high galactic latitude sources have been identified with other galaxies, namely M87 (Vir XR-1, Bradt et al, 1967) and the Large Magellanic Cloud (Lewin, 1968). Hence Cet XR-1 could be either an extragalactic source, or a source in close proximity to the Sun in our own galaxy.

Shukla and Wilson (1970) have recently observed a very strong source ($\sim 0{\cdot}7$ Sco XR-1) in Cetus at R.A. 2 hrs 14 min, Dec. $4^{\circ}33'$. This source has been named Cet XR-2, and its details are listed in Table 8.1 with those of Cet XR-1.

TABLE 8.1

Comparison of Cet XR-1 and Cet XR-2

	Cet XR-1	Cet XR-2
Observation Date	1 Dec 1967	26 Oct 1969
R.A., Dec	2 hr 0 min, -6°	2 hr 14 min, 4°33'
ℓ^{II}, b^{II}	165, -63°	159, -52°
Intensity (photons cm^{-2} sec^{-1})	∿ 1·5 (2-8 keV)	22·3 (1·5 - 10·0keV)

The BAC attitude solution, which assumed the extreme case of a 90° precession cone, yielded the position R.A. = 2·0h, Dec = -3 ° for Cet XR-1. The positions given in Table 8.1 for Cet XR-1 and Cet XR-2 are separated by about 11°. The position of Cet XR-2 is 6° below the flight III ground-level horizon (see Figure 8.5) although for scan 3 it is 1° above the 100km horizon and at a vertical collimator response of ∿ ·47; for scan 4 it is 2½° above the 100km horizon at vertical collimator response of ∿ ·34. Hence the Cet XR-2 position would only have been observable on flight 3 by viewing tangentially across the top of the Earth's atmosphere, and because Cet XR-2 has such a soft spectrum (Shukla and Wilson, 1970) it may have been considerably attenuated. Hence it is possible that flight III observed Cet XR-2 at the intensity reported here for Cet XR-1. That is it is possible that Cet XR-1 and Cet XR-2 are the same object, although this implies

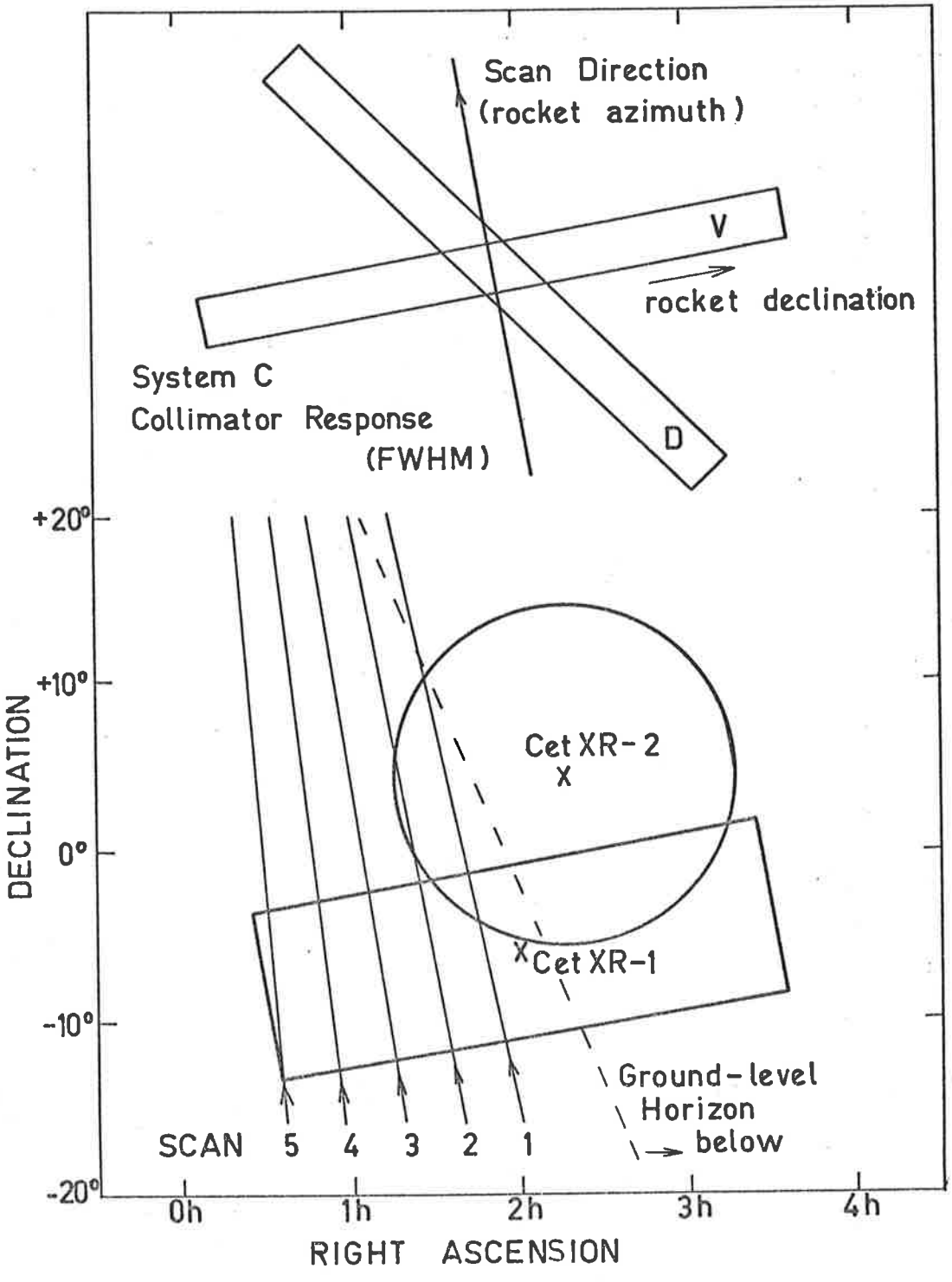

Figure 8.5 Showing the path swept out by the center of the collimator response of the C detectors relative to the positions of Cet XR-1 and Cet XR-2. The uncertainty in the positions of these two sources, and the angular responses of the C detectors are also shown.

a large error in the attitude solutions.

Shukla and Wilson quote an error of 10° for their Cet XR-2 position (see error circle in Figure 8.5) and the error given for the Cet XR-1 position in Barnden and Francey (1969) was 15°. This 15° error could arise if the diagonal detector peak was due to a statistical variation rather than a true source sighting. There would then be some uncertainty in the rocket declination of the source responsible for the vertical detector countrate peak. However the rocket azimuth of this peak is accurate to less than 5°. The minimum separation of the two positions obtained by changing the Cet XR-1 rocket declination is 10°. Thus the errors in the source positions do overlap (see Figure 8.6) indicating that these observations may have been of the same source.

On the other hand if both attitude solutions are correct and the two observations are of different sources, Cetus XR-2 was not observable on UAT flight III. This may have been wholly due to atmospheric absorption. On the other hand, the intensity of Cet XR-2 may have had a lower intensity at the time of the UAT flight III observation. That is Cet XR-2 may be another strongly variable source similar to Cen XR-2 (Harries and Francey, 1968) and Cen XR-4 (Conner et al, 1969).

Clearly the uncertainty of 15° in the UAT position for Cet XR-1 is most unsatisfactory. Thus one of the main aims of the UAT

flight IV experiment was to obtain an improved position for this source. However this flight was unsuccessful and it was the last flight of that particular programme.

8.5 Observations of other Sources

Results were also obtained on flight III for two other sources. Firstly, from Figure 8.3 it can be seen that every scan by the vertical detector observed the position of the variable source Cen XR-2, but at fairly low collimator response. The observation times for each scan were found, and the scans were then superposed. Although no peak was present it was possible to establish an upper limit of $\sim 1{\cdot}0$ photons cm^{-2} sec^{-1} for the intensity of this source (from 2-8keV).

This source had been observed at an intensity of ~ 20 photons cm^{-2} sec^{-1} in April 1967 (Harries and Francey, 1967; Cooke et al 1967). However by September 1967 the intensity had fallen to $\lesssim 0{\cdot}5$ photons cm^{-2} sec^{-1} (Chodil et al, 1968). Consequently the flight III result is consistent with these results.

Secondly, from Figure 8.3 it can be seen that during the last half of the flight the system C scans were close enough to Cygnus XR-2 to permit the superposition of 8 scans of the vertical detector and 3 scans of the diagonal detector. The result was a small peak $2{\cdot}7\sigma$ above background. Allowing for the collimator responses of the scans this implies a source of $\sim 0{\cdot}8$ photons sec^{-1} cm^{-2}. This is in reasonable agreement with other observations (Gorenstein et al, 1967;

Francey, 1971). This was the strongest known source which was observed on this flight, and as such is the only indication that the system 3 detectors were operating satisfactorily to the end of the flight.

APPENDIX 1

The relationship between Rigidity P and Energy E. Let p = particle momentum, m_o = particle rest mass, Ze = particle charge, and c = velocity of light. The magnetic rigidity P of a particle is defined by

$$P = \frac{pc}{Ze}$$

Now $$E = [(pc)^2 + (m_oc^2)^2]^{\frac{1}{2}} - m_oc^2$$

i.e. $$(E + m_oc^2)^2 = (pc)^2 + (m_oc^2)^2$$

i.e. $$(pc)^2 = (E + m_oc^2)^2 - (m_oc^2)^2$$

$$= E(E + 2m_oc^2)$$

Thus $$\left(\frac{pc}{Ze}\right)^2 = P^2 = \frac{1}{Z^2} \cdot \frac{E}{e}\left(\frac{E}{e} + \frac{2m_oc^2}{e}\right) \qquad (A1.1)$$

i.e. $$P(\text{volts}) = \frac{1}{Ze}\sqrt{E(eV)\left(E(eV) + \frac{2m_oc^2}{e}\right)}$$

and $$P(GV) = \frac{1}{Ze}\sqrt{E(GEV)\ E(GeV) + \frac{2m_oc^2}{10^9 e}} \qquad (A1.2)$$

from A1.1 $$P^2Z^2 = E^2 + E\,\frac{2m_oc^2}{e}$$ (P in volts, E in eV)

i.e. $$E^2 + \frac{2m_oc^2E}{e} - P^2Z^2 = 0$$

so $$E = -\frac{m_oc^2}{e} \pm \frac{1}{2}\sqrt{\left(\frac{2m_oc^2}{e}\right)^2 + 4P^2Z^2} \qquad (A1.3)$$

i.e. $$E(eV) = -\frac{m_oc^2}{e} + \sqrt{\left(\frac{m_oc^2}{e}\right)^2 + P^2(\text{volts})Z^2}$$

Equations A1.2 and A1.3 relate rigidity to energy and vice-versa.

APPENDIX 2

The Helio-asymptotic directions (at r = 10AU) for equatorial arrival ($\theta_A = 90^\circ$) for 24 equispaced arrival longitudes ϕ_A. A 4-sector spiral magnetic field model was used with $B_E = 5{\cdot}455\gamma$ and garden hose angle = 50°. Helio-asymptotic directions are given for the Earth in 3 different positions relative to the sector structure (i.e. $\Delta = 60^\circ$, 30° and 0° as in Figure 2.1b).

$\Delta=60^\circ$	75GeV		100GeV		200GeV		400GeV	
ϕ_A	Λ	Ψ	Λ	Ψ	Λ	Ψ	Λ	Ψ
0	9.2	342.2	-.7	352.5	-1.7	358.4	-1.1	359.6
15	1.6	1.3	-4.6	8.7	-3.4	13.6	-1.8	14.7
30	-4.0	18.1	-8.7	24.4	-5.3	28.8	-2.7	29.7
45	-9.9	33.7	-13.0	39.7	-7.2	43.9	-3.4	44.7
60	-13.4	48.2	-14.1	54.7	-7.4	58.9	-3.6	59.7
75	33.3	350.0	-15.2	69.3	-7.5	73.9	-3.7	74.7
90	21.8	275.4	-18.0	82.7	-8.1	88.8	-4.0	89.7
105	43.4	340.1	-14.3	329.6	-9.8	103.6	-4.6	104.7
120	40.7	324.1	33.1	293.6	-13.1	117.1	-5.8	119.6
135	32.5	313.6	34.3	356.7	-19.8	127.5	-7.9	133.8
150	-6.9	242.6	27.1	351.5	-18.5	123.3	-11.6	144.8
165	29.4	324.5	16.2	284.2	22.8	348.7	-3.1	142.3
180	-.3	263.9	2.9	342.8	-5.6	92.7	-.6	108.8
195	-3.1	322.0	-39.7	56.7	-40.4	79.0	-18.0	246.5
210	-49.7	24.4	-50.0	32.2	-66.4	27.2	-8.3	227.0
225	-43.4	356.6	-45.5	351.4	-50.6	296.5	-14.9	224.7
240	-29.7	328.7	-30.0	318.5	-27.0	277.3	-15.4	251.3
255	-15.2	308.1	-15.9	299.9	-13.1	274.4	-7.5	260.9
270	-6.5	293.7	-6.8	290.3	-5.6	278.2	-3.1	272.4
285	-.9	283.5	-.9	287.5	-.9	286.4	-.6	285.4
300	3.6	276.9	3.7	291.1	1.9	298.2	.9	299.6
315	7.4	274.6	7.5	301.7	2.6	312.3	1.2	314.4
330	13.4	286.1	6.6	317.8	1.6	327.6	.9	329.4
345	16.4	318.0	3.4	335.4	0.0	343.0	.2	344.5

$\Delta=30^\circ$	75GeV		100GeV		200GeV		400GeV	
ϕ_A	Λ	Ψ	Λ	Ψ	Λ	Ψ	Λ	Ψ
0	13.0	233.3	53.5	321.1	19.9	365.5	9.4	259.2
15	16.1	247.4	57.8	345.5	19.3	12.4	9.0	14.4
30	26.8	263.8	61.6	9.9	18.3	28.3	8.6	29.6
45	40.3	282.7	73.8	38.2	17.5	44.2	8.0	44.8
60	57.9	301.3	28.6	265.5	15.4	60.1	7.5	60.0
75	21.6	215.0	39.8	288.7	15.9	76.4	7.0	75.2
90	40.0	271.0	-16.9	126.9	17.8	93.3	7.1	90.6
105	21.8	230.5	9.6	229.6	21.0	111.3	8.0	106.0
120	20.4	237.0	44.4	290.5	27.9	131.9	9.4	121.6
135	24.3	241.2	54.4	278.8	49.0	170.4	12.7	137.2
150	16.8	240.9	48.3	275.4	47.4	344.1	24.0	152.3
165	13.8	229.7	30.8	279.7	40.4	346.6	59.6	330.0
180	23.1	258.7	46.5	322.8	36.8	307.7	-13.0	356.7
195	8.0	201.1	20.8	284.2	27.6	1.7	59.4	8.4
210	19.1	275.5	-3.2	17.7	33.3	293.0	32.9	243.1
225	6.0	244.6	-11.5	347.3	9.9	254.0	9.2	235.6
240	3.5	214.6	-5.8	317.1	-2.2	242.2	0.0	241.1
255	11.3	191.3	5.3	296.9	-5.5	274.3	-2.9	254.5
270	10.2	177.7	14.9	283.8	3.0	277.4	.9	272.2
285	9.2	175.1	21.2	276.1	8.3	285.0	3.8	285.1
300	9.8	184.3	25.5	273.3	12.4	296.0	6.1	299.1
315	10.7	197.5	29.6	275.7	15.3	309.6	8.7	313.8
330	10.9	209.2	35.7	284.0	17.7	324.7	8.9	328.8
345	11.6	220.7	43.6	299.8	20.0	340.4	9.7	344.0
$\Delta=0^\circ$								
0	36.8	224.2	25.5	215.7	34.9	353.1	16.8	358.6
15	41.4	237.6	27.0	223.6	37.1	10.2	17.5	14.1
30	-15.3	86.4	29.8	234.3	37.7	27.6	17.6	29.5
45	20.1	204.9	34.1	247.7	38.5	45.4	17.7	45.1
60	49.0	213.5	19.9	237.2	39.3	63.9	17.8	60.7
75	73.5	119.5	-21.2	68.5	40.4	83.5	17.9	76.4
90	63.4	170.1	-21.0	37.8	42.4	105.7	18.3	92.4
105	-41.1	63.5	42.5	219.2	48.7	133.9	19.8	108.8
120	-31.9	232.2	-11.9	80.5	56.9	179.1	23.6	125.8
135	63.0	300.8	-14.9	109.1	38.0	279.0	31.1	144.3
150	51.2	116.2	.1	212.9	19.0	277.3	48.2	168.3
165	17.6	210.6	74.1	117.1	35.4	298.7	70.6	214.7
180	61.8	210.7	-3.0	226.9	67.4	185.7	41.5	154.2
195	-31.6	72.2	49.0	270.3	55.9	113.6	48.6	113.5
210	47.4	249.8	68.0	201.0	76.6	49.0	68.1	225.5
225	39.8	217.7	81.3	247.7	61.4	290.8	34.8	242.8
240	33.0	195.7	67.8	274.9	37.8	273.8	19.9	250.7
255	27.7	182.4	54.1	267.6	25.7	271.4	13.0	260.3
270	25.0	175.2	45.2	257.8	20.5	274.9	9.7	271.7
285	25.5	172.6	43.5	244.3	19.5	282.3	9.5	284.5
300	28.5	175.6	41.4	229.0	21.8	292.7	10.7	298.4
315	30.2	186.2	37.5	220.4	25.6	305.6	12.6	313.0
330	31.8	199.1	32.1	214.3	28.8	320.5	14.3	328.0
345	33.9	211.7	26.9	212.0	32.0	336.5	15.6	343.3

APPENDIX 3

To show that the phase difference $\Psi_2 - \Psi_1$ between two cosmic ray orbits (1) and (2) which emanate from point P with pitch angles θ_{10} and $\theta_{10} + \delta\beta$.

Consider two cosmic ray orbits (1) and (2) which emanate from a point P with pitch angles θ_{10} and $\theta_{20} = \theta_{10} + d\beta$. The phases Ψ_1 and Ψ_2 of the orbits are equal at P. We require to show that at the points where these orbits intersect a plane which is normal to the local interplanetary magnetic field line

$$\Psi_1 - \Psi_2 \quad \alpha \quad d\beta$$

Now gyrofrequency ω for particle, charge e, mass m in a magnetic field B is

$$\omega = \frac{eB}{mc}$$

Now
$$\Psi = \int \frac{eB}{mc} \cdot dt = \int \frac{eB}{mc} \frac{dt}{dx_\parallel} \cdot dx_\parallel$$
$$= \int \frac{eB}{mc} \frac{1}{v_\parallel} \cdot dx_\parallel$$

where $x_\parallel$ and $v_\parallel$ are the components of the orbit length and particle density velocity parallel to the interplanetary magnetic field.

B is considered to be the same for both orbits where they cross any given plane normal to the local magnetic field.

Thus $\Psi_1 - \Psi_2 = \int \frac{eB}{mc} \left(\frac{1}{v_{\parallel 1}} - \frac{1}{v_{\parallel 2}} \right) \cdot dx_\parallel$

$$= \int \frac{eB}{mcv} \left(\frac{1}{\cos\theta_1} - \frac{1}{\cos\theta_2} \right) . \, dx_{\parallel} \qquad \text{(A3.1)}$$

where θ_1 and θ_2 are the pitch angles of orbits (1) and (2) at the plane in question.

We now derive an approximation for $\frac{1}{\cos\theta_1} - \frac{1}{\cos\theta_2}$

The Alfvén approximation yields

$$\frac{\sin^2\theta_1}{B} = \kappa_1 = \frac{\sin^2\theta_{10}}{B_o}$$

and $$\frac{\sin^2\theta_2}{B} = \kappa_2 = \frac{\sin^2\theta_{20}}{B_o}$$

But since $\theta_{20} = \theta_{10} + \delta\beta$

$$\kappa_2 = \frac{\sin^2(\theta_{10}+\delta\beta)}{B_o}$$

$$\approx \frac{\sin^2\theta_{10}}{B_o} + \frac{2\sin\theta_{10}\cos\theta_{10}\delta\beta}{B_o} \quad \text{for small } \delta\beta$$

$$= \kappa_1 + \sin 2\theta_{10} \, \frac{\delta\beta}{B_o}$$

Hence $\cos\theta_1 = (1 - \sin^2\theta_1)^{\frac{1}{2}} = (1 - \kappa_1 B)^{\frac{1}{2}}$

$$\cos\theta_2 = (1 - \sin^2\theta_2)^{\frac{1}{2}} = (1 - \kappa_1 B - \sin 2\theta_{10} \, \frac{B}{B_o} \delta\beta)^{\frac{1}{2}}$$

So $$\frac{1}{\cos\theta_1} - \frac{1}{\cos\theta_2} = \frac{1}{(1-\kappa_1 B)^{\frac{1}{2}}} - \frac{1}{(1-\kappa_1 B - \sin 2\theta_{10} \frac{B}{B_o} \delta\beta)^{\frac{1}{2}}}$$

$$= \frac{1}{(1-\kappa_1 B)^{3/2}} \left[1 - \left(1 - \frac{\sin 2\theta_{10}}{2(1-\kappa_1 B)} \frac{B}{B_o} \delta\beta \right)^{-\frac{1}{2}} \right]$$

and using $(1-z)^{-\frac{1}{2}} = 1 + \frac{1}{2}z$ for small z

$$= \frac{1}{(1-\kappa_1 B)^{3/2}} \left[1 - \left(1 + \frac{\sin 2\theta_{10}}{2(1-\kappa_1 B)} \frac{B}{B_o} \delta\beta \right) \right]$$

$$= - \frac{\frac{1}{2}\sin 2\theta_{10}}{(1-\kappa_1 B)^{3/2}} \frac{B}{B_o} \delta\beta$$

Substituting in Equation A3.1

$$\Psi_1 - \Psi_2 = - \frac{\frac{1}{2}\sin 2\theta_{10}\, e}{mcvB_o} d\beta \int \frac{B^2}{(1-\kappa_1 B)^{3/2}} \cdot dx_{\parallel}$$

i.e. $\Psi_1 - \Psi_2 \sim d\beta$

APPENDIX 4

The Origin-of-Scatter coefficients of the neutron monitor at Deep River, derived using MFP set 2 ($\lambda \alpha r^1$) for the scattering mean free paths. The coefficients here are expressed in percent of the total recorded flux. Coefficients are given for the five rigidity intervals in Table 5.4 and also over the whole rigidity range 0-60GV. For Deep River, N(>60) = 22·58%.

The coefficient given for r = J is the relative flux *last*-scattered between $\frac{J}{25}$ AU and $\frac{J+1}{25}$ AU, for the rigidity interval and time of day in question. The value given for r = 75 is the relative flux which is *last*-scattered outside r = 3·0 AU.

ORIGIN OF SCATTER COEFFICIENTS FOR RIGIDITY INTERVAL 1 OF 5 FOR 75 RADIAL INCREMENTS

HOUR UT R	2	4	6	8	10	12	14	16	18	20	22	24	R
1	0.000	0.000	0.000	0.000	0.000	0.000	0.000	0.000	0.000	0.000	0.000	0.000	1
2	0.000	0.000	0.000	0.000	0.000	0.000	0.000	0.000	0.000	0.000	0.000	0.000	2
3	0.000	0.000	0.000	0.000	0.000	0.000	0.000	0.000	0.000	0.000	0.000	0.000	3
4	0.000	0.000	0.000	0.000	0.000	0.000	0.000	0.000	0.000	0.000	0.000	0.000	4
5	0.000	0.000	0.000	0.000	0.000	0.000	0.000	0.000	0.000	0.000	0.000	0.000	5
6	0.000	0.000	0.000	0.000	0.000	0.000	0.000	0.000	0.000	0.000	0.000	0.000	6
7	0.000	0.000	0.000	0.000	0.000	0.000	0.000	0.000	0.000	0.000	0.000	0.000	7
8	0.000	0.000	0.000	0.000	0.000	0.000	0.000	0.000	0.000	0.000	0.000	0.000	8
9	0.000	0.000	0.000	0.000	0.000	0.000	0.000	0.000	0.000	0.000	0.000	0.000	9
10	0.000	0.000	0.000	0.000	.000	.000	0.000	0.000	0.000	0.000	0.000	0.000	10
11	0.000	0.000	0.000	0.000	.000	.000	0.000	0.000	0.000	0.000	0.000	0.000	11
12	0.000	0.000	0.000	0.000	.000	.000	0.000	0.000	0.000	0.000	0.000	0.000	12
13	0.000	0.000	0.000	0.000	.000	.000	0.000	0.000	0.000	0.000	0.000	0.000	13
14	0.000	0.000	0.000	0.000	.001	.001	0.000	0.000	0.000	0.000	0.000	0.000	14
15	0.000	0.000	0.000	.000	.003	.002	.000	0.000	0.000	0.000	0.000	0.000	15
16	0.000	0.000	0.000	.000	.007	.006	.000	0.000	0.000	0.000	0.000	0.000	16
17	0.000	0.000	.000	.001	.018	.014	.001	0.000	0.000	0.000	0.000	0.000	17
18	0.000	0.000	.000	.004	.040	.033	.004	0.000	0.000	0.000	0.000	0.000	18
19	0.000	.000	.000	.016	.088	.077	.016	0.000	0.000	0.000	0.000	0.000	19
20	0.000	.000	.002	.062	.203	.181	.060	0.000	0.000	0.000	0.000	0.000	20
21	0.000	.003	.015	.212	.449	.412	.199	0.000	0.000	0.000	0.000	0.000	21
22	.000	.034	.084	.690	.901	.859	.609	0.000	0.000	0.000	0.000	0.000	22
23	.019	.309	.480	2.202	2.054	1.869	1.757	.019	0.000	0.000	0.000	0.000	23
24	2.782	2.454	9.500	6.895	6.317	6.625	4.637	7.260	0.000	0.000	0.000	0.000	24
25	4.315	6.559	.001	0.000	0.000	.005	2.748	2.405	8.676	6.513	5.980	6.343	25
26	1.726	.590	.000	0.000	0.000	0.000	.051	.338	1.125	2.202	2.029	1.809	26
27	.701	.100	.000	0.000	0.000	0.000	.002	.050	.216	.801	.978	.922	27
28	.298	.023	0.000	0.000	0.000	0.000	.000	.008	.048	.319	.503	.473	28
29	.130	.006	0.000	0.000	0.000	0.000	.000	.001	.012	.134	.268	.248	29
30	.059	.002	0.000	0.000	0.000	0.000	0.000	.000	.003	.060	.146	.132	30
31	.027	.001	0.000	0.000	0.000	0.000	0.000	.000	.001	.028	.079	.071	31
32	.013	.000	0.000	0.000	0.000	0.000	0.000	.000	.000	.013	.044	.038	32
33	.006	.000	0.000	0.000	0.000	0.000	0.000	0.000	.000	.006	.024	.021	33
34	.003	.000	0.000	0.000	0.000	0.000	0.000	0.000	.000	.003	.014	.012	34
35	.002	.000	0.000	0.000	0.000	0.000	0.000	0.000	.000	.002	.007	.006	35
36	.001	.000	0.000	0.000	0.000	0.000	0.000	0.000	.000	.001	.004	.004	36

$\zeta_1(r,T)$

0.0 - 4.5 GV

200

$\tau_{15}(x,T)$ 0.0 - 4.5 GV 201

37	.000	0.000	0.000	0.000	0.000	0.000	0.000	0.000	0.000	.000	.002	.002	37
38	.000	0.000	0.000	0.000	0.000	0.000	0.000	0.000	0.000	.000	.001	.001	38
39	.000	0.000	0.000	0.000	0.000	0.000	0.000	0.000	0.000	.000	.001	.001	39
40	.000	0.000	0.000	0.000	0.000	0.000	0.000	0.000	0.000	.000	.000	.000	40
41	.000	0.000	0.000	0.000	0.000	0.000	0.000	0.000	0.000	.000	.000	.000	41
42	.000	0.000	0.000	0.000	0.000	0.000	0.000	0.000	0.000	.000	.000	.000	42
43	.000	0.000	0.000	0.000	0.000	0.000	0.000	0.000	0.000	.000	.000	.000	43
44	0.000	0.000	0.000	0.000	0.000	0.000	0.000	0.000	0.000	0.000	.000	.000	44
45	0.000	0.000	0.000	0.000	0.000	0.000	0.000	0.000	0.000	0.000	.000	.000	45
46	0.000	0.000	0.000	0.000	0.000	0.000	0.000	0.000	0.000	0.000	.000	.000	46
47	0.000	0.000	0.000	0.000	0.000	0.000	0.000	0.000	0.000	0.000	.000	.000	47
48	0.000	0.000	0.000	0.000	0.000	0.000	0.000	0.000	0.000	0.000	.000	0.000	48
49	0.000	0.000	0.000	0.000	0.000	0.000	0.000	0.000	0.000	0.000	0.000	0.000	49
50	0.000	0.000	0.000	0.000	0.000	0.000	0.000	0.000	0.000	0.000	0.000	0.000	50
51	0.000	0.000	0.000	0.000	0.000	0.000	0.000	0.000	0.000	0.000	0.000	0.000	51
52	0.000	0.000	0.000	0.000	0.000	0.000	0.000	0.000	0.000	0.000	0.000	0.000	52
53	0.000	0.000	0.000	0.000	0.000	0.000	0.000	0.000	0.000	0.000	0.000	0.000	53
54	0.000	0.000	0.000	0.000	0.000	0.000	0.000	0.000	0.000	0.000	0.000	0.000	54
55	0.000	0.000	0.000	0.000	0.000	0.000	0.000	0.000	0.000	0.000	0.000	0.000	55
56	0.000	0.000	0.000	0.000	0.000	0.000	0.000	0.000	0.000	0.000	0.000	0.000	56
57	0.000	0.000	0.000	0.000	0.000	0.000	0.000	0.000	0.000	0.000	0.000	0.000	57
58	0.000	0.000	0.000	0.000	0.000	0.000	0.000	0.000	0.000	0.000	0.000	0.000	58
59	0.000	0.000	0.000	0.000	0.000	0.000	0.000	0.000	0.000	0.000	0.000	0.000	59
60	0.000	0.000	0.000	0.000	0.000	0.000	0.000	0.000	0.000	0.000	0.000	0.000	60
61	0.000	0.000	0.000	0.000	0.000	0.000	0.000	0.000	0.000	0.000	0.000	0.000	61
62	0.000	0.000	0.000	0.000	0.000	0.000	0.000	0.000	0.000	0.000	0.000	0.000	62
63	0.000	0.000	0.000	0.000	0.000	0.000	0.000	0.000	0.000	0.000	0.000	0.000	63
64	0.000	0.000	0.000	0.000	0.000	0.000	0.000	0.000	0.000	0.000	0.000	0.000	64
65	0.000	0.000	0.000	0.000	0.000	0.000	0.000	0.000	0.000	0.000	0.000	0.000	65
66	0.000	0.000	0.000	0.000	0.000	0.000	0.000	0.000	0.000	0.000	0.000	0.000	66
67	0.000	0.000	0.000	0.000	0.000	0.000	0.000	0.000	0.000	0.000	0.000	0.000	67
68	0.000	0.000	0.000	0.000	0.000	0.000	0.000	0.000	0.000	0.000	0.000	0.000	68
69	0.000	0.000	0.000	0.000	0.000	0.000	0.000	0.000	0.000	0.000	0.000	0.000	69
70	0.000	0.000	0.000	0.000	0.000	0.000	0.000	0.000	0.000	0.000	0.000	0.000	70
71	0.000	0.000	0.000	0.000	0.000	0.000	0.000	0.000	0.000	0.000	0.000	0.000	71
72	0.000	0.000	0.000	0.000	0.000	0.000	0.000	0.000	0.000	0.000	0.000	0.000	72
73	0.000	0.000	0.000	0.000	0.000	0.000	0.000	0.000	0.000	0.000	0.000	0.000	73
74	0.000	0.000	0.000	0.000	0.000	0.000	0.000	0.000	0.000	0.000	0.000	0.000	74
75	0.000	0.000	0.000	0.000	0.000	0.000	0.000	0.000	0.000	0.000	0.000	0.000	75

ORIGIN OF SCATTER COEFFICIENTS FOR RIGIDITY INTERVAL 2 OF 5 FOR 75 RADIAL INCREMENTS

HOUR UT 2	4	6	8	10	12	14	16	18	20	22	24	
R												R
1	0.000	0.000	0.000	0.000	0.000	0.000	0.000	0.000	0.000	0.000	0.000	0.000	1
2	0.000	0.000	0.000	0.000	0.000	0.000	0.000	0.000	0.000	0.000	0.000	0.000	2
3	0.000	0.000	0.000	0.000	0.000	0.000	0.000	0.000	0.000	0.000	0.000	0.000	3
4	0.000	0.000	0.000	0.000	0.000	.000	.000	0.000	0.000	0.000	0.000	0.000	4
5	0.000	0.000	0.000	0.000	.000	.000	.000	0.000	0.000	0.000	0.000	0.000	5
6	0.000	0.000	0.000	0.000	.000	.001	.000	0.000	0.000	0.000	0.000	0.000	6
7	0.000	0.000	0.000	0.000	.001	.003	.001	0.000	0.000	0.000	0.000	0.000	7
8	0.000	0.000	0.000	0.000	.001	.005	.002	0.000	0.000	0.000	0.000	0.000	8
9	0.000	0.000	0.000	0.000	.003	.010	.004	0.000	0.000	0.000	0.000	0.000	9
10	0.000	0.000	0.000	0.000	.005	.018	.007	0.000	0.000	0.000	0.000	0.000	10
11	0.000	0.000	0.000	0.000	.010	.030	.014	0.000	0.000	0.000	0.000	0.000	11
12	0.000	0.000	0.000	0.000	.024	.050	.029	0.000	0.000	0.000	0.000	0.000	12
13	0.000	0.000	0.000	0.000	.042	.077	.048	0.000	0.000	0.000	0.000	0.000	13
14	0.000	0.000	0.000	0.000	.071	.121	.080	0.000	0.000	0.000	0.000	0.000	14
15	0.000	0.000	0.000	0.000	.128	.184	.130	0.000	0.000	0.000	0.000	0.000	15
16	0.000	0.000	0.000	0.000	.212	.281	.208	0.000	0.000	0.000	0.000	0.000	16
17	0.000	0.000	0.000	.000	.336	.420	.326	.005	0.000	0.000	0.000	0.000	17
18	0.000	0.000	0.000	.005	.526	.604	.502	.067	0.000	0.000	0.000	0.000	18
19	0.000	0.000	0.000	.014	.815	.930	.789	.114	0.000	0.000	0.000	0.000	19
20	0.000	0.000	0.000	.104	1.233	1.288	1.178	.247	0.000	0.000	0.000	0.000	20
21	0.000	0.000	0.000	.801	1.826	1.861	1.779	.801	0.000	0.000	0.000	0.000	21
22	0.000	0.000	0.000	2.327	2.785	2.831	2.777	1.823	0.000	0.000	0.000	0.000	22
23	0.000	0.000	0.000	4.884	4.091	3.886	4.076	4.951	0.000	0.000	0.000	0.000	23
24	0.000	0.000	5.115	9.553	5.592	5.099	5.750	9.690	2.849	0.000	0.000	0.000	24
25	4.858	7.875	10.615	.006	0.000	0.000	0.000	.001	12.858	7.765	4.708	4.229	25
26	3.550	3.996	1.166	.003	0.000	0.000	0.000	.001	1.246	4.130	3.546	3.322	26
27	2.552	2.143	.400	.001	0.000	0.000	0.000	.000	.394	2.205	2.586	2.636	27
28	1.744	1.245	.179	.001	0.000	0.000	0.000	.000	.164	1.298	1.735	1.801	28
29	1.204	.786	.089	.000	0.000	0.000	0.000	.000	.078	.784	1.263	1.278	29
30	.892	.496	.052	.000	0.000	0.000	0.000	.000	.043	.489	.954	.982	30
31	.710	.330	.029	.000	0.000	0.000	0.000	.000	.024	.320	.705	.789	31
32	.523	.230	.018	.000	0.000	0.000	0.000	.000	.015	.212	.523	.631	32
33	.355	.161	.012	.000	0.000	0.000	0.000	.000	.010	.143	.381	.437	33
34	.270	.111	.008	.000	0.000	0.000	0.000	.000	.006	.098	.283	.296	34
35	.230	.082	.005	.000	0.000	0.000	0.000	.000	.004	.071	.228	.260	35
36	.181	.060	.004	.000	0.000	0.000	0.000	.000	.003	.049	.179	.239	36

$\zeta_2(r,T)$ 4.5 - 8.5 GV

37	.133	.045	.002	.000	0.000	0.000	0.000	.000	.002	.035	.131	.179	37
38	.096	.032	.002	.000	0.000	0.000	0.000	.000	.001	.025	.096	.114	38
39	.076	.024	.001	.000	0.000	0.000	0.000	0.000	.001	.019	.078	.084	39
40	.065	.019	.001	.000	0.000	0.000	0.000	0.000	.001	.014	.064	.080	40
41	.055	.015	.001	.000	0.000	0.000	0.000	0.000	.000	.010	.050	.075	41
42	.042	.011	.001	.000	0.000	0.000	0.000	0.000	.000	.008	.038	.058	42
43	.031	.008	.000	0.000	0.000	0.000	0.000	0.000	.000	.006	.029	.040	43
44	.023	.006	.000	0.000	0.000	0.000	0.000	0.000	.000	.005	.024	.027	44
45	.020	.005	.000	0.000	0.000	0.000	0.000	0.000	.000	.004	.019	.023	45
46	.018	.004	.000	0.000	0.000	0.000	0.000	0.000	.000	.003	.015	.023	46
47	.015	.003	.000	0.000	0.000	0.000	0.000	0.000	.000	.002	.013	.021	47
48	.011	.002	.000	0.000	0.000	0.000	0.000	0.000	.000	.002	.010	.016	48
49	.008	.002	.000	0.000	0.000	0.000	0.000	0.000	.000	.001	.008	.010	49
50	.007	.002	.000	0.000	0.000	0.000	0.000	0.000	.000	.001	.006	.007	50
51	.006	.001	.000	0.000	0.000	0.000	0.000	0.000	.000	.001	.005	.007	51
52	.005	.001	.000	0.000	0.000	0.000	0.000	0.000	.000	.001	.004	.007	52
53	.004	.001	.000	0.000	0.000	0.000	0.000	0.000	.000	.000	.004	.006	53
54	.003	.001	.000	0.000	0.000	0.000	0.000	0.000	.000	.000	.003	.005	54
55	.002	.000	.000	0.000	0.000	0.000	0.000	0.000	.000	.000	.002	.003	55
56	.002	.000	.000	0.000	0.000	0.000	0.000	0.000	.000	.000	.002	.002	56
57	.002	.000	.000	0.000	0.000	0.000	0.000	0.000	.000	.000	.001	.002	57
58	.002	.000	.000	0.000	0.000	0.000	0.000	0.000	.000	.000	.001	.002	58
59	.001	.000	.000	0.000	0.000	0.000	0.000	0.000	0.000	.000	.001	.002	59
60	.001	.000	0.000	0.000	0.000	0.000	0.000	0.000	0.000	.000	.001	.002	60
61	.001	.000	0.000	0.000	0.000	0.000	0.000	0.000	0.000	.000	.001	.001	61
62	.001	.000	0.000	0.000	0.000	0.000	0.000	0.000	0.000	.000	.001	.001	62
63	.001	.000	0.000	0.000	0.000	0.000	0.000	0.000	0.000	.000	.000	.001	63
64	.000	.000	0.000	0.000	0.000	0.000	0.000	0.000	0.000	.000	.000	.001	64
65	.000	.000	0.000	0.000	0.000	0.000	0.000	0.000	0.000	.000	.000	.001	65
66	.000	.000	0.000	0.000	0.000	0.000	0.000	0.000	0.000	.000	.000	.001	66
67	.000	.000	0.000	0.000	0.000	0.000	0.000	0.000	0.000	.000	.000	.000	67
68	.000	.000	0.000	0.000	0.000	0.000	0.000	0.000	0.000	.000	.000	.000	68
69	.000	.000	0.000	0.000	0.000	0.000	0.000	0.000	0.000	.000	.000	.000	69
70	.000	.000	0.000	0.000	0.000	0.000	0.000	0.000	0.000	.000	.000	.000	70
71	.000	.000	0.000	0.000	0.000	0.000	0.000	0.000	0.000	.000	.000	.000	71
72	.000	.000	0.000	0.000	0.000	0.000	0.000	0.000	0.000	.000	.000	.000	72
73	.000	.000	0.000	0.000	0.000	0.000	0.000	0.000	0.000	.000	.000	.000	73
74	.000	.000	0.000	0.000	0.000	0.000	0.000	0.000	0.000	0.000	.000	.000	74
75	.000	.000	0.000	0.000	0.000	0.000	0.000	0.000	0.000	.000	.000	.000	75

ORIGIN OF SCATTER COEFFICIENTS FOR RIGIDITY INTERVAL 3 OF 5 FOR 75 RADIAL INCREMENTS

HOUR UT	2	4	6	8	10	12	14	16	18	20	22	24	
R													R
1	0.000	0.000	0.000	0.000	0.000	0.000	0.000	0.000	0.000	0.000	0.000	0.000	1
2	0.000	0.000	0.000	0.000	0.000	0.000	0.000	0.000	0.000	0.000	0.000	0.000	2
3	0.000	0.000	0.000	0.000	0.000	0.000	0.000	0.000	0.000	0.000	0.000	0.000	3
4	0.000	0.000	0.000	0.000	0.000	.007	.003	0.000	0.000	0.000	0.000	0.000	4
5	0.000	0.000	0.000	0.000	0.000	.040	.019	0.000	0.000	0.000	0.000	0.000	5
6	0.000	0.000	0.000	0.000	0.000	.052	.026	0.000	0.000	0.000	0.000	0.000	6
7	0.000	0.000	0.000	0.000	0.000	.074	.038	0.000	0.000	0.000	0.000	0.000	7
8	0.000	0.000	0.000	0.000	0.000	.104	.054	0.000	0.000	0.000	0.000	0.000	8
9	0.000	0.000	0.000	0.000	0.000	.142	.076	0.000	0.000	0.000	0.000	0.000	9
10	0.000	0.000	0.000	0.000	0.000	.192	.104	0.000	0.000	0.000	0.000	0.000	10
11	0.000	0.000	0.000	0.000	.052	.252	.182	0.000	0.000	0.000	0.000	0.000	11
12	0.000	0.000	0.000	0.000	.188	.323	.342	0.000	0.000	0.000	0.000	0.000	12
13	0.000	0.000	0.000	0.000	.210	.429	.416	0.000	0.000	0.000	0.000	0.000	13
14	0.000	0.000	0.000	0.000	.261	.505	.502	0.000	0.000	0.000	0.000	0.000	14
15	0.000	0.000	0.000	0.000	.532	.660	.647	0.000	0.000	0.000	0.000	0.000	15
16	0.000	0.000	0.000	0.000	.710	.846	.800	0.000	0.000	0.000	0.000	0.000	16
17	0.000	0.000	0.000	0.000	.926	.992	.997	.179	0.000	0.000	0.000	0.000	17
18	0.000	0.000	0.000	0.000	1.242	1.204	1.227	.816	0.000	0.000	0.000	0.000	18
19	0.000	0.000	0.000	0.000	1.505	1.438	1.440	.888	0.000	0.000	0.000	0.000	19
20	0.000	0.000	0.000	0.000	1.849	1.897	1.852	2.094	0.000	0.000	0.000	0.000	20
21	0.000	0.000	0.000	0.000	2.406	2.474	2.451	2.809	0.000	0.000	0.000	0.000	21
22	0.000	0.000	0.000	1.909	2.993	2.713	2.784	3.638	0.000	0.000	0.000	0.000	22
23	0.000	0.000	0.000	7.374	3.439	2.752	2.934	4.493	0.000	0.000	0.000	0.000	23
24	0.000	0.000	0.000	10.256	4.017	3.251	3.449	5.317	5.746	0.000	0.000	0.000	24
25	2.372	3.926	11.584	.217	.002	.000	.000	.020	8.781	5.656	2.934	2.173	25
26	2.028	3.065	3.161	.141	.002	.000	.000	.014	2.194	3.917	2.443	1.863	26
27	2.022	2.544	1.634	.091	.002	.000	.000	.012	1.040	2.509	2.230	1.943	27
28	1.953	1.889	1.020	.063	.001	.000	.000	.010	.673	1.710	1.912	1.949	28
29	1.618	1.421	.638	.057	.001	.000	.000	.008	.440	1.284	1.519	1.662	29
30	1.235	1.154	.488	.039	.001	.000	.000	.006	.293	.975	1.200	1.281	30
31	.977	.944	.329	.030	.001	.000	.000	.005	.221	.761	1.016	.984	31
32	.868	.793	.272	.023	.001	.000	.000	.005	.175	.595	.875	.853	32
33	.795	.663	.200	.021	.001	.000	.000	.004	.135	.457	.748	.775	33
34	.721	.549	.165	.019	.001	.000	.000	.003	.107	.366	.652	.707	34
35	.643	.461	.130	.015	.001	0.000	.000	.003	.080	.297	.579	.640	35
36	.560	.370	.100	.012	.000	0.000	.000	.002	.065	.272	.512	.580	36

$\zeta_3(r,T)$ 8.5 - 15.0 GV

37	.494	.304	.091	.010	.000	0.000	.000	.002	.056	.225	.445	.536	37
38	.456	.272	.074	.008	.000	0.000	.000	.002	.049	.174	.373	.511	38
39	.411	.246	.059	.007	.000	0.000	.000	.002	.041	.143	.309	.467	39
40	.338	.218	.053	.007	.000	0.000	.000	.002	.033	.121	.255	.374	40
41	.266	.190	.044	.006	.000	0.000	.000	.001	.026	.107	.224	.276	41
42	.214	.155	.036	.005	.000	0.000	.000	.001	.022	.095	.218	.195	42
43	.195	.127	.031	.004	.000	0.000	.000	.001	.021	.086	.207	.172	43
44	.205	.109	.029	.003	.000	0.000	.000	.001	.018	.074	.193	.198	44
45	.212	.097	.024	.003	.000	0.000	.000	.001	.016	.059	.166	.227	45
46	.206	.091	.021	.003	.000	0.000	.000	.001	.014	.050	.137	.242	46
47	.185	.084	.019	.003	.000	0.000	.000	.001	.012	.046	.114	.228	47
48	.149	.075	.017	.003	.000	0.000	.000	.001	.010	.039	.096	.187	48
49	.116	.066	.013	.002	.000	0.000	.000	.000	.008	.034	.086	.143	49
50	.088	.057	.012	.002	.000	0.000	.000	.000	.008	.031	.081	.098	50
51	.071	.047	.011	.002	.000	0.000	.000	.000	.007	.030	.077	.065	51
52	.070	.041	.010	.001	.000	0.000	.000	.000	.006	.026	.074	.055	52
53	.077	.037	.009	.001	.000	0.000	.000	.000	.006	.022	.068	.069	53
54	.082	.034	.007	.001	.000	0.000	.000	.000	.005	.019	.062	.083	54
55	.078	.031	.007	.001	.000	0.000	.000	.000	.004	.016	.053	.088	55
56	.074	.029	.006	.001	.000	0.000	.000	.000	.004	.015	.046	.091	56
57	.061	.026	.005	.001	.000	0.000	.000	.000	.003	.013	.040	.079	57
58	.051	.024	.005	.001	.000	0.000	.000	.000	.003	.011	.034	.069	58
59	.042	.021	.004	.001	.000	0.000	.000	.000	.003	.011	.030	.058	59
60	.037	.019	.004	.001	.000	0.000	.000	.000	.002	.011	.028	.047	60
61	.032	.016	.004	.001	.000	0.000	.000	.000	.002	.010	.027	.035	61
62	.027	.014	.003	.000	.000	0.000	.000	.000	.002	.008	.025	.025	62
63	.026	.013	.003	.000	.000	0.000	.000	.000	.002	.007	.025	.021	63
64	.027	.012	.003	.000	.000	0.000	.000	.000	.002	.006	.024	.022	64
65	.027	.011	.002	.000	.000	0.000	.000	.000	.001	.006	.021	.027	65
66	.026	.010	.002	.000	.000	0.000	.000	.000	.001	.005	.018	.030	66
67	.025	.009	.002	.000	.000	0.000	.000	.000	.001	.004	.016	.032	67
68	.023	.009	.002	.000	.000	0.000	.000	.000	.001	.004	.013	.032	68
69	.021	.008	.001	.000	.000	0.000	0.000	.000	.001	.004	.012	.030	69
70	.018	.007	.001	.000	.000	0.000	0.000	.000	.001	.004	.010	.026	70
71	.015	.006	.001	.000	.000	0.000	0.000	.000	.001	.004	.009	.021	71
72	.012	.005	.001	.000	.000	0.000	0.000	.000	.001	.003	.009	.015	72
73	.010	.005	.001	.000	.000	0.000	0.000	.000	.001	.003	.009	.009	73
74	.008	.004	.001	.000	.000	0.000	0.000	.000	.001	.002	.009	.005	74
75	.078	.040	.008	.001	.000	0.000	.000	.000	.005	.021	.086	.051	75

ORIGIN OF SCATTER COEFFICIENTS FOR RIGIDITY INTERVAL 4 OF 5 FOR 75 RADIAL INCREMENTS

OUR UT R	2	4	6	8	10	12	14	16	18	20	22	24	R
1	0.000	0.000	0.000	0.000	0.000	0.000	0.000	0.000	0.000	0.000	0.000	0.000	1
2	0.000	0.000	0.000	0.000	0.000	0.000	0.000	0.000	0.000	0.000	0.000	0.000	2
3	0.000	0.000	0.000	0.000	0.000	0.000	0.000	0.000	0.000	0.000	0.000	0.000	3
4	0.000	0.000	0.000	0.000	.002	.012	.005	0.000	0.000	0.000	0.000	0.000	4
5	0.000	0.000	0.000	0.000	.047	.162	.074	0.000	0.000	0.000	0.000	0.000	5
6	0.000	0.000	0.000	0.000	.039	.139	.063	0.000	0.000	0.000	0.000	0.000	6
7	0.000	0.000	0.000	0.000	.040	.152	.069	0.000	0.000	0.000	0.000	0.000	7
8	0.000	0.000	0.000	0.000	.044	.173	.078	0.000	0.000	0.000	0.000	0.000	8
9	0.000	0.000	0.000	0.000	.049	.200	.090	0.000	0.000	0.000	0.000	0.000	9
10	0.000	0.000	0.000	0.000	.052	.221	.099	0.000	0.000	0.000	0.000	0.000	10
11	0.000	0.000	0.000	0.000	.241	.493	.393	.042	0.000	0.000	0.000	0.000	11
12	0.000	0.000	0.000	0.000	.397	.696	.639	.073	0.000	0.000	0.000	0.000	12
13	0.000	0.000	0.000	0.000	.349	.659	.576	.060	0.000	0.000	0.000	0.000	13
14	0.000	0.000	0.000	0.000	.338	.707	.579	.054	0.000	0.000	0.000	0.000	14
15	0.000	0.000	0.000	.077	.659	.905	.881	.108	0.000	0.000	0.000	0.000	15
16	0.000	0.000	0.000	.092	.800	.960	.999	.133	0.000	0.000	0.000	0.000	16
17	0.000	0.000	0.000	.122	.947	1.058	1.138	.297	0.000	0.000	0.000	0.000	17
18	0.000	0.000	0.000	.237	1.200	1.347	1.438	.611	0.000	0.000	0.000	0.000	18
19	0.000	0.000	0.000	.202	1.198	1.523	1.525	.499	0.000	0.000	0.000	0.000	19
20	0.000	0.000	0.000	.665	1.799	1.585	1.637	1.681	.124	0.000	0.000	0.000	20
21	0.000	0.000	0.000	.748	1.859	1.496	1.581	1.801	.167	0.000	0.000	0.000	21
22	0.000	0.000	0.000	2.007	2.004	1.421	1.565	2.575	.145	0.000	0.000	0.000	22
23	0.000	0.000	.203	3.290	1.992	1.391	1.555	3.109	.556	0.000	0.000	0.000	23
24	0.000	0.000	.878	3.967	2.102	1.629	1.768	3.234	2.178	.037	0.000	0.000	24
25	.865	1.637	4.481	1.202	.091	.031	.041	.360	4.314	2.461	1.070	.726	25
26	.795	1.307	2.080	.605	.083	.026	.035	.250	1.628	1.550	.954	.663	26
27	.705	1.225	1.213	.475	.075	.022	.030	.229	1.061	1.429	.834	.604	27
28	.759	1.117	.995	.339	.067	.021	.029	.179	.811	1.156	.883	.682	28
29	.813	.990	.715	.268	.063	.021	.028	.157	.640	.950	.902	.768	29
30	.831	.863	.622	.246	.057	.022	.030	.146	.583	.808	.849	.815	30
31	.794	.723	.545	.233	.051	.023	.031	.132	.459	.654	.767	.799	31
32	.716	.619	.495	.192	.045	.022	.029	.106	.370	.580	.672	.741	32
33	.629	.570	.416	.160	.042	.021	.027	.093	.332	.556	.593	.644	33
34	.518	.522	.342	.146	.040	.020	.026	.088	.285	.500	.510	.515	34
35	.443	.485	.290	.140	.038	.019	.023	.084	.235	.440	.461	.420	35
36	.402	.443	.269	.128	.037	.018	.022	.077	.215	.394	.432	.359	36

$\Sigma_4(x,T)$ 15.0 - 30.0 GV 206

$\zeta_4(r,T)$ 15.0 - 30.0 GV 207

37	.380	.394	.249	.113	.034	.016	.019	.069	.209	.354	.407	.335	37
38	.383	.361	.215	.101	.031	.015	.018	.065	.193	.321	.402	.351	38
39	.387	.326	.196	.094	.030	.013	.016	.064	.187	.293	.383	.374	39
40	.371	.308	.183	.087	.029	.012	.014	.062	.179	.279	.355	.380	40
41	.351	.299	.185	.084	.028	.011	.014	.060	.167	.273	.328	.377	41
42	.327	.293	.178	.082	.026	.011	.013	.057	.144	.258	.303	.356	42
43	.307	.271	.175	.076	.023	.011	.014	.050	.130	.233	.278	.335	43
44	.296	.259	.160	.069	.022	.011	.014	.045	.118	.213	.270	.316	44
45	.275	.243	.144	.064	.021	.011	.015	.041	.108	.198	.253	.289	45
46	.260	.226	.124	.060	.019	.011	.015	.038	.098	.185	.246	.261	46
47	.250	.213	.112	.060	.019	.011	.014	.038	.089	.175	.243	.236	47
48	.244	.195	.101	.059	.018	.010	.013	.038	.079	.163	.242	.219	48
49	.233	.178	.097	.057	.018	.010	.013	.037	.073	.150	.228	.209	49
50	.250	.169	.091	.051	.018	.009	.012	.034	.074	.144	.232	.236	50
51	.242	.154	.086	.045	.017	.010	.011	.031	.073	.138	.217	.242	51
52	.234	.146	.081	.040	.017	.010	.012	.029	.073	.136	.202	.251	52
53	.220	.136	.073	.037	.015	.009	.011	.026	.073	.127	.186	.245	53
54	.205	.125	.069	.034	.015	.009	.010	.026	.072	.115	.173	.239	54
55	.175	.124	.070	.035	.015	.008	.009	.025	.071	.110	.154	.211	55
56	.160	.119	.067	.034	.014	.008	.009	.025	.065	.101	.143	.195	56
57	.138	.124	.072	.035	.014	.007	.008	.026	.061	.100	.132	.164	57
58	.122	.115	.071	.036	.014	.007	.008	.026	.057	.091	.121	.145	58
59	.108	.115	.073	.036	.013	.006	.007	.026	.052	.088	.114	.119	59
60	.099	.112	.070	.034	.013	.006	.007	.025	.047	.084	.110	.095	60
61	.096	.105	.063	.031	.011	.006	.007	.023	.044	.081	.105	.081	61
62	.098	.096	.056	.028	.011	.006	.007	.021	.040	.075	.102	.073	62
63	.105	.094	.050	.026	.010	.006	.007	.019	.037	.076	.104	.080	63
64	.119	.089	.046	.026	.010	.006	.008	.018	.034	.075	.108	.102	64
65	.126	.082	.040	.025	.009	.006	.007	.018	.031	.071	.106	.119	65
66	.133	.077	.038	.025	.009	.006	.007	.017	.029	.069	.108	.135	66
67	.132	.074	.036	.023	.009	.005	.007	.016	.029	.064	.105	.141	67
68	.134	.069	.035	.022	.009	.005	.007	.015	.028	.060	.104	.149	68
69	.127	.067	.033	.021	.008	.005	.006	.014	.030	.057	.100	.147	69
70	.117	.061	.031	.019	.008	.005	.006	.013	.030	.054	.091	.141	70
71	.104	.059	.031	.018	.008	.005	.006	.012	.032	.052	.085	.125	71
72	.102	.055	.029	.017	.008	.005	.006	.012	.032	.048	.084	.125	72
73	.087	.053	.028	.016	.007	.005	.005	.012	.030	.045	.077	.103	73
74	.081	.055	.030	.016	.007	.004	.005	.012	.031	.047	.077	.098	74
75	1.796	1.103	.615	.370	.191	.132	.150	.283	.595	.930	1.640	2.108	75

ORIGIN OF SCATTER COEFFICIENTS FOR RIGIDITY INTERVAL 5 OF 5 FOR 75 RADIAL INCREMENTS

R	HOUR UT 2	4	6	8	10	12	14	16	18	20	22	24	R
1	0.000	0.000	0.000	0.000	0.000	0.000	0.000	0.000	0.000	0.000	0.000	0.000	1
2	0.000	0.000	0.000	0.000	0.000	0.000	0.000	0.000	0.000	0.000	0.000	0.000	2
3	0.000	0.000	0.000	0.000	0.000	0.000	0.000	0.000	0.000	0.000	0.000	0.000	3
4	0.000	0.000	0.000	0.000	0.000	0.000	0.000	0.000	0.000	0.000	0.000	0.000	4
5	0.000	0.000	0.000	0.000	0.000	.054	.032	0.000	0.000	0.000	0.000	0.000	5
6	0.000	0.000	0.000	0.000	0.000	.079	.053	0.000	0.000	0.000	0.000	0.000	6
7	0.000	0.000	0.000	0.000	0.000	.062	.040	0.000	0.000	0.000	0.000	0.000	7
8	0.000	0.000	0.000	0.000	0.000	.057	.037	0.000	0.000	0.000	0.000	0.000	8
9	0.000	0.000	0.000	0.000	0.000	.059	.037	0.000	0.000	0.000	0.000	0.000	9
10	0.000	0.000	0.000	0.000	0.000	.058	.036	0.000	0.000	0.000	0.000	0.000	10
11	0.000	0.000	0.000	0.000	.091	.087	.220	.062	0.000	0.000	0.000	0.000	11
12	0.000	0.000	0.000	0.000	.139	.100	.312	.093	0.000	0.000	0.000	0.000	12
13	0.000	0.000	0.000	0.000	.099	.092	.235	.066	0.000	0.000	0.000	0.000	13
14	0.000	0.000	0.000	0.000	.132	.222	.258	.092	0.000	0.000	0.000	0.000	14
15	0.000	0.000	0.000	0.000	.288	.636	.357	.186	0.000	0.000	0.000	0.000	15
16	0.000	0.000	0.000	0.000	.229	.480	.321	.151	0.000	0.000	0.000	0.000	16
17	0.000	0.000	0.000	.036	.302	.523	.392	.131	.030	0.000	0.000	0.000	17
18	0.000	0.000	0.000	.077	.356	.539	.467	.114	.051	0.000	0.000	0.000	18
19	0.000	0.000	0.000	.116	.317	.466	.456	.253	.044	0.000	0.000	0.000	19
20	0.000	0.000	0.000	.274	.435	.451	.707	.701	.157	0.000	0.000	0.000	20
21	0.000	0.000	0.000	.297	.421	.433	.560	.521	.176	0.000	0.000	0.000	21
22	0.000	0.000	0.000	.582	.641	.502	.573	.715	.374	0.000	0.000	0.000	22
23	0.000	0.000	.118	.431	.655	.514	.516	.656	.342	0.000	0.000	0.000	23
24	0.000	0.000	.180	.569	.765	.611	.594	.760	.586	.114	0.000	0.000	24
25	.186	.377	.593	.605	.167	.122	.102	.234	.615	.723	.312	.191	25
26	.202	.311	.496	.409	.167	.103	.093	.232	.410	.462	.284	.203	26
27	.162	.262	.383	.349	.166	.089	.091	.192	.375	.351	.217	.161	27
28	.141	.225	.328	.293	.144	.081	.094	.173	.322	.308	.210	.143	28
29	.136	.211	.292	.258	.127	.075	.090	.154	.277	.280	.202	.140	29
30	.144	.214	.261	.231	.113	.072	.078	.127	.231	.261	.207	.150	30
31	.162	.228	.245	.198	.106	.069	.069	.109	.215	.247	.223	.171	31
32	.188	.240	.235	.160	.104	.066	.063	.102	.208	.226	.242	.193	32
33	.213	.238	.227	.143	.107	.066	.060	.102	.184	.218	.244	.209	33
34	.228	.231	.216	.140	.105	.066	.061	.102	.165	.219	.238	.220	34
35	.230	.225	.200	.145	.099	.064	.063	.103	.154	.217	.230	.227	35
36	.227	.216	.183	.150	.095	.065	.067	.105	.146	.209	.221	.228	36

$S_5(r,T)$

30.0 - 60.0 GV

$\zeta_5(r,T)$ 30.0 - 60.0 GV

37	.216	.201	.164	.144	.091	.066	.069	.100	.138	.191	.207	.220	37
38	.203	.185	.152	.139	.087	.068	.071	.096	.134	.180	.192	.208	38
39	.189	.170	.144	.137	.084	.071	.073	.096	.131	.171	.175	.193	39
40	.175	.155	.137	.128	.084	.075	.077	.100	.121	.153	.160	.177	40
41	.161	.141	.136	.120	.086	.080	.080	.105	.111	.135	.147	.161	41
42	.146	.129	.138	.115	.088	.082	.082	.109	.107	.123	.136	.146	42
43	.132	.121	.142	.112	.089	.082	.081	.109	.107	.116	.126	.133	43
44	.120	.115	.138	.108	.087	.079	.079	.105	.108	.113	.119	.120	44
45	.109	.113	.130	.103	.081	.074	.077	.098	.109	.113	.114	.108	45
46	.100	.113	.123	.099	.074	.069	.074	.090	.110	.115	.112	.099	46
47	.092	.113	.117	.098	.068	.063	.071	.084	.113	.119	.111	.091	47
48	.086	.114	.114	.098	.064	.058	.068	.079	.117	.122	.110	.086	48
49	.083	.114	.111	.098	.061	.055	.065	.075	.116	.122	.110	.083	49
50	.084	.113	.108	.098	.058	.051	.062	.071	.111	.119	.108	.082	50
51	.087	.111	.106	.102	.057	.049	.059	.068	.106	.115	.106	.084	51
52	.092	.110	.107	.106	.057	.047	.057	.066	.102	.114	.107	.087	52
53	.098	.110	.107	.108	.056	.045	.053	.063	.098	.114	.108	.092	53
54	.102	.108	.107	.105	.055	.044	.051	.062	.096	.113	.112	.099	54
55	.105	.107	.106	.100	.055	.043	.048	.060	.094	.111	.117	.106	55
56	.107	.107	.105	.093	.055	.043	.045	.058	.092	.109	.122	.114	56
57	.110	.108	.104	.088	.056	.043	.043	.055	.091	.106	.126	.121	57
58	.112	.109	.102	.083	.058	.043	.042	.053	.089	.104	.128	.124	58
59	.114	.109	.100	.080	.060	.044	.041	.051	.088	.103	.126	.124	59
60	.116	.110	.100	.077	.063	.045	.040	.050	.086	.104	.123	.123	60
61	.119	.110	.100	.074	.064	.045	.040	.048	.083	.104	.119	.120	61
62	.119	.110	.097	.069	.064	.045	.039	.045	.080	.101	.115	.117	62
63	.119	.109	.093	.064	.062	.043	.037	.043	.074	.097	.112	.116	63
64	.117	.108	.088	.060	.059	.041	.036	.041	.070	.093	.107	.114	64
65	.115	.106	.085	.057	.055	.039	.035	.039	.066	.089	.104	.113	65
66	.113	.103	.082	.054	.052	.037	.034	.039	.062	.086	.101	.111	66
67	.111	.100	.080	.053	.050	.035	.033	.039	.061	.083	.099	.112	67
68	.106	.093	.078	.052	.048	.035	.033	.039	.059	.079	.096	.109	68
69	.103	.090	.075	.052	.047	.035	.032	.040	.060	.078	.094	.109	69
70	.099	.086	.072	.045	.040	.031	.029	.037	.057	.076	.092	.105	70
71	.095	.083	.066	.041	.035	.033	.030	.034	.053	.075	.089	.103	71
72	.094	.082	.064	.040	.035	.034	.031	.036	.052	.073	.087	.100	72
73	.089	.079	.063	.038	.024	.022	.018	.027	.050	.070	.083	.095	73
74	.088	.077	.056	.030	.024	.023	.020	.027	.034	.060	.080	.091	74
75	5.001	4.345	3.693	2.916	2.943	2.768	2.556	2.970	3.150	3.666	4.333	4.913	75

TOTAL ORIGIN OF SCATTER COEFFICIENTS FOR FLUX BETWEEN RIGIDITIES 0 AND 60 GV

UR R / UT	2	4	6	8	10	12	14	16	18	20	22	24	R
1	0.000	0.000	0.000	0.000	0.000	0.000	0.000	0.000	0.000	0.000	0.000	0.000	1
2	0.000	0.000	0.000	0.000	0.000	0.000	0.000	0.000	0.000	0.000	0.000	0.000	2
3	0.000	0.000	0.000	0.000	0.000	0.000	0.000	0.000	0.000	0.000	0.000	0.000	3
4	0.000	0.000	0.000	0.000	.002	.019	.008	0.000	0.000	0.000	0.000	0.000	4
5	0.000	0.000	0.000	0.000	.047	.256	.126	0.000	0.000	0.000	0.000	0.000	5
6	0.000	0.000	0.000	0.000	.039	.270	.143	0.000	0.000	0.000	0.000	0.000	6
7	0.000	0.000	0.000	0.000	.041	.291	.148	0.000	0.000	0.000	0.000	0.000	7
8	0.000	0.000	0.000	0.000	.045	.339	.172	0.000	0.000	0.000	0.000	0.000	8
9	0.000	0.000	0.000	0.000	.052	.411	.207	0.000	0.000	0.000	0.000	0.000	9
10	0.000	0.000	0.000	0.000	.057	.489	.246	0.000	0.000	0.000	0.000	0.000	10
11	0.000	0.000	0.000	0.000	.395	.862	.809	.104	0.000	0.000	0.000	0.000	11
12	0.000	0.000	0.000	0.000	.747	1.168	1.322	.166	0.000	0.000	0.000	0.000	12
13	0.000	0.000	0.000	0.000	.700	1.257	1.275	.126	0.000	0.000	0.000	0.000	13
14	0.000	0.000	0.000	0.000	.804	1.556	1.419	.146	0.000	0.000	0.000	0.000	14
15	0.000	0.000	0.000	.077	1.610	2.387	2.015	.295	0.000	0.000	0.000	0.000	15
16	0.000	0.000	0.000	.092	1.957	2.573	2.328	.284	0.000	0.000	0.000	0.000	16
17	0.000	0.000	.000	.159	2.528	3.007	2.854	.611	.030	0.000	0.000	0.000	17
18	0.000	0.000	.000	.322	3.364	3.727	3.638	1.608	.051	0.000	0.000	0.000	18
19	0.000	.000	.000	.348	3.924	4.433	4.226	1.754	.044	0.000	0.000	0.000	19
20	0.000	.000	.002	1.105	5.519	5.402	5.434	4.723	.281	0.000	0.000	0.000	20
21	0.000	.003	.015	2.058	6.962	6.675	6.570	5.933	.343	0.000	0.000	0.000	21
22	.000	.034	.084	7.516	9.324	8.326	8.309	8.751	.519	0.000	0.000	0.000	22
23	.019	.309	.800	18.182	12.232	10.413	10.837	13.228	.898	0.000	0.000	0.000	23
24	2.782	2.454	15.672	31.241	18.793	17.215	16.198	26.263	11.359	.151	0.000	0.000	24
25	12.595	20.374	27.274	2.030	.260	.157	2.892	3.020	35.244	23.118	15.004	13.662	25
26	8.301	9.269	6.903	1.158	.252	.129	.179	.835	6.601	12.261	9.257	7.859	26
27	6.143	6.275	3.631	.916	.242	.112	.123	.484	3.086	7.294	6.845	6.265	27
28	4.894	4.499	2.521	.695	.212	.102	.123	.370	2.018	4.790	5.242	5.047	28
29	3.902	3.415	1.734	.583	.192	.096	.118	.320	1.447	3.433	4.153	4.095	29
30	3.161	2.729	1.422	.516	.171	.094	.108	.279	1.153	2.592	3.356	3.361	30
31	2.670	2.226	1.149	.461	.158	.091	.100	.246	.920	2.010	2.790	2.814	31
32	2.307	1.882	1.020	.375	.150	.088	.092	.213	.767	1.625	2.355	2.457	32
33	1.998	1.633	.856	.324	.149	.087	.087	.199	.661	1.380	1.990	2.086	33
34	1.740	1.413	.731	.305	.146	.086	.087	.193	.563	1.186	1.698	1.749	34
35	1.548	1.253	.626	.300	.137	.083	.087	.190	.472	1.027	1.506	1.553	35
36	1.371	1.089	.557	.289	.132	.083	.088	.184	.429	.924	1.348	1.409	36

$$\zeta(x,I) = \sum_{i=1}^{5} \zeta_i(x,T)$$

0.0 - 60.0 GV

$$\zeta(x,T) = \sum_{i=1}^{5} \zeta_i(x,T)$$

0.0 - 600.0 GV

37	1.225	.943	.506	.266	.126	.082	.088	.172	.405	.805	1.193	1.272	37
38	1.139	.850	.443	.249	.119	.083	.089	.163	.377	.701	1.064	1.185	38
39	1.064	.766	.400	.238	.114	.084	.089	.162	.360	.626	.945	1.119	39
40	.949	.700	.375	.223	.113	.087	.091	.164	.333	.567	.834	1.011	40
41	.832	.644	.366	.210	.114	.091	.094	.167	.305	.525	.750	.889	41
42	.730	.587	.353	.202	.114	.093	.095	.167	.274	.483	.694	.755	42
43	.665	.527	.348	.192	.113	.093	.095	.160	.258	.441	.641	.679	43
44	.644	.490	.327	.181	.109	.090	.094	.151	.245	.405	.605	.661	44
45	.615	.458	.299	.170	.102	.085	.092	.140	.233	.373	.553	.647	45
46	.584	.434	.267	.162	.094	.080	.089	.129	.223	.353	.511	.625	46
47	.541	.414	.247	.160	.087	.074	.085	.123	.214	.341	.481	.576	47
48	.491	.387	.231	.160	.082	.069	.082	.118	.205	.326	.458	.508	48
49	.441	.360	.221	.157	.079	.065	.078	.113	.198	.307	.432	.445	49
50	.428	.340	.210	.151	.076	.060	.073	.105	.192	.295	.426	.424	50
51	.405	.312	.203	.148	.075	.058	.071	.099	.186	.284	.405	.398	51
52	.401	.298	.198	.148	.074	.057	.069	.095	.182	.276	.387	.400	52
53	.400	.283	.189	.146	.071	.054	.064	.090	.177	.263	.366	.413	53
54	.392	.268	.183	.140	.071	.053	.061	.088	.173	.247	.349	.427	54
55	.361	.263	.183	.135	.069	.051	.057	.085	.169	.238	.326	.408	55
56	.343	.255	.178	.128	.069	.051	.054	.083	.161	.225	.313	.403	56
57	.311	.258	.181	.124	.070	.050	.052	.082	.155	.218	.299	.366	57
58	.287	.248	.177	.120	.072	.050	.050	.080	.149	.206	.284	.341	58
59	.266	.246	.177	.116	.074	.050	.048	.078	.143	.202	.270	.303	59
60	.254	.241	.174	.112	.075	.051	.048	.074	.136	.199	.261	.266	60
61	.248	.231	.166	.105	.076	.051	.047	.071	.129	.194	.252	.237	61
62	.244	.220	.156	.097	.075	.051	.046	.066	.122	.185	.243	.216	62
63	.251	.216	.146	.090	.072	.049	.045	.062	.112	.181	.241	.217	63
64	.264	.208	.137	.086	.069	.047	.044	.059	.105	.174	.239	.239	64
65	.269	.199	.127	.082	.064	.044	.042	.057	.098	.166	.231	.260	65
66	.273	.190	.123	.079	.061	.043	.041	.056	.092	.160	.227	.277	66
67	.268	.184	.118	.076	.059	.041	.040	.055	.091	.151	.221	.285	67
68	.262	.171	.114	.075	.057	.041	.039	.055	.089	.143	.214	.289	68
69	.252	.166	.110	.073	.055	.040	.038	.054	.091	.139	.206	.287	69
70	.234	.154	.105	.064	.049	.037	.035	.050	.087	.134	.193	.273	70
71	.214	.149	.098	.059	.043	.038	.036	.046	.085	.130	.184	.249	71
72	.208	.142	.094	.057	.043	.039	.037	.048	.085	.124	.181	.241	72
73	.186	.137	.092	.054	.031	.027	.024	.038	.081	.118	.170	.208	73
74	.177	.136	.087	.046	.031	.027	.025	.039	.066	.108	.166	.195	74
75	6.875	5.488	4.316	3.287	3.134	2.899	2.707	3.253	3.750	4.617	6.059	7.072	75

BIBLIOGRAPHY

Ables, J.G., Barouch, E., McCracken, K.G., 1967, Planet. Space Sci, 15, 547.

Axford, W.I., 1965, Planet. Space Sci., 13, 115.

Barnden, L.R. and Francey, R.J., 1969, Proc. ASA, 1, 236.

Barnden, L.R., 1971, to be published in Solar Physics.

Barnden, L.R., and McCracken, K.G., 1971, Proc. 6th Latin American Conference on Cosmic Rays.

Boyd, R.L.F., 1965, Space Sci. Rev., 4, 35.

Bradt, H., Mayer, W., Naranan, S., Rappaport, S. and Spada, G., 1967, Astrophys. J., 150, L199.

Brunberg, E.A. and Dattner, A., 1953, Tellus, 2, 135 and 3,269.

Coleman, P.J. Jr., Davis, L. Jr., Smith, E.J. and Jones, D.E., 1967, J. Geophys. Res., 72, 1637.

Conforto, A.M., and Simpson, J.A., 1957, Il Nuovo Cimento, 6, 1052.

Conner, J.P., Evans, W.D. and Belian, K.D., 1969, Astrophys. J., 157, L157.

Davies, R.D., 1965, Proc. 9th Int. Conf. Cosmic Rays, p35.

Dolan, J.F., 1970, Astron. J., 75, 223.

Dorman, L.I., Kaminer, N.S. and Kebuladze, T.V., 1967, Geomag. and Aeron., 7, 714.

Dorman, L.I., Kaminer, N.S. and Kebuladze, T.V., 1969, Geomag. and Aeron., 9, 653.

Duggal, S.P. and Pomerantz, M.A., 1970, Proc. 11th Int. Conf. Cosmic Rays.

Elliot, H., Thambyahpillai, T., Peacock, D.S., 1969, Proc. 11th Int. Conf. Cosmic Rays.

Fairfield, D.H., and Ness, N.F., 1967, J. Geophys. Res., 72, 2379.

Fenton, A.G., McCracken, K.G., Rose, D.C. and Wilson, B.G., 1969 Can. J. Phys., 37, 970.

Fisher, P.C. and Meyerott, A.J., 1966, IEEE Trans. Nucl. Sci., NS-13, 580.

Forman, M.A., and Gleeson, L.J., 1971, unpublished.

Francey, R.J., 1970, Unpublished Thesis.

Francey, R.J., 1971, Nature, 229, 233.

Giacconi, R. and Gursky, H., 1965, Space Sci. Rev., 4, 151.

Giacconi, R., Gursky, H., Waters, J.R., Rossi, B., Clark, G., Garmire, G., Oda, M., and Wada, M., 1966, Proc. International School of Physics, 'Enrico Fermi', course 35, Academic Press, N.Y. p73.

Gleeson, L.J. and Axford, W.I., 1967, Astrophys. J., 149, L115.

Gleeson, L.J., 1969, Planet. Space Sci., 17, 31.

Gorenstein, P., Giacconi, R., and Gursky, H., 1967 Astrophys. J., 150, L85.

Gould, R.J., 1967, Amer. J. Phys., 35, 376.

Greenstadt, E.W., Green, I.M., Inouye, G.T., Sonett, C.P., 1970, Planet. Space Sci., 18, 333.

Harries, J.R. and Francey, R.J., 1968, Aust. J. Phys., 21, 715.

Harries, J.R., 1968, Unpublished Thesis.

Hashim, A. and Thambyahpillai, T., 1969, Planet. Space Sci., 17, 1879.

Hayakawa, S., Matsuoka, M., and Sugimoto, D., 1966, Space Sci. Rev., 5, 109.

Hirshberg, J., Alksne, A., Colburn, D.S., Bame, S.J. and Hundhausen, A.J., 1970, J. Geophys. Res., 75, 1.

Jacklyn, R.M., 1965a, Il Nuovo Cimento, 36, 1135.

Jacklyn, R.M., 1965b, Proc. 9th Int. Conf. Cosmic Rays.

Jacklyn, R.M., 1966, Nature, 211, 690.

Jacklyn, R.M. and Vrana, A., 1969, Proc. A.S.A., 1, 278.

Jokipii, J.R. and Coleman, P.J., 1968, J. Geophys. Res., 73, 5495.

Jory, F.S., 1956, Phys. Rev., 103, 1068.

Lazarus, A.J. and Binsack, J.H., 1969, Ann. IQSY 3, 378.

Lewin, W.H.G., 1968, Nature, 220, 249.

Lockwood, J.A. and Razdan, H., 1963, J. Geophys. Res., 68, 1581.

Lockwood, J.A. and Webber, W.R., 1967, J. Geophys. Res., 72, 3395.

Lockwood, J.A. and Webber, W.R., 1969, J. Geophys. Res., 74, 5599.

McCracken, K.G., Rao, U.R. and Shea, M.A., 1962, Technical Report No. 77, Massachusetts Institute of Technology.

McCracken, K.G. and Rao, U.R., 1965, Proc. 9th Int. Conf. on Cosmic Rays (London).

McCracken, K.G., Rao, U.R., Fowler, B.C., Shea, M.A., Smart, D.F., 1965, IQSY Instruction Manual No. 10.

Malmfors, K.G., 1945, Arkiv for Matematik, Astronomi och Fysik 32A, No. 8.

Mathews, T., 1963, Phil. Mag., 8, 387.

Mathews, T., Venkatesan, D. and Wilson, B.G., 1969, J. Geophys. Res., 74, 1218.

Morrison, P., 1967, Annual Rev. Astron. Astrophys., 5, 325.

Palmeira, R.A.R., Bukata, R.P. and Gronstal, P.T., 1969, Planet. Space Sci., 17, 1913.

Parker, E.N., 1963, Interplanetary Dynamical Processes, Interscience Publishers, Inc., New York.

Parker, E.N., 1964, Planet. Space Sci., 12, 735.

Quenby, J.J., 1967, Planet. Space Sci., 15, 257.

Rao, U.R., McCracken, K.G. and Venkatesan, D., 1963, J. Geophys. Res., 68, 345.

Rao, U.R. and Sarabhai, V.A., 1964, Planet. Space Sci., 12, 1055.

Rao, U.R. and Agrawal, S.P., 1970, J. Geophys. Res., 75, 2391.

Schatten, K.H., Ness, N.F., Wilcox, J.M., 1968, Solar Phys., 5, 240.

Schatten, K.H. and Wilcox, J.M., 1969, J. Geophys. Res., 74, 4157.

Shukla, P.G. and Wilson, B.G., 1970, Nature, 228, 1077.

Swinson, D.B., 1969a, J. Geophys. Res., 74, 5591.

Swinson, D.B., 1969b, Proc. 11th Int. Conf. Cosmic Rays.

Swinson, D.B., 1970, "Solar Modulation Origin of 'Sidereal' Cosmic Ray Anisotropies", University of New Mexico preprint.

Wang, J.R., 1970, Astrophys. J., 160, 261.

Wibberenz, G., Hasselmann, K. and Hasselmann, D., 1969, Proc. 11th Int. Conf. Cosmic Rays.

Wilcox, J.M. and Ness, N.F., 1965, J. Geophys. Res., 70, 5793.

Wolfson, C.J. and Nobles, R.A., 1970, J. Geophys. Res., 75, 5553.

PUBLICATIONS

1. A New X-ray Object at High Galactic Latitude; Barnden, L.R. and Francey, R.J., Proc. A.S.A., 1, 236, 1969.

2. The Development of UAT Rocket Instrumentation for X-Ray Astronomy; Francey, R.J., Fenton, A.G., Fenton, K.B., Cooke, D.J., Barnden, L.R., Doherty, L.E., Gregory, A.G., McCracken, K.G., and Tuohy, I.R., Proc. A.S.A., 1, 240, 1969.

3. Cosmic Ray Modulation Produced by Radial Density Gradients in the Interplanetary Medium; Barnden, L.R., Solar Physics, 1971, to be published.

4. The Day to Day Modulation of the Cosmic Ray Anisotropy; Barnden, L.R., McCracken, K.G., Proc. 6th Latin Amer. Conf. Cosmic Rays, La Paz 1970.